Towards a Better Understanding of Inelastic Atom-Molecule Collisions

Gijsbertsen, A.

2006

document version
Publisher's PDF, also known as Version of record

Towards a Better Understanding of Inelastic Atom-Molecule Collisions

Arjan Gijsbertsen

Towards a Better Understanding of Inelastic Atom-Molecule Collisions
A. Gijsbertsen
Thesis Vrije Universiteit Amsterdam - Illustrated - With summary in Dutch
- With references

ISBN 90-8659-028-4

Printed by Ponsen & Looijen BV, Wageningen, The Netherlands

Cover: set of He-NO ion images collected via the R_{21} spectroscopic branch

VRIJE UNIVERSITEIT

Towards a Better Understanding of Inelastic Atom-Molecule Collisions

ACADEMISCH PROEFSCHRIFT

ter verkrijging van de graad Doctor aan
de Vrije Universiteit Amsterdam,
op gezag van de rector magnificus
prof.dr. L.M. Bouter,
in het openbaar te verdedigen
ten overstaan van de promotiecommissie
van de faculteit der Exacte Wetenschappen
op vrijdag 22 september 2006 om 15.45 uur
in de aula van de universiteit,
De Boelelaan 1105

door

Arjan Gijsbertsen

geboren te Rhenen

promotor: prof.dr. S. Stolte
copromotor: dr. H.V.J. Linnartz

Contents

Chapter 1

Introduction

Tho goal of this thesis is to obtain better understanding of atom-molecule scattering. Macroscopic chemical reactions and (transient effects in) mass and energy transfer phenomena should be regarded as a large set of elementary processes (or molecular encounters) that must be studied to understand these macroscopic effects. Atom-molecule scattering serves as a model system for such encounters and crossed molecular beam machines provide a powerful tool towards a better understanding of such processes. These machines allow experimentalists to study the outcome of gas phase encounters of molecules with atoms or other molecules under well defined conditions (collision energy and initial as well as final quantum state of the colliding molecules).

Collisions involving Nitric Oxide (NO) are the main subject of this study. In the past, several reaction dynamical studies - both experimental and theoretical - have focussed on the rotationally inelastic scattering of NO with a number of collision partners [1–7].

NO is both an interesting and a convenient model system. Radicals in general - as Nitric Oxide (NO) is with its unpaired electron - play an important role in combustion and atmospheric processes. It is a toxic air pollutant produced by combustion engines. NO is not only an important molecule from a chemical, but also from a biological point of view, being an intracellular signalling molecule in the bodies of mammals.

Due to the spin and orbital electronic angular momenta of its unpaired electron, NO has a non-zero angular momentum in its rotational ground state, while it is stable enough to be stored in a gas bottle. Furthermore, it is easily detected with spectroscopic methods as laser induced fluorescence (LIF) [5] and resonance enhanced multi-photon ionization (REMPI) [4,8]. Using the hexapole focussing technique [9], NO can be fully selected into a single quantum state (upper component of the Λ-doublet) as it undergoes a first order Stark effect [10]. The two components of the Λ-doublet within the same rotational level $(j, m, \overline{\Omega}, \epsilon = \pm 1)$ have opposite parity, but only a minute energy splitting. Employing (hexapole) selection of NO in a single quantum state before collision, the effect of parity changing and parity conservation on the differential cross section can be isolated from the effect of the excitation energy.

Although the outcome of a relatively simple collision process - for example a He-NO collision - can be calculated up to a reasonable degree, these calculations are computationally demanding and do usually not offer much insight in the actual physics behind it. For example, the rare gas - NO orientational dependence of the collision cross section

onto the final rotational state [2, 5, 6] could be reproduced using close-coupling calculations, but this behavior remained unexplained. The Quasi Quantum Treatment (QQT) - as presented in this thesis - provides a powerful tool for understanding collisions and for drawing several quantitative conclusions without the large numerical effort of coupled channel methods. It explains (and reproduces up to a reasonable degree) the oscillatory behavior of the steric asymmetry on the final rotational state [2] as well as the parity-pair effects that are observed in the differential cross sections for He-NO collisions [11].

The body of this thesis consists of an introduction, five articles, represented as chapters and one chapter with - until now - unpublished work. In the introduction, some theoretical and experimental background is presented that is not new, but meant to improve the readability of this thesis. Chapter 2 and 3 both question the sign of the steric asymmetry ratio. There is an unsolved discrepancy between most[1] theoretical and experiment results for collisions of rare gases and NO. There is good agreement as far as the absolute value of the steric asymmetry ratio (S) is concerned, but theory and experiments yield an opposite sign of S. What in the experiment seems to be a collision onto the O-end of the molecule, corresponds to a collision onto the N-end according to theoretical results. Chapter 2 gives a concise discussion of this sign-discrepancy, while chapter 3 bases this discussion firmly on theoretical grounds.

Chapter 4 describes the efforts to measure the sign of the permanent NO dipole. An erroneous sign of the NO dipole moment - which has never been measured - would solve the discrepancy for the steric asymmetry that is discussed in chapters 2 and 3. This experiment was carried out in the XUV physics group of Marc Vrakking at the Amolf institute and is ongoing work.

Chapter 5 and 6 report the results of He-NO and D_2-NO crossed beam ion imaging experiments, respectively. Full state selection allows for a systematic study of the effect of parity conservation and changing on the differential cross section. Chapter 5 contains, besides differential cross sections, a substantial amount of experimental information. The emphasis of Chapter 6 lies in the presence of parity pairs and the phenomenon of rotational rainbows. The scattering angle at which the differential cross section reaches its maximum is shown to be parity dependent.

The last chapter (7) describes and discusses the Quasi Quantum Treatment (QQT) that was developed in order to reach a better understanding of inelastic collisions and to allow for rapid quantitative calculations. It provides a first demonstration that quantum interferences between different orientations of the repulsive potential (that are present in the oriented wave function) are the source of the oscillation of the steric asymmetry as a function of the final rotational state. Application of the treatment to collisions of non-oriented molecules leads to a previously unrecognized propensity rule. The angular dependence of the cross sections for excitation to neighboring rotational states with the same parity is shown to be similar except of a pre-factor. The QQT provides a physical interpretation of the scattering amplitude that can be represented by a Legendre moment and a simple interference picture.

[1] except for Ar-NO calculations in Ref. [2]

1.1 The NO molecule

The Nitric Oxide (NO) molecule has an unpaired anti-bonding electron, consequently it is an open shell molecule which leads to half integer total angular momentum quantum numbers. The projection of the electronic spin angular momentum $\boldsymbol{S}$ onto the internuclear axis (z) is $\Sigma = \pm\frac{1}{2}$. In its electronic ground state, the projection of the electronic orbital angular momentum $\boldsymbol{L}$ is $\Lambda = \pm 1$. This leads to a $^2\Pi$ electronic state classification [12–14]. The rotation of the nuclear framework will be indicated as $\boldsymbol{O}$ while the total angular momentum is $\boldsymbol{j}$, with magnitude $\sqrt{j(j+1)}\hbar$.

For low rotational states, NO can be described in a Hund's case (a) [12, 15] coupling scheme, the orbital angular momentum L is strongly coupled to the internuclear axis. The rotation of the nuclear framework $\boldsymbol{O}$ points perpendicular to the nuclear axis. This leaves for the projection of $\boldsymbol{j}$ onto the internuclear axis $\Omega = \Sigma + \Lambda$, giving rise to two spin-orbit states: $\overline{\Omega} = \frac{1}{2}$ and $\overline{\Omega} = \frac{3}{2}$. $\overline{\Omega}$ is the absolute value of the projection Ω. The Hund's case (a) scheme breaks down in several cases. In highly excited rotational states, the rotation of the nuclear framework might become so fast that the electron cannot follow the nuclear rotation which leads to a decoupling of the orbital angular momentum from the internuclear axis. In lower excited rotational states it might happen that - if the absolute value of the spin-orbit coupling constant A_0 is relatively small compared to the rotational constant B_0 - the spin couples to the magnetic moment arising from any of the other angular momenta including that induced by the molecules rotation as a whole. This latter happens in the case of OH and is better described by Hund's case (b). In the limit of high j, Ω is no longer a good quantum number, although Λ is. $\boldsymbol{L}$ is still coupled to the internuclear axis. An intermediate Hund's case or Hund's case (b) provides a proper description.

Neglecting Λ-type doubling, the Hamiltonian consists of two components: one due to nuclear rotation $\boldsymbol{O} = \boldsymbol{j} - \boldsymbol{S} - \boldsymbol{L}$ and one due to spin orbit coupling $\boldsymbol{L} \cdot \boldsymbol{S}$ [13].

$$\mathcal{H}_\prime = \mathcal{H}_{rot} + \mathcal{H}_{SO} = A_0(\boldsymbol{L} \cdot \boldsymbol{S}) + B_0(\boldsymbol{j} - \boldsymbol{S} - \boldsymbol{L})^2 \tag{1.1}$$

The spin-orbit constant A_0 and the rotational constant B_0 necessary to calculate the rotational energy of a NO molecule in the $\nu = 0$, $X^2\Pi$ state are $A_0 = 123.13\ cm^{-1}$ and $B_0 = 1.6961\ cm^{-1}$ [17]. This Hamiltonian allows us to calculate the rotational energy of the molecule in a certain rotational state. The rotational part of the wave function of an NO molecule (assuming Hund's case (a)) is given by:

$$|j, m, \overline{\Omega}, \epsilon\rangle = \frac{1}{\sqrt{2}}\Big[|j, m, \overline{\Omega}\rangle + \epsilon|j, m, -\overline{\Omega}\rangle\Big]. \tag{1.2}$$

where m is the projection of $\boldsymbol{j}$ onto a space-fixed Z-axis and $\epsilon = \pm 1$ is the symmetry index. The parity of a (wave-) function is defined by its behavior under parity transformation (inversion), which acts as an unitary operator $\boldsymbol{P}$ on a wave function ψ.

$$\boldsymbol{P}\psi(\boldsymbol{r}) = \psi(-\boldsymbol{r}) = p\psi(\boldsymbol{r}) \tag{1.3}$$

The total parity p of a rotational state (eigenvalue of $\boldsymbol{P}$) is provided by Brown et al. [18].

$$p = (-1)^{j-\epsilon/2}. \tag{1.4}$$

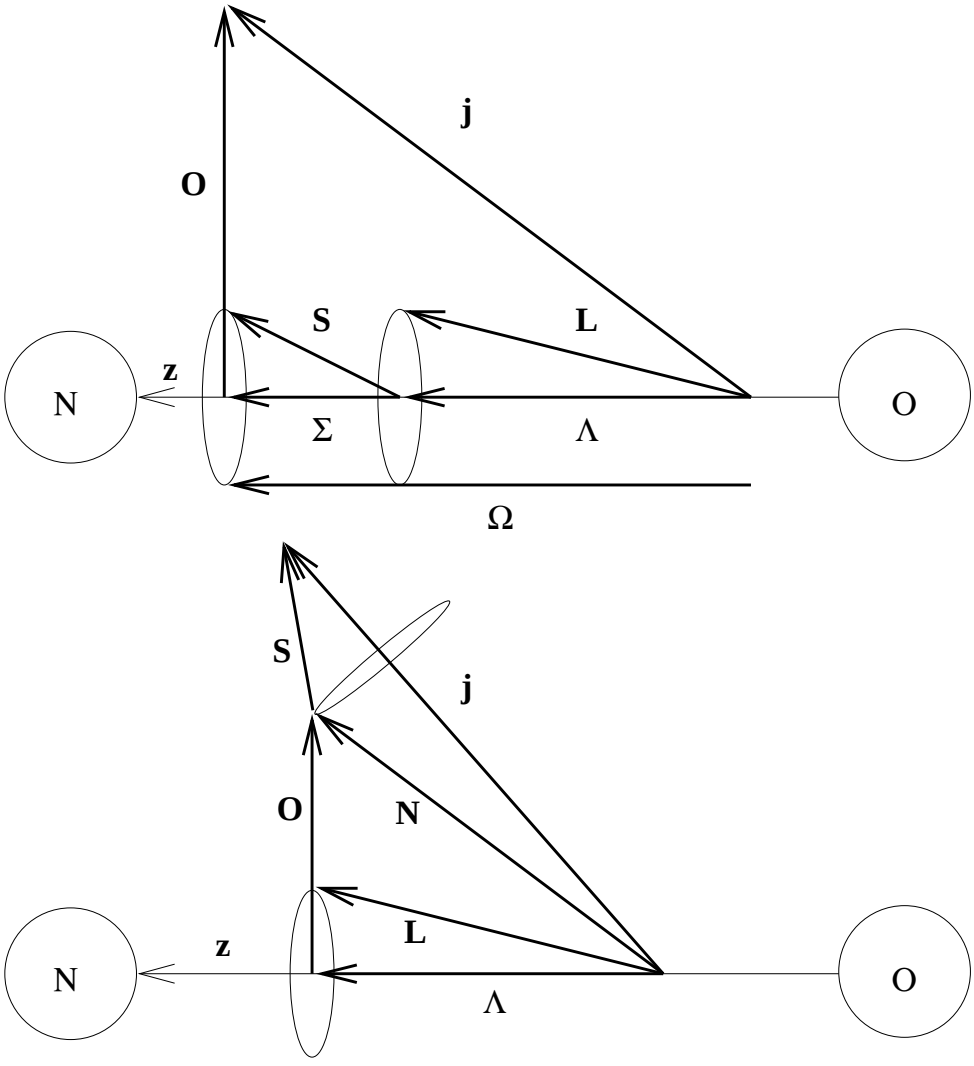

Figure 1.1: Hund's case (a) coupling (upper panel) and Hund's case (b) coupling (lower panel). In this figure we adopt the convention that the molecular axis points from the O towards the N atom [16].

For NO the $|j, m, \Omega\rangle$ rotational wave function can explicitly be written as [13]:

$$|j, m, \Omega\rangle = \sqrt{\frac{2j+1}{4\pi}} D^{j*}_{m,\Omega}(\phi, \gamma, 0) = (-1)^{m-\Omega} \sqrt{\frac{2j+1}{4\pi}} D^{j}_{-m,-\Omega}(\phi, \gamma, 0) \tag{1.5}$$

however, the function in Eq. 1.2 is strictly speaking only correct for $j = \frac{1}{2}$. For higher rotational states intermediate Hund's case coupling schemes are applied. For NO this effect remains rather small [16], but for example for OH it is large [19].

In case of intermediate Hund's case coupling, symmetrization of the case (a) wave functions to Ω leads to the following result [13, 19]:

$$\begin{aligned} |F_1, j, m, \epsilon\rangle &= a\,|j, m, \overline{\Omega} = \frac{1}{2}, \epsilon\rangle + b\,|j, m, \overline{\Omega} = \frac{3}{2}, \epsilon\rangle \\ |F_2, j, m, \epsilon\rangle &= a\,|j, m, \overline{\Omega} = \frac{3}{2}, \epsilon\rangle - b\,|j, m, \overline{\Omega} = \frac{1}{2}, \epsilon\rangle. \end{aligned} \tag{1.6}$$

The mixing coefficients are:

$$\begin{aligned} a &= \sqrt{\frac{X + (Y-2)}{2X}}, \\ b &= \sqrt{\frac{X - (Y-2)}{2X}}, \end{aligned} \tag{1.7}$$

with

$$X = \sqrt{4\Big(j + \frac{1}{2}\Big)^2 + Y\Big(Y - 4\Big)} \quad \text{and} \quad Y = \frac{A_0}{B_0}.$$

The rotational energy of a diatom in a $\nu = 0$, $^2\Pi$ state follows from Eq. 1.1 and 1.6. It is given by [13]:

$$E(j) = B_0 \left[\Big(j - \frac{1}{2}\Big)\Big(j + \frac{3}{2}\Big) \pm \sqrt{4\Big(j + \frac{1}{2}\Big)^2 + Y\Big(Y - 4\Big)} + Y - 2 \right] \tag{1.8}$$

The $\pm$ in Eq. 1.8 distinguishes between the upper F_2 (dominated by $\overline{\Omega} = \frac{3}{2}$ if $A_0 > 0$) and the lower F_1 (dominated by $\overline{\Omega} = \frac{1}{2}$ if $A_0 > 0$) spin-orbit state. For NO, the two spin orbit states - often indicated by $^2\Pi_{\frac{1}{2}}$ and $^2\Pi_{\frac{3}{2}}$ - differ about 121 cm^{-1} in energy, the latter having the highest energy.

For the $^2\Pi_{\frac{1}{2}}$ states that are well approximated by case (a) coupling, the Λ-type splitting varies linearly with j [13]. It can approximately be expressed as [20]:

$$W_\Lambda = W_g\Big(j + \frac{1}{2}\Big). \tag{1.9}$$

Burrus and Gordy [20] obtained for the energy splitting of the $j = \frac{1}{2}$ Λ-doublet $W_g = 0.0118$ cm^{-1}. The Λ-splitting for the $^2\Pi_{\frac{3}{2}}$ component is much smaller in its lowest $j = 3/2$ state (4×10^{-5} cm^{-1}) [21] but increases with the third power of j [13].

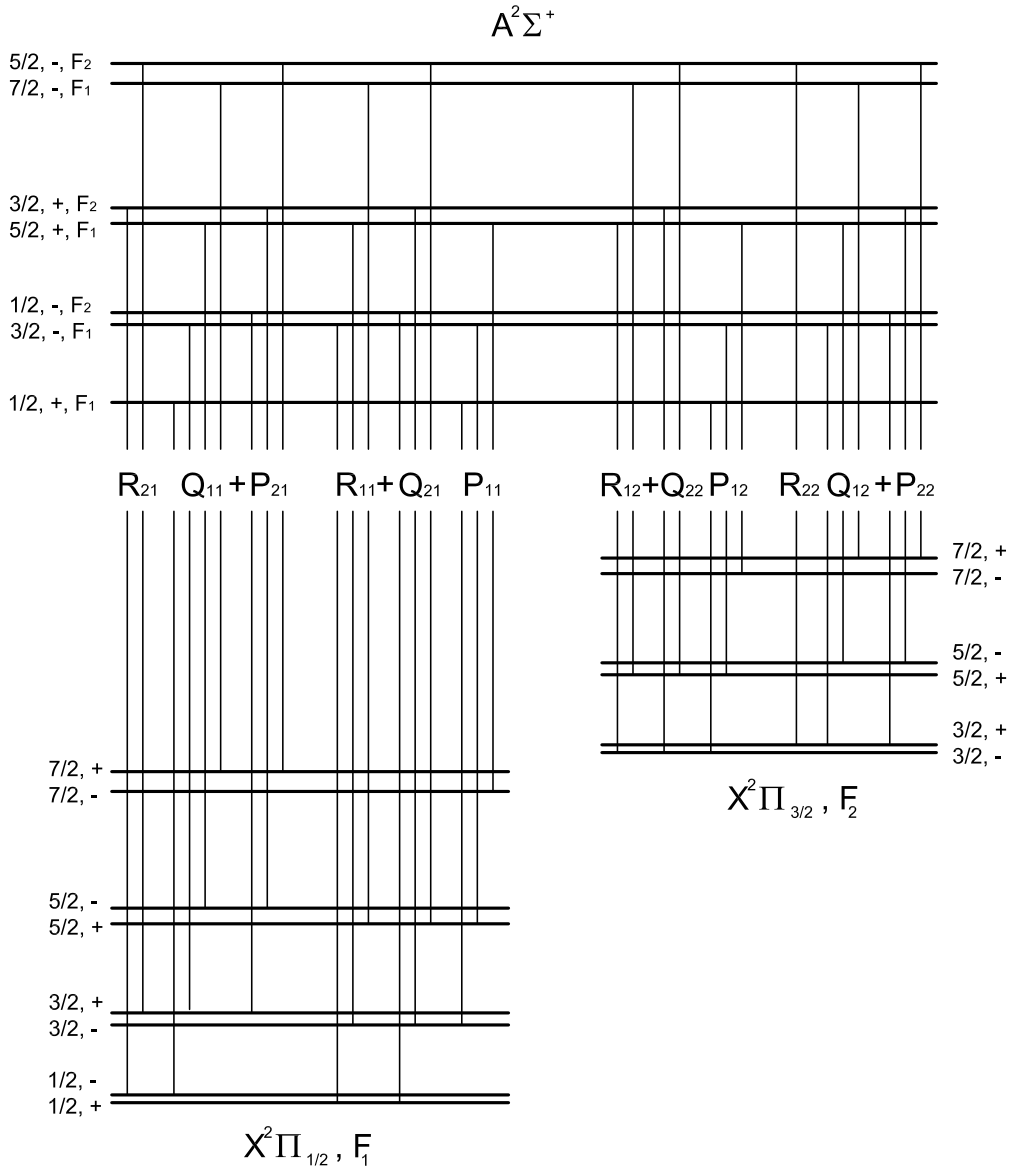

Figure 1.2: This figure gives the spectroscopic branches for the $A^2\Sigma^+ \leftarrow X^2\Pi$ transition used within this thesis following the Hund's case (a) convention. The rotational levels are labelled with their rotational quantum number j and overall parity ($\pm$). Recall that parity p and symmetry index ϵ relate as $p = (-1)^{j-\epsilon/2}$, the upper component of the Λ-doublet, always has $\epsilon = -1$, while the lower component has $\epsilon = 1$. The energy differences are taken arbitrarily and are not scaled to the actual values. In that case, the distance between the components of the Λ-doublet (and ρ-doublet) would be much smaller. For the branches that are connected via a +, we - with the bandwidth of our laser - cannot distinguish between spectroscopic signals from both branches.

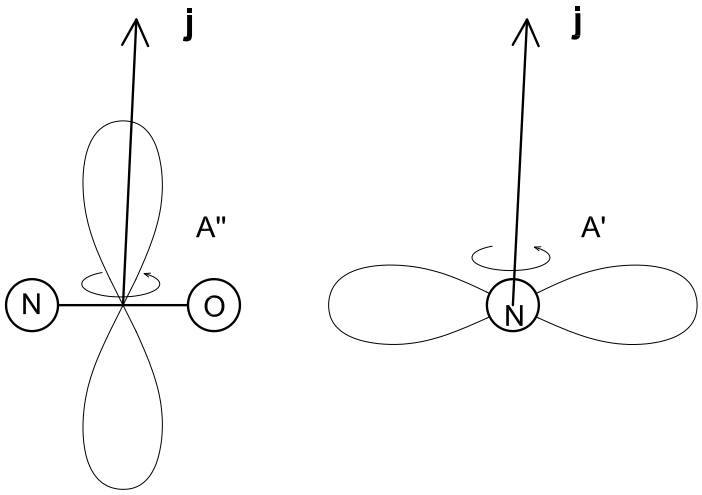

Figure 1.3: Schematic representation of A'' and A' symmetry cases for large j for NO.

In addition to $\epsilon = \pm 1$ (or e/f) labels, one assigns the components of the Λ-doublet using A' and A'' labels. These labels reflect whether the electronic wave function is respectively symmetric or anti-symmetric for reflection in the plane of rotation in the limit of large j quantum numbers [13, 22]. The azimuth angle χ around the NO-axis (z-axis of the molecule fixed frame) is used to designate the wave function of the unpaired $p\,\pi$ electron. This angle is set 0 in the rotational NO wave function as defined in Eq. 1.5. In the limit of large j, the rotation of the molecule is in the $x-z$-plane. At the x-axis, $\chi = 0$, at the y-axis (around which the molecule rotates in the high j limit), $\chi = \pi/2$. Fig. 1.3 depicts the eigenfunctions of the unpaired electron in the symmetric $^2\Pi(A')$ and antisymmetric $^2\Pi(A'')$ Λ-doublet states in the limit of large j. At low values of j, the eigenfunctions of the unpaired $p\,\pi$ electron will be a mixture of the symmetric and antisymmetric (large j) electron wave functions. A measure of the symmetry of the electron distribution is provided by [13]:

$$\Delta = \langle\Psi|\cos^2\chi - \sin^2\chi|\Psi\rangle = \pm\sqrt{\frac{X^2-(Y-2)^2}{4X^2}}. \tag{1.10}$$

In the low j limit, with both the electron lobes equally present $\Delta = 0$, while $\Delta = 1/2$ for the symmetric A' case and $\Delta = -1/2$ in the antisymmetric A'' case. Note that in case of pure Hund's case (a) $\Delta = 0$. Mixing between levels $\Pi_{1/2}$ and $\Pi_{3/2}$ manifolds with the same values of j and ϵ (see Eq. 1.6) is responsible for this effect. In this work, the highest considered j' value of He-NO is 12.5, which leads to a value of $|\Delta| = 0.13$. This corresponds to about one third of perfect orbital alignment at high j. Mixing will affect the alignment dependent detection probability [23], but this effect is ignored in our analysis in Chapter 5. Moreover, the presence of directed lobes also influences the outcome of collisions [24]. In the current work (Chapter 7) the outcome appears to be

dominated by parity effects.

The energy levels for an $X^2\Pi$ molecule like NO are drawn schematically - not scaled - in Fig. 1.2. This figure also shows the spectroscopic branches for available $A^2\Sigma^+ \leftarrow X^2\Pi$ transitions. There are usually three branches available for each rotational state, two of these coincide and could not be resolved throughout this work. Coinciding branches in Fig. 1.2 are connected via a "+".

1.2 Stark effect and hexapole focussing

Quantum state selection is essential in molecular beam experiments. In molecular dynamics research one attempts to obtain insight into reactions and collisions on the most elementary scale: that of single molecules. Having a set of molecules in different states as a starting point complicates the analysis of experimental results, or even makes it impossible.

Adiabatic expansion cools the molecules in the beam and assures that most of these molecules are in their lowest rotational state. Subsequent application of hexapole focussing allows for full state selection, in which molecules are selected in a single quantum state. Hexapole state selection exploits the (first order) Stark effect.

The technique of focussing polar molecules in static electric fields was developed in the 1950s [25]. Hexapole focussing is since these years used in several places [10,19,26–28] but did not evolve into a widely used method.

The Stark effect arises as a shift of the energy levels of an atom or a molecule in an electric field $\boldsymbol{E}$ [29]. The Z-axis is defined along $\boldsymbol{E}$. In such a field, the Hamiltonian $\mathcal{H}$ contains the additional term $V = -\boldsymbol{\mu_{el}} \cdot \boldsymbol{E} = -\mu_{el} E \cos\theta$, where $\boldsymbol{\mu_{el}}$ is the electric dipole moment vector of the molecule and θ is the polar angle between the dipole and the electric field.

$$\mathcal{H} = \mathcal{H}_0 - \mu_{el} E \cos\theta \tag{1.11}$$

This effect can be calculated via perturbation theory. As an example, the first order Stark correction to the energy will be calculated for NO. The NO wave-function in its electronic ground state is (Eq. 1.2):

$$|j, m, \overline{\Omega}, \epsilon\rangle = \frac{1}{\sqrt{2}}\Big[|j, m, \overline{\Omega}\rangle + \epsilon|j, m, -\overline{\Omega}\rangle\Big].$$

In this equation, j denotes the rotational angular momentum quantum number, m represents its projections onto the space fixed z-axis (for now defined along $\boldsymbol{E}$), $\overline{\Omega}$ is the absolute value of the projection of j onto the molecule fixed axis (defined along $\boldsymbol{\mu_{el}}$) and ϵ is the symmetry index that distinguishes between the upper ($\epsilon = -1$) and the lower ($\epsilon = 1$) component of the Λ-doublet.

Assuming a small energy splitting (W_Λ) between both Λ-doublet components (compared to their rotational constant B), the first order correction Stark energy matrix elements are (note that $\cos\theta = D^1_{0\,0}(0, \theta, 0)$):

$$-\mu_{el} E \ \langle j, m, \overline{\Omega}, \epsilon | D^1_{0\,0} | j, m, \overline{\Omega}, \epsilon'\rangle =$$
$$\frac{\mu_{el} E}{2}\Big[\langle j, m, \overline{\Omega}| \cos\theta |j, m, \overline{\Omega}\rangle + \epsilon\epsilon' \langle j, m, -\overline{\Omega}| \cos\theta |j, m, -\overline{\Omega}\rangle\Big]. \tag{1.12}$$

The diagonal matrix elements ($\epsilon = \epsilon'$) vanish. Using

$$|j, m, \Omega\rangle = \sqrt{\frac{2j+1}{4\pi}} D^{j\,*}_{m\Omega}(\phi, \theta, 0) \tag{1.13}$$

and from Eq. 3.119 and 3.125 of Ref. [13], the Stark effect $W^{(1)}$ (that does not invoke contributions for $j' \neq j$) follows as:

$$W^{(1)} = -\epsilon \left[\left(\frac{W_\Lambda}{2} \right)^2 + \left(\mu_{el} E \frac{\overline{m\Omega}}{j(j+1)} \right)^2 \right]^{\frac{1}{2}} + \epsilon W_\Lambda / 2. \tag{1.14}$$

For relatively high fields, $W^{(1)}$ becomes linear and reduces to

$$W^{(1)}_{lin} = -\epsilon \mu_{el} E \frac{\overline{m\Omega}}{j(j+1)}, \quad \text{where:} \quad \langle \cos\theta \rangle = \epsilon \frac{\overline{m\Omega}}{j(j+1)}. \tag{1.15}$$

In this equation one immediately sees that molecules in an "ϵ = negative" state are low field seeking - their energy increases when the field strength increases - while those in the "ϵ = positive" state seek high fields. The expectation value of $\cos\theta$ is indicated by $\langle \cos\theta \rangle$.

The second order correction to the energy level is given by [25, 29]:

$$W^{(2)} = (\mu_{el} E)^2 \sum_{j' \neq j} \frac{|\langle j\, K\, m | \cos\theta | j'\, K'\, m' \rangle|^2}{E^{(0)}_{j,K} - E^{(0)}_{j',K'}}, \tag{1.16}$$

the more general K also includes Ω. For Σ state diatomic and linear polyatomic molecules with energy eigenvalue $E^{(0)}_j = B\, j(j+1)$ this yields ($m' = m$ and $j' = j \pm 1$) for $K = 0$:

$$W^{(2)} = \frac{(\mu_{el} E)^2}{B j(j+1)} \; \frac{j(j+1) - 3m^2}{2(2j-1)(2j+3)}. \tag{1.17}$$

Note that states with $j(j+1) - 3m^2 > (<) 0$ are in low (high) field seeking states when $\mu_{el} E \ll 2B$. The general equation for $K \neq 0$ is provided in Ref. [30].

$$W^{(2)} = \frac{(\mu_{el} E)^2}{2B} \; \frac{(j^2 - K^2)(j^2 - m^2)}{j^3 (2j-1)(2j+1)} \; - \; \frac{[(j+1)^2 - K^2][(j+1)^2 - m^2]}{(j+1)^3 (2j+1)(2j+3)}. \tag{1.18}$$

For molecules in states that carry a first order Stark effect and are exposed to relatively weak electric fields ($\mu_{el} E \ll B$), these higher order energy terms can be neglected [26, 27]. Molecules can also be focussed via their second order Stark effect. Not a hexapole, but a quadrapole is ideal for this purpose [25, 27]. Focussing molecules employing their second order Stark effect in a hexapole [27] is however also possible. For OCS one observes a focussing maximum for the $|j\, m\rangle = |1\, 0\rangle$ state of the ground vibrational state via the second order Stark effect as well as maxima for the l-doubled $|jlM\rangle$ excited vibrational states via the first order Stark effect [27, 31].

Anderson in Ref. [32] provides a treatment to calculate the tracks that symmetric top molecules follow within a hexapole, calculating the Stark energy up to a high order. Errors may occur if only the first and or second order Stark effect are considered for trajectories

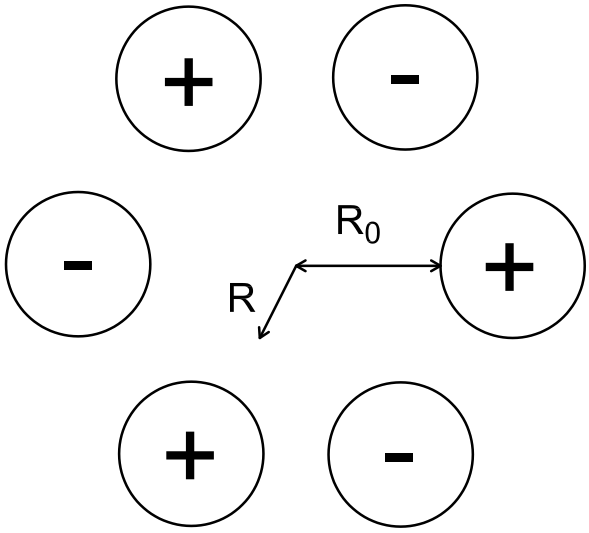

Figure 1.4: Schematic representation of a hexapole state selector. A positive voltage ($+V_0$) is applied on three of the rods, while a negative voltage ($-V_0$) is applied to the other rods. Molecules that reside in the upper (low field seeking) component of the Λ-doublet are pushed towards the center of the hexapole while those in the lower (high field seeking) component are pulled towards the rods. The hexapole is designed to the "Dutch convention": the rod diameter equals the hexapole inner radius R_0 [32].

in hexapole fields [32]. Within the scope of this thesis it is instructive to calculate an explicit expression for the path that is followed by a rigid rotor due to the first order Stark effect.

The potential of the hexapole field is [25]:

$$V = V_0 \Big(\frac{R}{R_0}\Big)^3 \cos 3\phi \tag{1.19}$$

where R_0 is the inner radius of the hexapole, and R and ϕ are cylindrical coordinates. An ideal hexapole field is given by $E = 3V_0R^2/R_0^3$. A schematic representation of a hexapole is provided in Fig. 1.4. Molecules in the hexapole feel a force $F = -dW/dR$, which for the first order Stark effect becomes:

$$F_{hex} = -\frac{dW^{(1)}}{dR} = \frac{\mu_{el} 6V_0 R}{R_0^3} \; \frac{\epsilon\overline{m\Omega}}{j(j+1)} \tag{1.20}$$

The distance from the pulsed nozzle to the entrance of the hexapole is given by L_1, the length of the hexapole by L_2, and the distance from the exit of the hexapole to the focal point is given by L_3. Within the hexapole, the molecules move with respect to R via:

$$\frac{d^2R}{dt^2} - CR = 0 \quad \text{with} \quad C = \frac{6V_0\mu_{el}}{m_M R_0^3} \; \frac{\epsilon\overline{m\Omega}}{j(j+1)}, \tag{1.21}$$

while their velocity in the z-direction remains constant. To avoid confusion, the mass of the molecules is for now indicated with m_M. If one assumes the nozzle to be a point source, the velocity of the (low field seeking $\epsilon < 0$) molecules along R at the entrance of the hexapole ($v_R(t = 0)$) is given by:

$$v_R(t = 0) = \frac{R(t = 0)v_z}{L_1}. \tag{1.22}$$

This initial condition - in order to lead to a trajectory - has to be substituted in:

$$R(t) = R(t = 0)\cos(\sqrt{C}t) + v_R(t = 0)\,\frac{1}{\sqrt{C}}\,\sin(\sqrt{C}t). \tag{1.23}$$

Note that in Eq. 1.23, the moment at which the molecules enter the hexapole is given by $t = 0$. The velocity v_R of the molecules before entrance of the hexapole and after their exit of the hexapole remains constant. To keep things simple, it will be assumed that the hexapole is long so that "edge effects" at the entrance and exit of the hexapole can be neglected. Further it is assumed that the acceptance angle of the hexapole is relatively small, so v_z is defined only by the expansion ($\sqrt{5kT/2m_M}$) and is independent of the position at which molecules enter the hexapole. Using $t = (z - L_1)/v_z$ in Eq. 1.23(which defines the pulsed nozzle at $z = 0$), the trajectory of the molecules in low field seeking states is given by:

$$R(z) = v_R(z = 0)\frac{z}{v_z} \quad \text{with} \quad 0 \le z \le L_1, \tag{1.24}$$

$$R(z) = R(z = L_1)\cos\Big(\sqrt{C}\frac{z - L_1}{v_z}\Big) + \frac{v_R(z = 0)}{\sqrt{C}}\sin\Big(\sqrt{C}\frac{z - L_1}{v_z}\Big) \quad \text{with} \quad L_1 \le z \le L_1 + L_2, \tag{1.25}$$

$$R(z) = v_R(z = L_1 + L_2)\frac{z - L_1 - L_2}{v_z} + R(z = L_1 + L_2) \quad \text{with} \quad L_1 + L_2 \le z \tag{1.26}$$

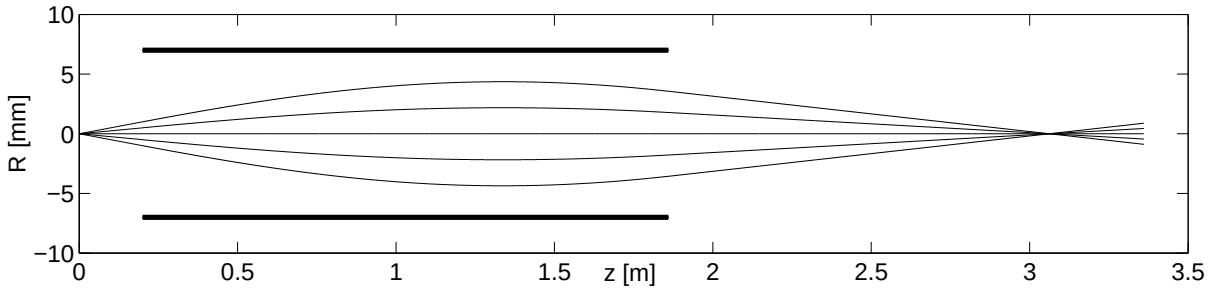

Figure 1.5: Hexapole focussing curves for NO, the hexapole considered in this figure is that of the crossed molecular beams machine at the Laser centre of the Vrije Universiteit [5,11]. The rod diameter and inner radius of the hexapole equal 7 mm.

Note that:

$$v_R(z = L_1 + L_2) = \frac{dR}{dt}\Big|_{z=L_1+L_2} = -\sqrt{C}R(z = L_1)\sin\left(\sqrt{C}\frac{L2}{v_z}\right) + v_R(z = 0)\cos\left(\sqrt{C}\frac{L_2}{v_z}\right) \tag{1.27}$$

As an example, some hexapole trajectories are plotted in Fig. 1.5. A very convenient equation that gives the focussing distance of a hexapole is provided by Stolte et al. [33]:

$$L_3 = \frac{L_1 + \frac{1}{\kappa}\tan\kappa L_2}{\kappa L_1 \tan\kappa L_2 - 1}, \tag{1.28}$$

with

$$\kappa = \sqrt{\frac{3V_{hex}\mu_{el}}{m_M {R_0}^3 v_z^2}\,\frac{-\epsilon\overline{m\Omega}}{j(j+1)}}$$

In these equations V_{hex} is the voltage difference between the rods: $V_{hex} = 2V_0$, L_3 is the distance between the exit of the hexapole and the focussing point.

The standard focussing equation for a hexapole [26]:

$$V_0 = \frac{(n\pi)^2 R_0^3}{6L_2^2}\frac{m_M v_z^2}{\mu_{el}}\frac{j(j+1)}{\epsilon\overline{m\Omega}} \tag{1.29}$$

is a convenient approximation for the hexapole voltage, but neglects the effect of the straight path before entering and after exciting the hexapole. It should only be used if the hexapole (nearly) covers the whole path of the molecules. On the other hand, Eqs. 1.26 and 1.28 are not exact either. These equations slightly underestimate the hexapole voltage needed for focussing of NO, as W_Λ is relatively large and cannot be neglected in Eq. 1.14. This leads to a nonlinear dependence of $W^(1)$ onto the electric field near the hexapole axis.

1.3 Collision Theory

For more detailed information on collision theory, the reader is referred to Refs. [33–38] and to chapter 3 and 7 of this work. This section focusses on some background knowledge

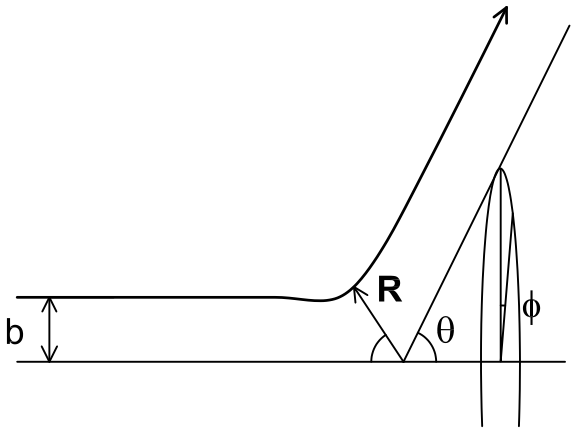

Figure 1.6: Classical scattering trajectory for scattering on a mostly repulsive shell. The center of the potential is approached, first some attraction is seen, then the repulsive part takes over. Note that in case of an anisotropic interaction potential ϕ in general does not remain constant during collision.

that is necessary to understand the main part of this thesis. The differential cross section, center-of-mass and laboratory systems, Newton diagram, rainbow and glory scattering will briefly be explained.

The main observables in crossed beam collision experiments are the differential and the integral cross sections. Potential Energy Surfaces (PESs) govern chemical reactions but cannot be observed directly. Theoreticians calculate PESs for a certain system, use the PESs to calculate differential or integral cross sections and then compare them to experimental values as a test.

In figure 1.6 a typical trajectory for scattering onto a mostly repulsive potential is drawn. The atom approaches the molecule with an impact parameter b, is first slightly attracted and then repelled. The scattering angles θ and ϕ are the spherical angles between the incoming and outgoing momenta outside the interaction region. It is the dependence of the amount of scattered molecules (into a certain state) on this angle that can be experimentally observed. This dependence is usually expressed as the differential cross section.

The differential cross section $\frac{d\sigma}{d\omega}$ is given by [34]

$$\frac{d\sigma}{d\omega} = \frac{\text{scattered current per unit solid angle}}{\text{incident current per unit surface}} \tag{1.30}$$

The integral collision cross section is depicted by σ while the solid angle element is given by $d\omega = \sin\theta d\theta d\phi$. Current stands for amount of incident particles per unit time. The integral cross section follows immediately as:

$$\sigma = \int_0^{2\pi} \int_0^{2\pi} \frac{d\sigma}{d\omega} sin\theta d\theta d\phi \tag{1.31}$$

In the case of inelastic scattering from an initial to a final ($i \rightarrow f$) state, σ should be replaced by $\sigma_{i \rightarrow f}$.

In case of an isotropic orientation distribution, the scattering process is cylindrically symmetric around the initial relative velocity (z-axis), which makes ϕ redundant. Upon substitution of $d\sigma = 2\pi b db$ and $d\omega = 2\pi \sin\theta d\theta$ one obtains for the differential cross section:

$$\frac{d\sigma}{d\omega} = \left| \frac{2\pi b db}{2\pi sin\theta d\theta} \right| = \left| \frac{b}{\sin\theta \frac{d\theta}{db}} \right| \tag{1.32}$$

It is easily seen that the differential cross section becomes large if $\sin\theta$ and $\frac{d\theta}{db}$ are close to 0. Singularities in the classical differential cross section at $\sin\theta \rightarrow 0$, (so $\theta = 0, \pi, \ldots$) are denoted glory effects The singularity at a maximum or minimum point of the deflection function $\theta(b)$ (where $\frac{d\theta}{db} = 0$) is called the rainbow singularity. The rainbow angle corresponds to that angle where the density of classical trajectories rises to infinity [34]. Quantum mechanically the singularities are smoothed and become maxima. The rainbow and glory angles correspond semi-classically to the angles of inflection and the maximum of the phase shift function $\eta(b)$.

Until now, scattering with respect to the origin of the potential is assumed. In collision experiments however, there are always two moving particles (with laboratory coordinates $\boldsymbol{r_1}$ and $\boldsymbol{r_2}$, velocities $\boldsymbol{v_1}$ and $\boldsymbol{v_2}$ and with masses m_1 and m_2) that collide. A more convenient coordinate system than the "laboratory" frame is the "center-of-mass" frame, sometimes also referred to as the "collision" frame. The center-of-mass of the collision system is taken as the origin of this coordinate system. The movement of the whole system is factored out, which leaves only the relative components. The center-of-mass velocity ($\boldsymbol{v_{cms}}$) - that is unaltered by the collision - and the relative velocity $\boldsymbol{v_{rel}}$ replace $\boldsymbol{v_1}$ and $\boldsymbol{v_2}$.

$$\boldsymbol{v_{cms}} = \frac{m_1}{m_1 + m_2}\boldsymbol{v_1} + \frac{m_2}{m_1 + m_2}\boldsymbol{v_2} \quad \text{and} \quad \boldsymbol{v_{rel}} = \boldsymbol{v_1} - \boldsymbol{v_2}. \tag{1.33}$$

The position vectors are obtained in a similar manner:

$$\boldsymbol{r_{cms}} = \frac{m_1}{m_1 + m_2}\boldsymbol{r_1} + \frac{m_2}{m_1 + m_2}\boldsymbol{r_2} \quad \text{and} \quad \boldsymbol{R} = \boldsymbol{r_1} - \boldsymbol{r_2}. \tag{1.34}$$

The kinetic energy T and the angular momentum L can be split up in a center-of-mass component and a relative component [34]:

$$T = \frac{1}{2}\mu_{el} v_{rel}^2 + \frac{1}{2}(m_1 + m_2) v_{cms} \tag{1.35}$$

$$L = \mu_{el} \boldsymbol{R} \times \boldsymbol{v_{rel}} + (m_1 + m_2)\boldsymbol{r_{cms}} \times \boldsymbol{v_{cms}} \tag{1.36}$$

$$\text{with reduced mass} \quad \mu_{el} = \frac{m_1 m_2}{m_1 + m_2}$$

As the potential energy is independent of the center-of-mass velocity and position, the center of mass motion may be omitted, which simplifies our calculations.

The relation between the center-of-mass frame and the laboratory frame are demonstrated in a Newton-diagram in Fig. 1.7. The center-of-mass velocity remains unaltered by the collision. The relative velocity can divided into two components for each of the

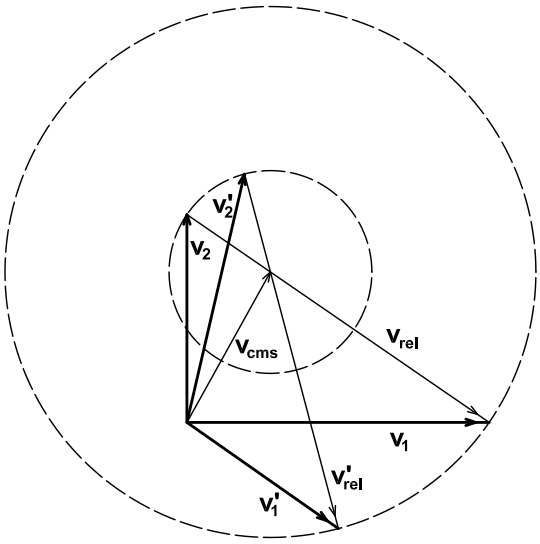

Figure 1.7: To illustrate the relation between the center-of-mass frame and the laboratory frame, this Newton diagram for elastic scattering of an arbitrary collision is plotted. Velocities after collision are marked with a prime. In case of inelastic scattering, part of the translational energy is transformed into internal energy, which leads to a smaller $\boldsymbol{v'_{rel}}$ and thus a smaller radius for the scattering spheres (indicated by the dashed circles).

particles. The particles have a velocity in the center-of-mass frame of

$$\boldsymbol{v_{1,cms}} = \frac{m_2}{m_1 + m_2}\boldsymbol{v_{rel}} \tag{1.37}$$

$$\boldsymbol{v_{2,cms}} = -\frac{m_1}{m_1 + m_2}\boldsymbol{v_{rel}}. \tag{1.38}$$

Note that $\boldsymbol{v_{2,cms}}$ points antiparallel to the relative velocity, while $\boldsymbol{v_{1,cms}}$ is directed parallel to v_{rel}. The scattering angles θ_1 and θ_2 are defined as the angles between $\boldsymbol{v_{1,cms}}$ and $\boldsymbol{v'_{1,cms}}$ and between $\boldsymbol{v_{2,cms}}$ and $\boldsymbol{v'_{2,cms}}$ respectively. In the case of inelastic scattering, part of the translational energy is transferred into internal energy. This leads to a smaller $\boldsymbol{v'_{rel}}$ and thus to scattering spheres with a smaller radius.

1.4 Ion Imaging

The goal of this section is to provide the reader with some basic knowledge concerning the ion imaging technique, making it easier to read the main part of this thesis. It does not have the pretention to be complete. For more detailed information the reader is referred to Ref. [39–41]. Experimental details can be found in Chapter 5.

The measurement of the velocity of particles (both its absolute value and direction) is necessary for several applications in molecular dynamics, often in combination with their internal energy [39]. Conservation laws help us to understand reactive and inelastic

encounters of molecules and photodissociation events, but are useful only if most velocities and internal energies are well known. Pure state selection (adiabatic expansion and hexapole state selection) provides a beam of molecules with well defined initial internal and translational energy and state-of-the-art spectroscopic techniques allow us to only ionize molecules (fragments) that are in selected final rotational states with well-defined internal energy. The ion-imaging technique provides the velocity distribution of the ionized fragments, thus leading to their final translational energy and completing the picture.

In the early days of ion imaging [42], molecules were ionized in a homogeneous electric field between a positive plate (repeller) and a negative grid. Upon ionization, the positive ions are accelerated along the electric field lines before entering the field free flight-tube. At the end of this tube a position sensitive detector is placed. All ions have the same velocity before entering the flight tube, their point of impact on the detector reflects their velocity component perpendicular to the tube.

The position sensitive detector usually consists of a set of two micro channel plates (MCPs), a phosphor screen and a CCD (Charge Coupled Device) camera. If an ion hits the MCP's, electrons are released and multiplied trough the channels of the MCPs. A cloud of electrons reaches the phosphor screen, that shows a bright dot at the position of electron impact. The position of such a bright spot can directly be related to the velocity of the molecule or fragment before ionization. The camera collects images that show the intensity on the phosphor screen. This intensity directly reflects the 2-dimensional velocity distribution of the detected molecule/fragment prior to ionization.

There are some disadvantages to working with grids. First, the openings in the grid behave like small electrostatic lenses, which leads to a blurring of the images. This effect becomes worse if the grid is positioned far away from the detector. A second disadvantage is that ions that originate from different places, but have the same velocity, end up at different positions on the detector. To collect sharp images, one needs a ionization volume that is as small as possible, which is especially disadvantageous when one has to cope with small signals.

Both these problems were solved when Eppink and Parker [43] introduced the velocity mapped imaging technique. The grid was replaced by an ion lens that projects the velocity (its component perpendicular to the flight tube) onto the detector. In this geometry, all molecules that have the same velocity perpendicular to the flight tube end up at the same position of the detector. Fig. 1.8 illustrates the improvement that is achieved when replacing the grid by a lens. It should be noted that the lens works perfect only for molecules in a plain perpendicular to the flight tube. Molecules that are ionized closer to the extractor or further away are not as well focussed. Most ideal would be to use a "laser sheet" for ionization.

The ion optics as used for the experiments described in chapters 5 and 6 are schematically drawn in Fig. 1.9. The ion lens is usually referred to as an extractor, the voltages indicated in the figure are typical. However, the voltages of the repeller and the extractor are often changed to $V_{rep} = 500$ V and $V_{ex} = 333$ V to enhance the size of the ion image (the resolution). The ratio between the repeller and extractor voltage is always (approximately) $V_{rep}/V_{ex} = 3/2$.

The length of the flight tube is 665 mm. The ions have a constant velocity over most of this distance, as the flight tube is at ground. When one neglects the acceleration of

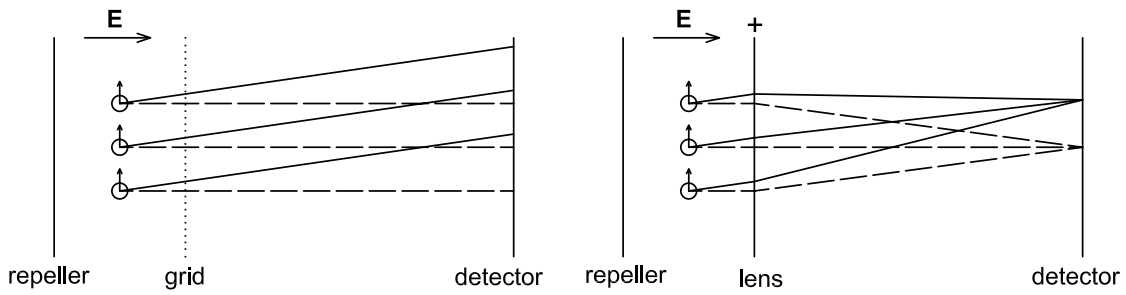

Figure 1.8: The difference between ion imaging using grids (left panel) and the velocity mapping technique (right panel) is shown. If molecules are ionized at different points - indicated by the circles - these molecules end up at different positions onto the detector. The dotted lines indicate the trajectories described by molecules that initially have no velocity, while in the case of the solid lines, the ion has an initial velocity with a direction indicated by the small arrow. Immediately after ionization, the molecules are accelerated due to (and along) the electric field $\boldsymbol{E}$. In the right panel (velocity mapping), the grid is replaced by a lens (extractor). As ions with the same initial velocity form a parallel beam, they are focussed in the focal plain. This leads to particularly sharp images.

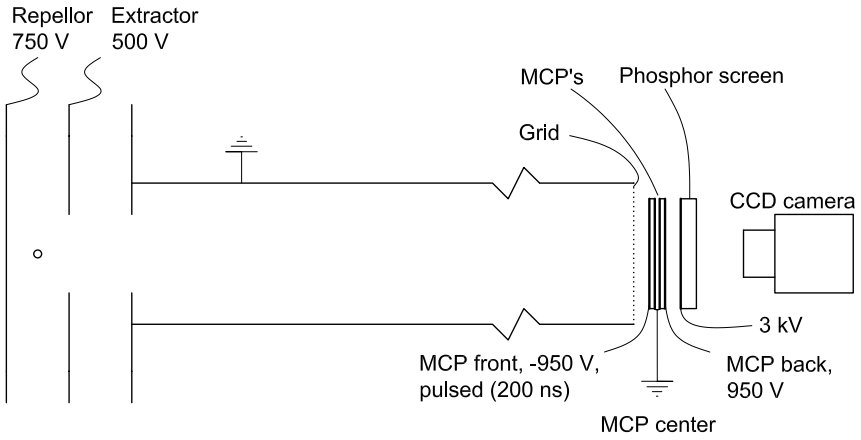

Figure 1.9: Schematic drawing of the (velocity mapped imaging) ion optics. The ionization volume (crossing point of the molecular and laser beams) is indicated by a small circle. The extractor is the electrostatic ion lens. Voltages indicated in this figure are typical for the experiment at the VU, although often slightly lower repeller and extractor voltages were used to enhance the resolution ($V_{rep} = 500$ V and $V_{ex} = 333$ V).

the ions in the beginning and close to the MCP, the time-of-flight of the ions is easily estimated. The potential in the ionization region is (in the case of Fig. 1.9) approximately 625 V, leading to a potential energy of 625 eV for singly ionized particles. This energy is completely transformed into translational energy, which (via $\frac{1}{2}m_M v^2$) immediately provides the velocity. Division of the length L of the flight tube by this velocity provides the time-of-flight. In convenient units the time-of-flight (TOF, in units of μs) can be written as:

$$TOF\ [\mu s] = 72\, L \sqrt{\frac{m_M}{nV}}, \tag{1.39}$$

with L $[m]$ the length of the flight tube, m_M $[amu]$ the mass of the ions, V $[V]$ the potential in the ionization region and n the charge of the ions in units of the elementary charge $[e]$. The time-of-flight in the configuration described in Fig. 1.9 is approximately 10 μs.

Gating the detector at a specific time allows one to only select ions with a specific mass and charge, reducing background signal due to oil, water etc.. This is done by pulsing the front plate of the MCP detector (see Fig. 1.9). The pulse width used is typically 200 ns, which is the minimum pulse width of the (home built) pulser.

Usually, a full (Newton) sphere of ions is crushed onto the detector. The initial velocity of the ions can be in all directions, although its magnitude (radius of the Newton sphere) is usually fixed by energy conservation. If there are more than one concentric spheres with different radii that are crushed onto the detector, then the "slice imaging" [44] technique can help. In such a case, the outer sphere contributes also to the area on the detector where the inner sphere is projected. This can make the analysis problematic, or if the outer sphere is much stronger than the inner one it can even make it impossible. In slice imaging, the detector is gated fast enough to detect only the center part of the Newton sphere. Ions with their initial velocity $\boldsymbol{v_i}$ along the extraction field $\boldsymbol{E}$ are the first to reach the detector. Those with lower velocity, or their velocity $\boldsymbol{v_i}$ antiparallel to the extraction field follow. The time difference Δt between molecules with their velocity $\boldsymbol{v_i}$ antiparallel and parallel to $\boldsymbol{E}$ can easily be approximated assuming an homogeneous extraction field. The force that works on the ions is qE (with $q = ne$ the charge), which leads to an acceleration of $a = qE/m$. The time needed to go from $v = v_i$ to $v = 0$ and back again (turning time) follows as $\Delta t = 2v_i m_M/(n\, e\, E)$, which in convenient units is:

$$\Delta t\ [ns] = 0.207\ \frac{v_i\, m_M}{n\, E} \tag{1.40}$$

with v_i in $[m/s]$, m_M in $[amu]$ and the electric field E in $[V/cm]$. In the case of high potentials at the ionization region, all molecules arrive within this Δt. It is however also possible that that molecules with $\boldsymbol{v_i}$ antiparallel to $\boldsymbol{E}$ (south pole) pass those with $\boldsymbol{v_i}$ perpendicular to $\boldsymbol{E}$ (equator). The first have a higher velocity in the flight tube than the latter ones.

In the configuration of Fig. 1.9 for the case of NO scattering, Δt is in the order of 10 ns. This becomes larger with decreasing the repeller and extractor voltage. The molecules from the "equator" of the Newton sphere end up at the detector approximately 100 ns after those from the "south pole".

An option to increase the arrival time difference is to pulse the extraction field some time after ionization, so the Newton sphere can expand before it is pushed towards the

detector [39]. In this case and assuming a homogeneous field, the Newton sphere expands along the flight tube direction.

The implementation off the slice imaging technique might prove useful in experiments following up those described in Chapters 5 and 6. When scattering NO off another molecule that can be rotationally excited, concentric scattering spheres for different final rotational states of that molecule are expected. The slice imaging technique might be necessary to resolve these scattering spheres. A time resolution of approximately 4 nanoseconds was achieved with the Kentech pulser used in the experiments described in Chapter 4.

Chapter 2

What is wrong with the steric asymmetry?

2.1 Abstract

The sign of the steric asymmetry S in rotationally inelastic state resolved atom-molecule collisions is questioned. Both experimental and theoretical results for collisions of Ar or He with NO (or ON) and Ar with OH (or HO) are discussed. Studies involve quantum state-selected crossed molecular beam experiments. In the case of NO, a striking oscillatory behavior of S as function of the rotational state after collision is observed. Full quantum mechanical scattering calculations with HIBRIDON reproduce the oscillation as far as the absolute value of S is concerned, but no consistency is obtained for the sign. On the other hand, comparable theoretical results for OH agree with experimental results for both absolute value and sign of S. The inconsistencies between experiment and the different theoretical approaches are described and possible solutions are discussed.

2.2 Introduction

In everyday life collisionally induced processes are non-directional. Specific orientations seem not to play a role as all orientations are present in a sample. However, one expects that nature will have directional preferences. For example, the collisional behavior of an NO molecule is expected to be somewhat different when the N-end or the O-end is hit. These orientational dependencies are important to unravel the dynamics of inelastic and reactive collisions. Nowadays, directional dependencies can be studied up to the level of individual quantum states using state of the art experimental and theoretical techniques. Careful initial molecular state preparation, using sophisticated molecular beam techniques allows experiments with quantum state controlled molecules and high resolution spectroscopic probes make it possible to study reaction products state-specifically.

Orientation effects in collisions of a diatomic molecule with a rare gas are described using the steric asymmetry ratio that is defined as

$$S = \frac{\sigma^{Head} - \sigma^{Tail}}{\sigma^{Head} + \sigma^{Tail}} \tag{2.1}$$

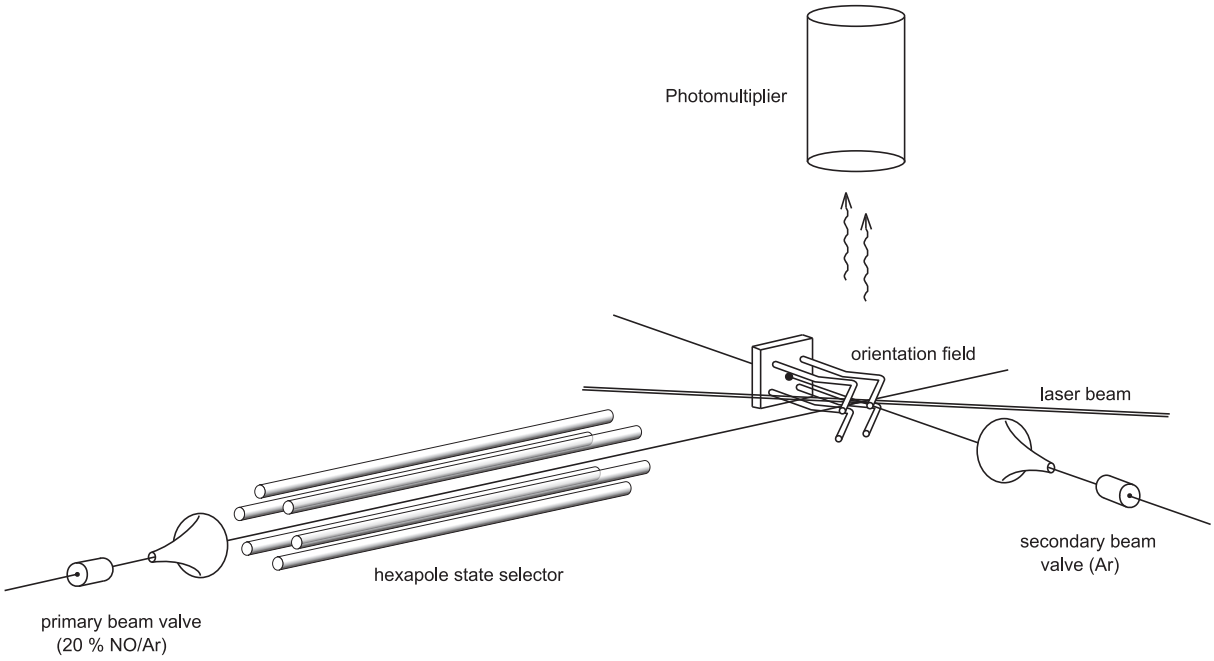

Figure 2.1: Experimental setup for Ar-NO collisions [47].

where σ^{Head} and σ^{Tail} denote the integral collision cross sections for molecules oriented preferentially with their head or tail towards the incoming atom. This means that when S is positive, head collisions contribute more to a specific final rotational state than tail collisions and vice versa. The steric asymmetry ratio indicates the anisotropy of the interaction potential and is an effective parameter as most instrumental errors cancel each other in nominator and denominator.

In recent work [45], a mathematical discussion is given on the sign of the steric asymmetry in previous work on inelastic collisions with oriented molecules. This work was done mainly on NO [1, 2, 5] and OH [46]. Ref. [45] made clear that inconsistencies exist on the sign of S between theory and experiment. This may have a number of reasons varying from a wrong definition to a fundamental physical problem.

In this comment, first a typical state-selective collision experiment is described to elucidate the discussion on the sign of S. A historical overview is given to summarize conclusions obtained so far and to emphasize the existing discrepancies. Finally, speculations on the reason of the emerged disagreement between theory and experiment are given.

2.3 Experimental details

To render a better insight into the experimental methods, collisions of a rare gas with NO will serve as an example in this section. The experiments with OH are similar. The experimental setup is a crossed beam machine as shown in Fig. 2.1 [47]. With a repetition rate of 10 Hz two pulsed valves - the NO beam valve with 16% NO in Ar and the rare gas

beam valve - are used to adiabatically expand gas pulses into a vacuum chamber, resulting in low final rotational temperatures. The cooled NO molecules are disposed mostly in the lowest rotational level of the electronic $^2\Pi$ ground state with total angular momentum quantum number $j = \frac{1}{2}$.

In the case of NO rotational levels carry a minute (parity) splitting, the so-called λ-doublet. The symmetry index $\epsilon = -1$ or 1 distinguishes between the two equally populated components of the λ-doublet (with respectively "f" and "e" labels). The molecules in the low field seeking (f) upper component of the λ doublet with symmetry index $\epsilon = -1$ are focussed into the collision region using a 2 m long hexapole. Molecules in the high field seeking (e) lower component ($\epsilon = 1$) of the λ doublet are pulled away from the center of the hexapole. This means that it is possible to prepare a molecular beam of molecules that are all in one single quantum state $j = \frac{1}{2}$, $\overline{\Omega} = \frac{1}{2}$, $\epsilon = -1$. $\overline{\Omega}$ denotes the (absolute value of the) projection of the total angular momentum on the molecular axis. $\overline{\Omega}$ can take values $\frac{1}{2}$ and $\frac{3}{2}$ as only the electron spin and orbit angular momenta have a non-zero projection on the molecular axis.

As a next step the hexapole focussed NO molecules (in the collision region) are oriented in an essentially homogeneous 13.5 kV/cm field, produced in between two pairs of rods that are placed perpendicular to the relative velocity v_{rel} (see Figs. 2.1 and 2.2). A negative voltage is applied onto the pair of He-rods (rare gas rods) or onto the pair of NO-rods to produce the orientation field, while the other pair of rods is at ground. The pairs of rods are labelled after the incoming particles that pass them first (Fig. 2.2). As the NO molecules are in a low field seeking state, they will orient with their negative ends towards the negative rods. Assuming that the NO dipole moment is such that N^-O^+ [48–53], application of the negative voltage onto the NO-rods yields O-end collisions whereas switching the negative voltage onto the He rods yields N-end collisions (Fig. 2.2).

Due to a collision with an Ar or a He atom, the oriented NO molecule can be excited to a higher rotational state (j', $\overline{\Omega}'$, ϵ'). The amount of molecules (giving the cross section σ) that is scattered into a certain (j', $\overline{\Omega}'$, ϵ') state is detected by Laser Induced Fluorescence (LIF) via the electronically excited $A\,\Sigma^+$ state of NO. Once the cross section for both N-end and O-end (head and tail) collisions measured, the steric asymmetry S is obtained following Eq. 2.1.

Experiments on collisions of Ar with NO [5, 16] were performed on the same experimental setup as those on collisions of He with NO [6]. The replacement of Ar ($v_{Ar} = 560$ m/s) in the rare gas beam by He ($v_{He} = 1760$ m/s) alters the direction of the relative velocity and the alignment of the orientation field has to be adapted. The orientation field lines have to be parallel to the relative velocity. Work on collisions of OH and Ar was performed by ter Meulen and coworkers, where a discharge ring was used to produce the OH radicals and a double hexapole was used for focussing [46].

2.4 Historic overview

First experimental evidence for large orientation effects in rotationally inelastic Ar-NO (ON) collisions, was obtained by Van Leuken et al. [2]. In their convention, the N-

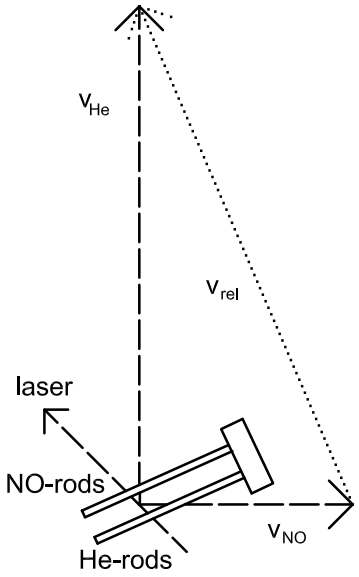

Figure 2.2: Orientation geometry. The pairs of rods are labelled after the incoming particles that pass them first. The orientation field is produced by applying a voltage on the pair of NO-rods or on the pair of He-rods, see also Fig. 2.1. The other pair remains grounded. It should be noted that $v_{NO} = 590$ m/s and that $v_{He} = 1760$ m/s.

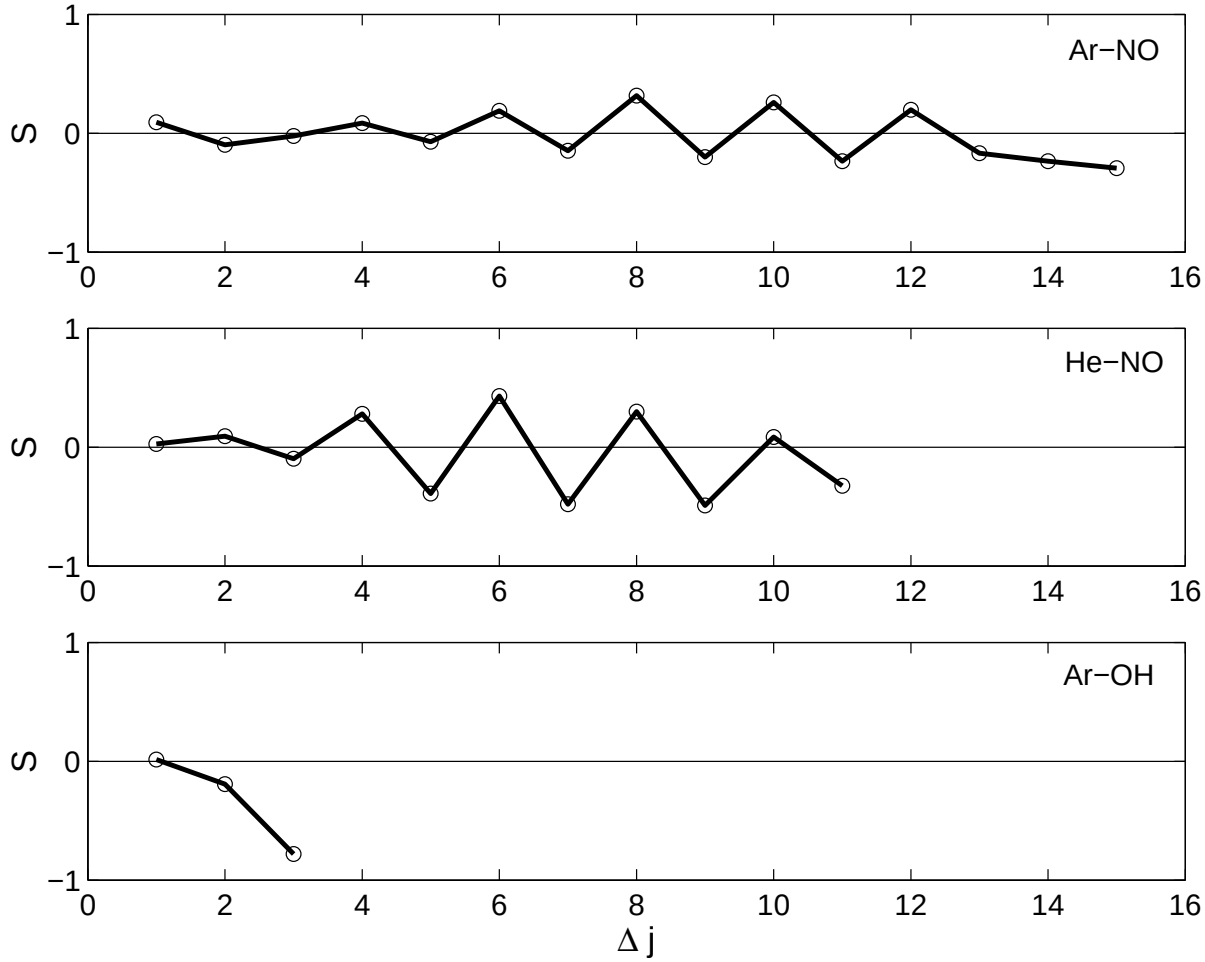

Figure 2.3: Experimental steric asymmetry ($\epsilon = \epsilon' = -1$) as a function of $\Delta j = j' - j$ for spin orbit conserving collisions of: NO with Ar (upper panel) at a collision energy of $E_{tr} = 475$ cm^{-1} [16], NO with He (center panel) at a collision energy of $E_{tr} = 509$ cm^{-1} [6,16] and OH with Ar (bottom panel) at a collision energy of $E_{tr} = 746$ cm^{-1} [46]. It should be noted that for experiments on NO the N-end is regarded as the head of the molecule, while for collisions with OH the O-end is regarded as head of the molecule. Earlier data for Ar-NO [5] have been improved using a flux to density transformation that transformed LIF intensities into proper state-to-state cross sections. This treatment enhanced the amplitude of S, but did not change its sign. The oscillation of S for collisions of NO with He shows the same sign but a larger amplitude.

end and the O-end of the NO molecule were defined as head and tail, respectively. They discovered that for Ar-NO, S exhibits a striking undulatory character at a collision energy of $E_{tr} = 475$ cm^{-1}. Later on these experimental studies were extended [5, 16, 47]. The $\Delta j = j' - j$ dependence of the steric asymmetry for Ar-NO collisions at $E_{tr} = 475$ cm^{-1} and for He-NO collisions at $E_{tr} = 509$ cm^{-1} is shown in Fig. 2.3 (upper and center panel, respectively). When the orientation field is applied such that the N-end of the NO molecule is favored to point towards the incoming rare gas atom, the collision yields mostly $\Delta j = even$ transitions. For O-end collisions, $\Delta j = odd$ transitions are found to be preferred.

The strong oscillation of S cannot be understood using only classical mechanics. Ar-NO and He-NO Potential Energy Surfaces (PESs) [54–56] show an egg-like shape in which the N-end extends further from the center-of-mass than the O-end. When one assumes Ar-NO collisions to be collisions between an egg shaped hard shell (NO) and a hard sphere (Ar), there is no way to explain the effect that N-end collisions yield mostly $\Delta j = even$, while O-end collisions yield mostly $\Delta j = odd$. The amount of torque that can be applied is limited by the collision energy and the lever. This lever is the distance between a line perpendicular to the shell (along which the force acts) and the center of mass. The (linear) momentum parallel to the hard shell is conserved, while that perpendicular to the shell is transformed into rotation. From a classical point of view one would expect that the end of the molecule where the largest torque can be applied (the N-end) is preferred for producing rapidly rotating molecules (large Δj). Molecules that after collision are in low rotational states (small Δj) are expected to be due mostly to collisions onto the end of the molecule where the maximally applied torque is smaller (O-end). No alternation (of S) is expected from this model; classical mechanics cannot describe the observations.

Moreover, for excitations to the highest allowed rotational states the oscillation decreases and a negative value for S (indicating O-end preference) has been observed for large Δj [1,2,5,16]. At that time, the sign of the experimental value of S was in agreement with the theoretical prediction of Refs. [1, 2, 5, 16]. Recently the experimental setup was improved to allow for more sensitive experiments and the latest experimental data by De Lange et al. also showed nice agreement with theory [5].

For collisions of Ar with OH, the oscillatory behavior of S as function of j' turned out to be absent [46] (see also Fig. 2.3, lower panel). O-end collisions mostly result in low rotational states while H-end collisions mostly yield high rotational states. Full quantum mechanical theoretical results correspond reasonably well to the experimental results. Van Beek et al. [46] defined the (negative) O-end of the molecule as being the head and the (positive) H-end as being the tail of the molecule (Eq. 2.1). This definition is opposite to what implicitly follows from the potential energy surfaces [57] that were used for close coupling calculations. In these PESs, $\theta = 0$ corresponds with an H-end (Tail) collision. For all NO PESs $\theta = 0$ corresponds with an N-end (Head) collision [6, 54–56]. When using these PESs in calculations, one should be well aware of and very careful with the orientation of the PESs.

Up to this point, theory and experiment seemed to correspond very well. Some recent results, however, raised some doubt concerning the sign of S. In the next section reasons to question the sign of S are given.

2.5 Reasons to doubt the sign of S

The first inducement to question the correctness of the sign of the steric asymmetry from previous measurements, were some results obtained with a new quasi quantum mechanical model [58]. These model calculations were performed to shed more light on the nature of the oscillations of S. Quantum mechanics alone does not provide physical insight in the reason of the steric effect. Results for He-NO and Ar-NO corresponded remarkably well to the experimental ones, only the sign turned out to be wrong. Calculations with the quasi quantum mechanical model on Ar-OH, however, reproduced the experimental sign of S [58].

Searching for reasons of the "erroneous" model calculations, it was noted that results for collisions with NO are opposite to that what is expected from a simple classical "ball-and-stick" model. When taking a close look at the upper panel of Fig. 2.3, one sees that for high rotational states S becomes negative. This implies that these high rotational states are mostly produced by collisions onto the O-end of the NO molecule. Looking at the Ar-NO PESs [54, 55] one would expect something different. For transitions to high rotational states, the repulsive part of the potential dominates. In the Ar-NO PESs introduced by Alexander [54, 55] one can immediately see that the N-end extends further from the center-of-mass. From a (classical) point of view one would expect the N-end to be preferred, as the torque that can be applied to the N-end is larger. When a stick is attached to a ball, it is easier to make the system rotate by hitting the stick, than by hitting the ball. From this simple classical ball-and-stick model an S is expected with a sign opposite to the sign resulting from the measurements.

For collisions of the less homo-nuclear OH molecule with Ar this becomes even more clear and indeed the ball-and-stick model corresponds to the measurements. The H-end (stick) is preferred for high rotational states in both experiment and theory [46]. The steric asymmetry for the Ar-OH system is plotted in the lower panel of Fig. 2.3. Recent full quantum mechanical (HIBRIDON) [45, 59] Ar-OH calculations, resulted in a sign opposite to the sign of previous results for S. Identical calculations on He-NO, however, yielded a sign of S that was similar to the experimental sign. The orientation of the potential energy surfaces was checked and did not account for this disagreement. Close inspection of the HIBRIDON source code showed that the prepared wave function carried an orientation that is opposite to the one assumed [1, 2]. This offers an explanation for the disagreement of the recent theoretical sign of S for Ar-OH with previous results and with the ball-and-stick model. However, when the theoretical sign of S for collisions of Ar with OH flips, it should also flip for Ar-NO and He-NO. There is still a disagreement between the experimental and theoretical sign of S for collisions with NO.

The fact that the Ar-OH PESs [57] were specified oppositely to the definition of S [46] (H-end as head instead of O-end) might be the reason that the disagreement between theory and experiment (due to an error in HIBRIDON) for Ar-OH was not found before. Very recently, some new close coupling scattering calculations have been performed on He-NO [60]. These calculations, that were unrelated to previous HIBRIDON calculations, also yielded a sign for S opposite to the experimental result for He-NO.

To summarize, a flip of the theoretical sign of S for collisions with NO, while keeping the sign for collisions with OH as it was reported before, makes all theoretical results

in agreement with the ball-and-stick model. There remains, however, a sign difference between the theoretical (HIBRIDON) and the experimental results for collisions with NO. It should be noted that the theoretical (MOLSCAT [61]) results for Ar-NO - as published in Ref. [2] - are consonant with the experimental results and thus oppose the ball-and-stick model, HIBRIDON calculations, recent CC calculation by Groenenboom [60] and the results using a Quasi Quantum Treatment (QQT, see chapter 7). The implementation of the adapted MOLSCAT calculations cannot be checked, as no documentation is left. A conclusion could be that something is wrong with the sign of S from the NO experiments.

Although tested before, it was decided to test the experimental sign of S once more. The oscillation for S is largest for the He-NO system which for this reason has been used. To orient the molecules during the experiment, a negative voltage was applied that can be switched onto the He or onto the NO-rods (see also Fig. 2.2). The absolute value of the small electric dipole of NO ($v = 0$, $X\,^2\Pi$) has been measured with high precision (0.1574 ± 0.014 D) by Hoy et al. [62] and their result is in reasonable agreement with the *ab initio* value (0.1732 D) [48]. All charge distributions calculated using *ab initio* methods correspond to N^-O^+. To our knowledge, the sign of the NO dipole moment has not been determined experimentally so far. The NO molecules are all in the low field seeking state that is selected by the hexapole. Orientation should be such that the N-end points towards the the rods to which the negative voltage is applied.

First the orientation field was taken out of the machine to measure the voltages on the rods. When the input of the HV-switch was 0, a negative voltage was measured on the He rods; when the input was 1, a negative voltage was observed on the NO-rods. This gives N-end and O-end collisions, respectively, as molecules in a low field seeking state orient with their positive end towards the positive electrode. The orientation field was placed back in the setup and LIF measurements were performed. Background subtracted signals were collected for $j' = 4.5$, $\Omega' = 0.5$, $\epsilon' = -1$ in the R_{21} branch (for both HV-switch inputs): when the HV-input was 0 (N-end collisions) a signal of 67 mV was recorded, when the HV input was 1 (O-end collisions), 29 mV was observed. For the steric asymmetry for $j = 4.5$ this gives: S = (67-29)/(67+29) = + 0.40 which means N-end preference as measured before (see also Fig. 2.3). The experimental error on S is estimated to be $\pm$ 0.15. As a consequence the discrepancy continues to exist and the question remains what the origin of the disagreement is. No answer to this question has yet been found. In the next section some speculations are given.

2.6 Concluding remarks

The current status is that "revised" *quantum mechanical calculations* (HIBRIDON) yield results that are consonant with the ball-and-stick model for the Ar-OH, Ar-NO and He-NO systems. Consonance with the ball-and-stick model means that high rotational states are preferentially the result of collisions on the end of the molecule at which the largest torque can be applied (the N-end for NO and the H-end for OH). *Experimental results* for the Ar-OH system correspond to the revised HIBRIDON calculations and to the ball-and-stick model. For collisions of NO with Ar and He, *experimental results* oppose the ball-and-stick model and consequently the sign of the (experimentally obtained) steric

asymmetry S opposes the "revised" quantum mechanical results.

An error in the experimental procedure for experiments with NO, introducing an erroneous sign, would solve all disagreements between theory and experiment. Some simple tests, however, appear to rule out such errors.

Another possibility to account for the sign difference for NO is an error in the He-NO and the Ar-NO PESs. This is very unlikely: there is good quantitative agreement between the absolute value of S in (Ar-NO and He-NO) experiment and theory [5,6]. The possibility that the CEPA and CCSD(T) PESs are not accurate enough, can be excluded. This does not exclude that the labels for the N-end and the O-end in the PESs can be wrong. It is, however, very unlikely to assume that the heavier O-end extends further from the center-of-mass than the N-end. Semi-quantum mechanical calculations and full quantum mechanical calculations that are independent of the HIBRIDON code support the finding that the simple classical ball-and-stick model can be applied.

For calculation of the experimental steric asymmetry, the head (N-end) of the NO molecule is assumed to be negative while the tail (O-end) should be positive. However, the actually *observed* steric asymmetry S is given by:

$$S = \frac{\sigma^- - \sigma^+}{\sigma^- + \sigma^+} \tag{2.2}$$

The cross sections σ^- and σ^+ indicate the cases in which the negative and the positive end of the molecule preferentially point towards the incoming atom. In terms of Eq. 2.1 the negative (positive) end of the molecule is defined as its head (tail). When the sign of the NO ($v = 0$, $X\,^2\Pi$) dipole moment would be reversed - N^+O^- instead of N^-O^+ - the experimental sign of S would be in agreement with the ball-and-stick model. Although the absolute value of the NO dipole moment is well known, even the highest precision experiments could not determine the sign of the NO dipole moment unambiguously, i.e. N^-O^+ or N^+O^- [63]. The sign of the dipole moment has not been measured, but it has been calculated. Large series of *ab initio* calculations reported N^-O^+ [48–53]. Taking into account indirect evidence from recent experiments by Matsiev and coworkers [64] and predictions by Drabbels and Wodtke [63], a flip of the sign of the dipole moment seems to be not feasible.

The origin of the sign difference between the theoretically and experimentally obtained values of S remains unclear for the moment. Some new experiments might shed light on this subject. Collision experiments can be repeated with rare isotopes of NO, to get an answer on the shape of the NO shell. In the case of $^{14}N^{18}O$, the center-of-mass is shifted towards the O-end of the molecule. It is expected that the N-end then is even more preferred for high rotational states and it will be interesting to see whether stronger effects are observed. Another approach would be to verify experimentally the sign of the dipole moment of NO. This might be achieved in an experiment in which the molecules are first oriented and subsequently dissociated using femtosecond laser pulses. Nevertheless, the situation is such that considerable progress has been obtained in the last years and that at least consistent definitions are used now. New experiments are necessary to unravel the remaining question: what is wrong with the steric asymmetry in NO-rare gas collisions?

Chapter 3

Sign of the steric asymmetry

3.1 Abstract

The sign of the theoretically predicted steric asymmetry S in rotational inelastic state resolved molecule-atom collisions is questioned. It is shown that the sign of the T-matrix obtained on a basis of non-oriented rotational states of the molecule depends on the choice of the Jacobi coordinates in which the collision problem is solved. Explicit expressions for the state-to-state dependence of the integral and differential cross sections for oriented and non-oriented molecules are presented. The effect of the choice of Jacobi angles and the inertial frame of reference on the sign of S are discussed in detail. The sign of the earliest obtained expression for the steric asymmetry of the integral cross section (as obtained by Van Leuken et al.) is found to be correct, whereas that of the orientational dependent contribution of the differential cross section (as obtained by Alexander and Stolte) requires a negative multiplication factor. Quantum mechanical calculations on collisions of OH with Ar are performed. These calculations do not agree with the experimental sign of S and cannot be interpreted in terms of a simple ball and stick model. Inspection of the HIBRIDON source code shows that the prepared wave function carries an orientation that is opposite to the one assumed. This could offer an explanation for the disagreement for S for Ar-OH collisions. For collisions of NO with Ar, the signs of the quantum mechanically calculated and the experimental values of S appear to disagree with the simple ball and stick model. The experimental sign of S has been reinvestigated. Previous experimental results are confirmed.

3.2 Introduction

Orientation effects in atom-molecule collisions are commonly described using the steric asymmetry S, that is defined as:

$$S = \frac{\sigma^{Head} - \sigma^{Tail}}{\sigma^{Head} + \sigma^{Tail}}. \tag{3.1}$$

Here σ^{Head} and σ^{Tail} denote the cross sections for molecules oriented preferentially with their head or tail towards the atom. The first striking experimental evidence for large

orientation effects in rotationally inelastic state-resolved NO (ON) and Ar collisions, was performed by Van Leuken et al. [2]. In their convention, the N-end and the O-end of the NO molecule were defined as head and tail, respectively. In addition, quantum mechanical scattering calculations were performed. Van Leuken and coworkers succeeded in deriving a contracted equation that expresses the difference between the integral cross sections for N-end preferred and O-end preferred collisions (respectively $\sigma^{NO}_{j,m_j,\overline{\Omega},E\rightarrow j',m'_j,\overline{\Omega}',\epsilon'}$ and $\sigma^{ON}_{j,m_j,\overline{\Omega},E\rightarrow j',m'_j,\overline{\Omega}',\epsilon'}$) into a weighted sum over products of T-matrix elements. The total angular momentum of a diatomic (or a symmetric top alike) molecule is denoted by j, having projections Ω and m_j along respectively the molecular axis and the space-fixed Z axis. The absolute value of Ω is written as $\overline{\Omega}$ and ϵ $(= -1, 1)$ gives the symmetry index that distinguishes between the two components of the Λ-doublet [22]. The index E indicates the electric orientation field at the scattering region.

In NO-Ar collisions the O-end was reported to be preferred for high rotational final states [1, 2, 5, 54]. This is not what one would expect from a simple ball and stick model that seems to apply very well in OH-Ar collisions [46]: the O-end is more round (ball) than the H-end (stick) that extends further from the center-of-mass (CM) of the OH molecule. As a consequence, high rotational final states prefer H-end collisions.

This paper focusses on the sign of the steric asymmetry. It is organized in the following way. Section 3.3 consists of a short summary of a number of relevant experimental and theoretical considerations. In section 3.4 the sign issue concerning the steric asymmetry is introduced. Experimental results for collisions of OH with Ar serve as a benchmark system here, as experimentally observed rotational state transitions exhibit a propensity in S that can qualitatively be understood in a simple ball and stick model. These experimental results for S are compared to those obtained from new close coupling calculations (HIBRIDON [59]) that have been carried out on the most recent UMP4 ab initio PES's for OH-Ar, developed by Kłos et al. [56]. Section 3.5 focusses on the parameters that are involved in defining the sign of the steric effect. We will show that the T transition matrix that results from HIBRIDON, $T^J_{j',l',\overline{\Omega}',\epsilon';j,l,\overline{\Omega},\epsilon}$, depends on the choice of Jacobi coordinates that parameterize the interaction PES's. The resulting scattering amplitude depends also on the actual choice of the inertial coordinate frame of the corresponding Center-of-Mass System (CMS). The cases of the space fixed Z-axis parallel and anti-parallel to the incoming relative velocity vector are considered.

If one chooses the Jacobi coordinates such that the displacement vector $\mathbf{R}$ points from the atom to the molecule, the relative velocity vector points oppositely to the conventional case in which the $\mathbf{R}$ points from the molecule to the atom. The outcome for the T-matrix will depend upon this choice of $\mathbf{R}$. This dependence is typically unimportant in cases other than those in which steric effects are concerned. In the fifth section an experimental investigation has been carried out that confirms the sign and magnitude of S that was found in earlier experiments. In the last section, we will close with a brief discussion and concluding remarks.

3.3 Experimental and theoretical considerations

To be experimentally observable, the determination of the steric asymmetry requires the application of a homogeneous electric orientation field **E** in a direction parallel or antiparallel to the relative velocity vector of the colliding particles. The NO-beam can be state selected in the upper component (u) of the Λ-doublet ($^2\Pi_{\frac{1}{2}}$, $j = \frac{1}{2}, \epsilon = \epsilon_u = -1$) by hexapole focussing. All focussed molecules reside in a low field seeking state for which $m_j = +\overline{m}_j$ and $m_j = -\overline{m}_j$ have equal probability. Having applied **E** at the scattering volume, either the O-end (tail) or the N-end (head) predominantly points towards the incoming Ar atom. The field strength is chosen such ($E \approx 16$ kV/cm) that it is sufficiently large to mix the selected $|j, m_j, \overline{\Omega}, \epsilon_u\rangle$ and the $|j, m_j, \overline{\Omega}, -\epsilon_u\rangle$ components of the Λ-doublet of opposite parity with (positive) mixing coefficients $\alpha(E)$ and $\beta(E)$. The oriented wave function follows as

$$\big|j, m_j, \overline{\Omega}, E\big\rangle = \alpha(E)\big|j, m_j, \overline{\Omega}, \epsilon_u\big\rangle \pm \beta(E)\big|j, m_j, \overline{\Omega}, -\epsilon_u\big\rangle. \tag{3.2}$$

with $\alpha(E)^2 + \beta(E)^2 = 1$ [47]. Note that this convention deviates from that of Ref. [1] in which the role of α and β is reversed and their absolute value is multiplied by $\sqrt{2}$. Because one has to do with a low field seeking state, $\alpha(E) > \beta(E) \geq 0$. The $\pm$ denotes which molecular end is preferred to point along **E**. Neglecting Hund case b mixing for the moment, the rotational wave function can, for arbitrary values of ϵ, be written as [13]

$$\big|j, m_j, \overline{\Omega}, \epsilon\big\rangle \equiv \frac{1}{\sqrt{2}}\left[\big|j, m_j, +\overline{\Omega}\big\rangle + \epsilon\big|j, m_j, -\overline{\Omega}\big\rangle\right] \tag{3.3}$$

Besides large enough for mixing, we assume E to remain small enough to keep the Stark shift of the spacing between the rotational energy levels minor. Test calculations showed that these shifts (in the order of Λ-doublet splitting) had negligible effect on the calculated cross sections [2]. As the energy may be assumed independent of the actual values of $\alpha(E)$ and $\beta(E)$, Van Leuken et al. [2] expressed the T-matrix elements for an incoming oriented rotational state $\big|j, m_j, \overline{\Omega}, E\big\rangle$ and non-oriented outgoing state $\big|j', m'_j, \overline{\Omega'}, \epsilon'\big\rangle$ as:

$$\begin{aligned} T_{j',m'_j,l',m'_l,\overline{\Omega}',\epsilon';j,m_j,l,m_l,\overline{\Omega},E} = {} & \alpha(E) T_{j',m'_j,l',m'_l,\overline{\Omega}',\epsilon';j,m_j,l,m_l,\overline{\Omega},\epsilon_u} + \\ & \pm\beta(E) T_{j',m'_j,l',m'_l,\overline{\Omega}',\epsilon';j,m_j,l,m_l,\overline{\Omega},-\epsilon_u} \end{aligned} \tag{3.4}$$

The orbital angular momentum of the incoming and outgoing state are respectively represented by the quantum numbers l and l', with projections m_l and m'_l on the Z axis. The uncoupled representation of the T-matrix $T_{j',m'_j,l',m'_l,\overline{\Omega}',\epsilon';j,m_j,l,m_l,\overline{\Omega},\epsilon}$, where the T-matrix relates to the scattering S-matrix as: $\mathbf{T} = \mathbf{1} - \mathbf{S}$, assumes incoming and outgoing waves with a single direction of the space fixed quantization axis. The uncoupled representation of the T-matrix relates to the coupled representation as:

$$\begin{aligned} T_{j',m'_j,l',m'_l,\overline{\Omega}',\epsilon';j,m_j,l,m_l,\overline{\Omega},\epsilon} = {} & \sum_{J,M_J} T^J_{j',l',\overline{\Omega}',\epsilon';j,l,\overline{\Omega},\epsilon} \times \\ & \times \langle J\ M_J\ |j'\ m'_j\ l'\ m'_l\ \rangle\ \langle J\ M_J\ |j\ m_j\ l\ m_l\ \rangle. \end{aligned} \tag{3.5}$$

The coupled T-matrix $T^J_{j',l',\overline{\Omega}',\epsilon';j,l,\overline{\Omega},\epsilon}$ is independent of $M = m_j + m_l = m'_j + m'_l$ and diagonal in J [65]. Unlike Alexander, who uses $T^J_{j',l',\overline{\Omega}',\epsilon';j,l,\overline{\Omega},\epsilon}$ [66], Van Leuken et al. use the coupled representation $T^J_{l',j',\overline{\Omega}',\epsilon';l,j,\overline{\Omega},\epsilon}$ [2]. Some algebra with Wigner $3j$ symbols leads to the straight forward relation between Alexander's and Van Leuken et al. coupled representations:

$$T^J_{j',l',\overline{\Omega}',\epsilon';j,l,\overline{\Omega},\epsilon} = (-1)^{l'+l+j'+j+2J} T^J_{l',j',\overline{\Omega}',\epsilon';l,j,\overline{\Omega},\epsilon} \tag{3.6}$$

Alexander relates the T-matrix expression of Eq. 3.5 to the dimensionless scattering amplitude for a transition between two states [1]

$$f_{j,m_j,\overline{\Omega},\epsilon\to j',m'_j,\overline{\Omega}',\epsilon'}(\hat{\mathbf{k}}') = \sqrt{\pi}\sum_{J,l,l'}(2l+1)^{\frac{1}{2}}(2J+1)i^{l-l'}\begin{pmatrix} j & J & l \\ m_j & -m_j & 0 \end{pmatrix}\times$$
$$\times\begin{pmatrix} j' & J & l' \\ m'_j & -m_j & m_j - m'_j \end{pmatrix} Y_{l',m_j-m'_j}(\hat{\mathbf{k}}')T^J_{j',l',\overline{\Omega}',\epsilon';j,l,\overline{\Omega},\epsilon} \tag{3.7}$$

where $(:::)$ is a Wigner 3j-symbol [13]. The sum extends over all allowed values of the initial and final orbital angular momenta l and l'. The initial and final wave vectors are denoted by $\mathbf{k}$ and $\mathbf{k}'$, the direction of the initial velocity vector $\hat{\mathbf{k}}$, defines the axis of m_j quantization in the so called "collision frame". Combination of Eqs. 3.4 and 3.7 gives

$$f_{j,m_j,\overline{\Omega},E\to j',m'_j,\overline{\Omega}',\epsilon'}(\hat{\mathbf{k}}') =$$
$$\alpha(E)f_{j,m_j,\overline{\Omega},\epsilon_u;j',m'_j,\overline{\Omega}',\epsilon'} \pm \beta(E)f_{j,m_j,\overline{\Omega},-\epsilon_u;j',m'_j,\overline{\Omega}',\epsilon'} \tag{3.8}$$

Eq. 3.8 relates directly to the differential scattering cross section of an oriented molecule [1].

$$d\sigma_{j,m_j,\overline{\Omega},E\to j',m'_j,\overline{\Omega}',\epsilon'} \;/\; d\omega = \frac{1}{k^2}|f_{j,m_j,\overline{\Omega},E\to j',m'_j,\overline{\Omega}',\epsilon'}(\hat{\mathbf{k}}')|^2 \tag{3.9}$$

Integration of the differential cross section $d\sigma_{j,m_j,\overline{\Omega},E\to j',m'_j,\overline{\Omega}',\epsilon'}/d\omega$ in Eq. 3.9 over all scattering angles, provides the integral scattering cross section $\sigma_{j,m_j,\overline{\Omega},E\to j',m'_j,\overline{\Omega}',\epsilon'}$. Using the scattering amplitude instead of the T-matrix for the treatment of molecular orientation offers a more direct insight into the underlying collision properties, leading to a better understanding of the origin and magnitude of the observed steric effects [2, 5, 16, 19, 46, 67, 68].

3.4 The sign of the steric asymmetry

For NO-Ar, S exhibits a striking undulatory character at a collision energy of $E_{tr} = 475$ cm^{-1}, as shown in Fig. 3.1. When the orientation field is applied such that N-end of the NO molecule is favored to point towards the Ar, the collision yields mostly Δj = even. For O-end collisions, Δj = odd is preferred [1, 2, 5, 16]. This effect is seen for both spin-orbit conserving and spin-orbit changing collisions. The value of the steric asymmetry as a function of $\Delta j = j' - j$ for collisions of both OH and NO with Ar turns out to be insensitive of ϵ'. In the search for a better understanding of the striking oscillatory behavior of S, a semi-quantum mechanical hard shell model is being developed. Application of this

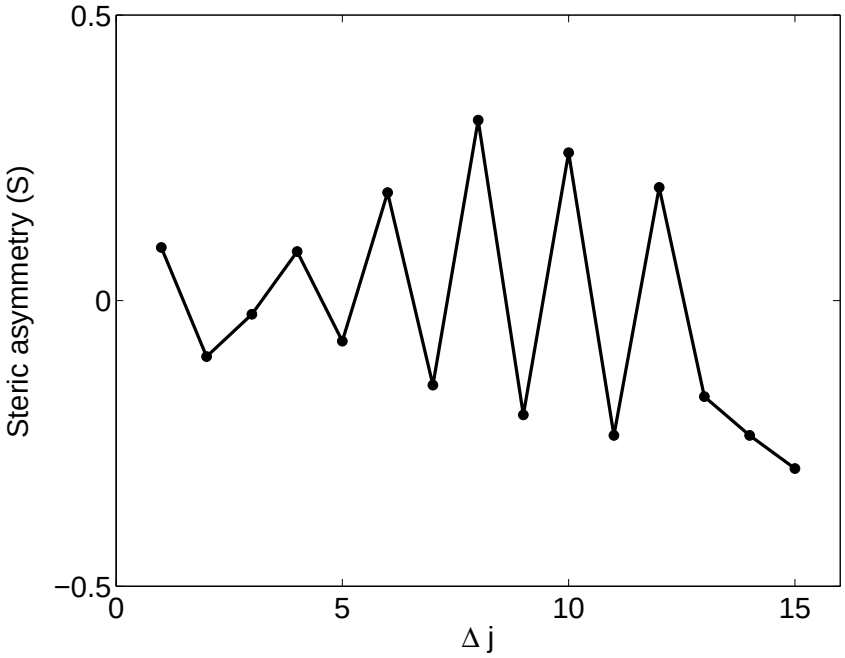

Figure 3.1: Experimental steric asymmetry ($\epsilon = \epsilon_u = \epsilon' = -1$) as a function of $\Delta j = j' - j$ for spin orbit conserving collisions of NO with Ar at a collision energy of $E_{tr} = 475$ cm^{-1} [16]. Earlier data [5] have been improved using a flux to density transformation that transformed LIF intensities into proper state-to-state cross sections. This treatment overall enhanced the amplitude of S, but not its sign.

model [58] to NO-Ar yields a similar undulatory behavior, but S has the improper sign compared to measurements and quantum mechanically calculated values. Application of this model to OH-Ar yields the "proper" sign of S compared to the reported measured and calculated values [19, 46].

To render insight into the "proper" sign of S, we turn to a recent study of Van Beek et al. [46]. This study reports about the steric dependence of (state resolved) rotational energy transfer for the 'hetero' nuclear OH-Ar collision system. A hexapole is used to select the OH beam predominantly in a $j = \overline{\Omega} = \overline{m}_j = \frac{3}{2}$, ϵ_u (f) state, that is oriented in the collision region using an electric field $\mathbf{E}$. In accordance with their experimental convention Schreel et al. and later Van Beek et al. define S such that according to Eq. 3.1 the O-end of the molecule corresponds to the head, while the H-end refers to the tail [19, 46]. At a collision energy of 746 cm^{-1} Van Beek et al. observed a general trend that was independent of the final spin-orbit state and of the Λ-doublet component. For excitation to low rotational states, S is typically small and positive, indicating a weak O-end preference. For excitation to a higher rotational state, S becomes large and negative, implying that H-end collisions are preferred. A simple ball and stick model explains this behavior. In the case of "tail" (H-end) orientation of the molecule, the H atom will have a much higher probability of pointing towards the Ar atom. For the "head" orientation, the O-end of the molecule is likely to shield off the H-end from the Ar atom. Due to the shape of the OH molecule, the torque that is exerted on the H-end ("stick") is much larger than that on the O-end ("ball") at a similar relative velocity ($\mathbf{v_{rel}}$). A large torque results in a high rotational excitation, as was noticed for the dependence of S on j' by van Beek et al. [46].

In addition to Van Beek's measurements, close coupling scattering calculations for OH-Ar were carried out on the CEPA [57] and on the UMP4 (unrestricted fourth-order Møller-Plesset [56]) ab initio OH-Ar Potential Energy Surfaces (PES's). For both PES's, the steric asymmetry as well as the integral inelastic cross sections (depending on $\overline{\Omega}'$ and ϵ') have been calculated with HIBRIDON [59]. These results agree reasonably with the experimental values. A close inspection of the HIBRIDON code, however, shows that the orientations that correspond with HIBRIDON's "heads" and "tails" labels relate directly to the choice of the Jacobi coordinates $\mathbf{R}$ (displacement vector between atom A and molecule BC), $\hat{\mathbf{r}}$ (BC bond vector, that points from the tail C towards the head B) and ϑ (angle between $\hat{\mathbf{r}}$ and $\mathbf{R}$). For NO-Ar, $\vartheta = 0$ corresponds with collinear Ar-NO configuration for both the CEPA [55] and the CCSD(T) [69] PES's. These PES's have been used to calculate scattering cross sections and steric asymmetries with HIBRIDON [59] and with a (modified [2]) version of MOLSCAT [61]. In the case of OH, for both the CEPA and the UMP4 PES's, $\vartheta = 0$ corresponds to the linear Ar-HO geometry. This means that HIBRIDON assumes the H-end of the OH molecule as being the head, while the H-end of the molecule is defined by Van Beek and coworkers as being the tail of the molecule. Without adapting HIBRIDON's definition to the experimental one, HIBRIDON is expected to provide results for S that carry a sign opposite to that of Van Beek's experimental value, which was reported not to be the case [46].

To investigate whether the theoretical results reported by Van Beek et al. carry the "proper" sign, steric asymmetries have been recalculated for OH ($\nu = 0\,, X^2\Pi_{\frac{3}{2}}\ j = \frac{3}{2}$) scattered by Ar at a collision energy of 451 cm^{-1} and 746 cm^{-1} on the UMP4 PES's.

Table 3.1: Experimental and theoretical steric asymmetries for rotational excitation of OH $X^2\Pi_{\frac{3}{2}}, j = \frac{3}{2}, \epsilon =$ -1 in collisions with Ar at a collision energy of 746 cm^{-1}. It should be noted that the published [46] steric asymmetry is defined as $S^E = (\sigma^{OH} - \sigma^{HO})/(\sigma^{OH} + \sigma^{HO})$, while the present calculations use the definition that follows from HIBRIDON in combination with the UMP4 and CEPA parameterization [56, 57]: $S^C = (\sigma^{HO} - \sigma^{OH})/(\sigma^{HO} + \sigma^{OH}) = -S^E$.

			Steric asymmetry [%]				
final state[1]			experimental	theoretical results on UMP4			"hard shell"
$\overline{\Omega}'$	J'	ϵ'	van Beek[2]	94% $\overline{m}_j = \frac{3}{2}^2$	94% $\overline{m}_j = \frac{3}{2}^3$	100% $\overline{m}_j = \frac{3}{2}^3$	100% $\overline{m}_j = \frac{3}{2}^3$
$\frac{3}{2}$	$\frac{5}{2}$	e	1.4 ± 0.4	5.8	4.9	5.0	-21.4
		f	5.0 ± 1.9	4.9	10.7	11.2	-22.5
	$\frac{7}{2}$	e	-19.3 ± 1.0	-5.7	-12.1	-14.0	-22.2
		f	-1.3 ± 3.5	-1.2	0	0.5	-20.5
	$\frac{9}{2}$	e	-78.1 ± 1.3	-82.1	-12.1	-52.6	-50.6
		f	-23.2 ± 25.4	-47.5	-5.8	-10.6	-36.8
$\frac{1}{2}$	$\frac{1}{2}$	e	9.6 ± 1.8	11.8	0.4	0.5	9.1
		f	22.3 ± 3.1	-1.3	-7.5	-10.8	8.4
	$\frac{3}{2}$	e	2.9 ± 2.2[4]	3.7	-3.6	-11.6	-25.4
		f	-24.1 ± 2.6	-18.1	-1.3	-3.3	-35.3
	$\frac{5}{2}$	e	2.9 ± 2.2[4]	-40.7	-1.3	-8.9	-34.6
		f	-25.8 ± 3.0	-34.6	-7.5	-10.9	-28.3

[1]The label "e" corresponds with $\epsilon' = 1$ and "f" corresponds with $\epsilon' = -1$.
[2]Values from [46].
[3]Present calculations, this work.
[4]Transitions for scattering into the $\frac{1}{2}$, $\frac{3}{2}$, e and $\frac{1}{2}$, $\frac{5}{2}$, e level cannot be separately resolved. Accordingly, the steric asymmetries in the experimental column is the combined steric asymmetry for the $\frac{3}{2}$, $\frac{3}{2}$, $f \rightarrow \frac{1}{2}$, $\frac{3}{2}$, e and $\frac{3}{2}$, $\frac{3}{2}$, $f \rightarrow \frac{1}{2}$, $\frac{5}{2}$, e excitations.

Calculations have been performed on three different cases: 94 % $\overline{m}_j = \frac{3}{2}$ and 6 % $\overline{m}_j = \frac{1}{2}$, 100 % $\overline{m}_j = \frac{3}{2}$ and on a "hard shell" assuming 100 % $\overline{m}_j = \frac{3}{2}$. The calculated steric asymmetries for three cases are shown in Table 3.1. From this table one immediately notices a reasonable agreement between the experimental and all theoretical amplitudes of S, resulting from the UMP4 PES's. The present calculations yield an overall smaller amplitude for S at high j', than the measured values. As far as the sign of S is concerned, there is a striking opposite trend for the experimental values (S^E) compared to our theoretically calculated values (S^C) based on the UMP4 PES's. The steric asymmetry as defined in the experiment $S^E = (\sigma^{OH} - \sigma^{HO})/(\sigma^{OH} + \sigma^{HO})$ should carry a sign opposite to that calculated by HIBRIDON reflecting the parameterization of the UMP4 and CEPA PES's $S^C = (\sigma^{HO} - \sigma^{OH})/(\sigma^{HO} + \sigma^{OH}) = -S^E$. To advance quantum mechanical calculations closer to the ball and stick model, a hard shell alike system was mimicked for the OH-Ar system. To damp the attractive well, the sum potential (V_{sum}) was multiplied with

$$\frac{1}{2}[1 - \tanh\{3(R - 7.08)\}] \tag{3.10}$$

and also set $V_{dif} = 0$. It should be noted that in this case R is in Bohr. The amplitude of S^C for the "hard shell" alike calculations (shown in Table 3.1) is much stronger than that for the full PES's, as it is no longer diluted by the attractive part of $V_{sum}(R)$. S^E shows a proper negative sign for nearly all rotational excited states, in accordance with the ball and stick model. Only the spin-orbit changing transition $j = \frac{3}{2}, \overline{\Omega} = \frac{3}{2}, E \rightarrow j' = \frac{1}{2}, \overline{\Omega} = \frac{3}{2}, \epsilon' = -1$ carries an opposite sign for S^E. Comparison of the results of the "hard shell" calculation with the outcome of the ball and stick model makes it plausible that the present HIBRIDON calculations provide the improper sign for S^C. One would not expect that the O-end is preferred to yield high rotational states. Steric asymmetries are shown in Table 3.1 and Fig. 3.2.

As there is not a perfect agreement among the absolute theoretical results for S^C on the UMP4 PES's as obtained in this study and in Ref. [70], integral state-to-state cross sections have been calculated to test the integration procedure. Truncating the summation over the coupled T-matrix elements in Eq. 3.7 at $J > 101$ ($E_{col} = 451\ cm^{-1}$) and at $J > 130$ ($E_{col} = 781\ cm^{-1}$), perfect agreement (Table 3.2) with "pure" theoretical integral state-to-state cross sections is reported [70]. We have no answer on the question why our results for S^C differ this much from previous calculations [70].

Although the NO-Ar system is more homo-nuclear than OH-Ar, one can also apply the ball and stick model on this system. The O-end is more round than the N-end, that extends further from the center-of-mass. From a ball and stick model one would conclude that the N-end will be preferred for high rotational states, but this is not what was found in earlier experiments and theory [1, 2, 5]. The only exception in respect to this finding is the first (erroneous) measurement of S by Van Leuken, that did not correspond with theoretical results in the same paper [2]. Except this experimental result, all published results for S of NO-Ar collisions show a negative value for S for high rotational states. This indicates that molecules with high rotational states mostly carry back on O-end collisions. There is no satisfactory explanation for this effect that goes against ones natural wit.

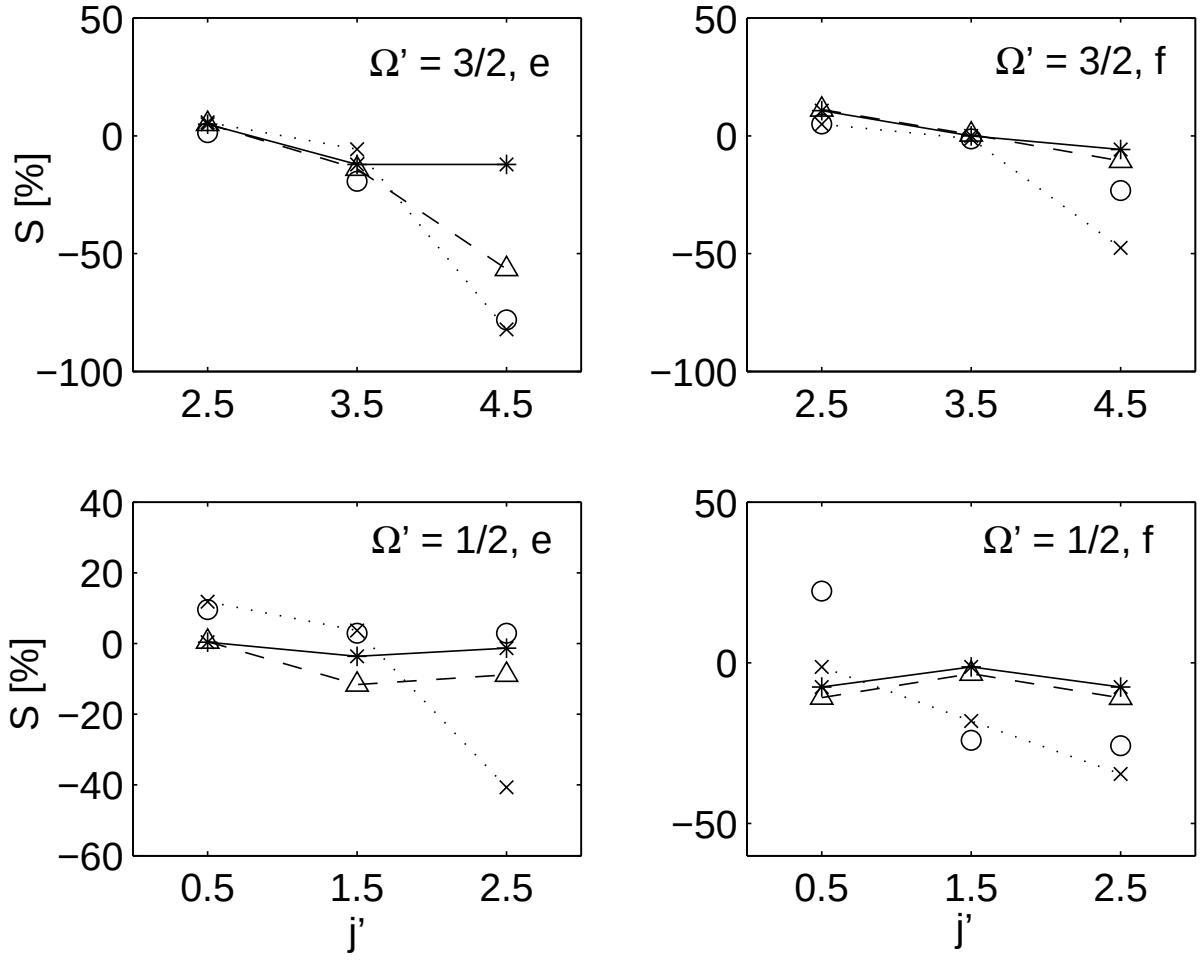

Figure 3.2: Steric asymmetries as a function of the final state of OH-Ar at $E_{tr} = 781$ cm^{-1}. Note that the experimental steric asymmetry is taken conform Ref. [19] and is defined as $S^E = (\sigma^{OH} - \sigma^{HO})/(\sigma^{OH} + \sigma^{HO})$, while the present theoretical results are plotted according to the definition following HIBRIDON parameterization and UMP4 and CEPA PES's $S^C = (\sigma^{HO} - \sigma^{OH})/(\sigma^{HO} + \sigma^{OH}) = -S^E$. Experimental values [46] are indicated with open circles "$\circ$", theoretical results on the UMP4 PES's with 94% $\overline{m}_j = \frac{3}{2}$ are given with a dotted line and a cross "$\times$" [46]. Theoretical results from our work [94% $\overline{m}_j = \frac{3}{2}$ and 6% $\overline{m}_j = \frac{1}{2}$] and [100% $\overline{m}_j = \frac{3}{2}$] are respectively given by a solid line and a star "*" and a dashed line in combination with a triangle "$\triangle$".

Table 3.2: Theoretical integral state-to-state cross sections [Å^2] for rotational excitation of OH $X^2\Pi_{\frac{3}{2}}$, $j = \frac{3}{2}, f$ in collisions with Ar are listed for comparison. A collision energy of 451 cm^{-1} and 746 cm^{-1} has been used. All calculations are based on the UMP4 PES's.

final state			E_{col} = 451 cm^{-1}		E_{col} = 746 cm^{-1}	
Ω'	J'	ϵ'	pure[1]	pure[2]	pure[1]	pure[2]
$\frac{3}{2}$	$\frac{3}{2}$	e	16.5	16.50	11.5	11.40
		f	...	...	...	...
	$\frac{5}{2}$	e	11.8	11.80	11.2	11.20
		f	2.42	2.42	1.62	1.62
	$\frac{7}{2}$	e	2.19	2.19	2.15	2.13
		f	0.350	0.35	0.756	0.75
	$\frac{9}{2}$	e	0.553	0.53	0.703	0.70
		f	0.013	0.01	0.090	0.09
$\frac{1}{2}$	$\frac{1}{2}$	e	2.10	2.10	2.19	2.22
		f	0.238	0.24	0.197	0.20
	$\frac{3}{2}$	e	0.524	0.52	0.826	0.83
		f	0.711	0.71	0.927	0.90
	$\frac{5}{2}$	e	0.458	0.46	0.598	0.60
		f	0.458	0.46	0.598	0.60
		total	37.86	37.73	32.76	32.64

[1] present result [2] Van Beek et al. [46]

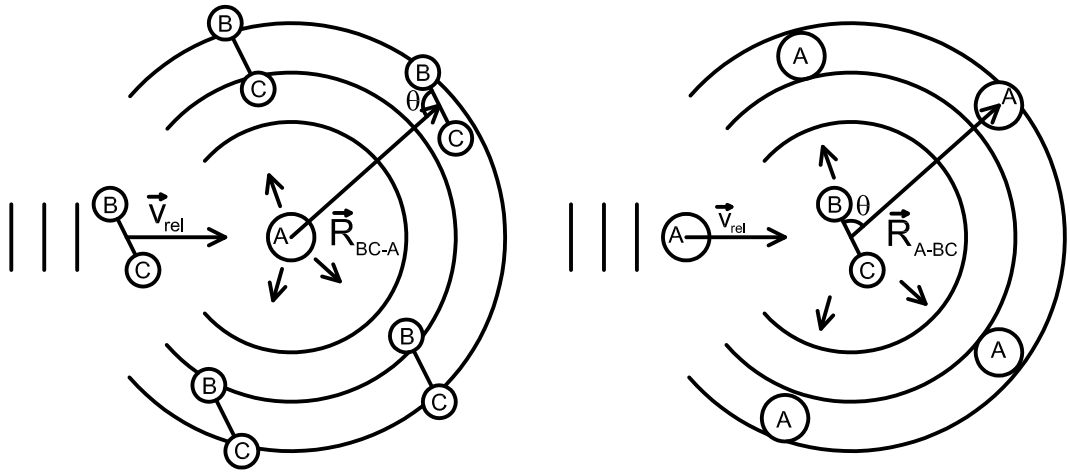

Figure 3.3: Incoming planar wave and outgoing spherical wave that represents a state-to-state collision between a molecule BC and an atom A. The right panel depicts this process in the (A-BC) CMS with $\mathbf{R} = \mathbf{R}_{A-BC}$, the left panel reflects the so-called inverted CMS with $\mathbf{R} = \mathbf{R}_{BC-A} = -\mathbf{R}_{A-BC}$. This figure elucidates that a change from one convention to another also alters the Jacobi angles θ. The Jacobi angles for both cases are related as $\theta_{A-BC} = \pi - \theta_{BC-A}$. Note that the θ has to be distinguished from the CMS scattering angle ϑ which denotes the angle between the outgoing and and incoming wave vectors $\hat{k}$ and $\hat{k}'$.

3.5 Theory

3.5.1 Schrödinger equation, T-matrix and scattering amplitude

The CMS in which the collision of an atom A and a diatomic molecule BC can be described allows for two distinguished conventions regarding the definition of $\mathbf{R}$. The convention followed in most theoretical procedures [54, 59, 61] uses the displacement vector of the center of A in respect to the CM of BC:

$$\mathbf{R} = \mathbf{R}_{A-BC} = \mathbf{R}_A - \mathbf{R}_{BC} \tag{3.11}$$

Alternatively, the "opposite" convention

$$\mathbf{R} = \mathbf{R}_{BC-A} = \mathbf{R}_{BC} - \mathbf{R}_A \tag{3.12}$$

provides an equally well suited definition of $\mathbf{R}$. Both conventions are illustrated in Fig. 3.3. For the simplest (elastic) case of the collision between the two particles A and BC, the scattering matrix $\mathbf{T}$ reduces to a row of dimensionless scalars. The value of these scalars does not bear any relation upon the chosen convention of $\mathbf{R}$ (see eg. [13, 34, 35]). In the case of rotationally inelastic scattering this also holds for the value of the CMS scattering angles (ϑ, ϕ), whereas the scattering matrix and the scattering amplitude could depend on the choice of $\mathbf{R} = \mathbf{R}_{A-BC}$ or $\mathbf{R} = \mathbf{R}_{BC-A}$. In this section we will show that a change

of convention will not cause any problem in relation to the state-to-state differential and integral cross sections, as long as one refrains from orientational dependence.

To elucidate the influence of the choice of $\mathbf{R}_{A-BC}$ or $\mathbf{R}_{BC-A}$ on the T-matrix, the set of (close) coupled differential equations that substantiate the Schrödinger equation of the scattering problem will be considered. When denoting the total wave function as:

$$\Psi^{J,M_J}_{j,l,\overline{\Omega},\epsilon}(\hat{\mathbf{r}},\mathbf{R}) = \sum_{j',l',\overline{\Omega}',\epsilon'} \frac{1}{R} U^{J,M_J}_{j',l',\overline{\Omega}',\epsilon'}(R) \sum_{m'_j,m'_l} \langle j', m'_j, l', m'_l | J, M_J\rangle \\ |j', m'_j, \overline{\Omega}', \epsilon'\rangle Y_{l',m'_l}(\hat{\mathbf{R}}), \tag{3.13}$$

the set of close coupled equations that has to be solved numerically becomes [54, 65]:

$$\left[-\frac{\hbar^2}{2\mu}\frac{d^2}{dR^2} + \frac{\hbar^2 l(l+1)}{2\mu R^2} + \langle j,l,\overline{\Omega},\epsilon,J,M_J|V|j,l,\overline{\Omega},\epsilon,J,M_J\rangle\right] U^{J,M_J}_{j,l,\overline{\Omega},\epsilon}(R) + \\ + \sum_{j',l',\overline{\Omega}',\epsilon'} (1-\delta_{j,j'}\delta_{l,l'}\delta_{\overline{\Omega},\overline{\Omega}'}\delta_{\epsilon,\epsilon'}) \times \\ \times \langle j',l',\overline{\Omega}',\epsilon',J,M_J|V|j,l,\overline{\Omega},\epsilon,J,M_J\rangle U^{J,M_J}_{j',l',\overline{\Omega}',\epsilon'}(R) = 0. \tag{3.14}$$

The radial part of the wave function of Eq. 3.13 obeys to the boundary condition:

$$\lim_{R\to\infty} U^{J,M_J}_{j',l',\overline{\Omega}',\epsilon'}(R) = \delta_{j,j'}\delta_{l,l'}\delta_{\overline{\Omega},\overline{\Omega}'}\delta_{\epsilon,\epsilon'} \exp[-i(k_{j,\overline{\Omega}}\cdot R - l\frac{\pi}{2})]\sqrt{\frac{k_{j',\overline{\Omega}'}}{k_{j,\overline{\Omega}}}} \times \\ \times(\delta_{j,j'}\delta_{l,l'}\delta_{\overline{\Omega},\overline{\Omega}'}\delta_{\epsilon,\epsilon'} - T^J_{j',l',\overline{\Omega}',\epsilon';j,l,\overline{\Omega},\epsilon}) \exp[i(k_{j',\overline{\Omega}}\cdot R - l'\frac{\pi}{2})] = 0. \tag{3.15}$$

When one assumes that the equations above correspond to the convention $\mathbf{R} \equiv \mathbf{R}_{A-BC}$, Eq. 3.14 can easily be adapted to the case $\mathbf{R} = \mathbf{R}_{BC-A}$, applying the inversion operator $i_{\mathbf{R}}$

$$Y_{l,m_l}(\hat{\mathbf{R}}_{A-BC}) = i_{\mathbf{R}} Y_{l,m_l}(\hat{\mathbf{R}}_{BC-A}) = (-1)^l Y_{l,m_l}(\hat{\mathbf{R}}_{BC-A}). \tag{3.16}$$

Eq. 3.16 leads to

$$\left[-\frac{\hbar^2}{2\mu}\frac{d^2}{dR^2} + \frac{\hbar^2 l(l+1)}{2\mu R^2} + \langle j,l,\overline{\Omega},\epsilon,J,M_J|V|j,l,\overline{\Omega},\epsilon,J,M_J\rangle\right] \times \\ \times U^{J,M_J}_{j,l,\overline{\Omega},\epsilon}(R_{BC-A}) + \sum_{j',l',\overline{\Omega}',\epsilon'} (1-\delta_{j,j'}\delta_{l,l'}\delta_{\overline{\Omega},\overline{\Omega}'}\delta_{\epsilon,\epsilon'}) \times \\ \times \langle j',l',\overline{\Omega}',\epsilon',J,M_J|V|j,l,\overline{\Omega},\epsilon,J,M_J\rangle (-1)^{l+l'} U^{J,M_J}_{j',l',\overline{\Omega}',\epsilon'}(R_{BC-A}) = 0. \tag{3.17}$$

Application of the boundary condition of Eq. 3.15 onto the solutions of the coupled equations Eqs 3.14 and 3.17 leads immediately to:

$$T^{(J),A-BC}_{j',l',\overline{\Omega}',\epsilon';j,l,\overline{\Omega},\epsilon} \equiv T^J_{j',l',\overline{\Omega}',\epsilon';j,l,\overline{\Omega},\epsilon} = (-1)^{l+l'} T^{(J),BC-A}_{j',l',\overline{\Omega}',\epsilon';j,l,\overline{\Omega},\epsilon}. \tag{3.18}$$

As elucidated in Eq. 3.5 T-matrix elements $T^{(J),A-BC}_{j',l',\overline{\Omega}',\epsilon';j,l,\overline{\Omega},\epsilon}$ and $T^{(J),BC-A}_{j',l',\overline{\Omega}',\epsilon';j,l,\overline{\Omega},\epsilon}$ may be uncoupled, for example, to the regular collision frame or to the reversed collision frame.

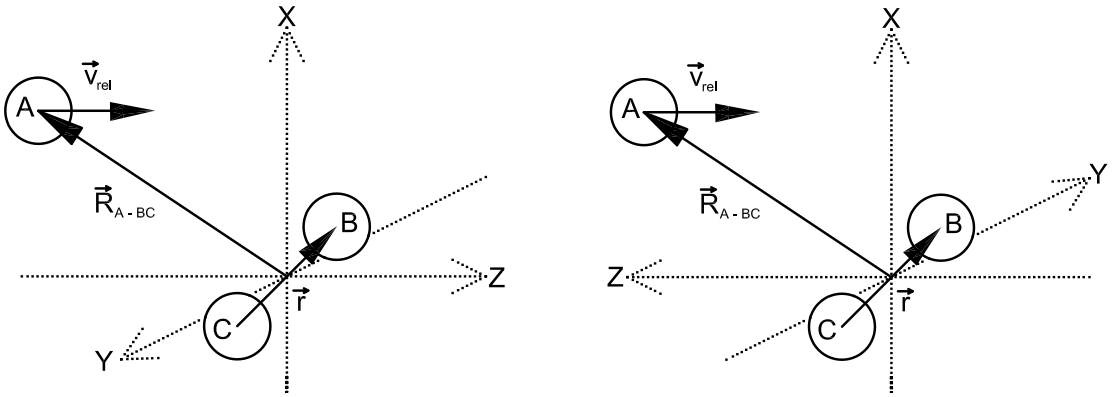

Figure 3.4: Two convenient CM inertial frames in which a collision between a molecule and an atom can be described. In the regular collision frame (left panel) the relative velocity $\mathbf{v_{rel}}$ is directed parallel to the Z axis of m_j and m_l quantization. In the reversed collision frame (right panel) $\mathbf{v_{rel}}$ is directed antiparallel to the Z axis, thus giving the opposite sign for all m_j and m_l quantum numbers. Both panels depict the A-BC CM system with $\mathbf{R} = \mathbf{R}_{A-BC}$. The T-matrix elements themselves do not depend on the choice of the coordinate frame. Eq. 29 of Ref. [71] relates the scattering amplitudes to the T-matrix for arbitrary orientation of the coordinate frame of which the Z axis provides the quantization axis. Application of this expression leads to an extra multiplication factor $(-1)^{l+l'}$ to the T matrix elements in Eq. 3.7 when one applies this formula for the reversed collision frame. Note that the same multiplication factor $(-1)^{l+l'}$ appears in Eq. 3.18 when one switches from the (A-BC) CMS ($\mathbf{R} = \mathbf{R}_{A-BC}$) to the inverted CMS ($\mathbf{R} = \mathbf{R}_{BC-A}$).

Substitution of Eq. 3.18 into Eq. 3.7 yields the scattering amplitude in the (BC-A) collision frame:

$$f^{BC-A}_{j,m_j,\overline{\Omega},\epsilon\rightarrow j',m'_j,\overline{\Omega}',\epsilon'}(\hat{\mathbf{k}}') = \sqrt{\pi}\sum_{J,l,l'}(2l+1)^{\frac{1}{2}}(2J+1)i^{l-l'}\begin{pmatrix} j & J & l \\ m_j & -m_j & 0 \end{pmatrix}\times$$
$$\times\begin{pmatrix} j' & J & l' \\ m'_j & -m_j & m_j-m'_j \end{pmatrix}Y_{l',m_j-m'_j}(\hat{\mathbf{k}}')(-1)^{l+l'}T^{(J),A-BC}_{j',l',\overline{\Omega}',\epsilon';j,l,\overline{\Omega},\epsilon}. \quad (3.19)$$

As noted by Alexander [54], the absence of coupling between incoming and outgoing states of different total parity leads to:

$$T^{(J)}_{j',l',\overline{\Omega}',\epsilon';j,l,\overline{\Omega},\epsilon} = 0 \qquad \text{unless} \qquad (-1)^{l+l'} = \epsilon\epsilon'(-1)^{j'-j}. \quad (3.20)$$

Application of Eq. 3.20 in Eq. 3.19 yields:

$$f^{BC-A}_{j,m_j,\overline{\Omega},\epsilon\rightarrow j',m'_j,\overline{\Omega}',\epsilon'}(\hat{\mathbf{k}}') = f^{A-BC}_{j,m_j,\overline{\Omega},\epsilon\rightarrow j',m'_j,\overline{\Omega}',\epsilon'}(\hat{\mathbf{k}}')\epsilon\epsilon'(-1)^{j'-j}. \quad (3.21)$$

As illustrated in Fig. 3.4, the relation between the scattering amplitudes of Eq. 3.21 remains valid either within the regular or within the reversed collision frame.

3.5.2 The m_j-dependent state-to-state collision cross section for non-oriented molecules

Application of Eq. 3.21 into Eq. 3.8 with $\beta(E) = 0$ and substituting this result in Eq. 3.9 gives:

$$d\sigma_{j,m_j,\overline{\Omega},\epsilon\rightarrow j',m'_j,\overline{\Omega}',\epsilon'} \;/\; d\omega = \frac{1}{k^2}|f^{A-BC}_{j,m_j,\overline{\Omega},\epsilon\rightarrow j',m'_j,\overline{\Omega}',\epsilon'}(\hat{\mathbf{k}}')|^2 =$$
$$\frac{1}{k^2}|f^{BC-A}_{j,m_j,\overline{\Omega},\epsilon\rightarrow j',m'_j,\overline{\Omega}',\epsilon'}(\hat{\mathbf{k}}')|^2. \quad (3.22)$$

Depending on the A-BC or BC-A sign convention for the intermolecular displacement vector, the scattering amplitudes and coupled T-matrix elements do not have to be equal in sign. Eq. 3.22 however, shows that their relation to the differential cross section $d\sigma_{j,m_j,\overline{\Omega},\epsilon\rightarrow j',m'_j,\overline{\Omega}',\epsilon'} \;/\; d\omega$, does not depend on the choice of the A-BC or BC-A convention. In addition to this, the insensitivity of the differential cross section to the sense of rotation in the (regular or reversed) collision frame $d\sigma_{j,m_j,\overline{\Omega},\epsilon\rightarrow j',m'_j,\overline{\Omega}',\epsilon'} \;/\; d\omega = d\sigma_{j,-m_j,\overline{\Omega},\epsilon\rightarrow j',-m'_j,\overline{\Omega}',\epsilon'} \;/\; d\omega$ [54] infers that non-oriented molecules do not yield a different outcome for scattering calculations in the collision and in the reversed collision frame.

Not only the dependence of the differential cross section on the scattering angle that is treated above, but also the dependence of the total cross section on the final state has experimentally been investigated [16, 46]. The total cross section can be obtained by numerical integration of the differential cross section $d\sigma_{j,m_j,\overline{\Omega},\epsilon\rightarrow j',m'_j,\overline{\Omega}',\epsilon'} \;/\; d\omega$ over the full range of $d\omega$. The rapid diffraction oscillations in the differential cross section can cause this integration to be cumbersome [54]. Alternatively, the integral cross section

can be obtained directly as an exact summation over products of T-matrix elements by making use of the orthogonality properties of the spherical harmonics $Y_{l',m_j-m'_j}(\hat{\mathbf{k}}')$. The contributions to this summation are restricted by Eq. 3.20.

$$\begin{aligned}\sigma_{j,m_j,\overline{\Omega},\epsilon\to j',m'_j,\overline{\Omega}',\epsilon'} = \frac{\pi}{k^2} \sum_{J,J'l,l',l'',(l+l'' \text{ even})} \sqrt{2l+1}\sqrt{2l''+1} \times \\ \times(2J+1)(2J'+1) \begin{pmatrix} j & J & l \\ m_j & -m_j & 0 \end{pmatrix} \begin{pmatrix} j' & J' & l'' \\ m_j & -m_j & 0 \end{pmatrix} \times \\ \times \begin{pmatrix} j' & J & l' \\ m'_j & -m_j & m_j - m'_j \end{pmatrix} \begin{pmatrix} j' & J' & l' \\ m'_j & -m_j & m_j - m'_j \end{pmatrix} \times \\ \times(-1)^{(l-l'')/2} T^{J*}_{j',l',\overline{\Omega}',\epsilon';j,l'',\overline{\Omega},\epsilon} T^{J'}_{j',l',\overline{\Omega}',\epsilon';j,l,\overline{\Omega},\epsilon}. \end{aligned} \tag{3.23}$$

Since the detection selectivity for the scattered BC molecules is typically too low to resolve m'_j, the experimental observation relates to:

$$\sigma_{j,m_j,\overline{\Omega},\epsilon\to j',\overline{\Omega}',\epsilon'} = \sum_{m'_j} \sigma_{j,m_j,\overline{\Omega},\epsilon\to j',m'_j,\overline{\Omega}',\epsilon'}. \tag{3.24}$$

This allows one to contract Eq. 3.23

$$\begin{aligned}\sigma_{j,m_j,\overline{\Omega},\epsilon\to j',\overline{\Omega}',\epsilon'} = \frac{\pi}{k^2} \sum_{J,l,l',l'',(l+l'' \text{ even})} C^J_{l,l''}(j,m_j) \times \\ \times(-1)^{(l-l'')/2} T^{J*}_{j',l',\overline{\Omega}',\epsilon';j,l'',\overline{\Omega},\epsilon} T^{J}_{j',l',\overline{\Omega}',\epsilon';j,l,\overline{\Omega},\epsilon} \end{aligned} \tag{3.25}$$

with

$$\begin{aligned} C^J_{l,l''}(j,m_j) \equiv \sqrt{2l+1}\sqrt{2l''+1}(2J+1) \times \\ \times \begin{pmatrix} j & J & l \\ m_j & -m_j & 0 \end{pmatrix} \begin{pmatrix} j & J & l'' \\ m_j & -m_j & 0 \end{pmatrix}. \end{aligned} \tag{3.26}$$

Note that $C^J_{l,l''}(j,m_j) = C^J_{l'',l}(j,m_j) = (-1)^{l+l'} C^J_{l,l''}(j,-m_j)$. In experiments with NO [2,5] the initial state is selected in $j = \frac{1}{2}$, which leads to $\overline{m}_j = \frac{1}{2}$. Because of Eq. 3.26, $l'' = l' = J \pm \frac{1}{2}$.

$$C^J_{J-\frac{1}{2},J-\frac{1}{2}}(\frac{1}{2},m_j) = C^J_{J+\frac{1}{2},J+\frac{1}{2}}(\frac{1}{2},m_j) = \frac{2J+1}{2}. \tag{3.27}$$

Combination of Eq. 3.27 with Eq. 3.23 gives a convenient expression for the integral cross section:

$$\sigma_{\frac{1}{2},m_j,\overline{\Omega},\epsilon\to j',\overline{\Omega}',\epsilon'} = \frac{\pi}{2k^2} \sum_{J,l',l=J\pm\frac{1}{2}} (2J+1) \left[T^{J*}_{j',l',\overline{\Omega}',\epsilon';\frac{1}{2},l,\overline{\Omega},\epsilon} T^{J}_{j',l',\overline{\Omega}',\epsilon';\frac{1}{2},l,\overline{\Omega},\epsilon} \right]. \tag{3.28}$$

The explicit expression for the integral cross section of Eq. 3.28 for $j = \frac{3}{2}$ with $\overline{m}_j = \frac{3}{2}$ and/or $\overline{m}_j = \frac{1}{2}$ (OH experiments [19,46,70]) contains a more extended summation over l and l''. Non-zero contributions may occur in Eq. 3.26 when $l = l'' = J \pm \frac{3}{2}$, $l = l'' = J \pm \frac{1}{2}$

and $l = J \pm \frac{3}{2}, l'' = J \mp \frac{1}{2}$ or $l = J \mp \frac{1}{2}, l'' = J \pm \frac{3}{2}$. Application of Eq. 3.26 for $\overline{m}_j = \frac{3}{2}$ leads to:

$$C^J_{J\pm\frac{3}{2},J\pm\frac{3}{2}}(\frac{3}{2},\frac{3}{2}) = \frac{(2J+1\mp 2)(2J+1)}{8(2J+1\pm 1)} \tag{3.29}$$

$$C^J_{J\pm\frac{1}{2},J\pm\frac{1}{2}}(\frac{3}{2},\frac{3}{2}) = \frac{3(2J+1\mp 2)(2J+1)}{8(2J+1\mp 1)} \tag{3.30}$$

$$C^J_{J\pm\frac{3}{2},J\mp\frac{1}{2}}(\frac{3}{2},\frac{3}{2}) = C^J_{J\mp\frac{1}{2},J\pm\frac{3}{2}}(\frac{3}{2},\frac{3}{2}) = \frac{\sqrt{3(2J-1)(2J+3)}(2J+1)}{8(2J+1\pm 1)} \tag{3.31}$$

The integral cross section can be calculated after substitution of Eqs. 3.29 - 3.31 in Eq. 3.25

$$\begin{aligned}\sigma_{\frac{3}{2},\overline{m}_j=\frac{3}{2},\overline{\Omega},\epsilon\to j',\overline{\Omega}',\epsilon'} = \frac{\pi}{2k^2}\sum_{l',J}(2J+1)\times \\ \times\Bigg[\frac{1}{4}\sum_{l=J\pm\frac{3}{2}}\frac{(2J+1\mp 1)}{(2J+1\pm 1)}T^{J*}_{j',l',\overline{\Omega}',\epsilon';\frac{3}{2},l,\overline{\Omega},\epsilon}T^{J}_{j',l',\overline{\Omega}',\epsilon';\frac{3}{2},l,\overline{\Omega},\epsilon} + \\ +\frac{3}{4}\sum_{l=J\pm\frac{1}{2}}\frac{(2J+1\mp 2)}{(2J+1\mp 1)}T^{J*}_{j',l',\overline{\Omega}',\epsilon';\frac{3}{2},l,\overline{\Omega},\epsilon}T^{J}_{j',l',\overline{\Omega}',\epsilon';\frac{3}{2},l,\overline{\Omega},\epsilon} + \\ -\frac{\sqrt{3}}{2}\sum_{l=J\pm\frac{3}{2},l''=J\mp\frac{1}{2}}\frac{\sqrt{(2J-1)(2J+3)}}{2J+1\pm 1}\times \\ \times\mathrm{Re}(T^{J*}_{j',l',\overline{\Omega}',\epsilon';\frac{3}{2},l,\overline{\Omega},\epsilon}T^{J}_{j',l',\overline{\Omega}',\epsilon';\frac{3}{2},l'',\overline{\Omega},\epsilon})\Bigg]\end{aligned} \tag{3.32}$$

To complete the treatment for OH, application of Eq. 3.26 for $\overline{m}_j = \frac{1}{2}$ leads to:

$$C^J_{J\pm\frac{3}{2},J\pm\frac{3}{2}}(\frac{3}{2},\frac{1}{2}) = \frac{3(2J+1\pm 2)(2J+1)}{8(2J+1\pm 1)} \tag{3.33}$$

$$C^J_{J\pm\frac{1}{2},J\pm\frac{1}{2}}(\frac{3}{2},\frac{1}{2}) = \frac{(2J+1\pm 2)(2J+1)}{8(2J+1\mp 1))} \tag{3.34}$$

$$C^J_{J\pm\frac{3}{2},J\mp\frac{1}{2}}(\frac{3}{2},\frac{1}{2}) = C^J_{J\mp\frac{1}{2},J\pm\frac{3}{2}}(\frac{3}{2},\frac{1}{2}) = \frac{-\sqrt{3(2J-1)(2J+3)}(2J+1)}{8(2J+1\pm 1)} \tag{3.35}$$

The total cross section can be calculated after substitution of Eqs. 3.33 - 3.35 in Eq. 3.25

$$\sigma_{\frac{3}{2},\overline{m}_j=\frac{1}{2},\overline{\Omega}\epsilon\rightarrow j',\overline{\Omega}',\epsilon'} = \frac{\pi}{2k^2}\sum_{l',J}(2J+1)\times$$
$$\times\Bigg[\frac{3}{4}\sum_{l=J\pm\frac{3}{2}}\frac{(2J+1\pm 2)}{(2J+1\pm 1)}T^{J*}_{j',l',\overline{\Omega}',\epsilon';\frac{3}{2},l,\overline{\Omega},\epsilon}T^{J}_{j',l',\overline{\Omega}',\epsilon';\frac{3}{2},l,\overline{\Omega},\epsilon}+$$
$$+\frac{1}{4}\sum_{l=J\pm\frac{1}{2}}\frac{(2J+1\pm 2)}{(2J+1\mp 1)}T^{J*}_{j',l',\overline{\Omega}',\epsilon';\frac{3}{2},l,\overline{\Omega},\epsilon}T^{J}_{j',l',\overline{\Omega}',\epsilon';\frac{3}{2},l,\overline{\Omega},\epsilon}+$$
$$+\frac{\sqrt{3}}{2}\sum_{l=J\pm\frac{3}{2},l''=J\mp\frac{1}{2}}\frac{\sqrt{(2J-1)(2J+3)}}{2J+1\pm 1}\mathrm{Re}(T^{J*}_{j',l',\overline{\Omega}',\epsilon';\frac{3}{2},l,\overline{\Omega},\epsilon}T^{J}_{j',l',\overline{\Omega}',\epsilon';\frac{3}{2},l'',\overline{\Omega},\epsilon})\Bigg] \quad (3.36)$$

3.5.3 The m_j-dependent state-to-state collision cross section for oriented molecules

The next issue that will be addressed is whether the choice for either the $\mathbf{R}_{A-BC}$ or the $\mathbf{R}_{BC-A}$ displacement vector affects the orientational dependence of the collision cross section. As a first step notice that $|j,\pm m_j,\pm\overline{\Omega}\rangle$ and $|j,\mp m_j,\mp\overline{\Omega}\rangle$ correspond to wave functions that respectively favor head and tail orientation of the BC molecule along the Z axis (which is the quantization axis). As pointed out by Loesch [72] collisions on the C-end of the BC molecule are preferred when the B-end favors to point along $\mathbf{v_{rel}}$ in the (A-BC) CMS. In the (BC-A) CMS used by Stolte et al. [73, 74], collisions impinging onto the B-end of the BC molecule are preferred when the B-end favors points along $\mathbf{v_{rel}}$.

Depending on the direction of the orientation field in the scattering region ($\mathbf{E}\uparrow\uparrow\mathbf{v_{rel}}$ or $\mathbf{E}\uparrow\downarrow\mathbf{v_{rel}}$) collisions on the head or on the tail of BC are preferred. The oriented wave function in the regular collision frame may be written as:

$$\big|j,\pm\overline{m}_j,\overline{\Omega},E\big\rangle = \alpha(E)\big|j,\pm\overline{m}_j,\overline{\Omega},\epsilon_u\big\rangle + \beta(E)\big|j,\pm\overline{m}_j,\overline{\Omega},-\epsilon_u\big\rangle \quad (3.37)$$
$$\text{or as}\quad \big|j,\pm\overline{m}_j,\overline{\Omega},E\big\rangle = \alpha(E)\big|j,\pm\overline{m}_j,\overline{\Omega},\epsilon_u\big\rangle - \beta(E)\big|j,\pm\overline{m}_j,\overline{\Omega},-\epsilon_u\big\rangle \quad (3.38)$$

Taking the limit for a high field E ($\alpha(E)=\beta(E)=\frac{1}{2}\sqrt{2}$) and subsequent substitution of these states in Eq. 3.3 lead to:

$$\lim_{E\rightarrow\infty}\big|j,\pm\overline{m}_j,\overline{\Omega},E\big\rangle = \big|j,\pm\overline{m}_j,+\overline{\Omega}\big\rangle \qquad \text{or} \quad (3.39)$$
$$\lim_{E\rightarrow\infty}\big|j,\pm\overline{m}_j,\overline{\Omega},E\big\rangle = \epsilon_u\big|j,\pm\overline{m}_j,-\overline{\Omega}\big\rangle \quad (3.40)$$

The pairs of oriented wave functions that favor collisions onto the head (B) of BC in the regular frame of the (A-BC) CMS and onto the tail (C) in the regular frame of the (BC-A) CMS are represented by $\alpha(E)\big|j,\overline{m}_j,\overline{\Omega},\epsilon_u\big\rangle-\beta(E)\big|j,\overline{m}_j,\overline{\Omega},-\epsilon_u\big\rangle$ and $\alpha(E)\big|j,-\overline{m}_j,\overline{\Omega},\epsilon_u\big\rangle+\beta(E)\big|j,-\overline{m}_j,\overline{\Omega},-\epsilon_u\big\rangle$. The pair of wave functions $\alpha(E)\big|j,\overline{m}_j,\overline{\Omega},\epsilon_u\big\rangle+\beta(E)\big|j,\overline{m}_j,\overline{\Omega},-\epsilon_u\big\rangle$ and $\alpha(E)\big|j,-\overline{m}_j,\overline{\Omega},\epsilon_u\big\rangle-\beta(E)\big|j,-\overline{m}_j,\overline{\Omega},-\epsilon_u\big\rangle$ favor collisions onto the tail (C) of the molecule in the regular frame (A-BC) CMS and on the head in the regular frame of the (BC-A) CMS.

The orientation dependent contribution

$$\frac{1}{2}(d\sigma^{Head}/d\omega - d\sigma^{Tail}/d\omega) \equiv \frac{d}{d\omega}\,\Delta\sigma_{j,m_j,\overline{\Omega},E\to j',m'_j,\overline{\Omega}',\epsilon'} \tag{3.41}$$

of the cross section follows from Eq. 3.8 and Eq. 3.9, upon insertion of the proper sign for $\beta(E)$. In the A-BC CMS one obtains:

$$\begin{aligned}\frac{d}{d\omega}\,\Delta\sigma_{j,m_j,\overline{\Omega},E\to j',m'_j,\overline{\Omega}',\epsilon'} = \;& \frac{-m_j}{\overline{m}_j}\,\alpha(E)\beta(E)\frac{1}{k^2}\times \\ \times\left[f^{(A-BC)*}_{j,m_j,\overline{\Omega},\epsilon_u;j',m'_j,\overline{\Omega}',\epsilon'}(\hat{\mathbf{k}}')f^{(A-BC)}_{j,m_j,\overline{\Omega},-\epsilon_u;j',m'_j,\overline{\Omega}',\epsilon'}(\hat{\mathbf{k}}') + \mathrm{cc}\right].\end{aligned} \tag{3.42}$$

The complex conjugate is indicated by cc. Note that initial states with $m_j = 0$ cannot be oriented because of $m_j \cdot \Omega = 0$. When one compares Eq. 3.42 with Eq. 15 from Ref [1], a sign mismatch appears when one assumes positive values for α and β conform the caption of its Fig. 3. In HIBRIDON it is assumed that one works in the A-BC CMS, but the oriented wave function is taken in respect to the BC-A CMS similar to Ref. [2]. In the BC-A CMS, one gets:

$$\begin{aligned}\frac{d}{d\omega}\Delta\sigma_{j,m_j,\overline{\Omega},E\to j',m'_j,\overline{\Omega}',\epsilon'} = \;& \frac{m_j}{\overline{m}_j}\,\alpha(E)\beta(E)\frac{1}{k^2}\times \\ \times\left[f^{(BC-A)*}_{j,m_j,\overline{\Omega},\epsilon_u;j',m'_j,\overline{\Omega}',\epsilon'}(\hat{\mathbf{k}}')f^{(BC-A)}_{j,m_j,\overline{\Omega},-\epsilon_u;j',m'_j,\overline{\Omega}',\epsilon'}(\hat{\mathbf{k}}') + \mathrm{cc}\right].\end{aligned} \tag{3.43}$$

which yields the incorrect sign of S when one ignores the A-BC and BC-A dependence of the scattering amplitude that is based on the coupled T-matrix of Eq. 3.20. When taking this dependence into account by combining Eqs. 3.22, 3.42 and 3.43, identical outcome in the A-BC and the BC-A collision system results in $\frac{1}{2}(d\sigma^{Head}/d\omega - d\sigma^{Tail}/d\omega)$. This can offer an explanation for the discrepancy between the experimental and the theoretically calculated values of S for OH-Ar as presented in Section 3.

The expressions of Eqs. 3.42 and 3.43 both relate to the regular collision system. A switch from the regular to the reversed collision system also induces an additional sign change in Eqs. 3.42 and 3.43. The oriented states as defined in Eqs. 8 - 11 of [2] relate to the collision frame of the BC-A CMS. The m'_j summed orientational dependence of the integral A-BC collision cross sections becomes

$$\frac{1}{2}(\sigma^{Head} - \sigma^{Tail}) = \int_{4\pi} d\omega \sum_{m'_j} \frac{d}{d\omega}\Delta\sigma_{j,m_j,\overline{\Omega},E\to j',m'_j,\overline{\Omega}',\epsilon'} \tag{3.44}$$

which, after defining $\Delta\sigma_{j,m_j,\overline{\Omega},E\to j,\overline{\Omega},\epsilon'} \equiv \sum_{m'_j}\Delta\sigma_{j,m_j,\overline{\Omega},E\to j',m'_j,\overline{\Omega}',\epsilon'}$ and making use of Eqs. (1.58) and (2.32) of Ref. [13] can be expressed as:

$$\begin{aligned}\Delta\sigma_{j,m_j,\overline{\Omega},E\to j,\overline{\Omega},\epsilon'} = \;& \frac{-2\pi}{k^2}\alpha(E)\beta(E) \sum_{J,l,l',l''(l+l'' \text{ odd})} C^J_{l,l''}(j,\overline{m}_j)\times \\ & \times(-1)^{\frac{l-l''-1}{2}}\mathrm{Im}(T^{J,(A-BC)*}_{j',l',\overline{\Omega}',\epsilon';j,l,\overline{\Omega},\epsilon_u}T^{J,(A-BC)}_{j',l',\overline{\Omega}',\epsilon';j,l'',\overline{\Omega},-\epsilon_u}).\end{aligned} \tag{3.45}$$

In experiments studying the orientational dependence of state-to-state rotational energy transfer of NO [2,5], a state with $j = \frac{1}{2}$ and $\overline{m}_j = \frac{1}{2}$ is selected. In this case, the summation over l and l'' restricts to $l = J \pm \frac{1}{2}$, $l'' = J \mp \frac{1}{2}$. From Eq. 3.26 it follows that:

$$C^J_{J\pm\frac{1}{2},J\mp\frac{1}{2}}(\frac{1}{2},\frac{1}{2}) = \frac{1}{2}(2J+1). \tag{3.46}$$

Consequently, Eq. 3.45 can be reduced to

$$\begin{aligned}\Delta\sigma_{\frac{1}{2},m_j,\overline{\Omega},E\to j',\overline{\Omega}',\epsilon'} = \frac{-\pi}{k^2}\alpha(E)\beta(E)\sum_{J,l',\epsilon}(2J+1)\times \\ \times\mathrm{Im}(T^{J,(A-BC)*}_{j',l',\overline{\Omega}',\epsilon';\frac{1}{2},J+\frac{1}{2},\overline{\Omega},\epsilon}T^{J,(A-BC)}_{j',l',\overline{\Omega}',\epsilon';\frac{1}{2},J-\frac{1}{2},\overline{\Omega},-\epsilon}).\end{aligned} \tag{3.47}$$

This result can be transformed to the T-matrix $l+j \to J$ coupling scheme of Van Leuken et al., using Eq. 3.6:

$$\begin{aligned}\Delta\sigma_{\frac{1}{2},m_j,\overline{\Omega},E\to j',\overline{\Omega}',\epsilon'} = \frac{\pi}{k^2}\alpha(E)\beta(E)\sum_{J,l',\epsilon}(2J+1)\times \\ \times\mathrm{Im}(T^{J,(A-BC)*}_{l',j',\overline{\Omega}',\epsilon';J+\frac{1}{2},\frac{1}{2},\overline{\Omega},\epsilon}T^{J,(A-BC)}_{l',j',\overline{\Omega}',\epsilon';J-\frac{1}{2},\frac{1}{2},\overline{\Omega},-\epsilon}).\end{aligned} \tag{3.48}$$

Comparison of Eq. 3.48 with Eq. 21 of Ref. [2] shows that for the theoretical results:

$$(\sigma^{Head} - \sigma^{Tail})_{\text{This work}} = (\sigma^{Head} - \sigma^{Tail})_{\text{Van Leuken}}\ . \tag{3.49}$$

This implies that the theoretical sign of S as obtained by Van Leuken et al. [2] is correct.

The orientational dependence of OH in collisions has been studied for incoming oriented molecules with $\overline{\Omega} = j = \overline{m}_j = \frac{3}{2}$ [19,46,70]. In this case the summation over l and l'' in Eq. 3.45 reduces to respectively: $l = J \pm \frac{3}{2}, l'' = J \mp \frac{3}{2}, l = J \pm \frac{1}{2}, l'' = J \mp \frac{1}{2}, l = J+1 \pm \frac{1}{2}, l'' = J+1 \mp \frac{1}{2}$ and $l = J-1 \pm \frac{1}{2}, l'' = J-1 \mp \frac{1}{2}$. Application of Eq. 3.26 for $\overline{m}_j = \frac{3}{2}$ yields for these special cases:

$$C^J_{J\pm\frac{3}{2},J\mp\frac{3}{2}}(\frac{3}{2},\frac{3}{2}) = \frac{1}{8}\sqrt{\frac{(2J-1)(2J+3)}{2J(2J+2)}}(2J+1), \tag{3.50}$$

$$C^J_{J\pm\frac{1}{2},J\mp\frac{1}{2}}(\frac{3}{2},\frac{3}{2}) = \frac{3}{8}\sqrt{\frac{(2J-1)(2J+3)}{2J(2J+2)}}(2J+1), \tag{3.51}$$

$$C^J_{J+1\pm\frac{1}{2},J+1\mp\frac{1}{2}}(\frac{3}{2},\frac{3}{2}) = \frac{\sqrt{3}}{8}\frac{(2J-1)}{\sqrt{2J(2J+2)}}(2J+1), \tag{3.52}$$

$$\text{and}\quad C^J_{J-1\pm\frac{1}{2},J-1\mp\frac{1}{2}}(\frac{3}{2},\frac{3}{2}) = \frac{\sqrt{3}}{8}\frac{(2J+3)}{\sqrt{2J(2J+2)}}(2J+1). \tag{3.53}$$

Subsequent substitution of Eqs. 3.50-3.53 into Eq. 3.45 gives:

$$\Delta\sigma_{\frac{3}{2},\overline{m}_j=\frac{3}{2},\overline{\Omega},E\to j',m'_j,\overline{\Omega}',\epsilon'} = \frac{-\pi}{k^2}\alpha(E)\beta(E)\sum_{J,l',\epsilon}(2J+1)\times$$
$$\times\mathrm{Im}\Bigg[-\frac{1}{8}\sqrt{\frac{(2J-1)(2J+3)}{2J(2J+2)}}T^{J,(A-BC)*}_{j',l',\overline{\Omega}',\epsilon';\frac{3}{2},J+\frac{3}{2},\overline{\Omega},\epsilon}T^{J,(A-BC)}_{j',l',\overline{\Omega}',\epsilon';\frac{3}{2},J-\frac{3}{2},\overline{\Omega},-\epsilon}+$$
$$+\frac{3}{8}\sqrt{\frac{(2J-1)(2J+3)}{2J(2J+2)}}T^{J,(A-BC)*}_{j',l',\overline{\Omega}',\epsilon';\frac{3}{2},J+\frac{1}{2},\overline{\Omega},\epsilon}T^{J,(A-BC)}_{j',l',\overline{\Omega}',\epsilon';\frac{3}{2},J-\frac{1}{2},\overline{\Omega},-\epsilon}+$$
$$+\frac{\sqrt{3}}{8}\frac{(2J-1)}{\sqrt{2J(2J+2)}}T^{J,(A-BC)*}_{j',l',\overline{\Omega}',\epsilon';\frac{3}{2},J+\frac{3}{2},\overline{\Omega},\epsilon}T^{J,(A-BC)}_{j',l',\overline{\Omega}',\epsilon';\frac{3}{2},J+\frac{1}{2},\overline{\Omega},-\epsilon}+$$
$$+\frac{\sqrt{3}}{8}\frac{(2J+3)}{\sqrt{2J(2J+2)}}T^{J,(A-BC)*}_{j',l',\overline{\Omega}',\epsilon';\frac{3}{2},J-\frac{1}{2},\overline{\Omega},\epsilon}T^{J,(A-BC)}_{j',l',\overline{\Omega}',\epsilon';\frac{3}{2},J-\frac{3}{2},\overline{\Omega},-\epsilon}\Bigg]. \tag{3.54}$$

Similar to the case of $\overline{m}_j=\frac{3}{2}$ (yielding Eqs. 3.50-3.60) application of Eq. 3.26 for $\overline{m}_j=\frac{1}{2}$ gives:

$$C^J_{J\pm\frac{3}{2},J\mp\frac{3}{2}}(\frac{3}{2},\frac{1}{2}) = -\frac{3}{8}\sqrt{\frac{(2J-1)(2J+3)}{2J(2J+2)}}(2J+1), \tag{3.55}$$

$$C^J_{J\pm\frac{1}{2},J\mp\frac{1}{2}}(\frac{3}{2},\frac{1}{2}) = -\frac{1}{8}\sqrt{\frac{(2J-1)(2J+3)}{2J(2J+2)}}(2J+1), \tag{3.56}$$

$$C^J_{J+1\pm\frac{1}{2},J+1\mp\frac{1}{2}}(\frac{3}{2},\frac{1}{2}) = \frac{\sqrt{3}}{8}\frac{(2J+3)}{\sqrt{2J(2J+2)}}(2J+1), \tag{3.57}$$

$$\text{and}\quad C^J_{J-1\pm\frac{1}{2},J-1\mp\frac{1}{2}}(\frac{3}{2},\frac{1}{2}) = \frac{\sqrt{3}}{8}\frac{(2J-1)}{\sqrt{2J(2J+2)}}(2J+1). \tag{3.58}$$

Subsequent substitution of Eqs. 3.55-3.58 into Eq. 3.45 for $\overline{m}_j=\frac{1}{2}$ results in:

$$\Delta\sigma_{\frac{3}{2},\overline{m}_j=\frac{1}{2},\overline{\Omega},E\to j',m'_j,\overline{\Omega}',\epsilon'} = \frac{-\pi}{k^2}\alpha(E)\beta(E)\sum_{J,l',\epsilon}(2J+1)\times$$
$$\times\mathrm{Im}\Bigg[\frac{3}{8}\sqrt{\frac{(2J-1)(2J+3)}{2J(2J+2)}}T^{J,(A-BC)*}_{j',l',\overline{\Omega}',\epsilon';\frac{3}{2},J+\frac{3}{2},\overline{\Omega},\epsilon}T^{J,(A-BC)}_{j',l',\overline{\Omega}',\epsilon';\frac{3}{2},J-\frac{3}{2},\overline{\Omega},-\epsilon}+$$
$$-\frac{1}{8}\sqrt{\frac{(2J-1)(2J+3)}{2J(2J+2)}}T^{J,(A-BC)*}_{j',l',\overline{\Omega}',\epsilon';\frac{3}{2},J+\frac{1}{2},\overline{\Omega},\epsilon}T^{J,(A-BC)}_{j',l',\overline{\Omega}',\epsilon';\frac{3}{2},J-\frac{1}{2},\overline{\Omega},-\epsilon}+$$
$$+\frac{\sqrt{3}}{8}\frac{(2J+3)}{\sqrt{2J(2J+2)}}T^{J,(A-BC)*}_{j',l',\overline{\Omega}',\epsilon';\frac{3}{2},J+\frac{3}{2},\overline{\Omega},\epsilon}T^{J,(A-BC)}_{j',l',\overline{\Omega}',\epsilon';\frac{3}{2},J+\frac{1}{2},\overline{\Omega},-\epsilon}+$$
$$+\frac{\sqrt{3}}{8}\frac{(2J-1)}{\sqrt{2J(2J+2)}}T^{J,(A-BC)*}_{j',l',\overline{\Omega}',\epsilon';\frac{3}{2},J-\frac{1}{2},\overline{\Omega},\epsilon}T^{J,(A-BC)}_{j',l',\overline{\Omega}',\epsilon';\frac{3}{2},J-\frac{3}{2},\overline{\Omega},-\epsilon}\Bigg] \tag{3.59}$$

The equations above describe a recipe to calculate $\frac{1}{2}(\sigma^{Head} - \sigma^{Tail})$, which presents the numerator of S as defined in Eq. 3.1. Its denominator $\frac{1}{2}(\sigma^{Head} + \sigma^{Tail})$ can be calculated using Eq. 3.42 as:

$$\frac{1}{2}(\sigma^{Head} + \sigma^{Tail}) = \alpha^2(E)\ \sigma_{j,m_j,\overline{\Omega},\epsilon_u \rightarrow j',\overline{\Omega}',\epsilon'} + \beta^2(E)\ \sigma_{j,m_j,\overline{\Omega},-\epsilon_u \rightarrow j',\overline{\Omega}',\epsilon'} \tag{3.60}$$

In the case of $j = \frac{1}{2}$ and $j = \frac{3}{2}$, Eqs. 3.28, 3.32 and 3.36 provide a recipe for calculation of $\sigma_{j,m_j,\overline{\Omega},\epsilon \rightarrow j',\overline{\Omega}',\epsilon'}$. Substitution of $\sigma_{j,m_j,\overline{\Omega},\epsilon \rightarrow j',\overline{\Omega}',\epsilon'}$ in Eq. 3.60 yields S.

3.6 Re-evaluation of the experimental S

Except for the very first tentative observations [2], the experimentally obtained values of S for NO-Ar confirmed the theoretical predictions [1, 5, 69]. Both calculated and experimental values of S for high j' are in disagreement with a ball and stick model. The present (close-coupling) HIBRIDON calculations for OH-Ar result a sign for S that is improper compared to earlier measurements and which is also opposite to the ball and stick model. As argued in Section 4.3 below Eq. 3.43, this can be explained the fact that the oriented wave function in HIBRIDON carries an actual orientation that is opposite to the denoted one. The assumption that the ball and stick model is correct for OH-Ar, implies that the sign of S for HIBRIDON calculations (also for NO-Ar) has to be reversed. This raises the question whether the experimental results for NO-Ar have to be revised, possibly due to errors in the experimental procedure. Therefore the experimental sign of S has been reinvestigated to explore this possibility. As a first step, the direction of the orientation field in relation to the data acquisition and control software has been checked. Using a voltmeter, the voltage on the rods of the orientation field was measured and found to be in correspondence with the assumed value in the software.

To exclude the possibility that the previous experiments had been carried out incorrectly, the steric asymmetry has been remeasured for NO-He (at $E_{tr} = 514$ cm^{-1}) for a transition to the final state $j' = 4.5$, $\overline{\Omega}' = \frac{1}{2}$, $\epsilon' = -1$. This remeasurement has been carried out under similar conditions as in earlier measurements for NO-Ar and NO-He [5,16], but with a more powerful laser and a new data acquisition program. The earlier measurements on NO-Ar and NO-He showed that NO-He yields the same sign for S as NO-Ar [16]. In both measurements laser induced fluorescence from the $A^2\Sigma^+(v = 0)$ state was used to determine the total number of molecules scattered into the $j' = 4\frac{1}{2}, \overline{\Omega}' = \frac{1}{2}, \epsilon' = -1$ level of the vibrational ground state.

The laser system that was used in earlier work has been replaced by a more powerful excimer pumped dye laser system (Lambda Physik EMG 201 / FL 3002) equipped with a frequency doubling unit to generate the tunable $\lambda = 226$ nm (output 1.5 mJ/pulse). This new laser system required a new timing and control system for which new software was developed. New software for data acquisition was also developed and the orientation voltages were tested once again and found to be correct. A value of $S = 0.28 \pm 0.02$ was obtained earlier by De Lange et al. in the case described above [5]. Our remeasurement

yielded a value of $S = 0.39 \pm 0.15$ which confirms the correctness of De Lange's NO-Ar data collection procedure .

The next step in our re-evaluation was to look for physical explanations for an orientation of the NO molecule in the scattering region, opposite to the expected orientation. Opposite orientation of the NO molecule would change the sign of the theoretical predicted S, so N-end collisions are preferred for excitation to high rotational states. If a molecule in a low field seeking state undergoes a rapid change of the electric field along its path, this can result in a sudden change of the low field seeking state into that of a high field seeking state. This phenomenon is known under the name Majorana flop [73, 75]. When such an effect would occur in our setup the sign of the experimental reported S would reverse and agree with the proper sign (in accordance to the ball and stick model) of the theoretical S, as argued in this work. The presence of an orientational Majorana flop has been investigated experimentally by examining the LIF spectrum of the $A^2\Sigma^+(v = 0) \leftarrow X^2\Pi_{\frac{1}{2}}(v = 0)$, under the same conditions at which S was remeasured, Fig. 3.5. When no orientation field is present, one expects to see only two peaks for the hexapole state selected beam, the R_{21} and the Q_{11} branch. If a field is applied, mixing of Λ-doublet as defined in Eq. 3.8 will take place and the peak of the R_{11}/Q_{21} branches appears. Peaks belonging to the lower and high field seeking Λ-doublet state will occur and grow with increasing orientation field strength. This effect is seen, but in the case of a Majorana flop, the high field seeking R_{11}/Q_{21} peak ought to dominate the spectrum. In the experiment it does not. The experiment shows that it is the low field seeking component of the Λ-doublet that is present in the collision region. This component orients with its negative end towards the negative electrode of the orientation field rods.

3.7 Discussion and concluding remarks

Theoretical and experimental results for S in NO-Ar collisions showed an O-end preference for transitions to high final rotational states [2, 5]. From a (classical) ball and stick model one would expect the N-end to be preferred, as the torque that can be applied on the N-end is larger. For collisions of the less homo-nuclear OH molecule with Ar, the simple ball and stick model does apply. The H-end is preferred for high rotational states in both experiments and theoretical results [46]. To our knowledge, there is no satisfactory answer to the question why S for OH-Ar does behave as expected, while for NO-Ar it behaves oppositely. Application of a newly developed quasi-quantum mechanical model [58] yields reasonable values for the amplitude of S, but gives a sign for NO-Ar that is opposite to experimental one. For OH-Ar it yields the proper sign, so its result can in both cases be explained by the ball and stick model. The present quantum mechanical (HIBRIDON) calculations on collisions of OH-Ar (this work) yield an opposite sign of S: a preference for O-end collisions for transitions to high rotational states. Although this does not correspond to the ball and stick model, it is consonant with NO-Ar results.

Assuming that OH-Ar measurements are correct (as they can easily be understood), then HIBRIDON calculations yield the wrong sign for S. A sign error in the expressions of Van Leuken [2] for collisions involving NO is excluded, as can be concluded from the outcome of section 3.5.3. A feasible possibility is an error in the implementation of

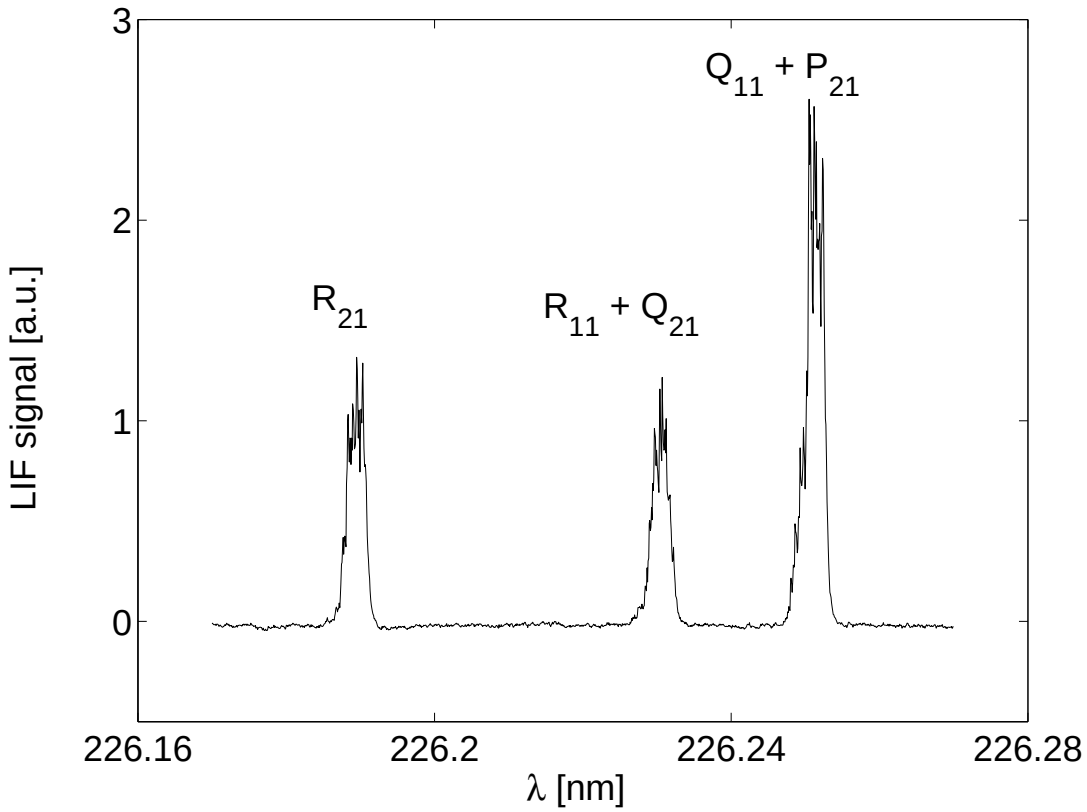

Figure 3.5: LIF excitation spectrum of $A^2\Sigma^+(v = 0) \leftarrow X^2\Pi_{\frac{1}{2}}(v = 0)$ transition of the hexapole state selected NO beam, taken under the same conditions at which S was remeasured. The spectrum is somewhat saturated and an orientation field of $E \approx 16$ kV/cm is applied that is expected to induce about 25% mixing with the lower component ($\epsilon = 1$) of the Λ-doublet [47]. The R_{21} and the Q_{11} originate from the hexapole selected upper ϵ = -1 component of the j = $\frac{1}{2}$ Λ-doublet. The R_{11}/Q_{21} transition, that originates from the lower component of the Λ-doublet is due to the mixing of the Λ-doublet, caused by the orientation field. When the field is switched off, the center peak (R_{11}/Q_{21} branch) disappears, while the other peaks remain. In absence of saturation and at equal population of both components of the Λ-doublet component, LIF intensities will be proportional to Hönl-London factors giving a ratio of $R_{21} : Q_{11} : R_{11}/Q_{21}$ as $1 : 2 : 3$. Clearly the spectrum shows approximately 25% mixing in the lower Λ-doublet component. This means that the NO molecules in the scattering region are in a low field seeking state. A Majorana flop is excluded.

HIBRIDON. In HIBRIDON it is assumed that one works in the A-BC CM system, while the oriented wave functions are taken in respect to the BC-A CMS. This inconsistency induces a switch of the sign of S. The possibility of implementation problems in the adapted version of MOLSCAT could not be explored, as its originator Prof. J. Snijders sadly passed away in 2003 and no documentation was left. It should however be noted that the sign of S in Ref. [2] was carefully checked because of its discrepancy with the early experimental results in the same paper.

When for NO-Ar the sign of quantum mechanical calculations has to switch as well, all theoretical results are consonant with the ball and stick model. The experimental results for NO-Ar have been checked and were found to be opposite to the ball and stick model. Experimentally, it has been shown that molecules in the collision region are in the low field seeking state. The negative end is assumed to correspond to the head (N-end) and the positive end to the tail (O-end) of the NO molecule. Under this assumption, the actually observed steric asymmetry S is given by:

$$S = \frac{\sigma^- - \sigma^+}{\sigma^- + \sigma^+} \tag{3.61}$$

The cross sections σ^- and σ^+ respectively indicate the cases in which the negative and the positive end of the molecule preferentially point towards the incoming atom. If the sign of the NO ($v = 0$, $X\,^2\Pi$) dipole moment would be reversed, N^+O^- instead of N^-O^+, the experimental sign of S would be in agreement with the ball and stick model.

The absolute value of the small electric dipole of NO($v = 0$, $X\,^2\Pi$) has been measured with high precision: 0.1574 ± 0.014 D by Hoy et.al [62], whose result is in reasonable agreement with the ab initio value: 0.1732 D [48]. Although the absolute value of the NO dipole moment is well known, even the highest precision experiments cannot determine the sign of the NO dipole moment, i.e. N^-O^+ or N^+O^- [63]. In all past experiments [76–78], the assumed sign of the NO ($v = 0$, $X\,^2\Pi$) dipole is based on the outcome of large series of ab initio calculations that all reported N^-O^+ [48–53]. Taking into account recent experiments by Matsiev and coworkers [64] and predictions by Drabbels and Wodtke [63], a flip of the sign of the dipole moment seems not to be feasible.

Except for the sign of S, there is a good quantitative agreement regarding the amplitude of S between NO-Ar collision experiments and their theory. Thus the possibility that the CEPA and CCSD(T) PES's are not accurate enough, can be excluded. Besides this, the observed excitation spectrum of the bound Ar-NO ($v = 0$, $X\,^2\Pi$) Van der Waals complex has been found to agree very well with its theoretical prediction based on the CEPA and on the CCSD(T) PES's [79]. This does not exclude that the labels for the N and the O-end in the PESs might be wrong. However, it is very unlikely to assume that the heavier O-end extends further from the center-of-mass than the N-end.

A very unlikely option is that van Beek et al. made an experimental error and that also their previous theoretical calculations carry the wrong sign for S [46]. In this case both NO-Ar and OH-Ar behave oppositely to the ball and stick model. The previous theoretical calculations [1, 2] for NO-Ar and the present calculated values of Table 3.1 for OH-Ar are found to agree with experiments.

The last option is that only the present HIBRIDON calculations (as listed in Table 3.1) are erroneous, due to errors outside the actual program (e.g. input parameters). Previous

calculations for both NO-Ar and OH-Ar could not carry these errors, which would explain the agreement between the theoretical and experimental sign for both cases. This cannot explain the opposite behavior of S for NO-Ar and OH-Ar, where OH-Ar does and NO-Ar does not behave as expected from a ball and stick model. Although this last option can never be excluded completely, no errors could be found.

Clearly, to render a satisfactory explanation for the sign issue concerning the steric asymmetry and to resolve the disagreement between the experimental and predicted theoretical values for S, further work is required.

Chapter 4

The sign of the NO dipole moment

4.1 Abstract

Intense femtosecond laser pulses are applied in an attempt to directly probe the sign of the permanent dipole moment of a molecule. A hexapole selects NO molecules in a low field seeking state ($j = \frac{1}{2}, \overline{\Omega} = \frac{1}{2}, \epsilon = -1$), subsequently the molecules are oriented along an electrostatic field of approximately 13 kV/cm. This field serves both for orientation of the molecules and for extraction of ions. The linearly polarized fs laser light aligns the oriented molecules along the laser polarization and induces Coulomb explosion. By rotating the laser polarization slightly off from parallel to the orientation/extraction field, the velocity map imaging technique allows one to spatially distinguish between the amount of fragments moving along and moving opposite to the electric field after explosion. Other than when resolving these amounts in time-of-flight, this technique is not limited to low orientation field strengths. Strong orientation effects were observed and correspond to the sign of the dipole moment of NO (v=0) being negative, such that N^-O^+. However, the observed orientation of both CH3F and OCS opposes that expected from the signs of their dipole moments. No definitive answer concerning the sign of the NO dipole moment can be given at this point.

4.2 Introduction

The development of intense femtosecond lasers capable of generating electric fields comparable to the strength of the Coulomb interactions that hold together molecules has motivated extensive fundamental research in the last twenty years. As a result, the way that molecules ionize and dissociate in intense laser fields is now well understood [80]. Studies of the interaction of atoms and molecules with intense laser fields have led to important spin-offs, such as the development of coherent light sources in the extreme ultra-violet part (XUV) part of the spectrum by means of the process of high harmonic generation [81]. In the last two years a new trend can be witnessed in molecular physics research using intense laser fields, where this field is beginning to make contributions to the determination of molecular structure [82,83], and molecular wave functions [84]. Here we present a study where recently acquired understanding concerning the alignment and

orientation of molecules in strong laser and DC electric fields is used to determine the sign of the permanent dipole moment in the ground electronic state. Our studies include measurements for the Nitric Oxide (NO) molecule, where the sign of the permanent dipole moment has been the subject of recent debates [45].

As reported by Townes and Schawlow [30], the sign of a permanent dipole moment can be experimentally obtained via the isotopic dependence of magnetic susceptibility factors. However, application of this technique led to the determination of a dipole moment of N_2O that opposed the theoretically calculated sign [85], thus shedding doubt on this approach as a secure method to determine the sign of a molecular dipole moment [1]. We propose the use of hexapole state selection in combination with Coulomb explosion imaging as a new method for the determination of the sign of permanent dipole moments.

As a result of the first-order Stark effect, a hexapole geometry (consisting of six rods that are held at alternating DC voltages) focusses molecules in low-field seeking states. Molecules in high-field seeking states are de-focussed. For symmetric top molecules, the first order Stark energy is given by [6, 9]:

$$U^{(1)} = -\langle \boldsymbol{\mu_{el}} \cdot \boldsymbol{E} \rangle = -\mu_{el} E \frac{m\Omega}{j(j+1)}, \quad \text{note that:} \quad \langle \cos\theta \rangle = \frac{m\Omega}{j(j+1)}. \tag{4.1}$$

Here the quantum numbers m and Ω are the projections of the total angular momentum $\boldsymbol{j}$ onto a space fixed z axis (defined along the DC field direction $\boldsymbol{E}$) and onto a molecule fixed axis (defined along the permanent dipole moment μ_{el}), respectively. Molecules with $m\Omega > 0$ are in high-field seeking states and are pulled towards the hexapole rods: their potential energy decreases with the electric field strength E. Molecules in low-field seeking states - i.e. with $m\Omega < 0$ - are pushed towards the (low field) center of the hexapole and are focussed. Low field seeking molecules orient preferentially with their permanent dipole moment (pointing from the negative to the positive charge) aligned anti-parallel to the applied DC electric field, while molecules in high-field seeking states orient preferentially with their permanent dipole aligned parallel to the DC field.

For example, in the case of NO, the two components of the $\boldsymbol{j} = \frac{1}{2}$ Λ-doublet are a high- and a low-field seeking state, that respectively align parallel and anti-parallel to an applied DC field. The wave function of a symmetric top alike molecule is given by [13]:

$$\Psi_{j,m,\Omega} = \sqrt{\frac{2j+1}{8\pi^2}} D^{*j}_{m,\Omega}(\phi, \theta, \chi). \tag{4.2}$$

After substitution of $j = \frac{1}{2}$ and integration over the - for reasons of symmetry - redundant Euler angles ϕ and χ, the square of the wave function immediately provides the orientation probability distribution:

$$W(\theta) = |\Psi_{j,m,\Omega}|^2 = |d^j_{m,\Omega}(\theta)|^2. \tag{4.3}$$

[1] Jalink et al. [86] performed a crossed beam experiment and obtained results in agreement with the theoretically calculated sign of the dipole moment of N_2O. They crossed the beam of oriented N_2O molecules with an effusive Ba beam and detected the BaO^* yield as a function of N_2O orientation.

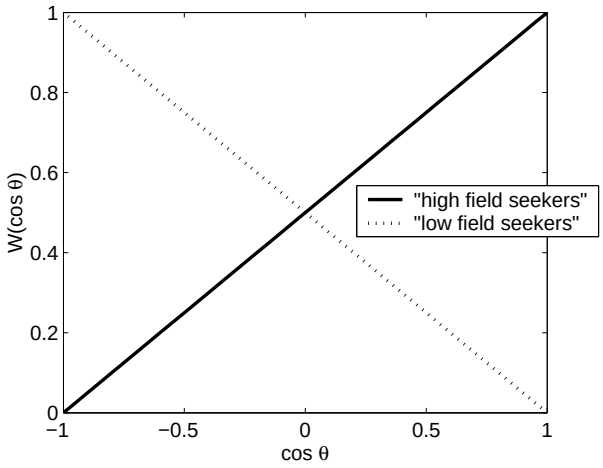

Figure 4.1: The probability distribution $W(\cos\theta)$ of ground state NO molecules in a high uniform electric field $\boldsymbol{E}$. The angle θ gives the angle between $\boldsymbol{\mu_{el}}$ and $\boldsymbol{E}$. The continuous line indicates the distribution for high field seeking molecules with $j = \frac{1}{2}, m = \pm\frac{1}{2}, \Omega = \pm\frac{1}{2}$ while the dotted line provides the probability distribution for molecules in the low field seeking state with $j = \frac{1}{2}, m = \pm\frac{1}{2}, \Omega = \mp\frac{1}{2}$.

For respectively the low and high field seeking states it follows that:

$$\begin{aligned} W(\theta) &= \sin^2\frac{\theta}{2} \quad \text{for } j = \frac{1}{2}, m = \pm\frac{1}{2}, \Omega = \mp\frac{1}{2} \\ W(\theta) &= \cos^2\frac{\theta}{2} \quad \text{for } j = \frac{1}{2}, m = \pm\frac{1}{2}, \Omega = \pm\frac{1}{2} \end{aligned} \tag{4.4}$$

These distributions - for both low field and high field seeking molecules - are plotted versus $\cos\theta$ in Fig. 4.1. The two components of the Λ-doublet orient oppositely in a high electric field. If both components of the Λ-doublet are equally populated, no net orientation is present.

Orientation of the permanent dipole moment of high/low-field seeking states parallel/anti-parallel to a DC field is accompanied by orientation of the molecular frame. This is exploited in collision studies in the gas phase and on surfaces that target the observation of steric effects [5, 10]. In inelastic collisions the orientation dependence of the (final state dependent) collision cross section σ is defined as:

$$S = \frac{\sigma^{Head} - \sigma^{Tail}}{\sigma^{Head} + \sigma^{Tail}}. \tag{4.5}$$

In NO, a collision onto the N-end corresponds to a "Head" collision, whereas a "Tail" collision means that the NO is preferentially oriented with its O-end towards the incoming collision partner. In He-NO and Ar-NO rotationally inelastic collisions, experimental and theoretical values of S correspond reasonably well, but their sign is opposite [2]. If the dipole moment moment of NO would be opposite to the *ab initio* value - i.e. corresponding to

[2]except for Ar-NO calculations in Ref. [2]

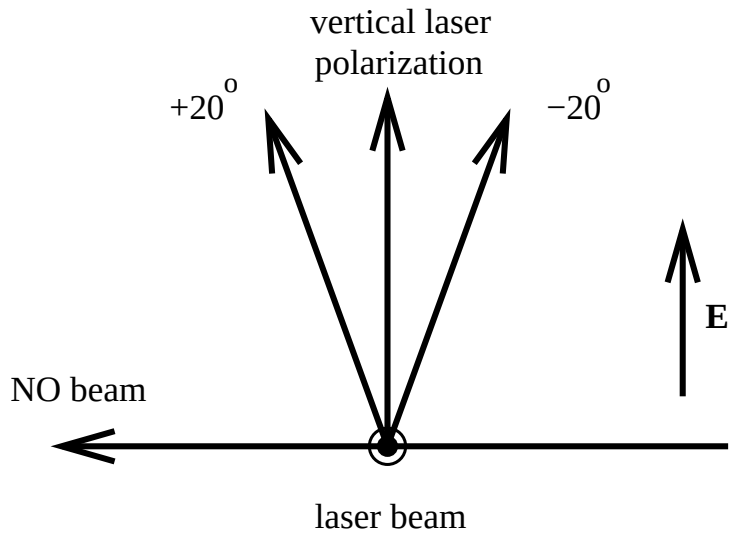

Figure 4.2: Schematic representation of the Amolf orientation experiment. Molecules are oriented in the 13 kV electric field $\boldsymbol{E}$. The laser polarization is slightly off from vertical to be able to distinguish between ions that moved upwards or downwards after explosion. The laser beam points out of the paper.

N^+O^- instead of N^-O^+ - the discrepancy between then the sign of the theoretical and experimental values of S would vanish [45, 87]. While the absolute value of the electric dipole of NO($v = 0$, $X\,^2\Pi$) has been measured [62] with high precision ($\mu_{el} = 0.1574 \pm 0.014$ D), even the highest precision experiments have been unable to determine the sign of the NO dipole moment [63], which has predicted by *ab initio* calculations to be negative [48–50, 53], corresponding to a configuration N^-O^+.

Friedrich and Herschbach [88] have analyzed the steric properties of polar molecules interacting with the combination of a DC electric field and a strong laser field that induces an adiabatic alignment by interacting with the anisotropic polarizability $\Delta\alpha = \alpha_{||} - \alpha_{\perp}$ [89]. They have shown that for moderate strengths of the DC electric field ($\omega = \mu_{el}\boldsymbol{E}/B \ll 1$, where B is the rotational constant of the molecule) and large strengths of the laser field ($\Delta\omega = \Delta\alpha\ I_L/B \gg 1$) both molecules in low-field and high-field seeking states orient themselves with their permanent dipole moment parallel to the direction of the field, hence reversing in the case of the low-field seeking states the orientation that occurs when only a DC electric field is present. Conversely, if the interaction with the laser pulse is impulsive ($\tau < 0.01 - 0.02\frac{1}{2Bc}$ [90], no reversal of the orientation is anticipated during the laser pulse.

4.3 Experiment and discussion

In the experiment, a mixture of 16 % NO in Ar (room temperature stagnation pressure 3 bar) was expanded into a vacuum chamber using a pulsed nozzle (General Valve, 25 Hz). After passing through a $\oslash = 4$ mm collimator, the beam entered a hexapole state selector positioned 40 cm from the nozzle. The 1 m long hexapole [10] focussed NO molecules

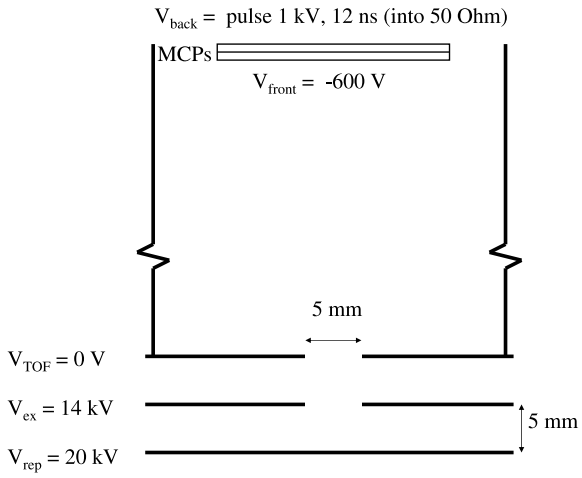

Figure 4.3: Schematic representation of the ion optics used in the Coulomb explosion experiment. The hexapole state selected molecules are oriented in the approximately 13 kV/cm extraction field between repeller and extractor. The time-of-flight (TOF) tube points perpendicular to the molecular beam direction, its length is 40 cm.

in the low-field seeking component of the $\boldsymbol{j} = \frac{1}{2}$ Λ-doublet into a velocity map imaging spectrometer [43], where the molecules were oriented in a 13 kV/cm DC electric field $\boldsymbol{E}$ between the repeller and the extractor, see Fig. 4.3. The focussed output from a linearly-polarized 1kHzz femtosecond laser (60 fs, $I = 1 \cdot 10^{15}$ W/m^2) entered the experimental chamber perpendicular to the NO beam axis, and was used to multiply ionize and fragment the molecules. The laser polarization was turned 20^o with respect to the DC electric field axis (see Fig. 4.2), creating a situation where fragments with a recoil velocity away from the imaging detector could be distinguished from fragments recoiling towards the imaging detector. N^{2+} and O^{2+} fragments resulting from Coulomb explosion of NO were detected on a position-sensitive detector consisting of a dual Microchannel (MCP) plate detector, followed by a phosphorscreen and a CCD camera system. To achieve a high time-of-flight resolution and distinguish between the N^{2+} and the O^{2+} fragments, a 12 ns, 1 kV pulse (Kentech SPSV) was applied to the back of the MCP detector, while -600 V DC was applied to the front of the MCP detector.

Representative images for the Coulomb explosion of oriented NO molecules with detection of N^{2+} ions and O^{2+} ions are shown in Figs. 4.4 and 4.5, respectively. To allow for a quantitative interpretation of the data, the integral of the images along the y-axis is plotted below the two-dimensional images. In both figures, the left image shows the fragment velocity distribution without applying any voltage to the hexapole. In this case the experiment contains equal contributions from both the high-field and low-field seeking component of the $\boldsymbol{j}=\frac{1}{2}$ Λ-doublet, and the image looks symmetric In the right images, a voltage is applied to the hexapole that focusses the low-field seeking state into the spectrometer, while de-focussing the high-field seeking state. In this case an increase in the

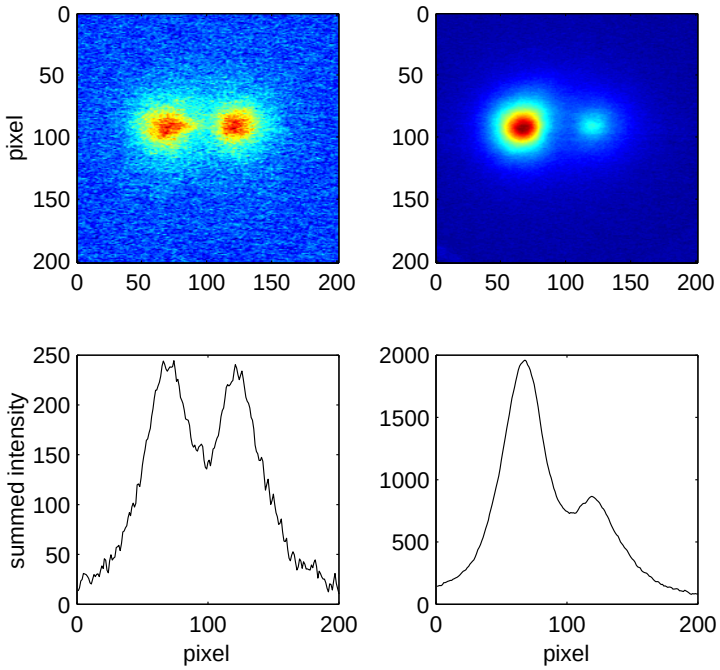

Figure 4.4: Ion images for the Coulomb explosion of oriented NO, where N^{2+} ions were detected using the geometry shown in Fig. 4.2; the left part of the image is due to fragments that recoil towards the imaging detector.

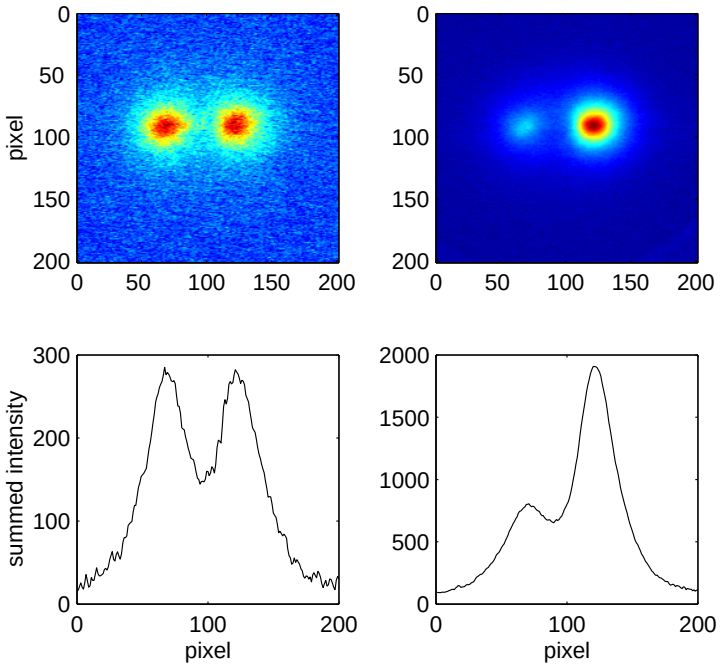

Figure 4.5: Ion images for the Coulomb explosion of oriented NO, where O^{2+} ions were detected using the geometry shown in Fig. 4.2; the left part of the image is due to fragments that recoil towards the imaging detector.

ion yield is observed and the images become strongly asymmetric.

From the figures it can be concluded that the N^{2+} fragments of the state-selected NO molecules preferentially recoil in the direction of the detector (i.e. along the DC electric field) while the O^{2+} ions preferentially recoil away from the detector. The laser polarization in Figs. 4.4 and 4.5 is $+20^o$, as defined in Fig. 4.2. The intensity on the right side of the images indicates the amount of fragments that recoil towards the imaging detector, while the left spot shows the ions from atoms that recoil towards the imaging detector.

Assuming that only impulsive alignment is present and that the orientation of the NO molecules does not change due to the (60 fs) laser pulse and the explosion process, the conclusion of the current experiment is easily drawn. In the images, the laser beam points from right to left, while the NO beam is oriented from top to bottom. The laser polarization in Figs. 4.4 and 4.5 is $+20^o$, as defined in Fig. 4.2. The intensity on the right side of the images indicates the amount of fragments that originally pointed downwards, while the left spot shows the ions from atoms that originally pointed upwards. From the figures one observes that for N^{2+} detection the left spot on the images dominates, while for detection of O^{2+} ions, the right spot is strongest. The N-end of the state selected NO molecules preferentially points upwards (towards the extractor, being the negative electrode), while the O-end preferentially orients downwards (towards the repeller, being the positive electrode). As the NO is in a low field seeking state, the dipole moment (for $v = 0$) is such that N is negative and O is positive (N^-O^+).

However, if we assume, following Friedrich and Herschbach [88] that molecules in low-field seeking states reverse their orientation as a result of adiabatic alignment in a strong laser field, then we conclude that prior to the laser excitation the NO molecule was oriented with its O atom pointing towards the detector, and hence, that the dipole moment of NO results from a charge distribution N^+O^- in the molecule, opposing the results from *ab initio* calculations [48–50, 53]. In this case one would also see orientation with the hexapole off. The orientation can be enhanced also in this case as the molecular beam with the hexapole on is much colder than with the hexapole off. The rotational constant of NO is 1.6 cm$^-$1, which leads to $\frac{1}{2Bc} = 10ps$. Adiabatic alignment is expected to occur for laser pulses that are longer than this time. In our case, with 60 fs laser pulses, no adiabatic alignment in expected.

In order to gain confidence in the ability of Coulomb explosion imaging for the determination of the direction of permanent dipole moments, further experiments were performed using CH_3F and OCS. The former has a permanent dipole where the F-side is negatively charged. Measurements detecting F^{2+} and H^+ ions revealed clear evidence for preferential recoil of the H^+ ions towards the detector (i.e. along the DC electric field direction) and of the F^{2+} ions away from the detector. Given the fact that low-field seeking states of CH_3F orient in a DC electric field with the F-atom pointing in the direction of the field. This results lends support to the predictions of Friedrich and Herschbach [88]. Similarly, in the case of OCS (which has its permanent dipole moment pointing towards the S atom), detected S^{2+} ions displayed a preferential recoil towards the detector (i.e. along the DC electric field direction), while detected O^{2+} displayed a preferential recoil away from the detector.

CH_3F has a rotational constant of [30] $B = 0.85$ cm^{-1}, that for OCS [91] is $B = 0.20$

cm^{-1}. This leads for $\frac{1}{2Bc}$ to 590 and 2500 fs, respectively, which is much more than the laser pulse duration. One would assume only impulsive alignment to be present for these molecules. Also the adiabatic orientation effects as described by Friedrich et al. [88] are not likely to be present.

At this point no final conclusion concerning the NO dipole moment can be drawn. In the near future, calculations will be performed to investigate the possibility of "wrong way" orientation induced by the fs detection laser.

Chapter 5

He-NO Differential cross sections

5.1 Abstract

The first measurements of differential inelastic collision cross sections of fully state-selected NO ($j = \frac{1}{2}$, $\Omega = \frac{1}{2}$, $\epsilon = -1$) with He are presented. Full state selection is achieved by a 2 m long hexapole, which allows for a systematic study of the effect of parity conservation and breaking on the differential cross section. The collisionally excited NO molecules are detected using a resonant (1+1') REMPI ionization scheme in combination with the velocity-mapped, ion-imaging technique. The current experimental configuration minimizes the contribution of non-colliding NO molecules in other rotational states $j,\overline{\Omega},\epsilon$ - that contaminates images - and allows for study of the collision process at an unprecedented level of detail. A simple method to correct ion images for collision-induced alignment is presented as well and its performance is demonstrated. The present results show a significant difference between differential cross sections for scattering into the upper and lower component of the Λ-doublet of NO. This result cannot be due to the energy splitting between these components.

5.2 Introduction

Detailed knowledge of rotationally inelastic collisions is of great importance in understanding energy transfer between molecules and atoms. The study of collisions of rare gases with (open shell) NO molecules has been used in the past to better characterize inelastic collisions and reactions. In the last decades much work has been reported on this subject. Early work on He-NO and Ar-NO collisions [92] resulted in integral inelastic cross sections and showed that these exhibit an oscillatory structure as a function of the final rotational state. Large anisotropy effects in the Ar-NO and He-NO potential were found by De Lange et al. [5, 6, 16]. In their experiments NO molecules were oriented, after which the integral state-to-state collision cross section was determined using Laser Induced Fluorescence (LIF). Typically, LIF provides only integral cross sections, while differential cross sections are nowadays usually obtained using ion-imaging techniques. Suits et al. [93] were the first to apply the latter technique to obtain differential cross sections for collisions of Ar with NO. The introduction of this technique triggered new research, espe-

cially after Eppink and Parker [43] improved the achievable resolution considerably with the implementation of electrostatic lenses. The velocity-mapped ion-imaging technique is now commonly used in the field of molecular dynamics [3, 4, 28, 39, 94–98]. Differential cross sections for inelastic collisions can also be measured using a movable detector [99], but this technique is more time consuming and experimentally difficult. The resolution depends on the scattering angle and only the scattering angle of the molecule in the laboratory frame can be obtained. Velocity-mapped ion-imaging provides the velocity vector of the scattered molecules (both its absolute value and the scattering angle).

Potential Energy Surfaces (PESs) govern chemical reactions. There is however no method to measure them directly, although some attempts were made to directly calculate potential energy surfaces from measured differential cross sections [100, 101]. In practice, theoreticians calculate PESs for a certain system, use the PESs to calculate differential cross sections (DCSs) and then compare the DCSs to experimental values as a test. The first measurement of inelastic differential cross sections for He-NO collisions was carried out by Wesley et al. [102] and compared to scattering calculations based on the Yang and Alexander CEPA PESs [103]. The measurements showed in all cases more forward scattering than the calculations. Also Kohguchi et al. [104] reported discrepancies between theory and experiment for Ar-NO differential cross sections. Elioff et al. [97] repeated these measurements for spin-orbit changing collisions and found a better correspondence to theory for the ratio between forward- and backward-scattered molecules than in Kohguchi's work.

The experiment described in this work is the first scattering experiment in which differential cross sections for scattering from a single Λ-doublet state are obtained. The molecules are prepared in a single quantum state before the collision and the detection of the scattered molecules is also fully state selective. This experiment provides the first opportunity to take a close look at the effect of parity breaking and parity conservation on the differential cross section. A hexapole state selector [2, 105] is used to select the NO molecules in the low field seeking upper component of the Λ-doublet with symmetry index $\epsilon = -1$ (f). It works as a positive lens for molecules in the low field seeking component, while it diverges molecules in the high field seeking lower component of the Λ-doublet with $\epsilon = 1$.

All previous crossed-beam ion-imaging work relies on adiabatic expansion alone for the initial state preparation. Besides resolving the Λ-doublet of the NO molecules in the beam, hexapole state selection suppresses the percentage of incoming molecules in higher rotational states ($j > 1/2$) into the scattering center. These molecules are less deflected by the hexapole and are not focussed into the scattering region, but undergo (passive) divergence over the length of the hexapole. The hexapole selected beam of molecules allows for measurements of differential cross sections for low final rotational states that were previously unmeasurable due to the presence of molecules in these rotational states in the beam, that obscured the forward scattered intensity.

Collision-induced alignment has been shown to influence ion images [106] and thus the values of the differential cross sections that are extracted from these images. Wade et al. [98] used vertical and horizontal laser polarization to determine the NO alignment after collision and used the alignment information to correct the differential cross sections. In this work, a simple, yet rigorous, method to cope with collision-induced alignment is

presented. The conservation of the projection m_a of the total angular momentum on the kinematic apse is exploited for alignment correction. Apse quantization was proposed and demonstrated to be a feasible approximation by Khare et al. [107]. Later on, Meyer et al. showed that the apse approximation yields good quantitative results for (among others) He-NO collisions [108] and Ne-NO collisions [109].

5.3 Experimental

In order to explore Λ-state selected differential cross sections, a previously used crossed-beam apparatus [2, 5, 6, 47] has been modified. The existing LIF detection system is replaced by newly designed ion optics for velocity-mapped ion-imaging. A XeCl excimer pumped dye laser system (Lambda Physik EMG 201 / FL 3002) is used for detection. The dye laser operates with Coumarin 47 dye and is equipped with a frequency doubling unit to generate tunable light around $\lambda \approx 226$ nm (output ≤ 1.5 mJ/pulse). The excimer laser generates around 90 mJ of $\lambda = 308$-nm light of which approximately 10 % is separated using a small mirror in front of the dye laser and is used in the ionization step of the 1+1' Resonance Enhanced Multi-Photon Ionization (REMPI) process [8]. As the excimer beam is rather divergent, a telescope consisting of an $f = 100$-mm and an $f = -50$-mm lens is placed immediately after the mirror that reflects the 10 %. The focus of this beam is made to coincide with the scattering center using an $f = 300$-mm lens. The $\lambda \approx 226$-nm laser beam is not focussed, but guided through an iris with a diameter of about 1 mm. The excitation and ionization beams are crossed at 90^o to get a well defined ionization volume, estimated to be 1 mm^3. When the tunable laser light is blocked, no signal can be observed, meaning that non-resonant ionization of NO in the ground state does not occur. When the $\lambda = 308$-nm ionization laser beam is blocked, the signal is typically less than 10% of that when both laser beams are on. As there is competition between (1+1) and (1+1') REMPI, the contribution of (1+1) REMPI to the signal is expected to be suppressed even more than 10 %.

The main advantages of using (1+1') REMPI in the crossed laser configuration are that it generates a well defined and rather isotropic detection volume and that the 308-nm light is less likely to ionize background molecules in the vacuum chamber than the 226-nm light. The small isotropic volume simplifies the extraction of differential cross sections from ion-images and reduces distortion of the images due to ionization near the edges of the electrostatic lenses. Using 308-nm light for ionization, the 226-nm light intensity can be reduced, which decreases the noise level. For most background gas molecules the 308-nm photon is below the ionization threshold. Using (1+1') REMPI it is possible to overcome saturation in the excitation step, whereas the ionization step is saturated.

A schematic drawing of the experimental setup is shown in Fig. 5.1. The primary beam consists of 16% NO in Ar, the secondary beam of pure He. Both beams are produced using General Valves, pulsed at a frequency of 10 Hz. The NO in the primary beam is rotationally cold due to adiabatic expansion, i.e. most of the NO molecules are in the lowest rotational state with angular momentum quantum number $j = \frac{1}{2}$. The beam passes two skimmers ($\oslash = 1$ mm and $\oslash = 0.7$ mm) that are situated 3 cm and 8 cm from the pulsed nozzle opening, respectively, before it enters the hexapole. The 2 m long hexapole

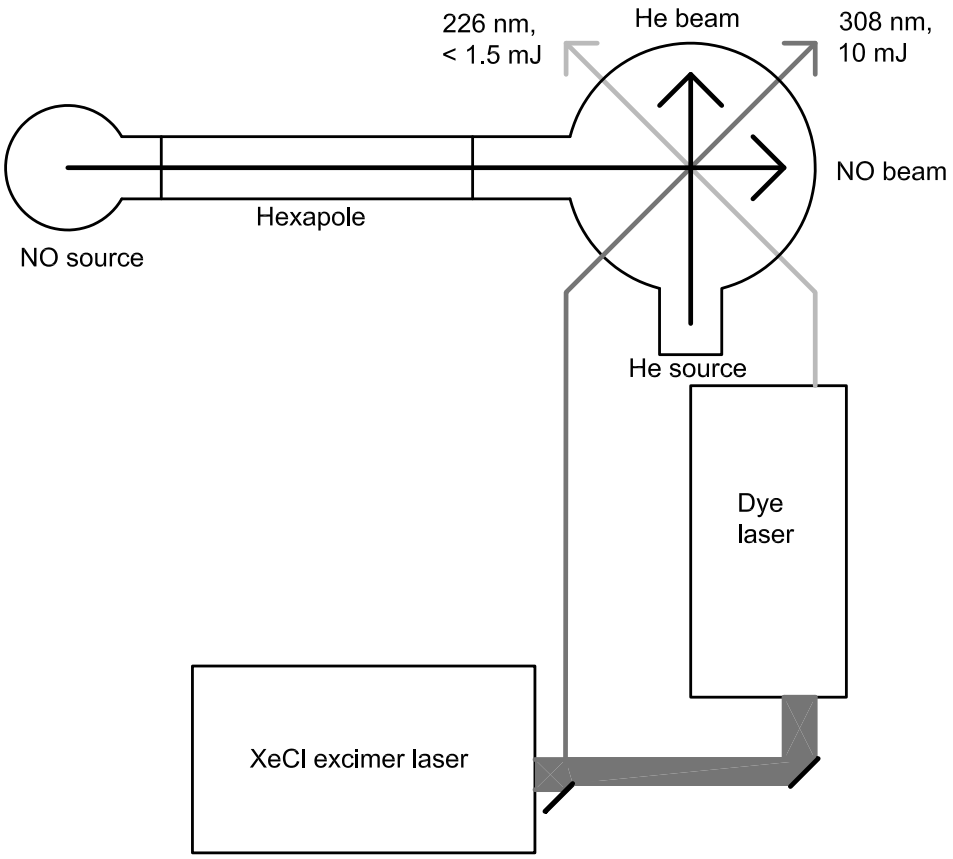

Figure 5.1: Schematic drawing of the crossed-beam ion-imaging setup. The Time-Of-Flight tube is perpendicular to the plane defined by the laser and molecular beams and points upwards.

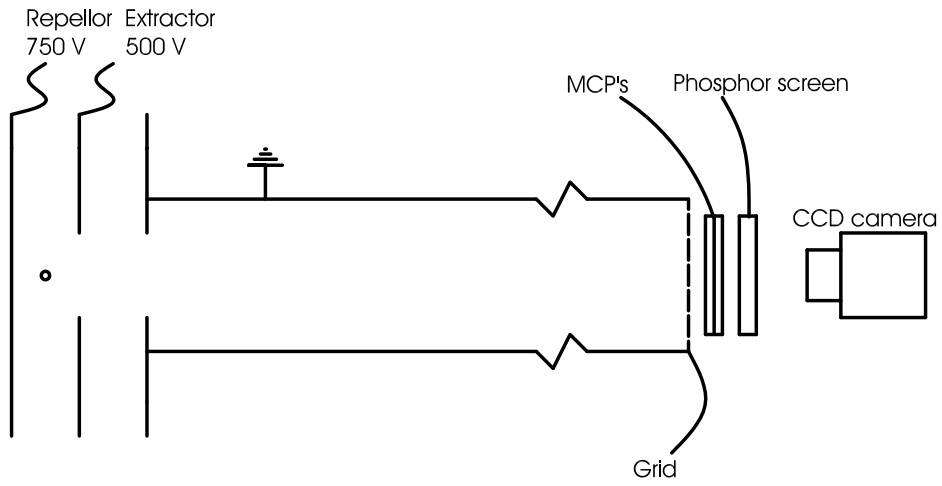

Figure 5.2: Schematic drawing of the ion optics. The crossing point of the molecular and laser beams is indicated by a small circle. The TOF tube is placed perpendicularly (pointing upwards) to the plane defined by the laser and molecular beams.

focusses molecules in the low field seeking ($\epsilon = -1$, f) upper component of the lambda doublet into the detection/collision region [105]. In the collision region, the NO beam is crossed at 90^o with a He beam. The He nozzle is positioned 8.5 cm from the scattering center, the beam of He atoms is collimated by a ($\oslash = 1.9$ mm) skimmer, positioned 1.5 cm from the nozzle. During the experiments (both beams on) the ion gauge pressure reading in the collision chamber is approximately $1 \cdot 10^{-6}$ mbar.

Because of hexapole focussing, the NO beam is very pure. Only the molecules in the $j = \frac{1}{2}$, $\Omega = \frac{1}{2}$, $\epsilon = -1$ state are focussed. The (1+1') REMPI signal difference (hexapole gain) when tuning the dye to the focussed ground state between "hexapole on" and "hexapole off" is approximately a factor of 70. The contribution of the other component of the Λ-doublet is negligible as it is diverged by the hexapole [5]. The amount of molecules in other quantum states is substantially less than 1%. Switching on the He beam does not weaken the ground state signal significantly, from which it can be concluded that less than 2% of the NO molecules collide. The contribution of double collisions can thus be ignored.

The ion optics and Time-Of-Flight (TOF) tube are placed perpendicularly to the drawing plane of Fig. 5.1 and a schematic drawing is given in Fig. 5.2. The distance between the repeller and extractor plates is 20 mm and the length of the TOF tube amounts to 550 mm. The TOF tube is at ground, the "back" of the MCP detector (facing the phosphor screen) is at 950 V while the "front" (facing the grid) is gated to a negative voltage (-950 V). A grid (transmission of 90 %) is positioned just before the MCPs. This grid prevents ions from being pulled towards the center of the detector when the front voltage is switched to -950 V. Simulations show that without the grid,

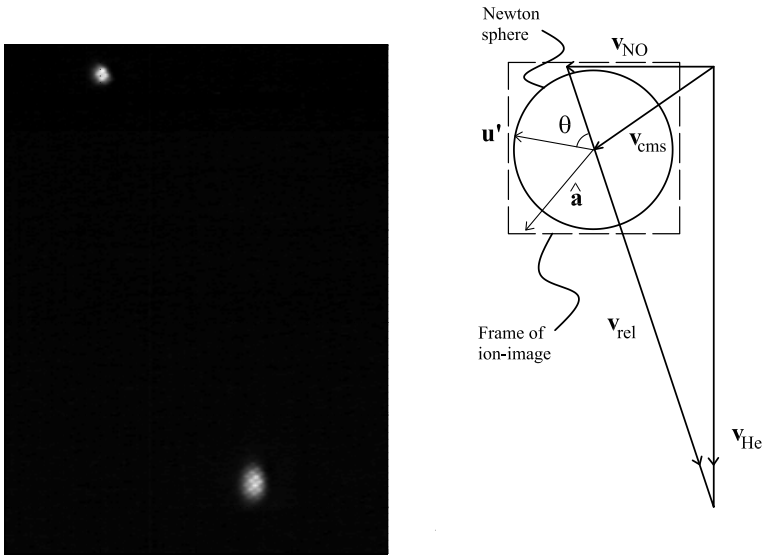

Figure 5.3: The left panel shows an ion image of two "beam spots". The top left spot is from the 16 % NO beam in Ar beam (593 m/s), while the lower spot is due to the 1 % NO in He beam velocity (1710 m/s). The camera is positioned such that the up-down direction of the ion-images coincides with the axis of the He beam, the left-right direction coincides with that of the NO beam. The right panel shows the corresponding Newton diagram. The vector $\boldsymbol{u'}$ indicates scattering with a velocity u' in the center-of-mass frame under an angle θ. The corresponding kinematic apse direction is indicated by $\hat{\boldsymbol{a}}$. Note that the u' distribution after collision is (cylindrically) symmetric around the relative velocity $\boldsymbol{v_{rel}}$. The dashed square indicates the frame of the recorded ion images that remains unaltered for all images in Figs. 5.4, 5.5 and 5.6.

the resolution decreases and that the molecular velocity component (before ionization) perpendicular to the TOF is no longer linear with the position of impact on the detector. This problem cannot be solved by putting the front of the MCPs at ground and gate the back at +2 kV. In that case the NO^+ ions would have less kinetic energy (600 V instead of 1.6 kV) when they hit the detector, yielding weak signals. Low repeller voltages are essential to facilitate the resolution required for detection of the small changes in NO velocity due to collisions with the light He atoms. Disturbances of the images because of the inhomogeneous field in the region near the detector are avoided using the grid in front of the detector. The ions see two parallel plates and are accelerated perpendicularly to the detector. The grid shows up in some images, but the effect on the differential cross sections is negligible.

To test and optimize the setup, about 1% NO was added to the He beam. Optimal repeller and extractor voltages are determined with NO in both the primary and in the secondary beam. The dye laser (226 nm) is tuned to the electronic transition starting from the $j = \frac{1}{2}$, $\Omega = \frac{1}{2}$, $\epsilon = -1$ state. Repeller and extractor voltages were tuned to the value at which the beam spots were as small as possible [39] and at which the primary (NO) and secondary (He) beam were on the horizontal and vertical axis, respectively. In

Fig. 5.3 the resulting image is shown that was recorded after optimization of the voltages. Typical values used throughout this work are 750 V for the repeller and 500 V for the extractor. Lower values of 500 V and 330 V can be applied successfully as well. The image in Fig. 5.3 provides information on the properties of the molecular beams. The resolution of the setup is determined from the (primary) NO-beam. Its velocity has been calculated and measured before [5, 16]. Using the value of 593 m/s, a resolution G of 7.7 m/s per pixel is found. The secondary beam is found to be a little slower than calculated for pure He (1710 m/s instead of 1760 m/s). This is assumed to be due to the 1% of NO that was added to facilitate detection. The FWHMs of the velocity distribution of the (primary) NO beam and the (secondary) He beam are estimated to be respectively 50 and 100 m/s (along the beam velocity). The velocity spread in the He beam is probably underestimated because only the 1 % NO seeded in He is actually detected and not the lighter He itself.

Knowing the velocities of the NO and the He beams, a Newton diagram is drawn to yield insight in the collision geometry (right panel of Fig. 5.3). The centers of the beam spots in the left panel of Fig. 5.3 correspond to the $\boldsymbol{v_{NO}}$ and $\boldsymbol{v_{He}}$ vectors in the right panel. For laboratory velocities the symbol "v" will be used, while "u" indicates a velocity in the center-of-mass frame. The $\boldsymbol{u'}$ distribution after collision is (cylindrically) symmetric around the relative velocity $\boldsymbol{v_{rel}}$. This scattering (Newton) sphere of the NO molecules is projected on the detector. For reasons of readability the scattering sphere for He is not drawn in the figure. The dashed square in the right panel of Fig. 5.3 denotes the frame of the ion images, as used for all images in Figs. 5.4, 5.5 and 5.6.

5.4 Extraction of differential cross sections

The detection probability of a scattered molecule depends on several factors. This makes it impossible to directly use the intensity on an outer ring of an ion image to determine the differential cross section. Asymmetries in the images can occur due to collision-induced rotational alignment, due to different residence times for slow and fast molecules within the detection volume and due to the Doppler shifts and laser alignment. The beam velocity distributions and instrumental factors cause blurring of the images. In this section, a method is given to correct for the most important of these distorting factors in order to extract reliable differential cross sections from the ion images in a straightforward procedure.

Currently no corrections for imperfect spatial positioning of the laser and for Doppler shift are applied to our data as the effect of these factors was found to be small. The center-of-mass velocity distribution of the NO molecules after collision ($\boldsymbol{u'}$) is small compared to the bandwidth of the laser (0.5 cm^{-1}). Hardly any change of the asymmetry of the images was observed when slightly detuning the frequency of the dye laser.

The blurring of the ion images due to the velocity spread in the beams as well as other instrumental factors is approximated by a single Gaussian blurring function. This function is fitted empirically to a computer generated image in order to match the sharpness of the experimental images.

The detection region is defined by four crossing beams: the NO beam, the He beam and

the two laser beams, each with a diameter of about one millimeter. It is an experimental challenge to overlap all four beams in time as well as in space. The resulting detection volume is small which restricts the maximally achievable signal. The advantages of this geometry, however, are that the ionization volume is nearly spherical and that due to the small detection volume relative to the size of the ion lenses edge effects from the latter are minimized. Because of the nearly spherical shape of the detection volume we make the approximation that the molecular detection probability $T(x, y)$ due to the molecule's residence time in the detection volume is inversely proportional to the absolute value of the velocity in the laboratory frame. The coordinates (x, y) indicate the position on the detector in pixels and relate directly to the x and y components of the velocity in the center-of-mass (u'_x and u'_y) frame via the resolution G ($x = u'_x/G$ and $y = u'_y/G$) with unit $m/s/pixel$.

$$T(x, y) \equiv \frac{1}{|\boldsymbol{v'}|} \Big/ \left\langle \frac{1}{|\boldsymbol{v'}|} \right\rangle \tag{5.1}$$

Normalization of this $T(x, y)$ is obtained by dividing by the average over all pixels ($\langle 1/|\boldsymbol{v'}| \rangle$). Appendix 5.8 shows the procedure to calculate $T(x, y)$. If the detection volume would be non-isotropic or not centered at the beam crossing, $T(x, y)$ will also depend on the (laboratory) scattering-angle. For example: molecules scattered along a single laser (LIF or 1+1 REMPI) [16] have a longer pathway through the detection volume than those scattered in another direction. If this were the case, an extra correction would be required.

Collision-induced alignment can also cause NO molecules to be non-uniformly detected, creating a further distortion of the ion image, which has to be corrected for. The alignment dependent detection probability is given by:

$$S_a(j' \rightarrow j^*) \equiv \sum_{m^*} \left| \left\langle \Psi^*(j^*, m^*) \;\middle|\; \hat{\boldsymbol{\mu}} \cdot \hat{\boldsymbol{\epsilon}} \;\middle|\; \boldsymbol{R}(\beta_p) \Psi'_a(j', m'_a) \right\rangle \right|^2 \tag{5.2}$$

The wave functions are referred to as $\Psi'_a(j', m'_a)$ and $\Psi^*(j^*, m^*)$, denoting respectively that of a rotational state after collision and that after laser excitation to the $^2\Sigma$ state. Note that m^* is defined along the polarization $\hat{\boldsymbol{\epsilon}}$ of the linearly polarized laser (laser frame). The wave function in the apse system $\Psi'_a(j', m'_a)$ (m'_a is defined along the kinematic apse) is transformed into the laser frame by the Euler angle rotation operator $\boldsymbol{R}(\beta_p) \equiv \boldsymbol{R}(0, \beta_p, 0)$. The angle between the laser polarization and the kinematic apse is given by β_p. Since $S_a(j' \rightarrow j^*)$ depends on β_p, it is not an ordinary Hönl-London factor. The scattered wave function can carry alignment, while the Hönl-London factors assume an isotropic m distribution. Until now no simple method to calculate $S_a(j' \rightarrow j^*)$ for each position (x, y) on the detector was available. Appendix 5.9 provides a simple but widely applicable correction treatment based on the approximate conservation of the projection m_a of the total angular momentum $\boldsymbol{j}$ on the kinematic apse ($m'_a = m_a$). It results in a value of $S_a(j' \rightarrow j^*)$ for every position on the detector. Khare [107] and Meyer [108] showed that m_a conservation is an appropriate assumption. $S(j' \rightarrow j^*)$ is evaluated for every pixel with coordinate (x, y) on the detector.

In the case of full saturation of the excitation step, the detection probability no longer depends on the scattering angle. Correction of the ion images with only the velocity

correction should in this case yield images that are symmetric in the relative velocity. If partial saturation occurs, the dependence of the detection probability on β_p becomes less.

$$S_{sat}(j' \rightarrow j^*) = S_0 + S_a(j' \rightarrow j^*) \tag{5.3}$$

The parameter S_0 indicates the saturation: when $S_0 \ll S_a(j' \rightarrow j^*)$, there is no saturation, when $S_0 \gg S_a(j' \rightarrow j^*)$ there is full saturation and the detection probability no longer depends on the scattering angle. To get an idea of the effect of the saturation correction, S_0 can be expressed in units of $\langle S_a(j' \rightarrow j^*)\rangle$, the value of $S_a(j' \rightarrow j^*)$ averaged over all pixels.

In order to actually extract differential cross sections from the ion images, first the experimental image $I_{ex}(x, y)$ is corrected for the laboratory velocity and alignment via Eqs. 5.1 and 5.2. For more information on the correction, see Appendix 5.8 and 5.9. The corrected image is given by:

$$I_{ex,c}(x, y) = \frac{I_{ex}(x, y)}{S_a(j' \rightarrow j^*)\ T(x, y)}. \tag{5.4}$$

In the case of (partial) saturation, $S_a(j' \rightarrow j^*)$ is replaced by $S_{sat}(j' \rightarrow j^*)$. The corrected image is now reasonably symmetric (but still blurred) and the intensity on the rim of the ion image already gives a good indication of the differential cross section. To obtain a proper differential cross section (DCS) from the blurred two-dimensional velocity distribution of the corrected image, a forward extraction method is applied. This method is in the spirit of Lorenz et al. [94]. The intensity $R_{ex}(\theta)$ on an about 6 pixels wide outer ring of the corrected ion image $I_{ex,c}(x, y)$ is used as a "trial DCS" ($DCS_0 = R_{ex}(\theta)$) to simulate an image. The blurring factor - that includes both the beam velocity distribution and instrumental blurring - is applied on the simulated image to make it as sharp as the corrected experimental image $I_{ex,c}(x, y)$. The intensity on a broad outer ring of the simulated image $R_{sim}(\theta)$ is compared to that of the same outer ring on the experimental image ($R_{ex}(\theta)$), after which the DCS is adapted.

$$DCS_i = \frac{R_{sim,i-1}(\theta)}{R_{ex}(\theta)}\mathrm{DCS}_{i-1} \tag{5.5}$$

Note that $R_{sim,i-1}$ has been simulated using DCS_{i-1}. The adapted trial DCS is used to simulate an image that is compared with the experimental one. This step is repeated several times ($i = 1, 2, 3, \ldots$) until the simulated and experimental images are as similar as possible. Two parameters have to be fitted during the optimization. The saturation parameter S_0 is chosen such that the asymmetry of the corrected experimental image is minimized, while the Gaussian blurring parameter is selected to make the simulated image as sharp as the experimental one.

5.5 Close-Coupling calculations of differential cross sections

The calculations of the differential cross sections were done using a full quantum close-coupling (CC) approach with two diabatic potentials ($V_{\mathrm{sum}} = \frac{1}{2}(A'' + A')$ and $V_{\mathrm{dif}} =$

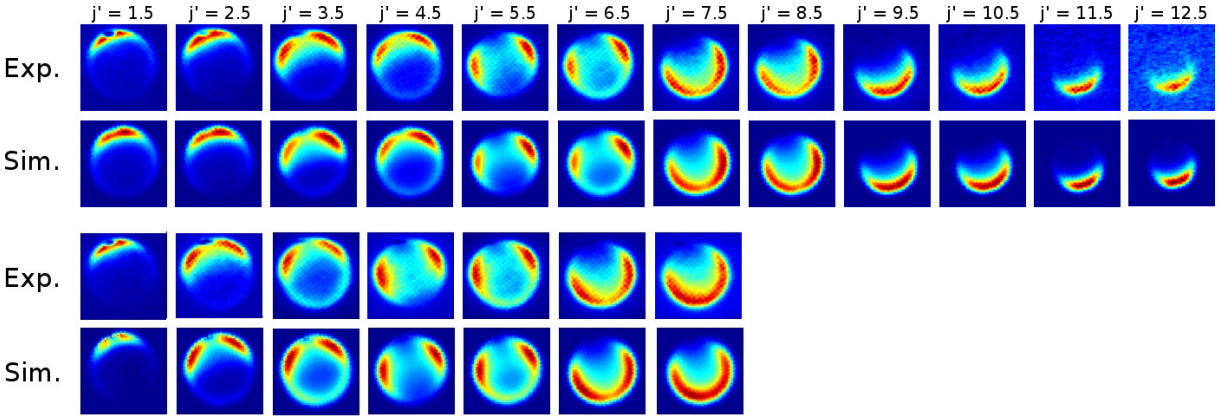

Figure 5.4: Experimental and simulated ion images. The images in the top rows are collected using the R_{21} branch ($\Omega' = 1/2$, $\epsilon' = -1$). The bottom rows show images collected using the P_{11} branch ($\Omega' = 1/2$, $\epsilon' = 1$). The experimental images are raw data, the simulated images are from the optimized extracted differential cross section and incorporate, blurring, velocity correction $T(x, y)$ and alignment correction $S_a(j' \rightarrow j^*)$. No saturation correction is applied: $S_0 = 0$. The frames of all images are identical and taken in accordance to the dashed square in the right panel of Fig. 5.3.

$\frac{1}{2}(A'' - A')$) for the He-NO($X^2\Pi$) system taken from Ref. [56]. The contour plots of the diabatic surfaces are shown in Ref. [6, 56]. Calculations of the steric dependence of the inelastic total collision cross section using these surfaces yielded a reasonably good agreement with experimental data [6].

The HIBRIDON suite of codes [59] was used for the scattering calculations. The methodology of scattering of the structureless partner with an open shell diatomic was described in detail before [6,45,66,69,104,109–111]. We refer the reader to these references for details. The close-coupling calculations at a collision energy $E_{\rm col} = 508.13$ cm^{-1} employed all partial waves up to a total angular momentum quantum number $J_{max} = 101.5$ and NO rotational levels up to $j' = 17.5$. The reduced mass of the He-NO system and the rotational constant of the NO molecule were taken as $\mu = 3.5314$ a.m.u. and $B = 1.69611$ cm^{-1}, respectively.

The description of the NO diatomic can be done in a Hund's case (a) coupling scheme. This is due to the relatively large spin-orbit coupling resulting in $^2\Pi_{1/2}$ (ground state spin-orbit manifold F_1) and $^2\Pi_{3/2}(F_2)$. Each spin-orbit state is further split into Λ-doublet components with symmetry index $\epsilon = 1$ (e) and $\epsilon = -1$ (f). Λ-doubling parameters, p and q for NO are $1.172 \cdot 10^{-2}$ and $6.7 \cdot 10^{-4}$, respectively. For the spin-orbit Hamiltonian $A * \hat{L}\hat{S}$ a spin-orbit constant of the NO molecule of $A = 123.1393$ cm^{-1} has been used.

The CC equations were propagated from R=3.7 a_0 to 35 a_0. From the CC calculations we were able to determine integral and differential cross sections for state-to-state transitions from the $j = 0.5$ initial state of NO, resolved for Λ-doublet and spin-orbit manifold (F_1 and F_2). The integral cross sections from these calculations are used to normalize the experimental results in this study.

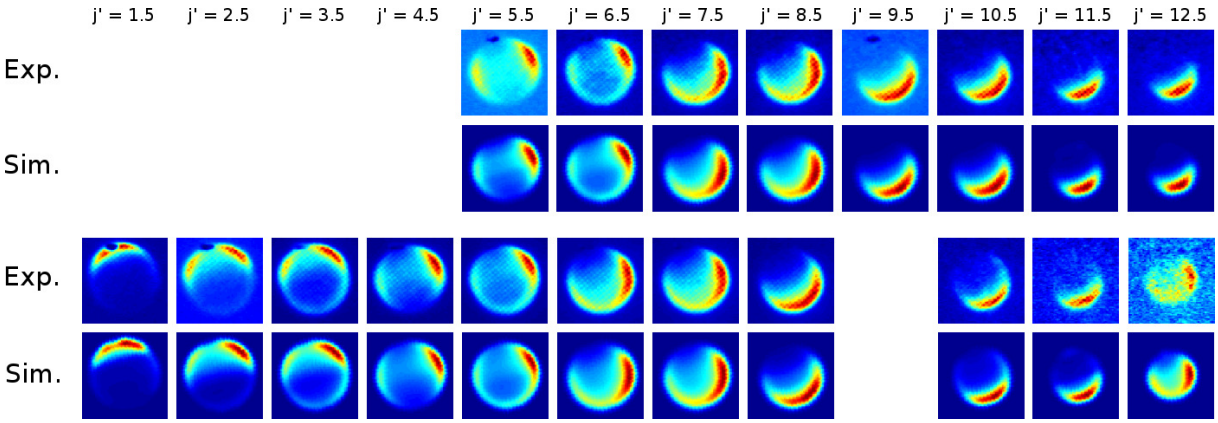

Figure 5.5: Experimental and simulated ion images. The images in the top rows are collected using the $Q_{11} + P_{21}$ branch ($\Omega' = 1/2$, $\epsilon' = -1$). The bottom rows show images collected using the $R_{11} + Q_{21}$ branch ($\Omega' = 1/2$, $\epsilon' = 1$). The experimental images are raw data, the simulated images are adapted using blurring, velocity correction $T(x, y)$ and alignment correction $S_{sat}(j' \rightarrow j^*)$. Partial saturation was included to reproduce the asymmetry: $S_0 \approx 1.5\langle S_a(j' \rightarrow j^*)\rangle$ where $\langle S_a(j' \rightarrow j^*)\rangle$ is the mean value of the alignment correction, averaged over all pixels. An "unsaturated" image would show even stronger asymmetry. The frames of all images are identical and taken in accordance to the dashed square in the right panel of Fig. 5.3.

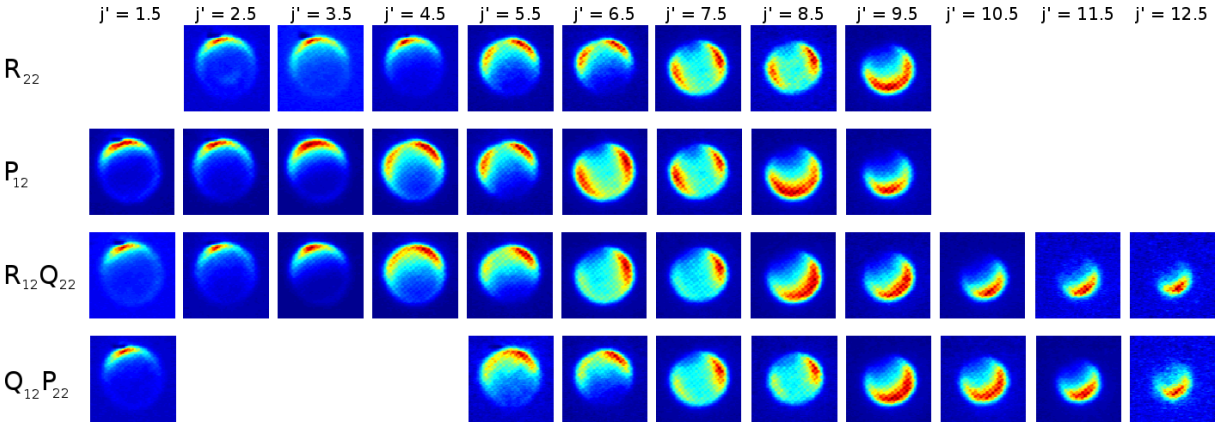

Figure 5.6: Experimental (raw) ion images for spin-orbit changing collisions. Simulated images from the extraction of the differential cross section are not presented for these branches, but correspond to the experimental images as well as in the case of spin-orbit conserving collisions. The frames of all images are identical and taken in accordance to the dashed square in the right panel of Fig. 5.3

5.6 Results and discussion

A nearly complete set of ion images for inelastic He-NO collisions at a collision energy of approximately 510 cm^{-1} is displayed in Figs. 5.4, 5.5 and 5.6. The raw experimental images are are shown. In Figs. 5.4 and 5.5 the raw experimental images are compared to simulated images from the extraction of differential cross sections, including the corrections discussed in section 5.4. A few images are missing because these could not be resolved spectroscopically. Table 5.1 lists the various spectroscopic branches of the $A \leftarrow X$ electronic transition that are available to detect the ion images. The symmetry index ϵ in Table 5.1 relates to the parity of a rotational state [18] as

$$p = (-1)^{j-\epsilon/2}. \tag{5.6}$$

The symmetry index ϵ is -1 for the upper component (f) of the Λ-doublet and 1 for the lower (e) component. Note that the parity of states within one branch alternates with $\Delta j = j' - j$. For example, final states with even Δj from the R_{21} branch have the same parity as those with odd Δj in the P_{11} (and vice versa).

Taking a first look at the experimental images one notices that there is little contamination of the images due to background signal. The He beam is switched from "on" to "off" after 100 laser shots. This procedure is repeated typically 20 times. The images with the He beam "off" are subtracted from those with the He beam "on". The excimer/dye laser system and General Valves run at 10 Hz, consequently collecting an image takes approximately 7 minutes. Some of the highest rotational states ($\Delta j > 10$) however, required twice the integration time.

The hexapole state selector eliminates all but one quantum state from the NO molecular beam. The product images show little contamination with scattering from other states or with direct detection of uncooled molecules present in the NO beam. These conditions lead to particularly crisp images. Only for scattering into the lower Λ-doublet component of the lowest rotational state ($j' = 1/2, \epsilon' = 1$) the ion image shows a strong distortion in the forward direction due to some residual NO in this state in the molecular beam (see Fig. 5.7). Because of this distortion it has not been used to extract a differential cross section and is not plotted in Fig. 5.5. For scattering into all higher rotational states this effect caused no problems.

The overall behavior of the images is as expected. For low rotational states, forward scattering dominates, while images for high rotational states show mostly backward scattering. In order to transfer more translational energy into rotation, collisions with reversed momentum are preferred. The only exception to this behavior is the $j' = 12.5$ image in the $R_{11} + Q_{21}$ branch that shows sideways scattering, while the images for $j' = 10.5$ and $j' = 11.5$ only show backward scattering. The diameter of the projected scattering spheres decreases with j': the amount of translational energy after collision has to decrease if the amount of rotational energy increases. The radii of the projected spheres correspond well to this energy loss. This confirms the correctness of the velocity calibration. Images for scattering into $\overline{\Omega}' = 3/2$ states (spin-orbit changing collisions) show more forward scattering than spin-orbit conserving collisions ($\overline{\Omega}' = 1/2$). This can be explained by the guess that spin-orbit changing collisions are particularly sensitive to the attractive part of the potential.

Table 5.1: Branches used to collect ion images indicating which Ω', ϵ' states (after collision) are probed. For each of the branches, images for several j' (up to $j' = 12.5$) are collected.

Branch	Ω'	ϵ'
P_{11}	$\frac{1}{2}$	1
R_{21}	$\frac{1}{2}$	-1
P_{12}	$\frac{3}{2}$	1
R_{22}	$\frac{3}{2}$	-1
$R_{11} + Q_{21}$	$\frac{1}{2}$	1
$P_{21} + Q_{11}$	$\frac{1}{2}$	-1
$R_{12} + Q_{22}$	$\frac{3}{2}$	1
$P_{22} + Q_{12}$	$\frac{3}{2}$	-1

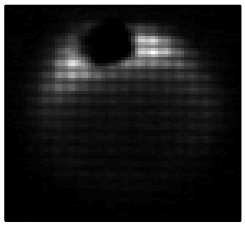

Figure 5.7: Ion image for $j = \frac{1}{2}, \epsilon = -1 \rightarrow j' = \frac{1}{2}, \epsilon' = 1$ scattering ($R_{11} + Q_{21}$ branch). The black spot is due to background subtraction. This background signal is due to the small amount of molecules that still resides in this state (the lower component of the Λ-doublet) after the hexapole. This image was recorded under different imaging conditions.

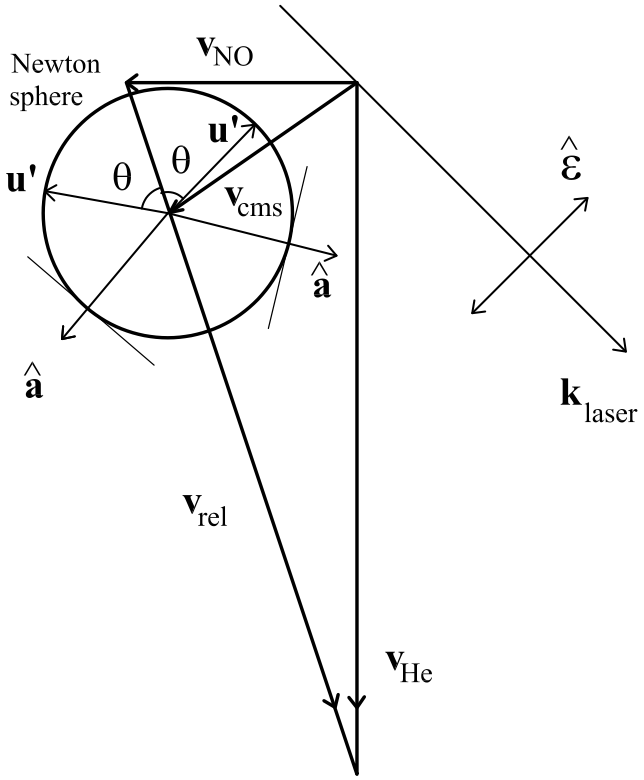

Figure 5.8: Newton diagram for He-NO collisions to illustrate the effect of alignment on the detection probability. The vectors labelled with $\boldsymbol{u'}$ indicate scattering with a velocity in the center-of-mass frame under an angle θ. Remind that scattering is symmetric in respect to the relative velocity. The kinematic apse orientations corresponding to the drawn scattering vectors are indicated with $\hat{\boldsymbol{a}}$. A thin line is drawn perpendicular to $\hat{\boldsymbol{a}}$ in order to indicate the plane (perpendicular to the paper) in which the vector $\boldsymbol{\Delta j}$ is found. The propagation and polarization directions of the 226-nm laser are indicated in the figure with $\boldsymbol{k}_{\text{laser}}$ and $\hat{\boldsymbol{\epsilon}}$.

The uncorrected images from single P and R branches are reasonably symmetric in the relative velocity vector, while those for Q branches (combined with a P or R branch) show significant asymmetry. In each case, the left side of the ion images from Q branches shows less intensity than the right side (see Figs. 5.4, 5.5 and 5.6). The images have been collected within a period of about three days, not in a particular order and the laser bandwidth is relatively large compared to the differences in NO center-of-mass velocities. This rules out Doppler effects as well as the spatial overlap of the lasers and the other beams as a possible reason for the asymmetry stated above. Collision-induced rotational alignment is the prime suspect for the effect. A qualitative classical explanation of this effect is described here.

In Fig. 5.8 the vectors labelled $\boldsymbol{u'}$ indicate scattering under an arbitrary angle θ. The corresponding kinematic apse $\hat{\boldsymbol{a}}$ is also drawn in the figure. The momentum component

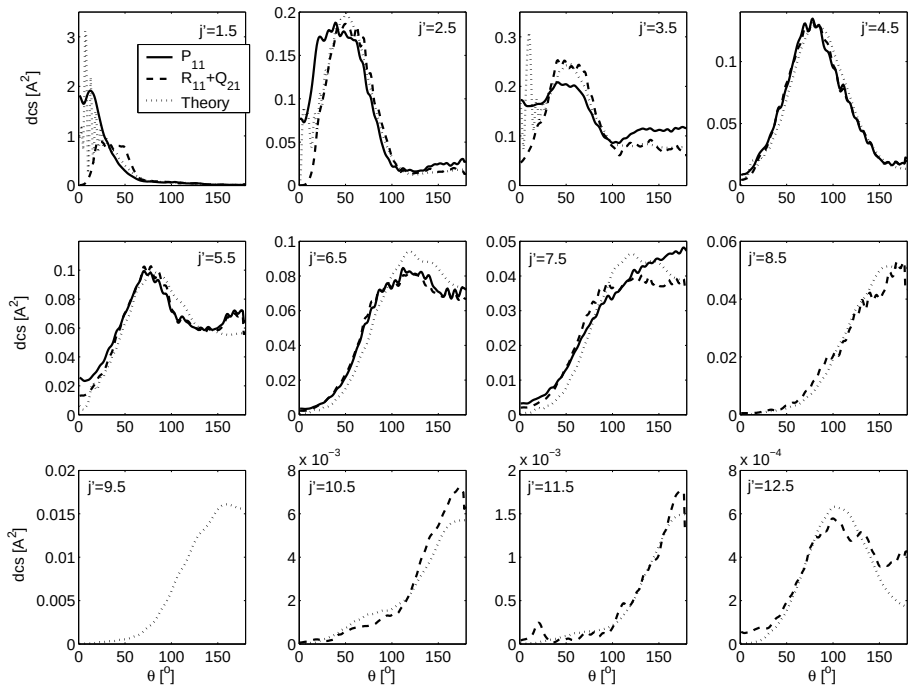

Figure 5.9: Differential cross sections for spin-orbit conserving ($\Omega' = \frac{1}{2}$) transitions, into the lower component of the Λ-doublet ($\epsilon' = 1$). Experimental results are given for different branches and compared to HIBRIDON calculations. The ion-images from which these differential cross sections are derived are found in Figs. 5.4 and 5.5. Note that both theory and experiment show sideways scattering for $j' = 12.5$ ($\Omega' = \frac{1}{2}, \epsilon' = 1$) while one would expect strong backward scattering for such a high rotational state. To transfer a lot of translational energy into rotation, collisions with reversed momentum are usually preferred.

that is transformed into rotation ($\boldsymbol{\Delta p} = \boldsymbol{p'} - \boldsymbol{p}$) points along the kinematic apse $\hat{\boldsymbol{a}}$,

$$\hat{\boldsymbol{a}} \equiv \frac{\boldsymbol{p'} - \boldsymbol{p}}{|\boldsymbol{p'} - \boldsymbol{p}|} \tag{5.7}$$

where $\boldsymbol{p}$ and $\boldsymbol{p'}$ denote the linear momenta before and after collision respectively. When the collision is impulsive and takes place very rapidly, there is essentially no change in the collision geometry during the time interval in which the intermolecular forces act. The internuclear distance $\boldsymbol{R}$ between the scattering partners remains unchanged during this interval. Conservation of total angular momentum yields a simple relation for the transferred amount of rotational angular momentum [107, 112]:

$$\boldsymbol{\Delta j} = -\Delta(\boldsymbol{R} \times \boldsymbol{p}) = -(\boldsymbol{R} \times \boldsymbol{\Delta p}). \tag{5.8}$$

It follows directly that $\boldsymbol{\Delta j} \perp \boldsymbol{\Delta p}$. In quantum mechanical terms this means that $m_a = m'_a$. For the repulsive He-NO collision system this is expected to be an excellent approximation.

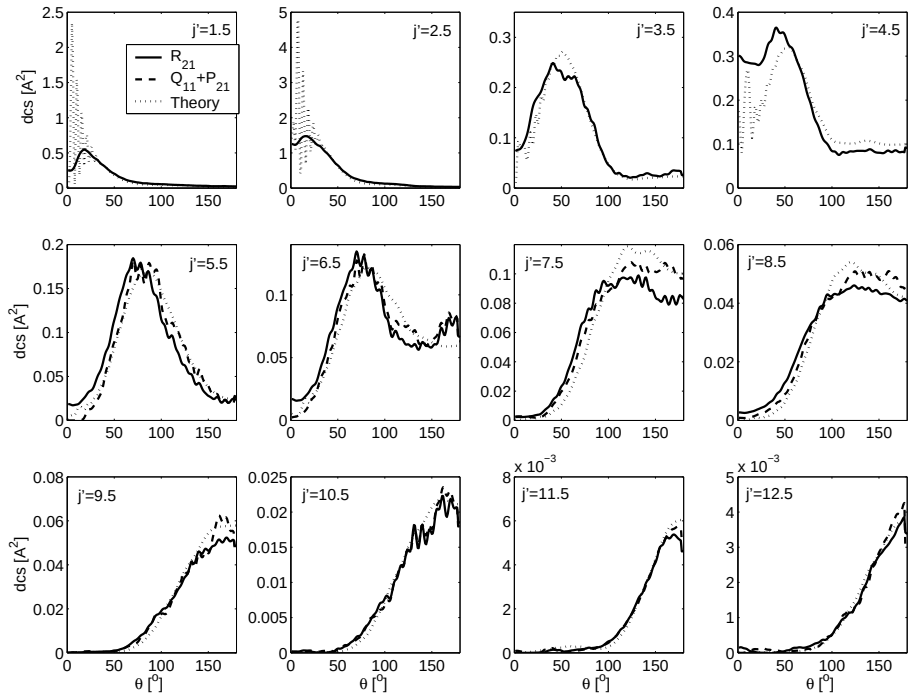

Figure 5.10: Differential cross sections for $\Omega' = \frac{1}{2}$, $\epsilon' = -1$. Experimental results are given for different branches and compared to HIBRIDON calculations. The ion-images from which these differential cross sections are derived are found in Figs. 5.4 and 5.5.

To reach qualitative understanding of the alignment effects in the ion-images, we assume for now that $\boldsymbol{j'} \approx \boldsymbol{\Delta j}$. This is only correct for $\Delta j \to \infty$. A quantitative treatment (at arbitrary j') as used to correct the ion-images is found in Appendix 5.9. For Q branch transitions, the transition dipole moment $\boldsymbol{\mu}$ points parallel to the rotational angular momentum vector ($\boldsymbol{\mu} \parallel \boldsymbol{j'}$). The detection probability as a function of the angle between $\boldsymbol{j'}$ and the laser polarization $\hat{\boldsymbol{\epsilon}}$ for a Q branch transition is given by [113]:

$$|\hat{\boldsymbol{\mu}} \cdot \hat{\boldsymbol{\epsilon}}|^2 = |\hat{\boldsymbol{j'}} \cdot \hat{\boldsymbol{\epsilon}}|^2. \tag{5.9}$$

For a P or R branch transition $\boldsymbol{\mu}$ points perpendicularly to $\boldsymbol{j'}$, which leads to a reversed dependence of the detection probability upon the angle between $\boldsymbol{j'}$ and $\hat{\boldsymbol{\epsilon}}$ [113]:

$$|\hat{\boldsymbol{\mu}} \cdot \hat{\boldsymbol{\epsilon}}|^2 = \frac{1}{2}(1 - |\hat{\boldsymbol{j'}} \cdot \hat{\boldsymbol{\epsilon}}|^2). \tag{5.10}$$

The laser light is polarized horizontally, bisecting the direction of the NO and He beams (see Fig. 5.8). In this figure, a thin line is drawn perpendicularly to $\hat{\boldsymbol{a}}$ in order to indicate the plane (perpendicular to the paper) in which $\boldsymbol{j'}$ is isotropically distributed. Note that since $\boldsymbol{j'}$ is isotropically distributed in that plane, $0 \leq |\hat{\boldsymbol{j'}} \cdot \hat{\boldsymbol{\epsilon}}|^2 \leq \frac{1}{2}$. It immediately follows that the alignment dependence for detection via a Q-branch transition is stronger than in the case of a P or R branch transition. In the left-scattered case in Fig. 5.8, $\hat{\boldsymbol{\epsilon}}$ and $\boldsymbol{j'}$ are nearly perpendicular resulting in a low intensity for a Q-branch transition and a high

intensity for a P or a R branch transition. In the right side of the images, where $\hat{\boldsymbol{\epsilon}}$ and $\boldsymbol{j'}$ are have larger parallel components, this effect is the other way around.

The raw experimental ion images for P and R branches are already near-symmetric in the relative velocity without correction (Figs. 5.4 and 5.6). This is because the detection probability due to the velocity of the molecules after collision and that due to alignment (Appendix 5.8 and 5.9) more-or-less cancel for detection via these branches. No saturation correction has to be applied for these branches to reproduce the experimental ion images with the simulated ones. The left side of the images corresponds to a larger laboratory velocity and thus to a lower detection probability than the right side. This is of course independent of the used spectroscopic branch. Roughly speaking, for P and R branch transitions the detection probability on the left side of the images is larger than on the right side, for Q branch transitions this effect is reversed. This makes ion images using a Q branch transitions for excitation strongly asymmetric as the detection probabilities due to alignment and due to the velocity of the molecules add, while when using P and R branch transitions they nearly cancel. The asymmetry is weakened because each absorption line in a Q branch coincides with one in a P or R branch, but the latter ones are generally weaker. In order to reproduce experimental ion-images obtained using the P+Q and R+Q branches, some saturation has been assumed. This is easily explained because these (combined) branches are stronger than single P and R branches. In Appendix 5.9 (Fig. 5.15) it was already shown that a P branch at low rotational states shows slightly more asymmetry than a R branch. This small effect is also seen in the experimental (and simulated) results in Fig. 5.4, which supports exploiting m_a conservation (along the apse) for collision-induced alignment correction.

The differential cross sections that have been obtained from all ion-images are plotted and compared to theory in Figs. 5.9, 5.10, 5.11 and 5.12. The theoretical results are from new close coupling HIBRIDON [59] calculations on RCCSD(T) potential energy surfaces [56]. Because the experiment does not provide total cross sections, experimental results have been normalized on the integral cross section obtained from the current HIBRIDON calculations

$$\sigma_{j,\Omega,\epsilon\rightarrow j',\Omega',\epsilon'} = \int_0^\pi DCS_{j,\Omega,\epsilon\rightarrow j',\Omega',\epsilon'} \sin(\theta) d\theta. \tag{5.11}$$

For the final states that have been studied using two different branches, both experimental differential cross sections are plotted as this gives information on the correctness of the extraction routine and the error in the measurements in general. Overall there is good agreement between theory and experiment and between the experimental results of different branches, indicating the high quality of the PESs and supporting the current extraction method including the apse based alignment correction (see Section 5.4).

The substantial differences between theory and experiment as in Ref. [102] might be explained by a combination of theoretical and experimental factors. As discussed by De Lange et. al. [6], the anisotropy of the currently used RCCSD(T) potential energy surface is stronger than that of the CEPA surface used in [102]. However, the observed discrepancies in Ref. [102] cannot be fully contributed to theory [6]. Excellent state selection and the correction for collision-induced alignment improves the reliability of the current experimental differential cross sections compared to those in Ref. [102]. However,

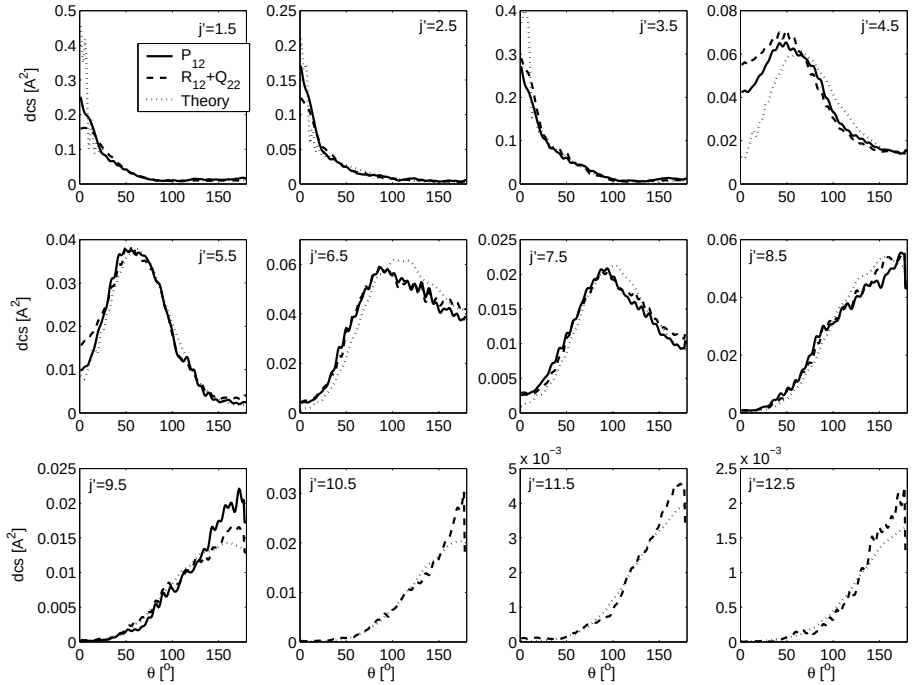

Figure 5.11: Differential cross sections for spin-orbit changing ($\Omega' = \frac{3}{2}$) transitions, into the lower component of the Λ-doublet ($\epsilon' = 1$). Experimental results are given for different both branches and compared to HIBRIDON calculations. The ion-images from which these differential cross sections are derived are found in Fig. 5.6.

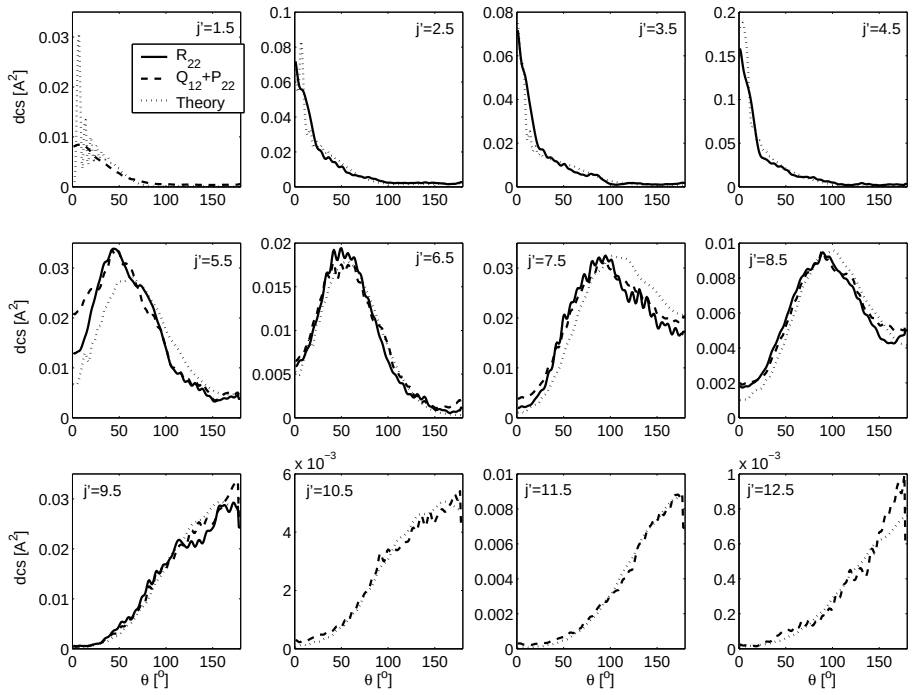

Figure 5.12: Differential cross sections for $\Omega' = \frac{3}{2}$, $\epsilon' = -1$. Experimental results are given for different branches and compared to HIBRIDON calculations. The ion-images from which these differential cross sections are derived are found in Fig. 5.6.

the current differential cross sections cannot directly be compared to the experimental results in Ref. [102] as the current results originate from the scattering out of the upper component of the Λ-doublet. In the experiment in [102], both components are equally present before collision.

Large differences are both observed and calculated between scattering into a $j', \epsilon' = -1$ and a $j', \epsilon' = 1$ state for both spin-orbit changing and spin-orbit conserving collisions. Scattering into the $\epsilon' = 1$ component of the Λ-doublet favors larger scattering angles than scattering into the $\epsilon' = -1$ component at the same j'. These differences have not been observed before and this is the first experiment that enables such a study. Scattering into the $\epsilon' = 1$ state (lower component of the Λ-doublet) appears to yield the same ion-image (and a similar differential cross section) as scattering into the $\epsilon' = -1$ state (upper component of the Λ-doublet) with one less quantum of rotational angular momentum j'. The differential cross section for scattering into a $j' = \nu, \epsilon' = 1$ is similar to that of a $j' = \nu+1, \epsilon' = -1$ final state. This effect cannot be explained by the small energy splitting between the two components of the Λ-doublet, for $\Omega' = 1/2$ ranging from approximately 0.01 cm^{-1} for low to 0.1 cm^{-1} for high rotational states in this study. For $\Omega = 3/2$ it ranges approximately from $4 \cdot 10^{-5}$ cm^{-1} to 0.01 cm^{-1}. This leaves only a quantum mechanical effect to explain this observation, that will be addressed in Ref. [58].

Some differences between experiment and theory are seen for low rotational states. Theoretical differential cross sections show rapid oscillations in the forward direction (close to $\theta = 0$) that are not seen in the experimental outcome. These oscillations are due

to diffraction and the experimental resolution is too low to resolve these oscillations. Besides this, it is consistently found - independent of spin-orbit changing or conserving collisions - that the differential cross section for the first sideways scattered rotational state is predicted by theory to be less forward scattered than the experiment shows. These four differential cross sections are the only ones where a significant difference between experiment and theory exists. A slight underestimation of the attractive part of the PESs might cause this difference, but it cannot be fully excluded to be due to experimental factors. The forward direction is suspected to cause some problems during extraction of differential cross sections as the direction of the apse there is poorly defined. On the other hand, if the apse model fails, one also expects this to happen for the lowest rotational states, which is not the case. Except for these small differences, there is good agreement between theory and experiment.

5.7 Concluding remarks

For the first time, quantum-state-resolved differential cross sections arising from single parity states have been recorded. The differential cross sections are plotted in Figs. 5.9, 5.10, 5.11 and 5.12. A 2 meters long hexapole state selector was used to select the upper component of the Λ-doublet of the lowest rotational state ($j = 1/2, \Omega = 1/2, \epsilon = -1$) from a molecular NO beam expansion. The fully state-selected beam was crossed with a Helium beam and velocity-mapped ion-imaging was applied to record ion-images. The absence of molecules in other rotational states in the molecular beam due to hexapole focussing leads to particularly crisp images.

The present work provides the first experimental evidence for differences in the differential cross section between parity-breaking and parity-conserving transitions. We find that scattering into the $\epsilon' = 1$ component of the Λ-doublet favors larger scattering angles than scattering into the $\epsilon' = -1$ component at the same j'. The differential cross sections for scattering into the lower component of the Λ-doublet $j = 1/2, \epsilon = -1 \rightarrow j' = \nu, \epsilon = 1$ is very similar to that of scattering into the upper component $j = 1/2, \epsilon = -1 \rightarrow j' = \nu + 1, \epsilon = -1$. These final states carry the same parity. The energy splitting between the two components of the Λ-doublet is too small to explain this observation.

We exploit m conservation along the kinematic apse during collision to correct for collision-induced alignment. A straight forward method to take this alignment into account is presented. The experimental results support this method. The distortion of the ion-images is well reproduced and differential cross sections for scattering into the same rotational state, extracted from different spectroscopic branches, correspond nearly perfectly to each other.

The experimental differential cross sections correspond well to those calculated in close coupling (HIBRIDON) calculations based on RCCSD(T) potential energy surfaces (PESs) [114]. Together with a previous experiment where steric asymmetries for collisions of He with (oriented) NO were measured [6], this forms a thorough test for the ground electronic state PESs. The PESs are accurate in the energy range that is probed in these experiments ($E_{tr} < 510\ cm^{-1}$). However, a slight underestimation of forward scattering for a few rotational states might be caused by underestimation of the attractive part of

the PESs.

5.8 Appendix: velocity correction

It is assumed that the NO detection probability ($T(x,y)$) due to the molecular residence time in the detection volume is inversely proportional to the absolute value of the velocity in the laboratory frame. The coordinates (x,y) indicate the position position on the detector in pixels and relate directly to the x and y components of the velocity in the center-of-mass (u'_x and u'_y) frame via the resolution G ($x = u'_x/G$ and $y = u'_y/G$).

$$T(x,y) \equiv \frac{1}{|\boldsymbol{v'}|} \Big/ \left\langle \frac{1}{|\boldsymbol{v'}|} \right\rangle \tag{5.12}$$

Normalization is obtained by dividing with the average over all pixels ($\langle 1/|\boldsymbol{v'}| \rangle$).

The velocity in the laboratory frame can be approximated for each pixel in the ion-images, assuming an ideal velocity distribution in the beams. The velocity in the lab frame follows as:

$$\boldsymbol{v'} = \boldsymbol{v_{cms}} + \boldsymbol{u'} \tag{5.13}$$

The absolute value of the velocity in the center-of-mass frame $|\boldsymbol{u'}|$ follows from energy conservation. It is dependent on the rotational state after collision j'. The components u'_x and u'_y in x and y direction (along the NO and He velocity vector, respectively) are defined by the position (x,y) on the detector and the resolution G. The component u'_z can now be specified as:

$$u'_z = \sqrt{|\boldsymbol{u'}|^2 - {u'_x}^2 - {u'_y}^2}. \tag{5.14}$$

For positions on the detector (x,y) where $|\boldsymbol{u'}|^2 - {u'_x}^2 - {u'_y}^2 < 0$, we will use $u'_z = 0$. The center-of-mass velocity $\boldsymbol{v_{cms}}$ is given by:

$$\boldsymbol{v_{cms}} = \boldsymbol{v_{NO}} + \frac{m_{He}}{m_{NO} + m_{He}} (\boldsymbol{v_{He}} - \boldsymbol{v_{NO}}) \tag{5.15}$$

The laboratory velocity now follows as:

$$\boldsymbol{v'} = \begin{pmatrix} v_{NO} \\ 0 \\ 0 \end{pmatrix} + \frac{m_{He}}{m_{NO} + m_{He}} \begin{pmatrix} -v_{NO} \\ v_{He} \\ 0 \end{pmatrix} + \begin{pmatrix} u'_x \\ u'_y \\ \sqrt{|\boldsymbol{u'}|^2 - {u'_x}^2 - {u'_y}^2} \end{pmatrix} \tag{5.16}$$

with an absolute value of:

$$|\boldsymbol{v'}| = \left[\left(v_{NO} - \frac{m_{He} v_{NO}}{m_{NO} + m_{He}} + u'_x \right)^2 + \left(\frac{m_{He} v_{He}}{m_{NO} + m_{He}} + u'_y \right)^2 + |\boldsymbol{u'}|^2 - {u'_x}^2 - {u'_y}^2 \right]^{\frac{1}{2}} \tag{5.17}$$

Eq. 5.16 can be extended to correct for the Doppler shift, but because of the small center-of-mass velocity differences of the scattered molecules this is not done here. As an example, the detection probability factor for $j' = 4.5$ as derived from Eq. 5.12 is plotted in Fig. 5.13. From this figure it can be seen that for the current images, $T(x,y)$ turns out to be a factor of 2 larger in the top-right angle than in the bottom-left angle of the images. This is a substantial effect that cannot be neglected in extracting differential cross sections from ion-images.

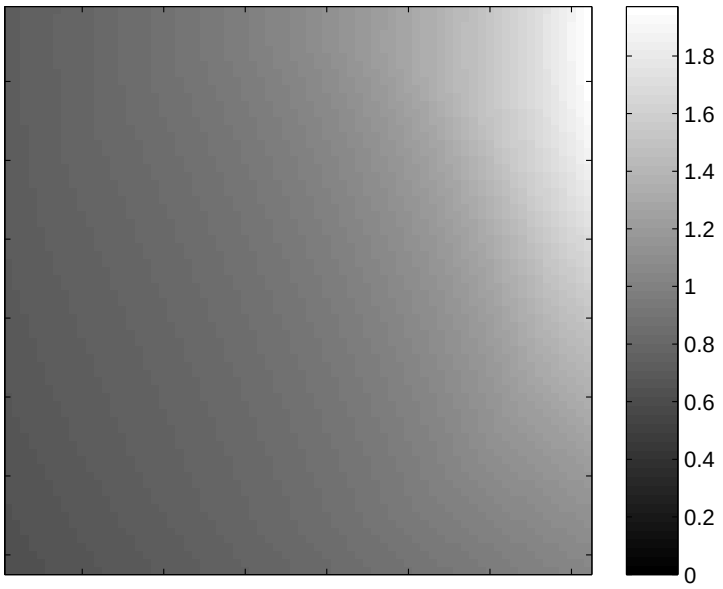

Figure 5.13: The laboratory velocity detection probability $T(x, y)$, at each position on the image (here for $j' = 4.5$) is given by the intensity. Molecules with low laboratory velocity remain in the detection volume for a longer time and are thus more likely to be detected than fast molecules. The frame of this figure corresponds to the dashed square in Fig. 5.3, which corresponds to the area of the ion-images in Figs. 5.4, 5.5 and 5.6. Note that values of $T(x, y) < 0.8$ do not occur within the frame.

5.9 Appendix: collision-induced alignment

A simple but widely applicable correction treatment based on the m conservation along the kinematic apse is derived here. The alignment dependent detection probability is proportional to:

$$S_a(j' \rightarrow j^*) \equiv \sum_{m^*} \left| \left\langle \Psi^*(j^*, m^*) \mid \hat{\boldsymbol{\mu}} \cdot \hat{\boldsymbol{\epsilon}} \mid \boldsymbol{R}(\beta_p)\Psi'_a(j', m'_a) \right\rangle \right|^2 \tag{5.18}$$

The wave functions will be referred to as $\Psi_a(j = \frac{1}{2}, m_a = \pm\frac{1}{2})$, $\Psi'_a(j', m'_a)$ and $\Psi^*(j^*, m^*)$, denoting respectively the rotational states before collision, after collision (in the apse frame) and after laser excitation to the $^2\Sigma$ state. Note that m^* is defined along the electric field of the linearly polarized laser (laser frame). The wave function in the apse system $\Psi'_a(j', m'_a)$ is transformed into the laser frame, the angle between the laser polarization and the kinematic apse is described as β_p. During excitation to the $^2\Sigma$ state the projection of the rotational angular momentum in the laser frame remains conserved. The wave function after a collision will be aligned due to the collision. If one assumes that the projection m_a of the total angular momentum $\boldsymbol{j}$ on the kinematic apse is conserved during collision, it is relatively easy to take this effect into account. The kinematic apse direction is given by:

$$\hat{\boldsymbol{a}} = \frac{\boldsymbol{k'} - \boldsymbol{k}}{|\boldsymbol{k'} - \boldsymbol{k}|} \tag{5.19}$$

where $\boldsymbol{k}$ and $\boldsymbol{k'}$ denote the momentum vectors before and after collision, respectively. Khare [107] and Meyer [108] showed that m_a conservation along the kinematic apse is a reasonable approximation. Rotation of the wave function $\Psi'_a(j', m'_a)$ over the angle between the apse and the laser polarization β_p provides the aligned wave function in the laser frame:

$$\boldsymbol{R}(\beta_p)\Psi'_a(j', m_a) = \sum_{m'} d^j_{m',m_a}(\beta_p)\ \Psi'(j', m') \tag{5.20}$$

Note that $0 \leq \beta_p \leq 90^o$. Substitution of Eq. 5.20 in Eq. 5.18 gives:

$$S_a(j' \rightarrow j^*) = \sum_{m'} \left| d^j_{m',m_a}(\beta_p) \left\langle \Psi^*(j^*, m^*) \mid \hat{\boldsymbol{\mu}} \cdot \hat{\boldsymbol{\epsilon}} \mid \Psi'(j', m') \right\rangle \right|^2 \tag{5.21}$$

In order to distinguish between the apse alignment dependent detection probability and the ordinary Hönl-London factors, these are respectively written as $S_a(j' \rightarrow j^*)$ and $S(j' \rightarrow j^*)$. Jacobs and Zare [115] show that the (m-dependent) detection probability or rate constant for linearly polarized light is proportional to the well known Hönl-London factors multiplied with a 3-j symbol:

$$\left| \left\langle \Psi^*(j^*, m^*) \mid \hat{\boldsymbol{\mu}} \cdot \hat{\boldsymbol{\epsilon}} \mid \Psi'(j', m') \right\rangle \right|^2 = S(j' \rightarrow j^*) \begin{pmatrix} j^* & 1 & j' \\ m' & 0 & -m' \end{pmatrix}^2 \delta_{m^*,m'} \ . \tag{5.22}$$

The Hönl-London factors $S(j' \rightarrow j^*)$ for a $X^2\Pi \rightarrow\ A^2\Sigma^+$ transition where first derived by Earls [116] and are also available from Ref. [13]. Together this gives:

$$S_a(j' \rightarrow j^*) = S(j' \rightarrow j^*) \sum_{m'} \left| d^j_{m',m_a}(\beta_p) \begin{pmatrix} j^* & 1 & j' \\ m' & 0 & -m' \end{pmatrix} \right|^2 \tag{5.23}$$

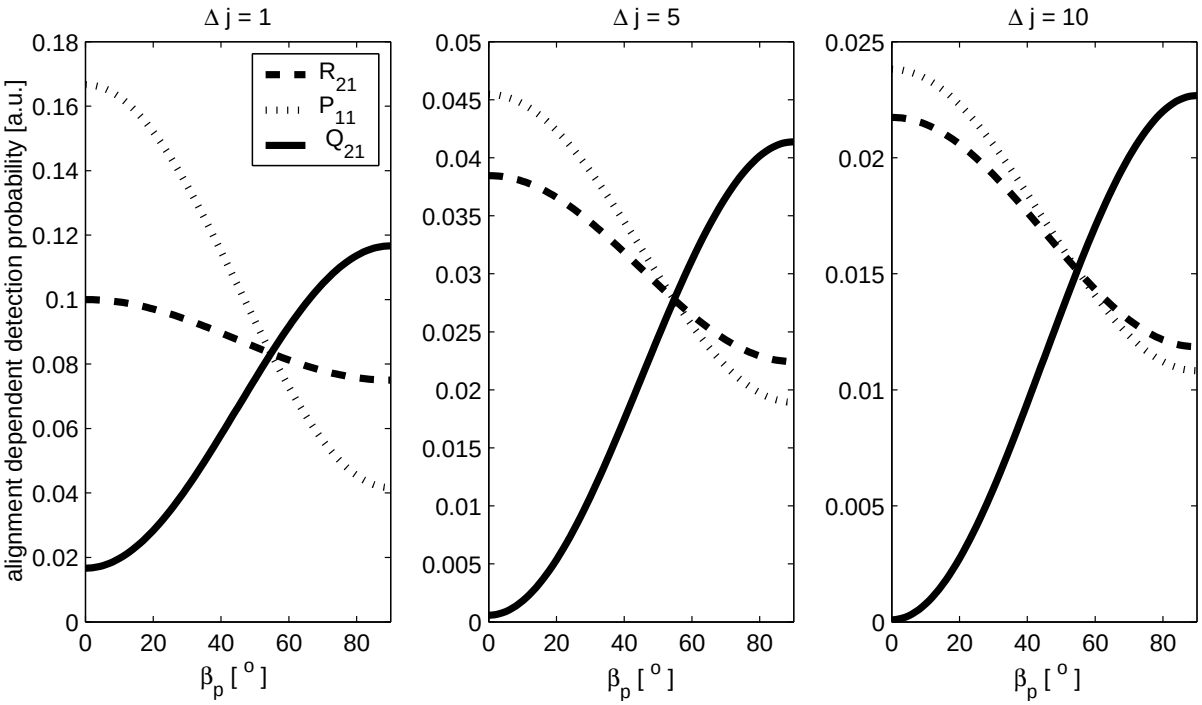

Figure 5.14: The alignment dependent detection probability ($S_a(j' \to j^*)/S(j' \to j^*)$) is plotted against the angle β_p between the apse and the laser polarization for three different values of Δj and for three different branches.

Note that the detection probability is independent of the sign of m_a. Eq. 5.23 provides a novel and simple method to correct ion-images for collision-induced alignment. Every pixel on an image corresponds to a certain final momentum (velocity). With the final rotational state defined and therefore the final velocity of the NO molecules defined, each position on the detector can be associated with a particular kinematic apse via Eq. 5.19. Fig. 5.14 shows the dependence of the detection probability (divided by the Hönl-London factor) $S_a(j' \to j^*)/S(j' \to j^*)$ on the angle β_p between the apse and the electric field of the laser. This is plotted for three different Δj, for a Q, an R and a P branch transition. Already at $\Delta j = 10$, the expected limiting behavior for $j' \to \infty$ emerges, as argued in section 5.6 below Eqs. 5.9 and 5.10. In Fig. 5.15 the detection probability $S_a(j' \to j^*)$ is given for four branches and one rotational state. The size of the images in Fig. 5.15 corresponds to the size required to record an entire ion-image of the scattered NO product. Note that the Q_{11} strongly dominates over the P_{21} because its Hönl-London factor for the Q_{11} transition is about a factor of three larger than that for the P_{21} transition. The R_{11} and Q_{21} branches carry a similar value of the Hönl-London factor, but as expected the Q branch character dominates the alignment dependent detection probability. The alignment dependence of the detection probability for a Q branch transition is about a factor of two stronger than and opposite to that of a P or R branch transition. This is clearly demonstrated in Eqs. 5.9 and 5.10 and Fig. 5.14.

In the event of full saturation of the $A \leftarrow X$ transition, the detection probability no

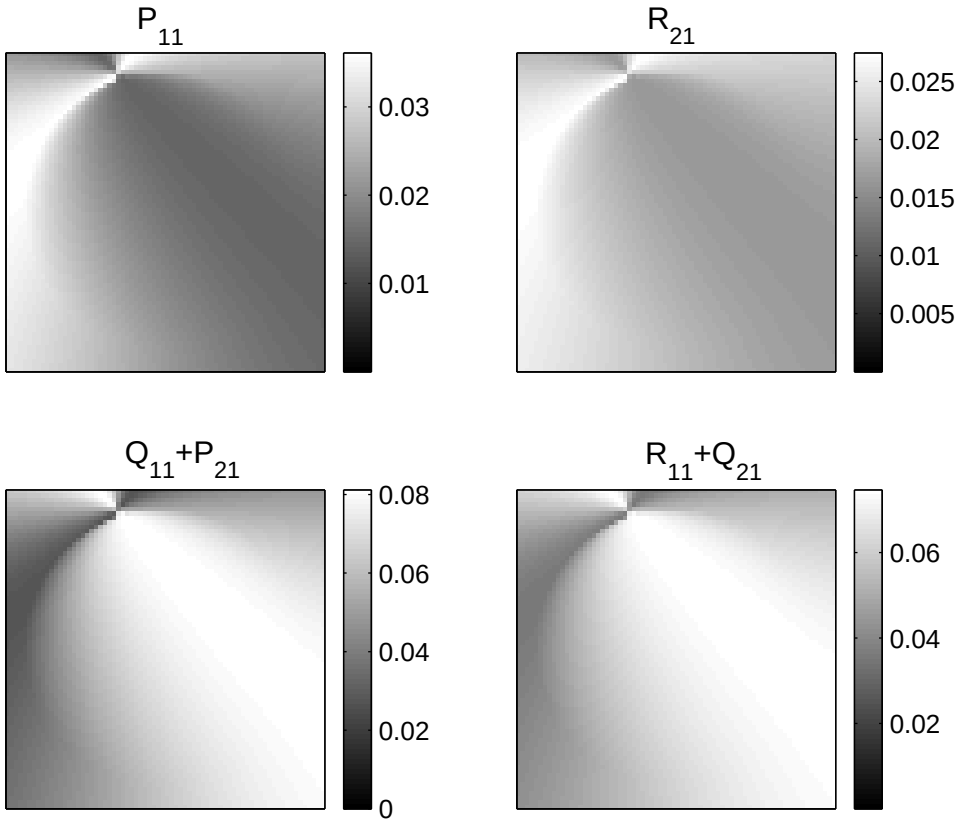

Figure 5.15: The alignment dependent detection probability $S_a(j' \to j^*)$ at each position on the image (here for $j' = 4.5$) is given by the intensity for several branches. The angle between the apse and the laser polarization defines the detection probability via Eq. 5.23. The size of each of the frames in this figure corresponds to the dashed square in Fig. 5.3, which corresponds to the frames of the ion-images in Figs. 5.4, 5.5 and 5.6. Note that the apse is undefined when $\boldsymbol{k'} = \boldsymbol{k}$ (see Eq. 5.19). The dynamic range of each of the images is taken from 0 to its maximum value.

longer depends on the scattering angle. In that case, correction of the ion-images with only the velocity correction should yield undistorted ion-images. If partial saturation occurs, the dependence of the detection probability on β_p becomes less.

$$S_{sat}(j' \rightarrow j^*) = S_0 + S_a(j' \rightarrow j^*). \tag{5.24}$$

The parameter C indicates the saturation: if $S_0 << S_a(j' \rightarrow j^*)$, there is no saturation, if $S_0 >> S_a(j' \rightarrow j^*)$ there is full saturation and the detection probability no longer depends on the scattering angle. To get an idea of the effect of the saturation correction, C can be expressed in terms of the value of $S_a(j' \rightarrow j^*)$ averaged over all pixels $\langle S_a(j' \rightarrow j^*) \rangle$.

Chapter 6

Parity-dependent rotational rainbows

6.1 abstract

The $(j', \overline{\Omega}', \epsilon')$ dependent differential collision cross sections of D_2 with fully state selected $(j = 1/2, \overline{\Omega} = 1/2, \epsilon = -1)$ NO have been determined at a collision energy of about 550 cm^{-1}. The collisionally excited NO molecules are detected by (1+1') resonance enhanced multi-photon ionization (REMPI) combined with the velocity-mapped ion-imaging technique. The results are compared to He-NO scattering results and tend to be more forward scattered for the same final rotational state. Both for collisions of the atomic He and the molecular D_2 with NO, scattering into pairs of rotational states with the same value of $n \equiv j' - \epsilon\epsilon'/2$ yield the same angular dependence of the cross section. This "parity propensity rule" remains present both for spin-orbit conserving as for spin-orbit changing transitions. The maxima in the differential cross sections - that reflect rotational rainbows - have been extracted from the D_2-NO and the He-NO differential cross sections. These maxima are found to be distinct for odd and even parity pair number n. Rainbow positions of parity changing transitions (n is odd) occur at larger scattering angles than those of parity conserving transitions (n is even). Parity conserving transitions exhibit - from a classical point of view - a larger effective eccentricity of the shell. No rainbow doubling due to collisions onto either the N-end and the O-end were observed. From a classical point of view the presence of a double rainbow is expected. Rotational excitation of the D_2 molecules has not been observed.

6.2 Introduction

Crossed molecular beam machines [117] provide an important tool towards a better understanding of the dynamics of chemical elementary processes [35,104]. These machines allow experimentalists to study the outcome of (gas phase) encounters of molecules with atoms and/or other molecules under well defined conditions (collision energy and initial state of the colliding molecules). All macroscopic chemical reactions consist of a large number of elementary chemical processes that must be studied to understand macroscopic chemical

reactions and energy transfer. Steering these reactions is a longstanding goal in molecular sciences and for this it is necessary to understand and to predict the outcome of a single molecular encounter.

Since the pioneering work of Yuan T. Lee, John C. Polanyi and Dudley R. Herschbach, an enormous progress in the field of reaction dynamics has been achieved. An important development within that progress has been the introduction of the ion-imaging technique [93]. This method allows one to record the whole (2D) velocity distribution of reaction products in a single measurement. The velocity-mapped ion-imaging technique [39, 43] - that uses electrostatic lenses to project the velocity distribution onto the detector - is nowadays a common tool in the field of molecular dynamics [3, 4, 28, 39, 95, 96].

In the past, several reaction dynamical studies - both experimentally and theoretically - have focussed on the rotationally inelastic scattering of NO with a number of collision partners [1–4]. The main reason for this is that NO is both an interesting and convenient model system. It is a radical, with non-zero angular momentum in its rotational ground state, while it is stable enough to be stored in a gas bottle. Furthermore, it is easily detected with spectroscopic methods as laser induced fluorescence (LIF) [5] and resonance enhanced multi-photon ionization (REMPI) [4, 8]. Using the hexapole focussing technique [9], NO can be fully selected into a single quantum state (upper component of the Λ-doublet) as it undergoes a first order Stark effect [10]. The two components of the Λ-doublet within the same rotational level have opposite parity, but only a minute energy splitting. Parity propensity effects for Hund's case (a) molecules are far more important than the effects of the orientation of the unpaired electron charge cloud. The latter effects are responsible for the A' and A'' symmetry of the PESs [1]. By (hexapole) selection of NO in a single quantum state before collision, the effect of parity changing and parity conservation on the differential cross section can be isolated from the effect of the excitation energy.

It was shown recently, that interesting physical effects emerge for inelastic He-NO scattering experiments when full (hexapole) state selection is applied [11]. The angular dependence of the cross section for excitation to pairs of states with the same parity was noted to be similar. In the present study we will asses this effect quantitatively, by a direct comparison of the differential cross sections for two different systems. This parity propensity follows directly from a simple Quasi-Quantummechanical Treatment (QQT) [58], which also provided some new insights into the orientation dependence of the inelastic collision cross section.

In our search towards a better understanding of inelastic collisions, additional velocity-mapped ion-imaging measurements on D_2-NO inelastic scattering have been performed. This collision system is very close to He-NO, but still distinguishable [102] and provides thus valuable information about the effect of a small difference of the interaction potential on the differential cross section. In the current work, we focus on "parity pairs" and the position of the rotational rainbows. Classical rotational rainbows [34] are reflected by the maxima in the rotationally inelastic scattering angular distributions.

6.3 Experimental

The experimental setup has been described in detail in Ref. [11] and only the most relevant conditions are mentioned here. A beam of 16 % NO seeded in Ar expands from a General Valve, which forms the first step of state selection. Due to adiabatic cooling, most of the NO molecules are in their rotational ground state with rotational quantum number $j = \frac{1}{2}$. Via two skimmers, the NO beam enters a 1.6 meters long hexapole. The hexapole focusses molecules in the low field seeking upper component of the λ-doublet ($j = \frac{1}{2}, \overline{\Omega} = \frac{1}{2}, \epsilon = -1$) into the collision region and diverges molecules in the lower component ($j = \frac{1}{2}, \overline{\Omega} = \frac{1}{2}, \epsilon = 1$). The parameter ϵ denotes the symmetry index, while $\overline{\Omega}$ ($= |\Omega|$) is the (absolute value of the) projection of the electronic angular momentum onto the molecular axis. Molecules in higher rotational states are much less affected by the hexapole and the resulting divergence of the molecular beam over the three meters distance from nozzle to collision region reduces the relative amount of molecules in higher rotational states in the beam by approximately a factor of 70 (hexapole gain of the focussed state).

The hexapole focussed beam of NO molecules (v_{NO} = 593 m/s) is crossed in the collision chamber by a beam of D_2 molecules (v_{D_2} = 1830 m/s) [102]. These velocities result in a nominal collision energy of 551 cm^{-1}, which is slightly larger than in the case of He-NO scattering (514 cm^{-1}) [11]. An encounter of a D_2 molecule with a NO molecule can in principle induce rotation of the NO and/or the D_2 molecule. Energetically it is allowed to excite the NO molecules up to $\Delta j = j' - j = 16$ while the D_2 molecules can be excited up to $\Delta j = 4$. The rotationally excited NO molecules are ionized via a (1+1') resonance enhanced multi photon ionization (REMPI) scheme [8] along the electronic $A\,^2\Sigma^+ \leftarrow X\,^2\Pi$ transition using an excimer (XeCl) pumped dye laser laser with a bandwidth of about 0.1 cm^{-1}. Velocity-mapped ion-imaging is applied to obtain the two dimensional velocity distribution of the scattered NO molecules.

To suppress contributions from other ionized molecules (oil or water) to the ion images, time-of-flight (TOF) gating is applied. The contributions to the images of thermal NO and of non-colliding molecules in the NO beam at the collision center are minimized by subtracting background images. The D_2 beam is switched from "on" to "off" after each 100 laser shots. This procedure is repeated typically 20 times. The images with the D_2 beam "off" are subtracted from those with the D_2 beam "on". As the excimer/dye laser system and General Valves run at 10 Hz, collecting an image takes approximately 7 minutes. Because of low signal, some of the highest rotational states ($\Delta j > 10$) required twice the integration time.

Differential cross sections are extracted from the ion images following the extraction procedure described in Ref. [11]. In this procedure, collision-induced rotational alignment, the detection probability due to different residence times for slow and fast molecules within the detection volume and blurring of the images are explicitly taken into account. An empirical blurring factor is used to make the simulated images as sharp as the experimental ones. To correct for alignment, the assumption is used that the projection m_a of the rotational angular momentum $\boldsymbol{j}$ on the kinematic apse is conserved. The alignment dependent correction accounts for (partial) saturation.

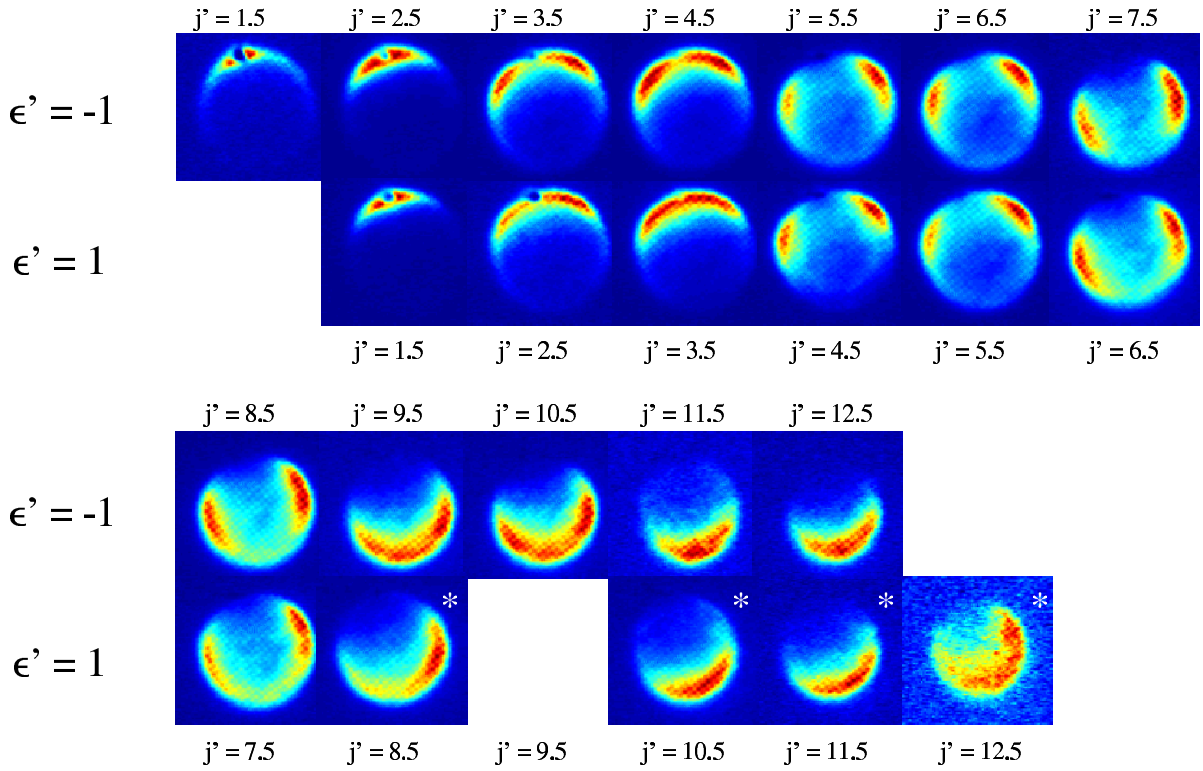

Figure 6.1: Set of raw experimental ion images for spin-orbit conserving ($\overline{\Omega} = \overline{\Omega}' = 1/2$) D_2-NO scattering. The images for $\epsilon' = -1$ are collected using the R_{21} spectroscopic branch. The majority of the images for $\epsilon' = 1$ are collected via the P_{11} branch, those labeled with a star * are from the combined $R_{11} + Q_{21}$ branch that exhibits more asymmetry with respect to the $\boldsymbol{v_{rel}}$. This is due to the combination of collision-induced alignment and the residence time of the molecules in the detection region. For a P and R branch transition the effects of alignment and residence time nearly cancel, while for Q branch transitions those add, yielding very asymmetric ion images. The images are plotted such that two images above each other relate to the same parity pair $n = j' + \frac{\epsilon'}{2}$. The missing image for $j' = 9.5, \epsilon' = 1$ could not be collected due to overlapping spectral lines.

6.4 Results and discussion

6.4.1 Differential cross sections and parity pairs

A set of (raw) velocity mapped ion images for spin-orbit conserving collisions ($\overline{\Omega} = \overline{\Omega}' = 1/2$) [1] is plotted in Fig. 6.1. The projected Newton sphere is cylinder-symmetric around the relative velocity ($\boldsymbol{v_{rel}} = \boldsymbol{v_{D_2}} - \boldsymbol{v_{NO}}$). The camera is oriented such that $\boldsymbol{v_{NO}}$ points from right to left, while $\boldsymbol{v_{D_2}}$ points from the top to the bottom of the images. The resulting orientation of $\boldsymbol{v_{rel}}$ is from top-left to bottom-right.

The intensity on an outer ring of an ion image (on both sides of $\boldsymbol{v_{rel}}$) gives a first impression of the differential cross section. Note that the intensity on the top-left part of the images is due to forward scattered molecules, while backward scattered molecules are detected at the lower-right part of the image. In the images it is clearly seen that forward scattering is preferred for NO scattering into low rotational states, while for high final rotational states backward scattering dominates. The ion images for spin-orbit changing transitions ($\overline{\Omega}' = \frac{3}{2}$) are not shown in this work, but are of a similar quality as those in Fig. 6.1. Rotational excitation of the D_2 molecules is not observed in the ion images. This should show up as small projected Newton sphere dominated by backward scattering in the images for low rotational states of the NO molecules.

For He-NO collisions [11] it was found that scattering - at the same value of j' - into the upper component of the Λ-doublet ($\epsilon = -1 \rightarrow \epsilon' = -1$) yields more forward scattering than into the lower component of the Λ-doublet ($\epsilon = -1 \rightarrow \epsilon' = 1$). Such a difference is also found in the present D_2-NO images.

Scattering into the lower component of the λ-doublet seems to be "one rotational quantum ahead" of scattering into the upper component of the Λ-doublet. For example, similar images are collected for excitation to the $j' = 4.5, \epsilon' = 1$ and the $j' = 5.5, \epsilon' = -1$ states, as is the case for the $j' = 5.5, \epsilon' = 1$ and the $j' = 6.5, \epsilon' = -1$ states, etc. This similarity holds both for spin-orbit conserving and spin-orbit changing transitions. Note that these final states carry the same parity and for this reason the pairs are referred to as "parity pairs". The parity for a rotational state j, ϵ follows from:

$$p = (-1)^{j-\epsilon/2}. \tag{6.1}$$

The parity of a rotational state relates to the symmetry properties of its wave function $\psi(\boldsymbol{r})$ and is defined by its behavior under parity transformation (inversion), which acts as an operator $\boldsymbol{P}$ on a wave function ψ:

$$\boldsymbol{P}\psi(\boldsymbol{r}) = \psi(-\boldsymbol{r}) = p\psi(\boldsymbol{r}) \tag{6.2}$$

Note that $\boldsymbol{r}$ represents here both electronic and nuclear coordinates.

To illustrate the presence of parity pairs, the images in Fig. 6.1 are plotted such that two images above each other belong to the same pair. The parity pairs are numbered as:

$$n = j' - \frac{\epsilon\epsilon'}{2}, \tag{6.3}$$

[1] Since Hund's case (a) coupling dominates [16] for the here achievable final rotational states of NO. Labels $\overline{\Omega}' = \frac{1}{2}$ and $\overline{\Omega}' = \frac{3}{2}$ correspond to scattering into the F_1 and F_2 levels.

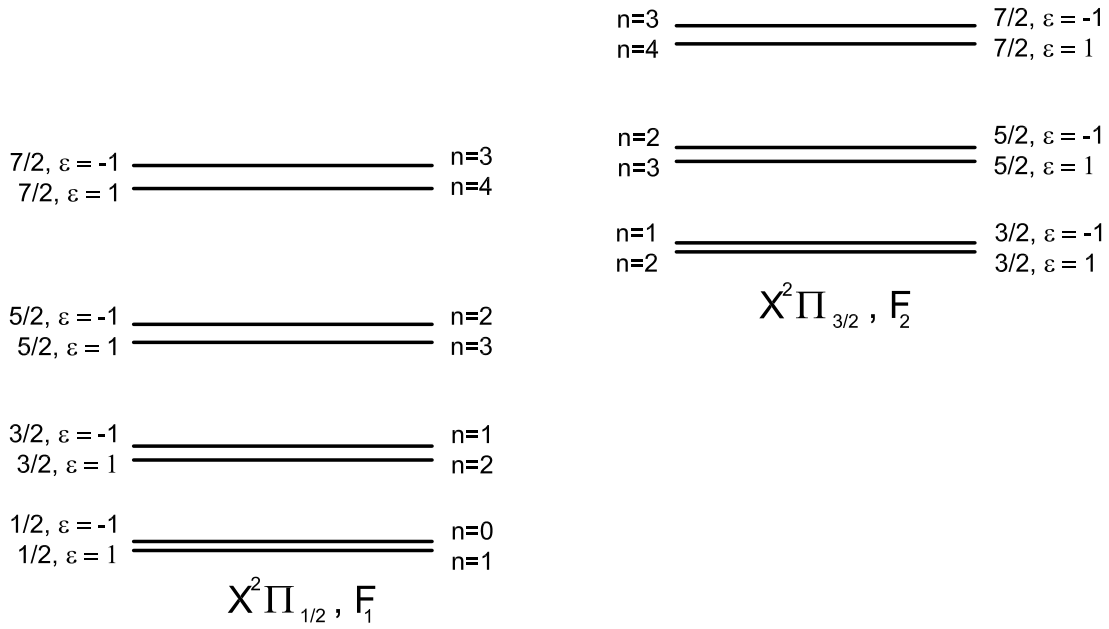

Figure 6.2: The rotational levels of the NO molecule are labeled with their rotational quantum number j and symmetry index $\epsilon = \pm 1$). Recall that parity p and ϵ relate as $p = (-1)^{j-\epsilon/2}$. The parity pair numbers n in this figure relate to the experimental case where $j = 1/2, \epsilon = -1$. Parity pairs are observed for both spin-orbit conserving as for spin-orbit changing transitions, but the differential cross sections of a parity pair n for spin-orbit conserving transitions does not correspond to that of the same pair n for a spin-orbit changing collision. The energy differences are taken arbitrarily and are not scaled to the actual values. In that case, the distance between the components of the Λ-doublet would be much smaller.

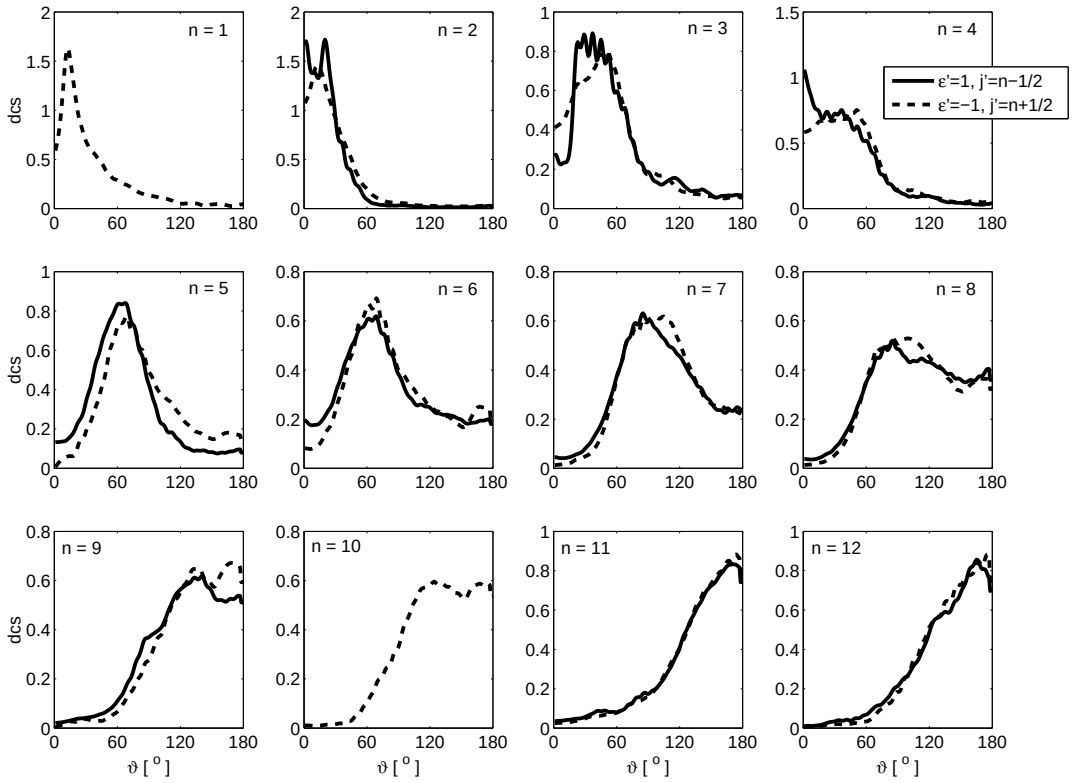

Figure 6.3: Differential cross sections for (D_2 - NO) scattering into $\overline{\Omega}' = \frac{1}{2}$. The differential cross sections are plotted per parity pair and normalized such that the integral $\int$ dcs $d\vartheta = 1$. The differential cross section for $j' = 12.5, \epsilon' = 1$ is plotted separately in Fig. 6.5.

which reduces in our experiment to $n = j' + \epsilon'/2$ as $\epsilon = -1$. Figure 6.2 provides a schematic representation of the NO energy levels including the parity pair number n for the (current experimental) case $j = 1/2, \epsilon = -1$. The physical background of pairs with these labels is discussed in detail in Ref. [58]. The integral that leads to the differential cross section contains a phase shift factor and a Legendre polynomial $P_{j'-\epsilon\epsilon'/2}$. If the energy spacing between the rotational levels is small, the phase shift factor has little influence. Because of the Legendre polynomial, excitation to a pair of rotational states with the same label n should show a similar angular dependence of the cross section. Even Legendre polynomial contribute for parity conserving transitions, while odd Legendre polynomials contribute for parity breaking transitions.

In the case of NO the electron cloud of the unpaired electron is nearly cylinder symmetric with respect to the internuclear axis (Hund's case(a)). The mixing between $\overline{\Omega} = 3/2$ and $\overline{\Omega} = 1/2$ is small, so the angular distribution of an $\epsilon = 1 \rightarrow \epsilon' = -1$ transition is nearly equal to that of $\epsilon = -1 \rightarrow \epsilon' = 1$ and the angular distribution of an $\epsilon = -1 \rightarrow \epsilon' = -1$ transition is nearly equal to that of $\epsilon = 1 \rightarrow \epsilon' = 1$.

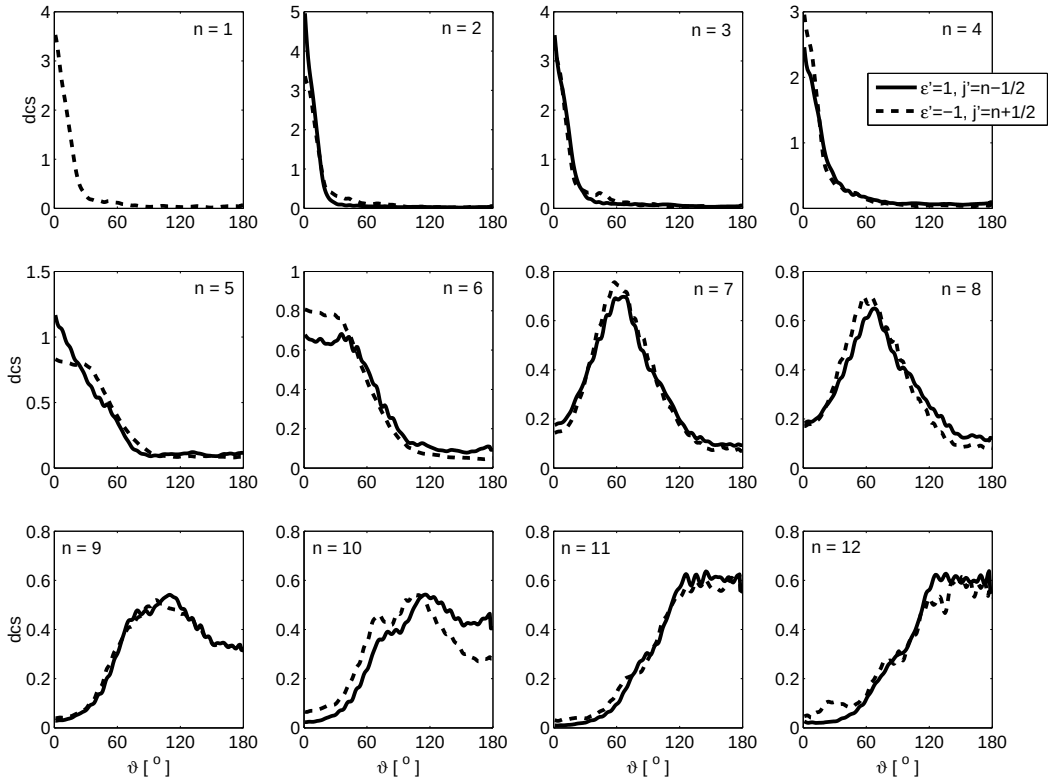

Figure 6.4: Differential cross sections for (D_2 - NO) scattering into $\overline{\Omega}' = \frac{3}{2}$. The differential cross sections are plotted per parity pair and normalized such that the integral $\int$ dcs $d\vartheta = 1$. The differential cross section for $j' = 12.5, \epsilon' = 1$ is plotted separately in Fig. 6.5.

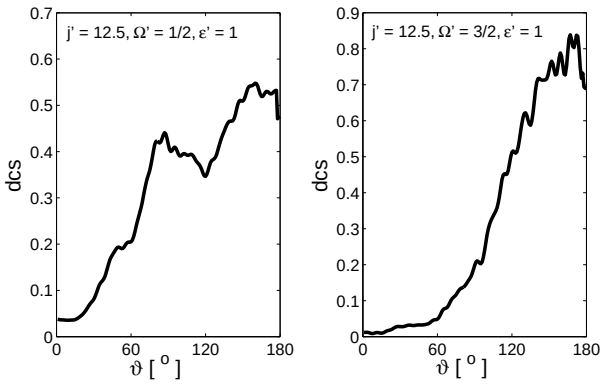

Figure 6.5: Differential cross sections for (D_2 - NO) scattering into the highest observed rotational state $j' = 12.5$ of the lower component of the Λ-doublet ($n = 13$). Note that the differential cross section for $\Omega' = \frac{1}{2}, \epsilon' = 1$ has a strong sideways scattered contribution. From a simple classical model this cannot be understood. A similar, but even more pronounced effect was observed for He-NO collisions [11].

The D_2-NO differential cross sections that are extracted from the images (indicated in the figures as "dcs") are shown in Fig. 6.3. The extracted cross sections for spin-orbit changing collisions ($\overline{\Omega}' = \frac{3}{2}$) are shown in Fig. 6.4. Tables with D_2-NO differential cross sections can be found online [2]. To illustrate the pairwise structure, the differential cross sections that form a pair are plotted in the same panel. Those for excitation to the $j' = 12.5$ states of the $\epsilon' = 1$ state are plotted separately in Fig. 6.5. For the purpose of comparison, all differential cross sections are normalized with respect to each other such that the integral $\int$ dcs $d\vartheta = 1$. Note that this is not the usual integral cross section ($\int$ dcs $\sin\vartheta d\vartheta$). Normalization on the total cross section suppresses information for scattering angles close to 0^o and 180^o. As we focus on the shape of the differential cross section all scattering angles are equally important. The plotted cross section is the average of two experimental results if two spectroscopic branches were available to collect data.

An interesting observation in Fig. 6.5 is that - opposite to what one would expect from a classical point of view - the cross sections for scattering into the ($j' = 12.5, \Omega' = \frac{1}{2}, \epsilon' = 1$) is more-or-less dominated by sideways scattering. This effect has been observed to be even more pronounced for He-NO scattering, but no satisfactory explanation is available yet. If we extrapolate the observed pairwise structure, the differential cross section for the $j' = 12.5, \Omega' = \frac{1}{2}, \epsilon' = 1$ should be similar to that of the $j' = 13.5, \Omega' = \frac{1}{2}, \epsilon' = -1$ final rotational state. This latter state is classically not allowed. Energetically it is, but the maximally applied torque is too small to allow for such a high rotational state [118]. Quantummechanically these transitions are allowed, but with a much smaller cross section.

[2]See EPAPS Document for tables with D_2-NO differential cross sections. This document can be reached through a direct link in the online articles HTML reference section or via the EPAPS homepage (http://www.aip.org/pubservs/epaps.html).

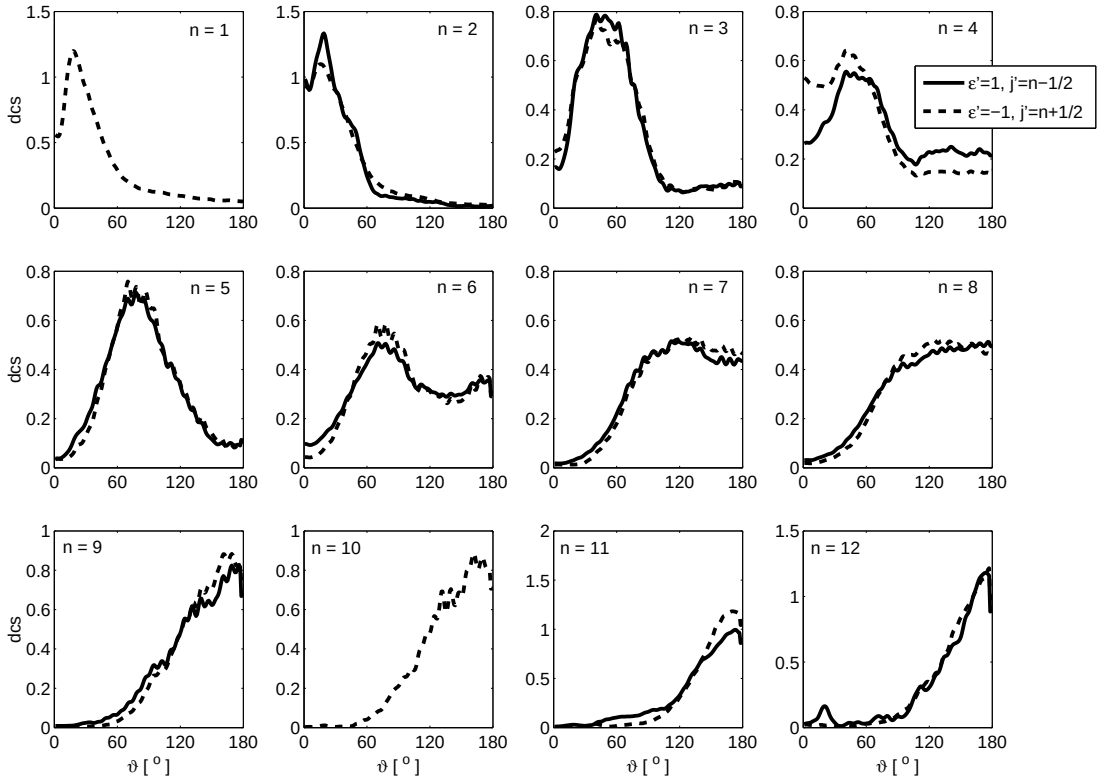

Figure 6.6: Differential cross sections for (He - NO) scattering into $\Omega' = \frac{1}{2}$. The differential cross sections are plotted per parity pair and normalized such that the integral $\int$ dcs $d\vartheta = 1$.

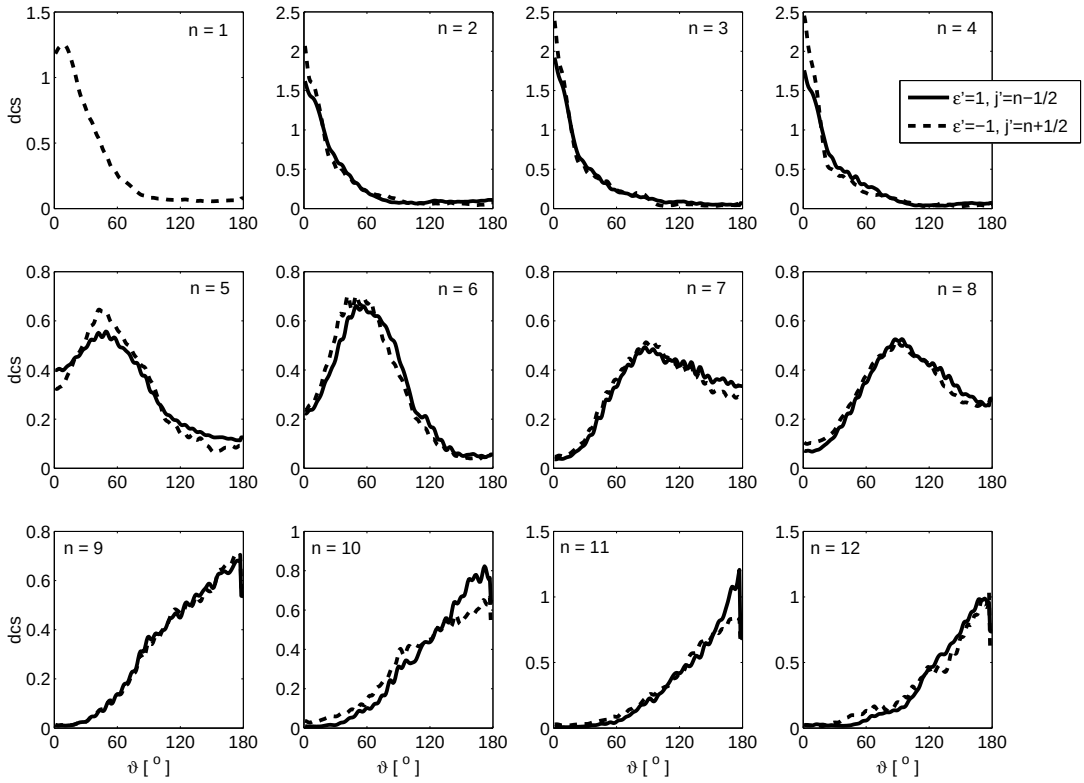

Figure 6.7: Differential cross sections for (He - NO) scattering into $\Omega' = \frac{3}{2}$. The differential cross sections are plotted per parity pair and normalized such that the integral $\int$ dcs $d\vartheta = 1$.

Experimental differential cross sections (as published in Ref. [11]) for He-NO collisions are plotted (grouped per parity pair) in Figs. 6.6 and 6.7 to show the presence of parity pairs and to allow for a systematic comparison with those for D_2-NO scattering in Figs. 6.3 and 6.4. In agreement with the CC calculations [11] of the He-NO differential cross sections, the angular dependence of the experimental cross section within a parity pair n have been to be remarkably similar for both collision systems.

In addition to parity pairs n of the differential cross sections of D_2-NO and He-NO, as plotted in Figs. 6.3 - 6.7 there is also some resemblance between the differential cross section of $n = 1$ and $n = 2$, of $n = 3$ and $n = 4$, etcetera. These pairs can be labeled via k, where $k = n/2$ if $n =$"even" and $k = (n+1)/2$ if $n =$"odd". See for an example of such a pair the images for $j' = 4.5, \epsilon = 1$ and $j' = 5.5, \epsilon = 1$. Although the images turn out to be quite similar for these cases, significant differences between the resembling differential cross sections are present. For excitation to states with $n =$ "even" slightly more forward scattering is observed than for $n =$ "odd". This becomes most clear in the cross sections for $n = 5$ and $n = 6$ in Fig. 6.6.

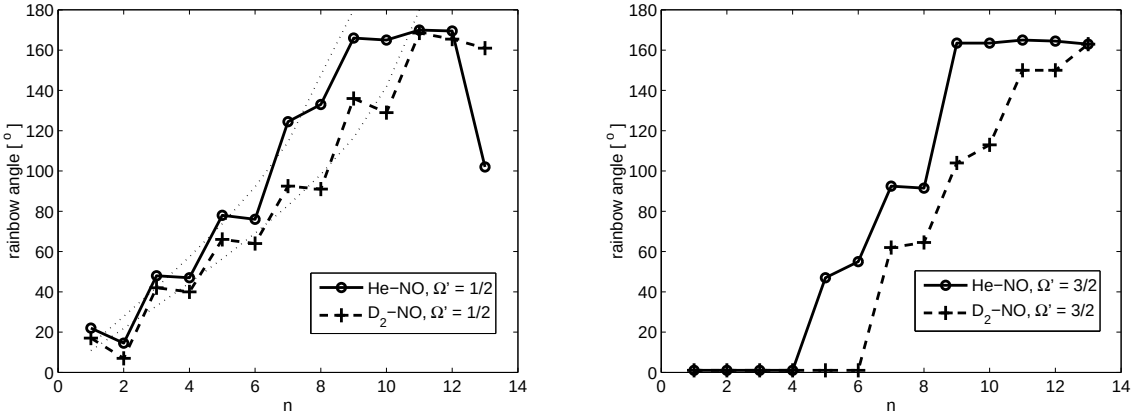

Figure 6.8: The positions of the rotational rainbows for each parity pair $j' + \epsilon'/2$ are plotted for both D_2 - NO and He - NO scattering. The left panel shows the rainbow maxima for spin orbit conserving ($\Omega' = 1/2$) collisions, while the right panel shows the rainbow maxima for spin orbit changing ($\Omega' = 3/2$) collisions. The results are averaged over both components of the pairs. To guide the eye, the points for He-NO and D_2-NO are connected via lines.

Upon a close inspection of the finest details of Figs. 6.3 - 6.7 one notices imperfections that can mostly be attributed to statistical uncertainties in the ion images. Especially in the near forward direction the differential cross sections are often imperfect due to background subtraction and due to diffraction which shows up as a rapid oscillation beyond our angular resolution. These oscillations contribute only for $n \leq 4$ as can be seen in the CC results of Ref [11]. The false maximum in the backward direction (ϑ very close to 180^o) can be caused by a small inaccuracy in the extraction procedure. Overall there is excellent agreement between the differential cross sections within each parity pair.

6.4.2 Rotational rainbows

At first sight, there is not much difference between the differential cross sections for He-NO and D_2-NO. Both cases clearly exhibit the pairwise behavior and range from forward to backward scattering when Δj is raised. The D_2-NO cross sections are slightly more forward scattered than those of He-NO. The scattering angles at which the measured differential cross sections of He-NO and D_2-NO reach their maximum angle ϑ_m are plotted in Fig. 6.8 as a function of the parity pair number n. These maxima ($\vartheta_m(n)$) reflect the classical rotational rainbow angles ($\vartheta_r(\Delta J)$). Here ΔJ is the (classical) continuous equivalent of the quantum step Δj. The angle $\vartheta_r(\Delta J)$ corresponds to the minimum scattering angle at which a specific amount of incoming translational momentum is transformed into molecular rotation. At $\vartheta = \vartheta_r(\Delta J)$, the classical (double) differential cross section $\frac{d^2\sigma}{d\omega d\Delta J}$ becomes singular. This can be understood by considering the scattering from a (non-rotating) nearly convex hard shell [118]. A schematic representation of such a hard shell scattering process is shown in Fig. 6.9.

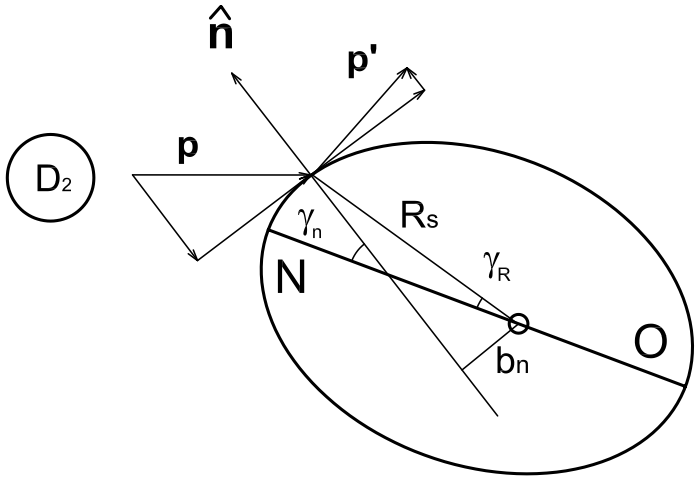

Figure 6.9: Schematic representation of a hard ellipsoid NO shell colliding with a D_2 molecule. The incoming linear momentum p is decomposed into a component parallel and one perpendicular to the hard shell. The parallel component is conserved during collision, while the perpendicular one is partly transferred into rotation.

The initial conditions at which ΔJ is transferred into rotation are uniquely defined when one specifies γ_n: the angle between the surface normal $\hat{\boldsymbol{n}}$ and the molecular axis $\hat{\boldsymbol{r}}$ at the impact position of the atom onto the molecular shell. The incoming momentum is given by $\boldsymbol{p} = \mu \boldsymbol{v_{rel}}$, with μ the reduced mass and $\boldsymbol{v_{rel}}$ the relative velocity of the system. At the point of impact $\boldsymbol{R_s}$, the perpendicular component of the incoming momentum $\boldsymbol{p}_\perp = (\boldsymbol{p}\cdot\hat{\boldsymbol{n}})\hat{\boldsymbol{n}}$ is responsible for ΔJ. The perpendicular component of the momentum after collision $\boldsymbol{p}'_\perp$ points opposite to that before collision: $\hat{\boldsymbol{p}_\perp}' = \hat{\boldsymbol{p}'_\perp}$. The parallel component of the momentum $\boldsymbol{p}_{||} = \boldsymbol{p} - \boldsymbol{p}_\perp$ remains conserved during the collision $\boldsymbol{p}'_{||} = \boldsymbol{p}_{||}$. The magnitude of the rotational excitation is proportional to the effective impact parameter b_n at the point of impact [119]. This impact parameter is the shortest distance between the surface normal and the center-of-mass of the molecule.

For a convex shell, there are three values of γ_n at which $b_n = 0$: two at each end of the molecule ($\gamma_n = \gamma_R = 0, \pi$) and one near the equator ($\gamma_n = \gamma_R \approx \pi/2$). The angle γ_R depicts the position vector of the shell $\boldsymbol{R_s}$ with respect to the center-of-mass of the molecule. In between these zero positions of b_n there are two maximum values, one on each side of the molecule, that allow for maximum rotational excitation [120]. In the case of an ellipsoid [119] this is at $b_n = A - B$ where A and B are its major and minor axis, respectively. All together this implies that there are (except at $b_n = 0$ and at its maximum value) four angles (γ_n) that lead to the same value of b_n.

From conservation of energy and angular momentum it can be shown that:

$$k_\perp \equiv p_\perp/\hbar = \frac{1 + \mu b_n^2(\gamma_n)/I}{2b_n(\gamma_n)}\ \Delta J \tag{6.4}$$

$$\text{and} \quad k'_\perp = \sqrt{k_\perp^2 - \mu \Delta J^2/I} \tag{6.5}$$

where I is the moment of inertia of the molecule. At fixed values of ΔJ and incoming momentum k, the smallest scattering angle occurs at the maximum value of b_n. Note that since $k_{||}$ is conserved, the scattering angle ϑ increases with $k_\perp$. At backward scattering ($\vartheta = 180^o$), the substitution of $k = k_\perp$ determines the lower limit of b_n for which this transition is possible. The scattering angle ϑ relates to $\boldsymbol{k}$ as:

$$\vartheta = \arctan\left(\frac{k_\perp}{k_{||}}\right) + \arctan\left(\frac{k'_\perp}{k_{||}}\right) \tag{6.6}$$

Four values of γ_n (leading to the same value of b_n) contribute to $\frac{d^2\sigma}{d\omega d\Delta J}$ at the same scattering angle ϑ. In general, the differential cross section becomes the sum over these four contributions:

$$\frac{d^2\sigma}{d\omega d\Delta J} \propto \sum_{i=1}^{4} \frac{d^2\sigma(\gamma_{n,i})}{d\omega d\Delta J} = \sum_{i=1}^{4} \frac{d^2\sigma(\gamma_{n,i})}{d\omega_n d\Delta J} \frac{d\omega_n}{d\omega}. \tag{6.7}$$

Note that $d\omega = \sin\vartheta d\vartheta d\varphi$ and $d\omega_n = \sin\gamma_n d\gamma_n d\varphi_n$.

A singularity in the (double) differential cross section appears when $d\omega/d\omega_n = 0$. This derivative can be expressed as:

$$\frac{d\omega}{d\omega_n} \propto \frac{sin\vartheta}{\sin\gamma_n} \frac{d\vartheta}{d\gamma_n} = \frac{sin\vartheta}{\sin\gamma_n} \frac{d\vartheta}{db_n} \frac{db_n}{d\gamma_n}. \tag{6.8}$$

The singularity occurs if $\frac{db_n}{d\gamma_n} = 0$, in other words, for collisions onto the two maximum values of the effective impact parameter. The classical differential cross section for a specific value of ΔJ at its smallest scattering angle (ϑ_r) will approach infinity. For the special case of an ellipsoid hard shell, the rotational rainbow angle ϑ_r takes place at [119]:

$$\sin\left(\frac{1}{2}\vartheta_r\right) = \frac{\Delta j}{2k(A-B)} \tag{6.9}$$

Previous theoretical studies [121–123] at comparable collision energies and similar anisotropic systems, conclude that the classical rotational rainbow angle ϑ_r is usually substantially smaller than the scattering angle found for maximum scattered intensity. This effect is especially pronounced at large scattering angles.

To extract θ_m, the scattering angle of the maxima from the experimental results, the differential cross sections (in Figs. 6.3-6.7) were smoothed. A zero-phase (forward and reverse) filtering routine was applied to remove fast oscillations in the differential cross sections. Differential cross sections obtained from three ion images (for D_2-NO with $j' = 3.5, \Omega' = 1/2, \epsilon' = 1$, for D_2-NO with $j' = 9.5, \Omega' = 1/2, \epsilon' = -1$ and for for He-NO with $j' = 7.5, \Omega' = 1/2, \epsilon' = 1$) were omitted, mainly because of experimental inaccuracies. The decision to leave these cross sections out were based on three criteria: the maxima of the extracted differential cross section are 1. far away from the result via a different spectroscopic branch, 2. far away from the corresponding theoretical value [11] and 3. far away from the rainbow maximum of the differential cross sections for other final rotational states within a parity pair. These experimental differential cross sections are nevertheless included in (the calculations for) Figs. 6.3 - 6.7. Note that most of the data points in

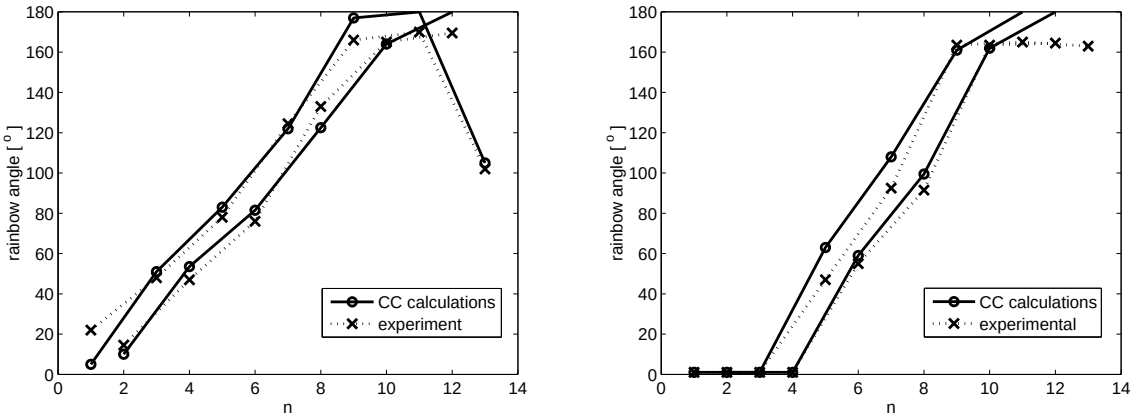

Figure 6.10: Experimental He-NO rainbow maxima from Fig. 6.8 are compared to values from CC calculations [11]. Results for spin orbit conserving transitions are found in the left panel, while the right panel shows results for spin orbit changing transitions. The maxima for parity changing transitions ($j' + \epsilon'/2 =$ odd) are at larger scattering angles than those for parity conserving transitions ($j' + \epsilon'/2 =$ even). To elucidate this, separate lines are drawn that connect the data points for both cases. The filtering of the data causes a slight underestimation of the scattering angle with maximum differential cross section when it is close to 180^o.s

Figs. 6.8 and 6.10 are based on four separate differential cross sections. Typically two spectroscopic transitions are available for one rotational state and two rotational states form a parity pair.

The observation that D_2-NO collisions yield more forward scattering than He-NO collisions could indicate a more anisotropic interaction potential. On the other hand, ion images for $\Delta j > 12.5$ could not be obtained, as their cross section were too small for both He-NO and D_2-NO. This opposes the explanation of a larger anisotropy causing more forward scattering for D_2-NO: larger anisotropy would allow classically for a larger Δj. No PESs are available for D_2-NO collisions, but detailed PESs are available for He-NO collisions [114]. Inspection of the V_{sum} contour plot in Ref. [6] gives (at E = 500 cm^{-1}) for a collision onto the N-end $B = 4.40\ a_0$, $A_N = 5.65\ a_0$ and for a collision onto the O-end $A_O = 5.25\ a_0$. To estimate the difference in anisotropy between the He-NO and D_2-NO potentials, Eq. 6.9 has been fitted to the experimental data for spin orbit conserving collisions in Fig. 6.8. For now we approximate $\Delta J \approx j' + \epsilon'/2$. This fit yields for He-NO $(A - B)_{He-NO} = 0.76\ a_0$ and for D_2-NO $(A - B)_{D_2-NO} = 0.93\ a_0$. The $(A - B)$ values from this rough estimation are not too far away from the values derived from the *ab initio* potential. However, from this simple (classical) view, one would assume that double rainbows are present: recall that there is a maximum of b_n on both the N-end and on the O-end of the NO molecule. Such double maxima were indeed observed for Ne-CO scattering [124, 125] and attributed to this effect, but remain absent in this work. The Ne-CO system is more asymmetric than He-NO as the C-end extends much more from the center-of-mass compared to the O-end (Ne-CO), than the N-end extends compared

to the O-end (He-NO).

Westley et al. [102] did not observe double maxima for D_2-NO and He-NO scattering (note that both components of the Λ-doublet were present in the incoming NO beam) and concluded that the asymmetry was too small to resolve these two rainbows. From the current results however, one would expect that their differential cross sections contain four maxima. Not only one for each side of the molecule, but also for the parity conserving component and the parity changing component. If both components of the Λ-doublet are present before collision, one cannot distinguish between parity changing and parity conserving transitions (for example $j = \frac{1}{2}, \epsilon = 1 \rightarrow j' = \frac{13}{2}, \epsilon' = 1$ and $j = \frac{1}{2}, \epsilon = -1 \rightarrow j' = \frac{13}{2}, \epsilon' = 1$ show up in the same ion image). Eq. 6.3 shows that both curves with labels $n = 6$ and $n = 7$ contribute to the same ion image when both components of the Λ-doublet of $j = \frac{1}{2}$ are populated before collision. From Fig. 6.8 it becomes clear that the maxima in the cross section of the two contributing curves can be far ($> 40^o$) apart from each other.

In Fig. 6.10 the experimentally observed maxima for He-NO scattering are compared to those obtained in CC calculations [11]. In this figure, the points for parity changing transitions (n = odd) are connected by a line (for reasons of clarity) as are those for parity conserving (n = even) transitions. We conclude that parity changing transitions show a more forward scattered maximum of the cross section than parity conserving ones. The molecule appears to be less anisotropic for parity changing collisions than for parity conserving ones.

In contrast to Westley et al. [102], we observe that the D_2-NO maxima of the differential cross section are substantially more forward scattered than those of He-NO in case of spin-orbit changing transitions (see Figs. 6.8 and 6.10). For both He-NO and D_2-NO the spin-orbit changing collisions, ϑ_m remains small up to a large value of n, after which the differential cross section changes to completely backward scattering very rapidly. It is impossible to fit such a curve using Eq. 6.9. Overall we conclude that spin-orbit changing collisions at the same value of n turn out to be more forward scattered than in the case of spin-orbit conserving transitions.

6.5 Concluding remarks

Differential cross sections for fully quantum state selected NO molecules ($j = \frac{1}{2}, \Omega = \frac{1}{2}, \epsilon = -1$) colliding with D_2 are obtained using the velocity-mapped ion-imaging technique. The detection step is fully quantum state resolved (j', Ω', ϵ'), which allows for an investigation of the effect of changing and conservation of parity on the differential cross section. The D_2-NO differential cross sections for various final states are plotted in Figs. 6.3, 6.4 and 6.5. In both the spin-orbit conserving and changing case, He-NO collisions show maxima of the differential cross sections at larger scattering angles than those found in the present study (D_2-NO). This possibly could indicate a larger anisotropy of the D_2-NO shell compared to the He-NO potential, but in this would also allow for excitation to higher rotational states which is not observed.

Parity pairs are observed in the differential cross sections for both spin-orbit conserving and spin-orbit changing collisions. The present results show a significant difference

between differential cross sections for scattering into the upper and lower component of the Λ-doublet of NO. The angular dependence of the cross sections is found to depend on the parity pair number $n = j' - \epsilon\epsilon'/2$. For excitation to pairs of neighboring j' states with the same parity, the angular dependence of the cross section turns out to be similar, what indicates that the differential cross section is proportional.

Is was shown that there exists a large difference between maxima (rainbow positions) for parity conserving and for parity changing transitions. If no full (hexapole) state selection is applied, this means that 4 rotational rainbows might contribute to the differential cross sections: two for scattering from both sides of the molecule, one for parity conserving transitions and one for parity changing transitions. It should be explored in future experimental studies if these four maxima can be observed separately. Parity propensity rules are expected to become less pronounced with increasing anisotropy of the interaction potential.

Chapter 7

Quasi Quantum Treatment

7.1 abstract

Rotationally inelastic scattering of rare gas atoms and oriented NO molecules exhibits a remarkable alternation in the sign of steric asymmetry between even and odd changes in rotational quantum number. This effect has also been found in full quantum mechanical scattering calculations. However, until now no physical picture has emerged for the alternation. In this work, a newly developed Quasi-Quantum Treatment (QQT) provides a first demonstration that quantum interferences between different orientations of the repulsive potential (that are present in the oriented wave function) are the source of this alternation. Further, from application of the treatment to collisions of non-oriented molecules a previously unrecognized propensity rule is derived. The angular dependence of the cross sections for excitation to neighboring rotational states with the same parity is shown to be similar except for a pre-factor. Experimental results are presented to support this rule. Unlike conventional quantum mechanical (or semiclassical) treatments, QQT requires no summation over the orbital angular momentum quantum number l or integration over the impact parameter b. This eliminates the need to solve large sets of coupled differential equations that couple l and rotational state channels among which interference can occur. The QQT provides a physical interpretation of the scattering amplitude that can be represented by a Legendre moment. Application of the QQT on a simple hard-shell potential leads to near-quantitative agreement with experimental observations.

7.2 Introduction

Inelastic scattering of open shell molecules provides detailed information on collision induced energy transfer, necessary for understanding fundamental processes in chemical reactions [35, 104]. It has been a long standing goal in molecular sciences to steer chemical reactions and for this it is a prerequisite to understand and predict the outcome of a reactive encounter. One pathway to achieve this goal is to exploit nature's preference for directionality and to control (steer) a reaction by orienting molecules before they collide and eventually react.

Measurements of rotationally inelastic scattering of rare gases with oriented NO molecules

- i.e. N-end or O-end collisions - have shown a large dependence on the initial orientation [1,2,5,6,16,45]. This dependence can be expressed by the molecular steric asymmetry ratio (S):

$$S_{i\to f} = \frac{\sigma_{R-NO} - \sigma_{R-ON}}{\sigma_{R-NO} + \sigma_{R-ON}}, \tag{7.1}$$

in which σ_{R-NO} and σ_{R-ON} denote the cross sections for rotational energy transfer from the initial (i) to final (f) state when the rare gas atom R impinges onto the N-end or the O-end, respectively.

In experiments described in Refs. [2, 5, 6, 16], a hexapole has been used to state-select NO in the upper component ($\epsilon = -1$) of the Λ-doublet of the $^2\Pi_{1/2}$ rotational ground state ($j = 1/2$), where ϵ is the symmetry index ($\epsilon = -1, 1$) and j the rotational angular momentum quantum number. The NO molecules are subsequently oriented in a homogeneous electrostatic field. When a beam of Ar or He crosses the beam of oriented NO, collisions induce rotational excitation of the NO molecules from the rovibrational ground state to higher rotational levels ($j = \frac{1}{2}, \overline{\Omega} = \frac{1}{2}, \epsilon \to j', \overline{\Omega}', \epsilon'$). Here $\overline{\Omega}$ is (the absolute value of) the projection of j on the molecular axis. Laser Induced Fluorescence (LIF) was used to measure the ratio of inelastic collision cross sections in the two orientations in these experiments [2, 5, 6].

Until now, no clear physical explanation could be given for the observed dependence of $S_{i\to f}$ on the final rotational state of the NO molecule: collisions with an odd change in rotational quantum number $\Delta j = j' - j$ have a strong preference for collisions on the N-end, whereas final rotational states with even Δj result mostly from O-end collisions. A full quantum treatment (using HIBRIDON [1, 6, 59]) yields a fair agreement with the observed orientation dependence of the total cross section, but provides no understanding of the undulatory dependence of S on Δj [54]. In conventional scattering calculations the desired cross sections are obtained from multiple summations over products of T-matrix elements and provide no intuitive picture of the underlying collision propensity. Theoretical exact close coupling (CC) calculations and experimental results are presented in Fig. 7.1 to illustrate the dependence of S on Δj.

Alexander and Stolte [1] showed that the undulatory behavior of S is insensitive to the angular dependence of the long range part of the Ar-NO potential. Its most prominent features are governed by the anisotropy of the repulsive part of the potential, to which S is very sensitive. However, Alexander and Stolte [1] did not succeed in establishing an explanation for the observed alternation of $S_{i\to f}$ as a function of $\Delta j = j' - j$, nor to provide a clear link between this behavior and the shape of the anisotropic potential. In this paper we will explain the observed steric effects by introducing a Quasi Quantum Treatment (QQT) of the collision problem. The alternation between N-end and O-end preference is demonstrated in this work to correspond to a quantum interference phenomenon between scattering events from different molecular orientations.

The conventional exact CC solution of the scattering problem of a rare gas atom R and a hetero nuclear rigid diatomic (NO) requires the expansion of the incoming plane wave e^{ikZ} into an infinite sum of Legendre polynomials $P_l(\cos\theta)$, where θ is the scattering angle. Each $P_l(\cos\theta)$ is multiplied by an incoming and outgoing spherical wave $e^{\pm i(kR - l\pi/2)}/(kR)$ to yield the proper plane wave. The absolute value of the position vector is written as R,

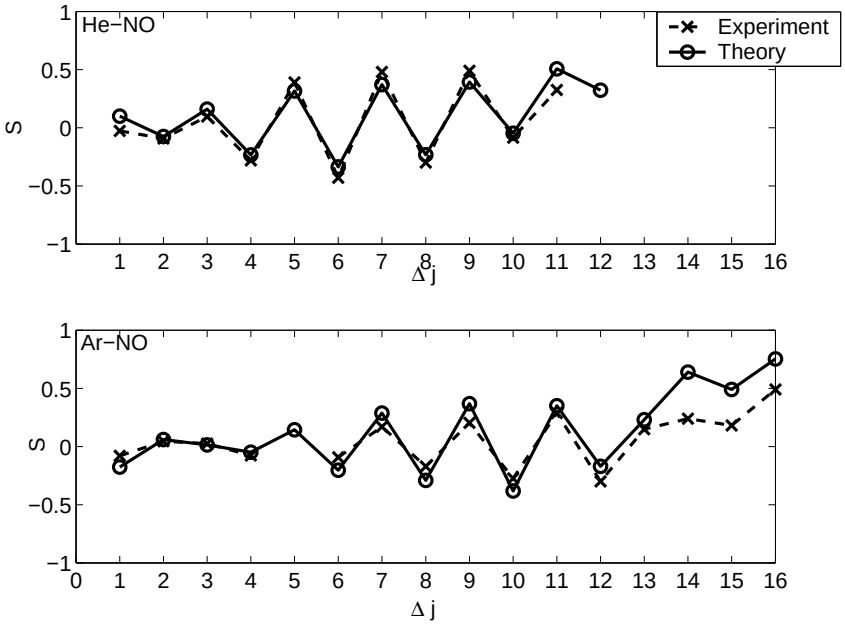

Figure 7.1: The dependence of the observed and theoretical steric asymmetry ratio on the rotational excitation $\Delta j = j' - j$ with $\overline{\Omega}' = 1/2, \epsilon' = -1$ is plotted for He colliding with NO at $E_{tr} = 514$ cm^{-1} (top) [6] and for Ar colliding with NO at $E_{tr} = 475$ cm^{-1}(bottom) [16]. If collisions onto the N-end have a larger cross section for excitation to a certain rotational state, S is positive and vice versa. The experimental steric asymmetry SA has been multiplied with -1 to match the plotted theoretical (HIBRIDON) result $S_{i\to f}$ [6] as well as a simple ball-and-stick model [45]. This convention is used throughout this chapter, which leads to a sign of S that for Ar-NO collisions opposes the predictions of Ref. [2]. Ar-NO calculations in Ref. [2] yield a sign of S that is consonant with experimental results, but opposes the ball and stick model and the sign of S from recent (He-NO) CC calculations [6]. There still is an unresolved sign discrepancy between theory (HIBRIDON) and experiment as discussed in detail in Refs. [45] and [87].

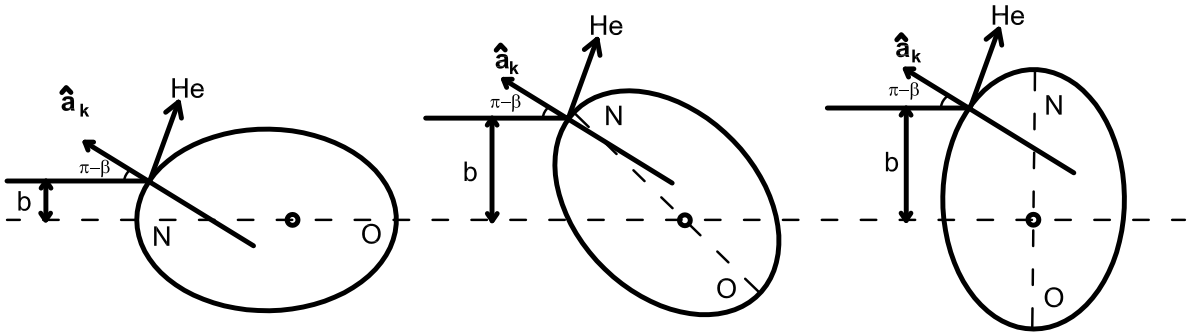

Figure 7.2: All orientations are present in the oriented wave function. Constructive and destructive interference between these waves will occur dependent on the difference in path length. The potential can cause scattering under a certain angle for many different impact parameters. Note that for a hard shell as drawn here, the kinematic apse $\hat{\boldsymbol{a}}$ coincides with the surface normal $\hat{\boldsymbol{n}}$.

the orbital quantum number as l and the incoming wave number k is given by:

$$k \equiv \frac{1}{\hbar} \sqrt{\frac{2E_{tr}}{(m_{NO}\ m_R)/(m_{NO}+m_R)}}. \tag{7.2}$$

The semi classical impact parameter b (see Fig. 7.2) relates to the orbital angular momentum quantum number l as

$$b \approx \frac{l+\frac{1}{2}}{k}. \tag{7.3}$$

The quantum number l couples with the NO rotational quantum number j to yield the total angular momentum quantum number J. Both J and the overall parity of the total wave function are conserved by the scattering Hamiltonian. To solve the He-NO inelastic scattering problem at $E_{tr} \approx 500$ cm^{-1}, the maximum value of J becomes as large as 120.5 [11, 60]. At each value of J one has to solve a large set of coupled differential equations that contain all relevant scattering channels $j, l, \overline{\Omega}, \epsilon$ that influence the outcome of the scattering process. In the example of He-NO, the number of coupled differential equations that need to be solved numerically is typically as large as 1300 at a single value of J and parity [60]. State of the art computational possibilities still exclude exact calculations on molecule-molecule scattering for which there are many more channels. An exception is the case of low collision energies or large splitting between the rotational states (H_2-like molecules). Conventional quantum treatments provide good qualitative results, but these elaborate numerical methods yield little insight into the actual physics behind phenomena and their behavior under different circumstances. Calculation times are often too long to adjust the input parameters and learn the behavior of the system as function of these parameters. To overcome theoretical limitations, a large number of approximative methods to solve inelastic scattering problems have been developed since the 1960s [65]. Among these, the semiclassical version of the infinite order sudden (IOS) approximation has turned out to be particularly useful as it facilitates rapid calculation [126–129].

Generally speaking there are two types of sudden approximation. In the first one, the molecular axis is assumed to remain fixed in space and the scattering paths are fully determined by the isotropic part of the potential. A rotational transition probability is treated as a time-dependent perturbation resulting from the anisotropic part of the potential. The exponential form of the S-matrix is not approximated, but the resulting phase shifts are from a first order approximation of the anisotropy of the potential. The angle between the specified molecular axis and the position vector $\boldsymbol{R}$ between the center-of-masses of the atom and molecule is the main collision variable [9, 130, 131].

Following Curtiss [132], Pack [133] and McGuire and Kouri [134] described collisions of atoms and diatomics in terms of body fixed or rotating coordinate frames. In this second type of sudden approximation, the molecular axis $\boldsymbol{r}$ is assumed to remain fixed in respect to $\boldsymbol{R}$ and not in space ($\hat{\boldsymbol{R}} \cdot \hat{\boldsymbol{r}} \equiv \cos\gamma$). The centrifugal term in the Schrödinger equation is simplified by approximating $\bar{l} = l$ and $l' = \bar{l}$ (with l and l' the initial and final orbital angular momentum), which drastically reduces the number of coupled equations. This decoupling of the centrifugal barrier is also referred to as the "centrifugal sudden approximation". It leads to a phase shift calculation that is of infinite order in the anisotropy of the potential for each orientation angle γ of the molecule. When the energy of the rotational states is taken into account, one refers to this method as the "Coupled States" (CS) approximation. When this energy is ignored, one speaks about the "Infinite Order Sudden" (IOS) approximation.

Nowadays the IOS approximation is often applied when one is prevented from carrying out numerically demanding close coupling calculations for practical reasons. The IOS and CS approximations usually yield satisfactory results in the calculation of m, m' degeneracy averaged collision cross sections, but are well known to err in predicting the m, m' or steric dependence of the inelastic collision cross section (m and m' are the projections of the rotational angular momentum $\boldsymbol{j}$ on a space fixed axis). This shortcoming can be alleviated by assuming a hard-shell-like "Point Contact Interaction" (PCI) at the turning point [71, 135]. Later Khare, Kouri and Hoffman [107, 136] showed explicitly that there is a propensity for preserving j_z when using an apse (geometric or kinematic) as quantization axis. The two apses coincide for elastic collisions and point about parallel to $\boldsymbol{R}$ at the turning point in the case of a near-isotropic (near-spherical) potential. The kinematic apse (KA) direction is that along which momentum is transferred in the hard shell approximation. In general, the kinematic apse is Δj dependent while the geometric apse is not. It was shown that one can obtain reasonable differential cross sections quantized in the space-fixed frame, by calculating and transforming only the $\Delta m = 0$ scattering amplitude from the KA frame for a given $j \rightarrow j'$ transition [112, 136].

A distinctive Quasi Quantum Treatment (QQT) is presented in the current study, the l, l' and J quantum numbers are replaced by angular variables that provide a direct connection between the incoming and outgoing states and momenta. The present work builds on pioneering work of Hoffman [137], who developed a classical kinetic theory for a mixture of dilute gases of rigid convex molecules. Molecular orientation variables, not impact parameters, were used to evaluate the collision integrals. Evans and coworkers [138, 139] succeeded in extending Hoffman's angular parametrization to the calculation of the classical bimolecular rate constant, the energy-dependent reaction cross section and the steric dependence of the differential cross sections for general diatom-diatom

collisions. In the present study, we will exploit the l, l', J replacement by angular variables to gain understanding and to calculate differential cross sections and steric asymmetries for scattering on anisotropic (heteronuclear) potentials. The straightforward expressions derived in this way provide an intuitive basis for understanding the source of the observed steric asymmetry.

This paper is organized in 6 sections and an appendix. Section 7.3 describes the main ideas behind the QQT and applies it to both fully state selected, non-oriented molecules (section 7.3.1) and to oriented molecules (section 7.3.2). A previously unrecognized propensity rule for the differential cross section follows from this treatment. In section 7.4 a hard shell approximation is introduced to obtain the molecule fixed scattering amplitude. This scattering amplitude, which contains the phase shift, is necessary to obtain quantitative results from the QQT. The quantitative QQT results are discussed in section 7.5 and compared to experimental results. Some conclusions and a future outlook are given in section 7.6. In the appendix, a short discussion is given concerning the impact the QQT has on the discrepancy in the sign of the steric asymmetry ratio [45, 87]. This discussion directly relates to our results but does not belong to the central focus of the present study.

7.3 Quasi Quantum Treatment

The QQT aims at the simplification and approximation of exact quantum treatments. It presents an intuitive basis for understanding the physics behind the steric asymmetry and - more generally - the relation between inelastic collisions and the anisotropy of the inter-molecular potential.

For scattering trajectories (rays) to interfere, the trajectories from a single initial state need to be scattered under an identical angle and into the same final molecular state. The impact parameter b gives the distance between a straight line along the the trajectory of the incoming particle long before collision and the (center-of-mass) origin the collisions system that resides at the center-of-mass of the NO molecule (see Fig. 7.2). The orbital angular momentum before collision (with quantum number l) is fixed by $\boldsymbol{k}$ and the impact parameter b. Traditionally, to calculate differential cross sections, a summation over l is made that in the classical limit can be replaced by integration over $b \approx l/k$ (for example see Ref. [126]). For elastic (atom-atom) scattering on a Lennard-Jones type of the potential, there are only three trajectories with different impact parameters that lead to the same scattering angle [140] and thus interfere. One of the three trajectories is mostly caused by the repulsive part of the potential, the other two are due to the attractive part [140].

In the case of an anisotropic potential, even when neglecting the attractive part, the repulsive part of the potential allows scattering into a certain angle for many impact parameters. This is demonstrated in Fig. 7.2 using a hard egg-shaped potential. Solving this scattering problem numerically involves a large set of coupled $(j, l, \epsilon, j', l', \epsilon')$ differential equations at each value of J, which makes these treatments time-consuming [65, 141]. Calculating steric asymmetries for the He-NO collision system with current technology takes a set of several parallel processors several days [60].

Approximations can be introduced to reduce the size of the calculations. The projec-

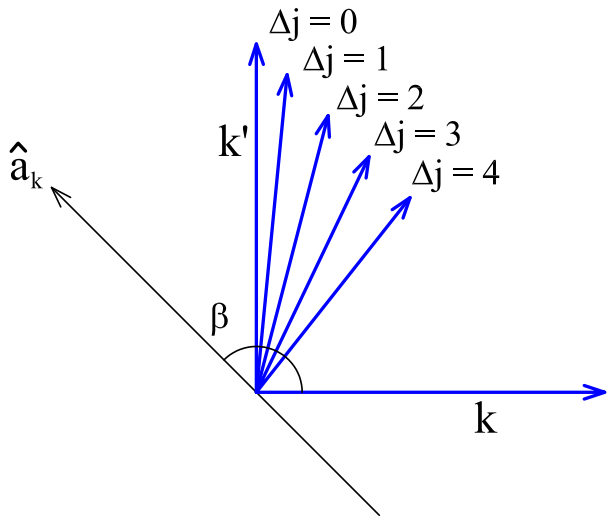

Figure 7.3: Part of the incoming momentum $\boldsymbol{k}$ is transformed into rotation. The orientation of the apse (β) and the translational energy loss due to rotational excitation Δj fixes the scattering angle.

tion m_a of the total angular momentum $\boldsymbol{j}$ on an apse $\hat{\boldsymbol{a}}$ is approximately conserved during the collision, when the repulsive part of the potential dominates (in the sudden approximation). Apse quantization was proposed and demonstrated to be a feasible approximation by Khare et al. [107,136,142]. Later on, Meyer et al. experimentally showed that the apse approximation yields good quantitative results for (among others) He-NO collisions [108] and Ne-NO collisions [109]. In this work, the kinematic apse will be used, which - in contrast to the geometric apse - relies on the final rotational state. The kinematic apse is defined as [107]:

$$\hat{\boldsymbol{a}}_k = \frac{\boldsymbol{k}' - \boldsymbol{k}}{|\boldsymbol{k}' - \boldsymbol{k}|}. \tag{7.4}$$

The spherical angles which define the direction of the kinematic apse in the collision frame ($\hat{\boldsymbol{Z}} \equiv \hat{\boldsymbol{k}}$) are defined as β and α. The orientation of the molecular axis with respect to the kinematic apse is given by the spherical angles γ_a and ϕ_a.

In the QQT the commonly-used sum over l (or integral over the impact parameter b) is replaced by an integral over the apse angles β and α. The scattering angle is determined fully by the angle of the kinematic apse with the incoming momentum and the final rotational state. When one integrates over b, scattering into the same angle and thus interfering contributions originate from many values of b (see Fig. 7.2), making the integral cumbersome to evaluate. Fig. 7.3 schematically shows the scattering angle of the outgoing momentum for different final rotational states at a *single* direction of kinematic apse. Note that $\frac{1}{2}\pi \leq \beta \leq \pi$ for scattering with $k' \leq k$. No interfering contributions from different apse orientations occur as there is a direct relation between apse angle and scattering angle.

To find the relation between the scattering angle (θ), the incoming momentum (k)

and the angle between apse and incoming momentum (β), the energy of each rotational level of the NO-molecule $E(j)$ has to be known. The amount of kinetic energy that is converted into rotation is given by:

$$E(j') = \frac{1}{2\mu}(k^2 - k'^2), \tag{7.5}$$

where μ is the reduced mass. In experiments of Refs. [2, 5, 6] and [11] the molecules are prepared in the upper component of the Λ-doublet of the rotational ground state ($j = \frac{1}{2}, \overline{\Omega} = \frac{1}{2}, \epsilon = -1$). In collisions with rare gas atoms, the NO molecules are excited to higher rotational states ($j', \overline{\Omega}', \epsilon'$). The spin-orbit constant A_0 and the rotational constant B_0 used to calculate the rotational energy of a NO molecule in the $\nu = 0$, $X^2\Pi$ state are $A_0 = 123.13\ cm^{-1}$ and $B_0 = 1.6961\ cm^{-1}$ [17].

In the current treatment the attractive part of the rare gas - NO interaction will be neglected; the maximum well depth for He-NO and Ar-NO (25 and 116 cm^{-1} respectively [56, 69]) is much smaller than the kinetic energy compared to a collision energy of ≈ 500 cm^{-1}. Only spin-orbit conserving $\Omega' = \Omega$ transitions are considered. Spin orbit changing transitions are expected to be governed by the difference potential energy surface V_{diff} [1] which is not included in the present treatment.

The first goal is to calculate the state-to-state differential cross section, $d\sigma/d\omega$, which is related to the dimensionless scattering amplitude by:

$$\frac{d\sigma_{j,m,\Omega\to j',m',\Omega'}}{d\omega} = \frac{1}{k^2}|f_{j,m,\Omega\to j',m',\Omega}(\vartheta,\varphi)|^2. \tag{7.6}$$

The scattering amplitude is defined as the coefficient of the outgoing wave in

$$\Psi \propto \Psi_{j,m,\Omega}e^{i\boldsymbol{k}\cdot\boldsymbol{R}} + \sum_{j',m'} \Psi_{j',m',\Omega} f_{j,m,\Omega\to j',m',\Omega}(\vartheta,\varphi)\frac{ie^{ik'R}}{\sqrt{kk'}R}. \tag{7.7}$$

In Ref. [143], it was shown that Eq. 7.7 is a proper asymptotic solution of the Schrödinger equation. Integration of the differential cross section over $d\omega = \sin\vartheta\ d\vartheta\ d\varphi$ provides the total cross section $\sigma_{j,m,\Omega\to j',m',\Omega}$.

The conventional scattering amplitude $f_{j,m,\Omega\to j',m',\Omega}(\vartheta)$ can be expressed in a newly introduced scattering amplitude $g_{j,m,\Omega\to j',m',\Omega}(\beta)$. The azimuthal angles α and φ are redundant because of cylindrical symmetry; note $\alpha = \varphi$. The scattering amplitudes are related via a Jacobian:

$$f_{j,m,\Omega\to j',m',\Omega}(\vartheta) = \sqrt{\frac{\sin\beta}{\sin\vartheta}\left|\frac{\partial\beta}{\partial\vartheta}\right|}\ g_{j,m,\Omega\to j',m',\Omega}(\beta). \tag{7.8}$$

Note that Eq. 7.8 does not specify the choice of the quantization axis. Recall that the projection of the total angular momentum on the apse (m_a) is (approximately) conserved during the scattering process ($m'_a = m_a$). Including m_a conservation in the calculation leads to an enormous simplification. The scattering amplitude in the apse frame (where the apse $\hat{\boldsymbol{a}}_k$ serves also as quantization axis) is defined as:

$$\begin{aligned} g_{j,m_a,\Omega\to j',m_a,\Omega}(\beta) &= C(\beta)\langle j', m_a, \Omega|\ g_{j\to j'}(\gamma_a;\beta)\ |j, m_a, \Omega\rangle = \\ & C(\beta)\int_0^{\pi}\int_0^{2\pi} \Psi_{j,m_a,\Omega}\ g_{j\to j'}(\gamma_a;\beta)\ \Psi^*_{j',m_a,\Omega}\ \sin\gamma_a\ d\phi_a d\gamma_a. \end{aligned} \tag{7.9}$$

$C(\beta)$ is a normalization factor that is discussed in detail later (see Eq. 7.17). For now we will proceed without quantifying the fixed molecule scattering amplitude $g_{j\rightarrow j'}(\gamma_a;\beta)$ that connects the incoming and outgoing wave functions and carries their phase shift. The angle γ_a of the molecular axis $\boldsymbol{r}$ with the apse $\hat{\boldsymbol{a_k}}$ is assumed to remain fixed during the collision. In section 7.4, a hard shell potential will be used to approximate $g_{j\rightarrow j'}(\gamma_a;\beta)$, but there is no restriction to such a potential. The absolute value of the molecule fixed scattering amplitude is taken as the square root of the apse-dependent classical differential cross section $\frac{d\sigma}{d\omega_a} \equiv \frac{d\sigma}{\sin\beta\ d\beta\ d\alpha}$ that is independent of the final rotational state.

$$|g_{j\rightarrow j'}(\gamma_a;\beta)| = k\sqrt{\frac{\partial^2\sigma(\gamma_a)}{|\sin(\beta)\partial\beta|\ \partial\alpha}}. \tag{7.10}$$

The integration of Eq. 7.9 contains the product of the initial and (complex conjugate of) the final wave function. The rotational wave function can be expressed as [13]:

$$\begin{aligned}\Psi_{j,m_a,\Omega} &= \sqrt{\frac{2j+1}{4\pi}} D^{j*}_{m_a,\Omega}(\phi_a,\gamma_a,0) = \\ &(-1)^{m_a-\Omega}\sqrt{\frac{2j+1}{4\pi}} D^{j}_{-m_a,-\Omega}(\phi_a,\gamma_a,0)\end{aligned} \tag{7.11}$$

The product of the wave functions that appears in the integral of Eq. 7.9 can - after using Eq. 3.116 of Ref. [13] - be contracted to:

$$\Psi^*_{j',m_a,\Omega}\Psi_{j=\frac{1}{2},m_a,\Omega} = \frac{1}{4\pi}\sqrt{j'+\frac{1}{2}}\ \left[P_{j'-\frac{1}{2}}(\cos\gamma_a) + \ \frac{m_a\Omega}{\overline{m_a\Omega}}\ P_{j'+\frac{1}{2}}(\cos\gamma_a)\right] \tag{7.12}$$

Here $\overline{m_a\Omega}$ denotes the absolute value of the product $m_a\Omega$. We first apply this result to fully state selected molecules (as in Ref. [11]) and after that to oriented molecules.

7.3.1 State-selected molecules

The pure parity wave function for an NO molecule in the laboratory frame (neglecting Hund case b mixing) can be written as:

$$|j,m_a,\overline{\Omega},\epsilon\rangle = \frac{1}{\sqrt{2}}\Big[|j,m_a,\overline{\Omega}\rangle + \epsilon|j,m_a,-\overline{\Omega}\rangle\Big]. \tag{7.13}$$

The parity of a wave function is defined by its behavior under parity transformation (inversion), which acts as an unitary operator $\boldsymbol{P}$ on a wave function ψ:

$$\boldsymbol{P}\psi(\boldsymbol{r}) = \psi(-\boldsymbol{r}) = p\psi(\boldsymbol{r}) \tag{7.14}$$

The total parity $p = \pm 1$ of a rotational state (eigenvalue of $\boldsymbol{P}$) is provided by Brown et al. [18]:

$$p = (-1)^{j-\epsilon/2}. \tag{7.15}$$

Using the result in Eq. 7.12, the differential cross section for scattering of $j = \frac{1}{2}, \overline{m}_a = \frac{1}{2}, \overline{\Omega} = \frac{1}{2}, \epsilon \rightarrow j', \overline{m}_a = \frac{1}{2}, \overline{\Omega} = \frac{1}{2}, \epsilon'$ is given by:

$$\frac{d\sigma_{j=\frac{1}{2},\epsilon\rightarrow j',\epsilon'}}{d\omega} = C(\beta)^2 \frac{j'+\frac{1}{2}}{4k^2} \frac{\sin\beta}{\sin\vartheta}\left|\frac{\partial\beta}{\partial\vartheta}\right| \; |g_{j'-\epsilon\epsilon'/2}(\beta)|^2 \tag{7.16}$$

$$\text{with:} \qquad g_n(\beta) = \int_{-1}^{1} g_{j\rightarrow j'}(\gamma_a;\beta) P_n(\cos\gamma_a) d\cos(\gamma_a).$$

Note that $n = j' - \epsilon\epsilon'/2$.

The factor $C(\beta)$ takes care of current density conservation along the kinematic apse, which lies along the direction of momentum transfer. The total differential cross section with respect to the apse (summed over all rotational states) for inelastic scattering has to be the same as its classical counterpart:

$$C(\beta)^2 = \frac{d\sigma_{class}}{d\omega_a} \Big/ \sum_{j',\epsilon'} \frac{j'+\frac{1}{2}}{4k^2} \; |g_{j'-\epsilon\epsilon'/2}(\beta)|^2 \tag{7.17}$$

with:

$$\frac{d\sigma_{class}}{d\omega_a} = \int_0^{2\pi}\int_0^{\pi} \Psi^*_{j,m_a,\overline{\Omega},\epsilon} \Psi_{j,m_a,\overline{\Omega},\epsilon} \frac{d\sigma(\gamma_a;\beta)}{d\omega_a} \sin\gamma_a d\gamma_a d\phi_a. \tag{7.18}$$

Recall that

$$d\omega_a = \sin\beta d\beta d\varphi. \tag{7.19}$$

In the case of $j = \frac{1}{2}$, Eq. 7.18 can be simplified as:

$$\frac{d\sigma_{class}}{d\omega_a} = \frac{1}{4\pi}\int_0^{2\pi}\int_0^{\pi} \frac{d\sigma(\gamma_a;\beta)}{d\omega_a} \sin\gamma_a d\gamma_a d\phi_a. \tag{7.20}$$

The effect of the weak j' dependence of the phase shift in $g_{j\rightarrow j'}(\gamma_a;\beta)$ for neighboring j' values is suppressed for the remainder of section 7.3 and $g_{j\rightarrow j'}(\gamma_a;\beta)$ is abbreviated as $g(\gamma_a;\beta)$. In Eq. 7.16, it can be seen that the differential cross sections for transitions from $j = \frac{1}{2}, \epsilon = -1$ to two neighboring rotational states with the same parity (for example $j' = 3.5, \epsilon' = 1$ and $j' = 4.5, \epsilon' = -1$) are similar, except for a different pre-factor $(j' + \frac{1}{2})$. This propensity rule immediately follows from Eq. 7.16:

$$\frac{d\sigma_{\frac{1}{2},\epsilon=-1\rightarrow\frac{3}{2},\epsilon'=1}}{d\omega} \approx \frac{2}{3}\frac{d\sigma_{\frac{1}{2},\epsilon=-1\rightarrow\frac{5}{2},\epsilon'=-1}}{d\omega} \propto \left|\int_{-1}^{1} g(\gamma_a;\beta) P_2(\cos\gamma_a) d\cos(\gamma_a)\right|^2$$

$$\frac{d\sigma_{\frac{1}{2},\epsilon=-1\rightarrow\frac{5}{2},\epsilon'=1}}{d\omega} \approx \frac{3}{4}\frac{d\sigma_{\frac{1}{2},\epsilon=-1\rightarrow\frac{7}{2},\epsilon'=-1}}{d\omega} \propto \left|\int_{-1}^{1} g(\gamma_a;\beta) P_3(\cos\gamma_a) d\cos(\gamma_a)\right|^2$$

$$\frac{d\sigma_{\frac{1}{2},\epsilon=-1\rightarrow\frac{7}{2},\epsilon'=1}}{d\omega} \approx \frac{4}{5}\frac{d\sigma_{\frac{1}{2},\epsilon=-1\rightarrow\frac{9}{2},\epsilon'=-1}}{d\omega} \propto \left|\int_{-1}^{1} g(\gamma_a;\beta) P_4(\cos\gamma_a) d\cos(\gamma_a)\right|^2$$

et cetera.

The current treatment explains the surprising observation that differential cross sections come in "parity pairs" as seen in ion imaging (velocity mapping) experiments [11].

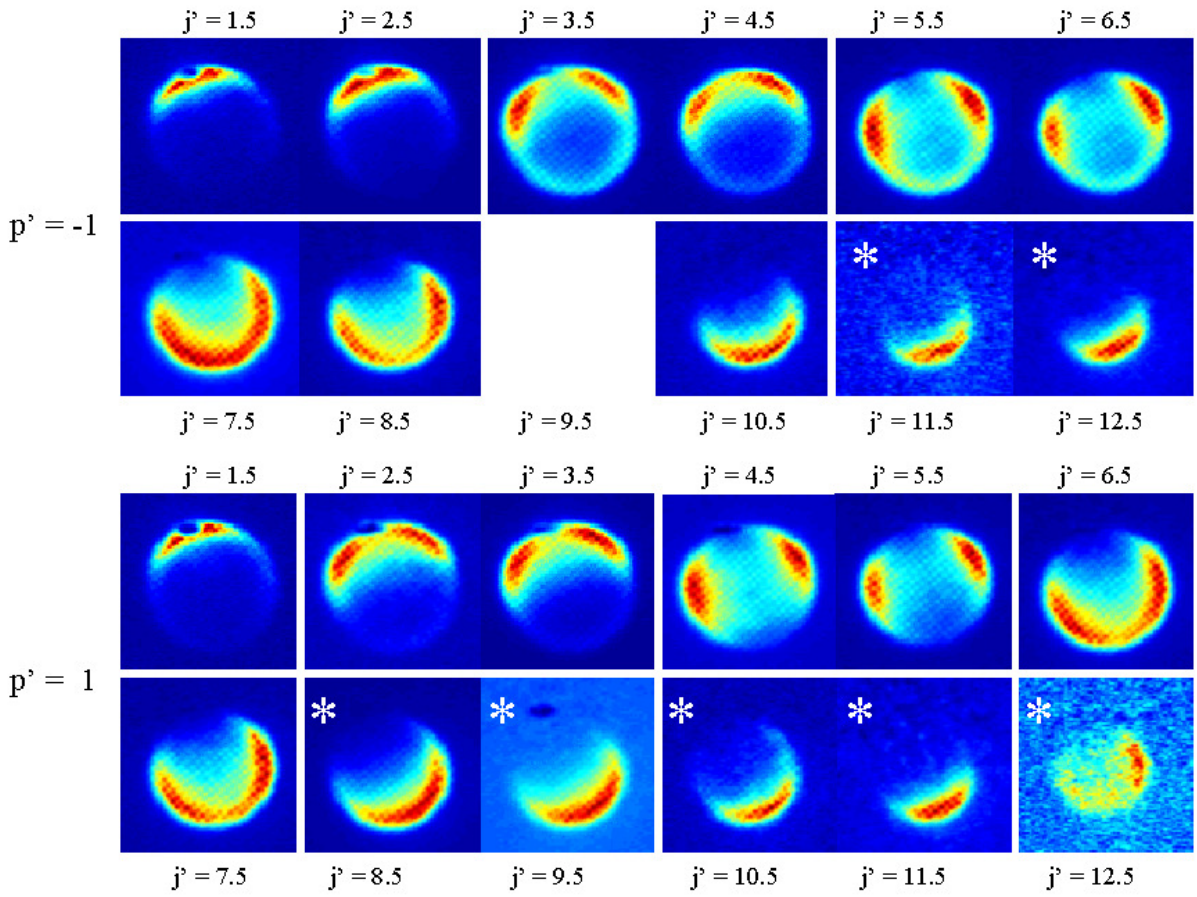

Figure 7.4: Ion images for He-NO collisions at $E_{tr} = 514 \quad cm^{-1}$. Marked images (*) are from P+Q or Q+R branch transitions. These images are more sensitive to collision induced rotational alignment and therefore show more asymmetry than those from single P and R branches [11]. The parity pairs are grouped and separated from the other images by white lines. The image for $p' = -1, j' = 9.5$ could not be obtained because of two overlapping spectral lines. Images for $p' = 1, j' = 6.5$ and $p' = 1, j' = 7.5$ form a pair as well although they are displayed on different rows.

Ion images of product angular distributions for spin-orbit conserving He-NO collisions are plotted in Fig. 7.4. The top panel displays images for parity conserving transitions, while the lower panel shows images for parity breaking transitions. The "parity pairs" for each final rotational state with identical $j' - \epsilon\epsilon'/2$ are grouped in this figure and spaced from the other images. The intensity in the ion images reflects the 2-dimensional velocity distribution of the NO-molecules after collision with a He-atom. The intensity on an outer ring roughly reflects the differential cross section. For excitation to low j', the NO-molecules are mostly scattered in the forward direction, for high final rotational states, backward scattering is preferred. This can easily be understood. Glancing collisions - where little translational energy is transformed into rotational energy - are forward scattered, whereas head-on collisions allow for higher rotational states and will show mostly backward scattering.

Although the ion images of Fig. 7.4 clearly show the presence of parity pairs, these images remain unable to give information on the absolute value of the differential cross sections. To test the predicted (pre-factor) ratios between the differential cross section within the pairs, these ratios are compared to those obtained from quantum mechanical close coupling (HIBRIDON) [59] calculations [11]. The ratios A_n between HIBRIDON differential cross section within parity-pairs, are obtained with a least squares fit, where

$$\left[\left.\frac{d\sigma}{d\omega}\right|_{\Delta j=n+1} - A_n \left.\frac{d\sigma}{d\omega}\right|_{\Delta j=n} \right]^2 \qquad (\text{with} \quad n = 1, 2, 3, \ldots)$$

is minimized. The resulting close coupling ratios are compared to those from the QQT pre-factors in Table 7.1. For low final rotational states, there exists a good qualitative agreement with the ratios predicted from Eq. 7.16, although for the highest rotational states the agreement is less pronounced. Until now, no thorough explanation for the disagreement at high rotational states has become available, but at this region the contribution of spin orbit changing collisions becomes comparable compared to that of spin orbit conserving collisions. Additionally, the angular dependence of the differential cross sections turns out to be more distinctive for large j' [11].

The counter-intuitive result that the differential cross section to the upper j' component of each parity pair $j' - \epsilon\epsilon'/2$ is larger than that to the lower j' component opposes the "exponential gap" model [35, 92]. This rule of thumb predicts that the cross section for a small "gap" (the change of translational energy during collision) and thus a small j' is larger than to a higher one.

Application of classical S-matrix theory showed that collisions between rare gas atoms and nearly homo-nuclear $^1\Sigma$ molecules, favor rotational transitions with $\Delta j =$ even [144]. This propensity rule cannot simply be extended to collisions of $^2\Pi$ molecules like NO. Each rotational j state carries both parities in the two components of the Λ-doublet. Both in this work, as well as that by Drabbels et al. [145] the preference of Δj for conservation or breaking of parity was studied. For parity conserving collisions of He with NO it was observed that transitions with $\Delta j =$ even are preferred, while for parity breaking transitions both studies find a preference for $\Delta j =$ odd transitions. The $(2j'+1)$ pre-factor in Eq. 7.16 explains both propensities.

Table 7.1: Parity pairs for He-NO collisions. A least squares method was used to find ratios between differential cross sections from quantum calculations. For the QQT the ratio's between the pre-factors $(j' + \frac{1}{2})$ are provided. The ratio between the differential cross sections for the QQT might be slightly different due to the dependence of the phase shift on the final rotational state.

n	p'	$\frac{d\sigma}{d\omega}\Big\vert_{\Delta j=n+1} \Big/ \frac{d\sigma}{d\omega}\Big\vert_{\Delta j=n}$		
		QQT pre-factor		A_n (Quantum calc.)
1	1	3/2	1.50	1.54
2	-1	4/3	1.33	1.36
3	1	5/4	1.25	1.23
4	-1	6/5	1.20	1.30
5	1	7/6	1.17	1.16
6	-1	8/7	1.14	1.25
7	1	9/8	1.13	1.13
8	-1	10/9	1.11	1.07
9	1	11/10	1.10	1.32
10	-1	12/11	1.09	0.88
11	1	13/12	1.08	2.50

7.3.2 Oriented molecules

The result in Eq. 7.12 is applied to oriented molecules in this subsection. Under the influence of a static electric orientation field **E** the hexapole state selected wave function can be described as a linear combination of both components of the λ-doublet.

$$|j, m, \overline{\Omega}, E\rangle = \alpha(E)|j, m, \overline{\Omega}, \epsilon = -1\rangle \pm \beta(E)\frac{m}{\overline{m}}\ |j, m, \overline{\Omega}, \epsilon = 1\rangle \tag{7.21}$$

The $\pm$ indicates orientation. For "+" orientation there is preference for $\boldsymbol{r}$ to point parallel to the quantization axis ($\boldsymbol{r} \uparrow\uparrow \hat{\boldsymbol{Z}}$), while for "$-$" orientation these vectors point antiparallel ($\boldsymbol{r} \uparrow\downarrow \hat{\boldsymbol{Z}}$).

The parameters $\alpha(E)$ and $\beta(E)$ in Eq. 7.21 are the mixing coefficients. If the orientation field cannot be assumed infinitely high, mixing is not complete and $\alpha(E) > \beta(E) > 0$ with $\alpha^2 + \beta^2 = 1$. For an infinitely high orientation field $\mathbf{E}_\infty$, $\alpha(E) = \beta(E) = \frac{1}{\sqrt{2}}$, the wave function can then be written as:

$$\big|j, m, \overline{\Omega}, E_\infty\big\rangle = \frac{1}{\sqrt{2}}\left[\big|j, m, \overline{\Omega}, \epsilon = -1\big\rangle \pm \ \frac{m}{\overline{m}}\ \big|j, m, \overline{\Omega}, \epsilon = 1\big\rangle\right]. \tag{7.22}$$

We first focus on this more simple case. Substitution of Eq. 7.13 into 7.22 now yields:

$$\begin{aligned}
\Big|j, m, \overline{\Omega}, E_\infty\Big\rangle &= \Big|j, m, \Omega = \frac{m}{\overline{m}}\ \overline{\Omega}\ \Big\rangle \qquad \text{for "+" orientation,} \\
\Big|j, m, \overline{\Omega}, E_\infty\Big\rangle &= -\Big|j, m, \Omega = -\frac{m}{\overline{m}}\ \overline{\Omega}\ \Big\rangle \qquad \text{for "-" orientation.}
\end{aligned} \tag{7.23}$$

For convenience, the orientation is for now taken relative to the apse; m in Eqs. 7.22 and 7.23 is replaced by m_a.

$$\left|j, m_a, \overline{\Omega}, E_\infty\right\rangle = \left|j, m_a, \Omega = \frac{m_a}{\overline{m_a}}\ \overline{\Omega}\ \right\rangle \qquad \text{for "+" orientation,} \tag{7.24}$$

$$\left|j, m_a, \overline{\Omega}, E_\infty\right\rangle = -\left|j, m_a, \Omega = -\frac{m_a}{\overline{m_a}}\ \overline{\Omega}\ \right\rangle \qquad \text{for "-" orientation.} \tag{7.25}$$

Recall that orientation is defined such that for "+" orientation, the molecular axis $\boldsymbol{r}$ preferentially is parallel to the quantization axis, while for "-" orientation it preferentially is antiparallel. It should be noted that in Eq. 7.25 the apse serves as quantization axis $\hat{\boldsymbol{Z}} = \hat{\boldsymbol{a}}$. In NO, $\boldsymbol{r}$ points from the O-atom towards the N-atom. In the apse frame, the "+" orientation relates to a $R - NO$ collision geometry and the "-" orientation to a $R - ON$ geometry. Transformation from the apse frame to the collision frame - which weakens the orientation effects - will be done at a later stage. The orientation dependent scattering amplitude in the apse frame follows directly from the substitution of Eq. 7.12 in Eq. 7.9.

$$g_{\frac{1}{2},\pm\rightarrow j'}(\beta) = \pm C(\beta)\frac{1}{2}\sqrt{j' + \frac{1}{2}}\ \left[g_{j'-\frac{1}{2}}(\beta) \pm g_{j'+\frac{1}{2}}(\beta)\right]$$

$$\text{with:} \qquad g_n(\beta) = \int_{-1}^{1} g_{j\rightarrow j'}(\gamma_a;\beta) P_n(\cos\gamma_a) d\cos(\gamma_a). \tag{7.26}$$

This equation turns out to be very helpful to explain the oscillations of the steric asymmetry S as a function of the final rotational state.

To obtain a relation between the relevant scattering amplitudes, the recurrence relation for Legendre polynomials will be used.

$$P_{n+1}(x) = \frac{2n+1}{n+1}\ x\ P_n(x) - \frac{n}{n+1}\ P_{n-1}(x). \tag{7.27}$$

For large n this reduces to:

$$P_{n+2}(x) \approx 2xP_{n+1}(x) - P_n(x). \tag{7.28}$$

Around the center ($x \approx 0$), $P_n(x)$ dominates in Eq. 7.28. At the edges ($|x| \approx 1$), $2xP_{n+1}(x)$ dominates. Overall both terms are equally important as P_{n+1} is multiplied with $2x$ ($-1 < x < 1$). Note that the amplitude of the oscillations of $P_{n+1}(x)$ is only slightly smaller than that of $P_n(x)$. In Fig. 7.5 some Legendre polynomials are plotted to illustrate that $P_{n+2}(x) \approx -P_n(x)$ around $x \approx 0$.

Substitution of Eq. 7.28 in Eq. 7.26 gives

$$g_n(\beta) \approx -g_{n+2}(\beta) + 2\int_{-1}^{1} g_{j\rightarrow j'}(\gamma_a;\beta)\ \cos\gamma_a\ P_{n+1}(\cos\gamma_a) d\cos(\gamma_a). \tag{7.29}$$

If the contributions around the waist of the molecules ($\cos\gamma_a = 0$) dominate the integral, the second term in Eq. 7.29 can be neglected: $g_n(\beta) \approx -g_{n+2}(\beta)$. This will be the case when the phase shift η close to $\cos\gamma_a = 0$ is stationary [126]: i.e. η does not depend on $\cos\gamma_a$, which is expected for a prolate molecule like NO. Under these conditions it is

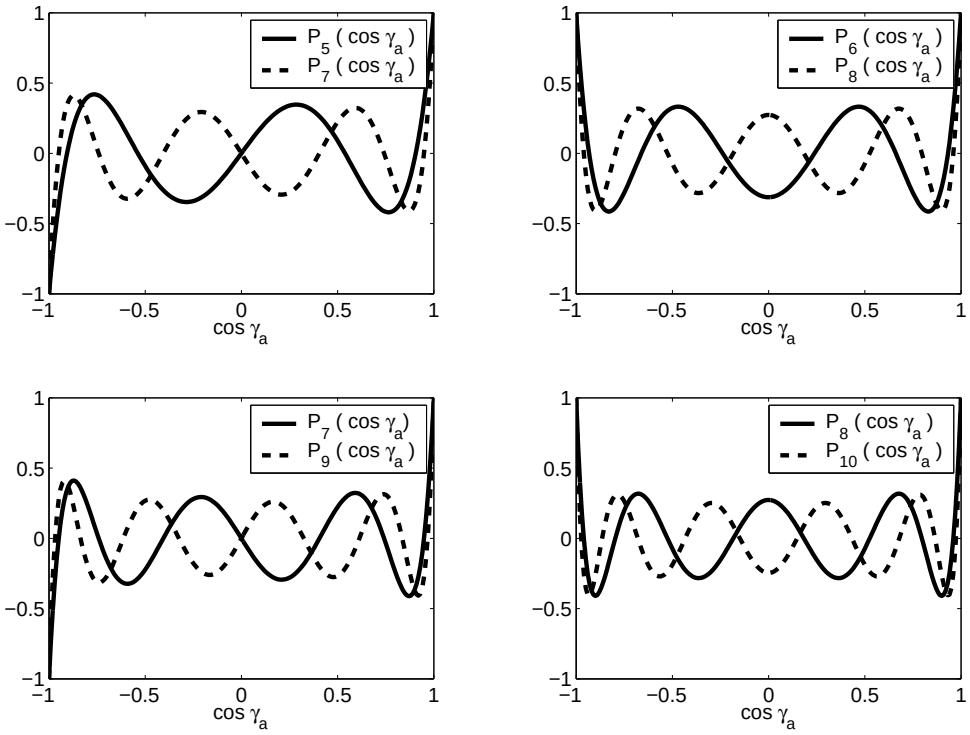

Figure 7.5: Example of Legendre polynomials. Roughly speaking, $P_n(\cos\gamma_a) \approx -P_{n+2}(\cos\gamma_a)$ in the (broad) region around $\cos\gamma_a = 0$.

easily shown why the orientation preference switches sign when increasing $j' \rightarrow j'+1$. The $\pm$ orientation dependent differential cross section for excitation to j' immediately follows from Eq. 7.26:

$$\frac{d\sigma_{\frac{1}{2},\pm\rightarrow j'}}{d\omega} = \frac{j'+\frac{1}{2}}{4k^2} C(\beta)^2 \, \frac{\sin\beta}{\sin\vartheta}\left|\frac{\partial\beta}{\partial\vartheta}\right| \, |g_{j'-\frac{1}{2}}(\beta) \pm g_{j'+\frac{1}{2}}(\beta)|^2. \tag{7.30}$$

For $j'+1$ this results in:

$$\frac{d\sigma_{\frac{1}{2},\pm\rightarrow j'+1}}{d\omega} = \frac{j'+\frac{3}{2}}{4k^2} C(\beta)^2 \, \frac{\sin\beta}{\sin\vartheta}\left|\frac{\partial\beta}{\partial\vartheta}\right| \, |g_{j'+\frac{1}{2}}(\beta) \pm g_{j'+\frac{3}{2}}(\beta)|^2. \tag{7.31}$$

Substitution of $g_{n+2}(\beta) \approx -g_n(\beta) \;\rightarrow\; g_{j'+\frac{3}{2}}(\beta) \approx -g_{j'-\frac{1}{2}}(\beta)$ yields:

$$\frac{d\sigma_{\frac{1}{2},\pm\rightarrow j'+1}}{d\omega} \approx \frac{j'+\frac{3}{2}}{4k^2} C(\beta)^2 \, \frac{\sin\beta}{\sin\vartheta}\left|\frac{\partial\beta}{\partial\vartheta}\right| \, |g_{j'-\frac{1}{2}}(\beta) \mp g_{j'+\frac{1}{2}}(\beta)|^2. \tag{7.32}$$

Comparing the right-hand sides of Eqs. 7.30 and 7.32 one notices that they are nearly similar, except for the pre-factor and the $\pm$ in the integral, which defines the orientation. The $\pm$ is exchanged for a $\mp$, which implies that the orientation preference is reversed when increasing $j' \rightarrow j'+1$.

Incomplete mixing due to finite field strength can be included in the model. Application of Eq. 7.21 as the initial wave function leads to the orientation-dependent differential cross section:

$$\frac{d\sigma_{\frac{1}{2},\pm,E\rightarrow j',\epsilon'}}{d\omega} = \frac{j'+\frac{1}{2}}{4k^2} C(\beta)^2 \, \frac{\sin\beta}{\sin\vartheta}\left|\frac{\partial\beta}{\partial\vartheta}\right| |\alpha(E) g_{j'+\epsilon'/2}(\beta) \pm \beta(E) g_{j'-\epsilon'/2}(\beta)|^2 \tag{7.33}$$

The observed steric asymmetry will in practice be smaller than what follows from integration of Eq. 7.33. Recall that orientation is until now defined along the apse: the product $m_a\Omega$ gives the orientation, where m_a is the projection of $\boldsymbol{j}$ on the apse. In experiments, molecules are oriented along an electric field that is usually fixed in the laboratory.

The projection of the total angular momentum on the $\hat{\boldsymbol{Z}}$-axis of the collision frame (parallel or antiparallel to the electric field $\boldsymbol{E}$) is defined by $m\Omega$ instead of $m_a\Omega$, where m is the projection of $\boldsymbol{j}$ on the $\hat{\boldsymbol{Z}}$-axis that points along the relative velocity. The final result is a linear combination of "+" and "-" orientation along the apse weighted by the axis distribution of the selected state. There will be a weakening of the steric asymmetry from the pure apse-oriented state, but the conclusions drawn before on the undulating behavior of S remain intact. The laboratory and apse frames are related by rotation through the polar angle β.

$$|j,m,\Omega\rangle = \sum_{m_a} d^j_{m_a,m}(\beta)|j,m_a,\Omega\rangle \tag{7.34}$$

In the scattering experiments with oriented NO molecules, the initial state is $j=\frac{1}{2}$. The differential cross section follows as:

$$\frac{d\sigma_{j=\frac{1}{2},m\Omega=\pm\frac{1}{4},E\rightarrow j',\epsilon'}}{d\omega} =$$
$$\sin^2\left(\frac{\beta}{2}\right)\frac{d\sigma_{j=\frac{1}{2},m_a\Omega=\mp\frac{1}{4},E\rightarrow j',\epsilon'}}{d\omega} + \cos^2\left(\frac{\beta}{2}\right)\frac{d\sigma_{j=\frac{1}{2},m_a\Omega=\pm\frac{1}{4},E\rightarrow j',\epsilon'}}{d\omega} \tag{7.35}$$

Table 7.2: Hard shell Legendre polynomial approximation coefficients as used in Eq. (7.36).

n	c_n for He-NO hard shell [Bohr]	c_n for Ar-NO hard shell [Bohr]
0	4.8637	5.8692
1	0.1983	0.1516
2	0.6908	0.6771
3	-0.0126	0.0142
4	-0.1497	-0.0999
5	-0.0012	0.0010
6	0.0263	0.0183

Where the $m\Omega/\overline{m\Omega} = 1$ provides a $R - ON$ configuration and $m\Omega/\overline{m\Omega} = -1$ gives a $R - NO$ configuration in the collision frame with $\hat{\boldsymbol{Z}} = \hat{\boldsymbol{k}}$. Note that $90^o \leq \beta \leq 180^o$, which implies that the first term with $\sin^2(\beta/2)$ is the strongest one. The "+" orientation in the collision frame is dominated by the "-" orientation in the apse frame because the quantization axis in the apse frame ($\hat{\boldsymbol{Z}} = \hat{\boldsymbol{a}}$) generally points opposite to that in the collision frame ($\hat{\boldsymbol{Z}} = \hat{\boldsymbol{k}}$).

7.4 Hard shell approximations

To be able to calculate differential and integral cross sections, it is necessary to provide an explicit expression for the molecule fixed scattering amplitude $g_{j\to j'}(\gamma_a;\beta)$, that contains the phase shift. In this section a hard shell potential is applied to obtain $g_{j\to j'}(\gamma_a;\beta)$. The use of more sophisticated potential energy surfaces - soft and / or including attraction - is not treated here. At our collision energy, the He-NO and Ar-NO potential energy surfaces are reasonably well described in a hard shell approximation. The aim of this work is to obtain a better insight into the physics of inelastic scattering.

The convex hard shell for Ar colliding with NO is approximated using the 475 cm^{-1} equipotential surface from Alexander's V_{sum} PESs [69]. The shell for He-NO uses the 514 cm^{-1} equipotential surface from V_{sum} PESs calculated by Kłos [114]. These equipotential surfaces are taken at the collision energies from Refs. [5, 6, 11]. The hard Ar-NO and He-NO potentials are shown in Fig. 7.6. As the amount of available *ab initio* points on the equipotential is limited, an interpolation has been used to establish the shell. The equipotential lines are expressed in a Legendre expansion:

$$R_s(\gamma_R) = \sum_{n=0}^{n_{max}} c_n P_n(\cos\gamma_R). \tag{7.36}$$

In this equation, γ_R is the polar angle between the position vector of the shell and the molecular axis while $R_s(\gamma_R)$ gives the distance from the origin of the potential to the hard shell (see also Fig. 7.7). The coefficients for this expansion have been calculated using a least squares optimization routine. For Ar-NO, 9 points were supplied and used for the fit while for He-NO the fit was made using 37 points. The c_n coefficients resulting from a fit to the expansion with $n_{max} = 6$ are shown in Table 7.2. As is shown in Fig. 7.6, both

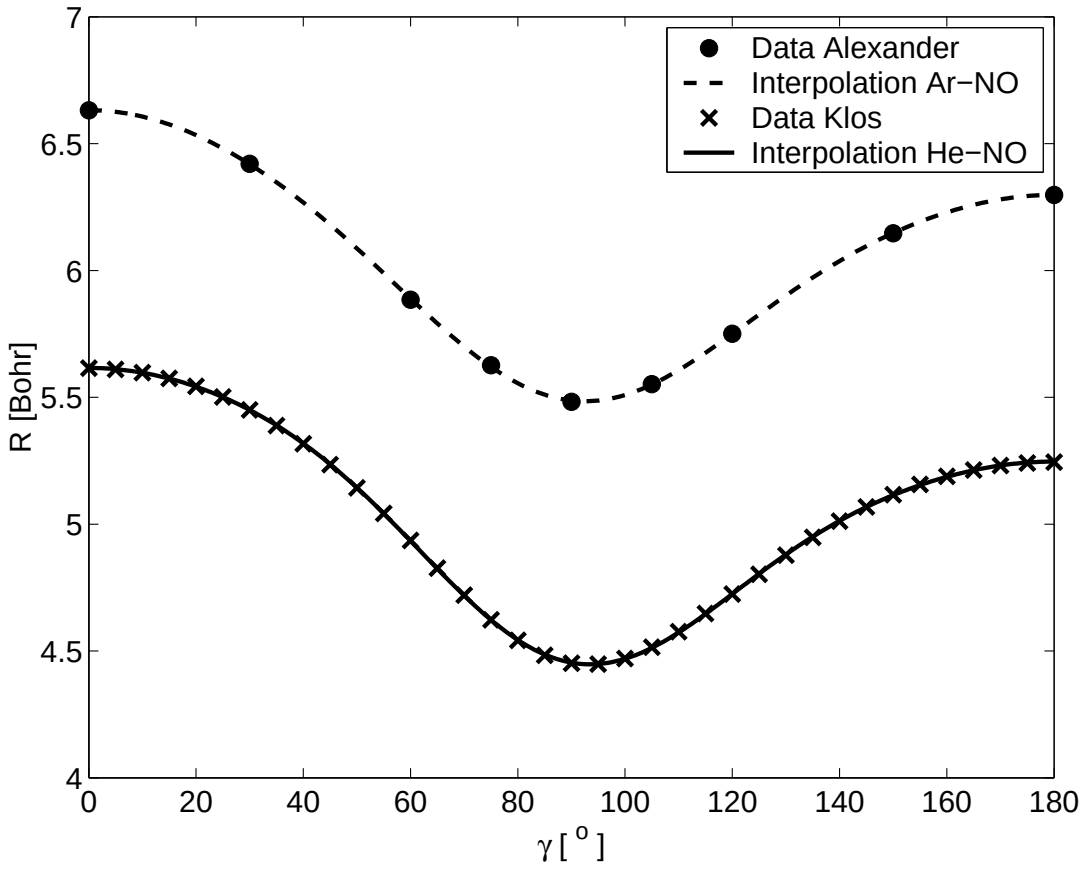

Figure 7.6: Calculated equipotential line and interpolation for NO-Ar $E_{tr} = 475 \quad cm^{-1}$ [69] and NO-He PESs $E_{tr} = 514 \quad cm^{-1}$ [56]. Coefficients from table 7.2 are used. The interpolation for Ar-NO is based on 9 data points, that for He-NO is based on 37 points.

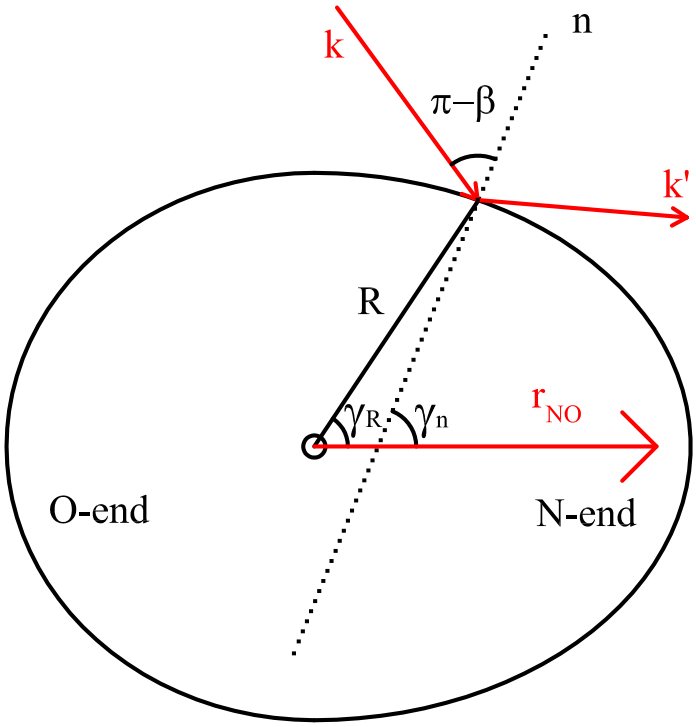

Figure 7.7: Schematic representation of a hard convex shell.

the He-NO and the Ar-NO *ab initio* equipotential surfaces are excellently described using Eq. 7.36 with the fitted c_n constants of Table 7.2.

The surface normal $\hat{n}$ - that points perpendicularly to the hard shell - coincides with the kinematic apse $\hat{\boldsymbol{a}}_k$. In the hard shell approximation, the scattering angle is determined only by the incoming momentum, the surface normal and the final rotational state. This is demonstrated in Fig. 7.8, where the incoming momentum $\boldsymbol{k}$ is decomposed in a component parallel ($\boldsymbol{k}_{\|}$) and perpendicular ($\boldsymbol{k}_{\perp}$) to the shell. The force that induces the rotation points perpendicular to the shell. The component of the momentum perpendicular to the hard shell is reversed and partly transformed into rotation. The component along the hard shell $\boldsymbol{k}_{\|}$ is conserved:

$$\boldsymbol{k}'_{\|} = \boldsymbol{k}_{\|}.$$

The hard shells can be exploited to find the molecule fixed scattering amplitude. This amplitude for a specific rotational excitation is written as:

$$g_{j\rightarrow j'}(\gamma_a;\beta) = g_{class}(\gamma_a;\beta)\ e^{i\eta(\gamma_a;\beta)}. \tag{7.37}$$

The $j \rightarrow j'$ dependent phase shift is denoted by $\eta(\gamma_a;\beta)$ and $g_{class}(\gamma_a;\beta)$ is a "classical" hard shell scattering amplitude that follows from the classical differential cross section in the apse frame. For a spherical potential g_{class} reduces to the square root of the classical differential cross section (in the apse frame)

$$g_{class}(\beta) = kR_s\sqrt{|cos\beta|}. \tag{7.38}$$

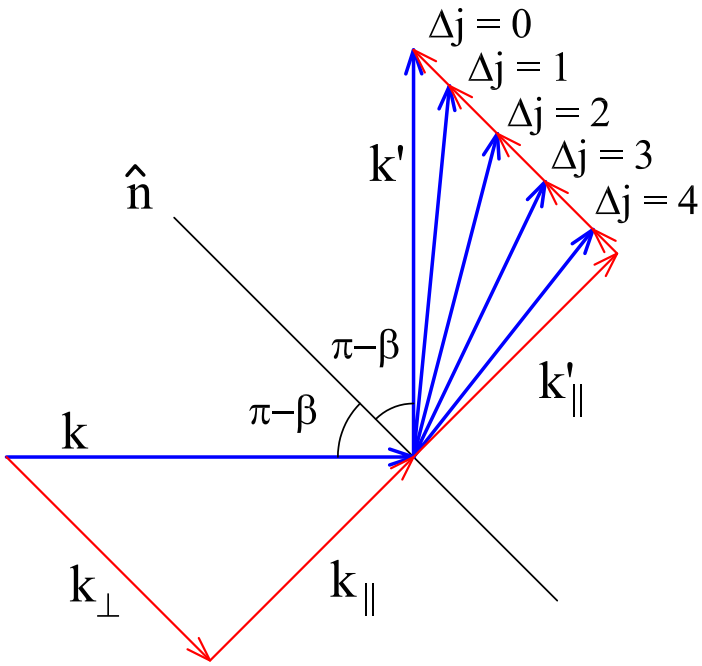

Figure 7.8: Assuming a hard shell, the scattering angle is defined by only the incoming momentum, the surface normal $\hat{n}$ (that coincides with the kinematic apse $\hat{\boldsymbol{a}}_k$) and the final rotational state.

In this case, R_s is independent of the position on the hard shell ($\gamma_R = \gamma_a$). Integration of Eq. 7.9 for elastic scattering - $\frac{d\eta(\gamma_a;\beta)}{d\gamma_a} = 0$ or a constant as function of γ_a - now yields the classical integral cross section.

$$\frac{1}{k^2}\int_{-1}^{0}\int_{0}^{2\pi}\left[kR_s\sqrt{|\cos\beta|}\right]^2 d\alpha\ d\cos\beta = \pi R_s^2$$

Note that in this spherical shell approximation, the current density conservation parameter $C(\beta)$ reduces to:

$$C(\beta)^2 = R_s^2|cos\beta| \Big/ \sum_{j',\epsilon'} \frac{j'+\frac{1}{2}}{4k^2} \quad |g_{j'-\epsilon\epsilon'/2}(\beta)|^2 \tag{7.39}$$

In order to calculate the phase shift η, the hard convex potential is used. The phase shift is defined as the path length difference difference between a path via the hard shell and the corresponding imaginary path through the origin of the potential (center-of-mass), divided by the local de Broglie wavelength and multiplied by 2π.

$$\eta(\gamma_a;\beta) = -\frac{R_s(\gamma_R)}{\hbar}\cos(\gamma_a - \gamma_R)(k'_\perp + k_\perp) \tag{7.40}$$

As $k_\perp = |k\cos\beta|$, it is easily seen that for a glancing collision, the phase shift is zero, while for a head-on collision the absolute value of the phase shift is at a maximum. The phase shift simply scales with $|\cos\beta|$. Once η is calculated for a certain position on the hard shell for $|\cos\beta| = 1$, multiplication by $|\cos\beta|$ provides the phase shift for collisions at the same γ_a for arbitrary direction of the apse.

Eq. 7.40 contains both γ_R and γ_a. In Fig. 7.7 it is shown that - unlike for a spherical shell - the angle γ_a between the normal (apse) $\hat{\boldsymbol{a}}_k$ and the molecular axis is not the same as the angle γ_R between $\boldsymbol{R_s}(\gamma_R)$ and the molecular axis. An unique relation between γ_R and γ_a follows from:

$$\gamma_a = -\arctan\left(\frac{d\ R_s(\gamma_R)\sin(\gamma_R)}{d\ R_s(\gamma_R)\cos(\gamma_R)}\right) \tag{7.41}$$

The expression for $g_{class}(\gamma_a;\beta)$ (Eq. 7.10) is no longer given by Eq. 7.38. Areas on the molecular shell that have a large radius of curvature will contribute more to the scattering amplitude than those with a small radius of curvature. By using the two radii of curvature ρ_1 and ρ_2 that support the differential surface dS as a function of γ_a and substituting their product for R_s^2 in Eq. 7.38 one obtains:

$$g_{class}(\gamma_a;\beta) = \sqrt{\rho_1\rho_2|cos\beta|}. \tag{7.42}$$

The radii of curvature ρ_1 and ρ_2 are calculated as:

$$\rho_1 = \frac{d\ C_f}{d\ \gamma_a}, \tag{7.43}$$

$$\rho_2 = \frac{R_s(\gamma_R)\sin(\gamma_R)}{\sin(\gamma_a)}. \tag{7.44}$$

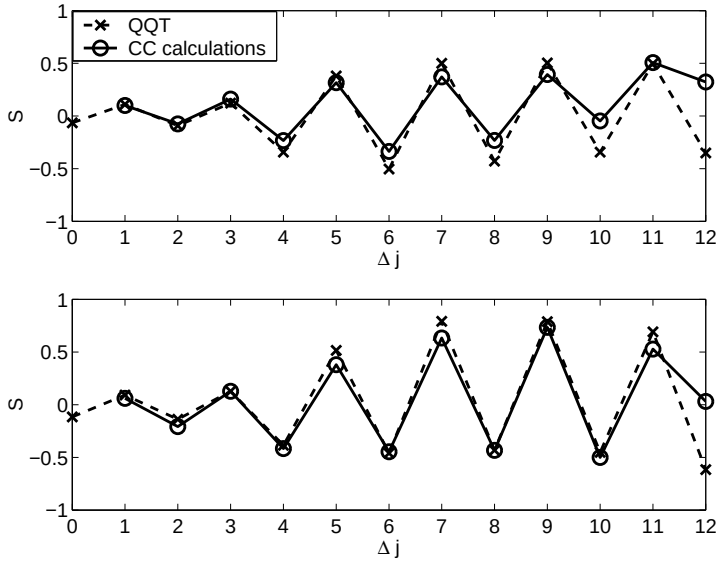

Figure 7.9: QQT results for the steric asymmetry ratio of He-NO collisions ($\Omega' = \frac{1}{2}$) are compared to results of CC (HIBRIDON) calculations [6]. Mixing coefficients used are $\alpha(E) = 0.883$ and $\beta(E) = 0.470$ [6], collision energy is approximately 510 cm^{-1}. The upper panel denotes $\epsilon' = -1$ while the lower shows results for $\epsilon' = 1$. In the case of perfect orientation (mixing) both panels should show the same result as both components of the Λ-doublet are equally populated before the collision.

$d\ C_f/d\ \gamma_a$ is the γ_a derivative of the arc length of the hard shell in a plane through the molecular axis. The second radius of curvature ρ_2 is given by the distance from the molecular axis to the hard shell along the surface normal. Note that $g_{class}(\gamma_a;\beta)$ is the square root of the fixed molecule differential cross section $d\sigma/d\omega_a$ in respect to the apse. With these results, the treatment can be applied to provide quantitative results. This is the subject of the next section.

7.5 Quantitative Results and Discussion

The general QQT of section 7.3 provides already some qualitative conclusions. In section 7.3.1 it was shown that the differential cross sections for collisions with fully state-selected (non-oriented) molecules show parity pairs and propensity rules. In section 7.3.2 it is argued why the steric asymmetry exhibits an oscillatory behavior as function of the final rotational state. The calculation of the molecule fixed scattering amplitude obtained from the hard shell approximation makes it possible to obtain quantitative results. In this section the hard shell QQT will be applied to He-NO scattering to result in calculated angle dependent differential cross sections for non-oriented molecules and steric asymmetries for collisions of He and Ar atoms with oriented molecules.

Upon substitution of Eqs. 7.40 and 7.42 in Eqs. 7.33 and 7.35 and subsequent evaluation of the integral, the differential cross section is obtained. Integration of the differential

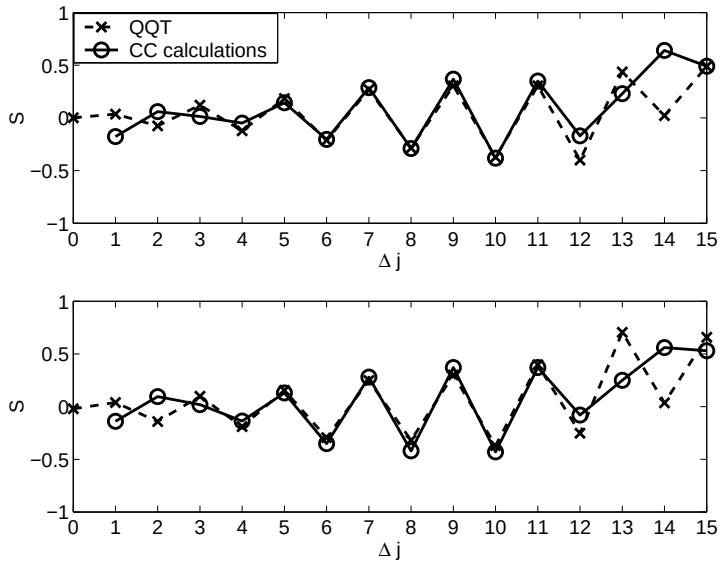

Figure 7.10: QQT results for the steric asymmetry ratio of Ar-NO collisions ($\Omega' = \frac{1}{2}, \epsilon' = 1$) are compared to results of CC (HIBRIDON) calculations [1, 16]. Mixing coefficients used are $\alpha(E) = 0.832$ and $\beta(E) = 0.555$ [5], collision energy is approximately 510 cm^{-1}. The upper panel denotes $\epsilon' = -1$ while the lower shows results for $\epsilon' = 1$. The differences between the QQT results and the CC results for $\Delta j \leq 3$ likely originate from attractive long range interactions that are neglected in the hard shell QQT calculations. Aoiz et al. [146] showed that the attractive part of the potential only has significant influence for $\Delta j \leq 3$.

cross section leads to a cross section that using Eq. 7.1 provides the steric asymmetry S. S is plotted in Figs. 7.9 and 7.10 for two cases: He-NO with $\epsilon' = 1$ and Ar-NO with $\epsilon' = -1$. Mixing is not complete so slightly more NO with $\epsilon = -1$ is present than with $\epsilon = 1$ before collisions. Mixing coefficients were taken from Ref. [6] for He-NO and from Ref. [5] for Ar-NO. The QQT results for S correspond remarkably well to the close coupling calculations (HIBRIDON). The experimental results have not been drawn in Figs. 7.9 and 7.10 for readability, but (except for the unresolved sign error [45, 87]) they correspond well to the theoretical (CC) values of S that are in the plot (see also Fig. 7.1). The amplitude of S for scattering to the $\epsilon = -1$ state is smaller than that for $\epsilon = 1$. CC calculations and experimental results show the same behavior.

In Eqs. 7.30 and 7.32 it was already shown that S shows an undulating behavior as function of the final rotational quantum state j'. These equations however give no information about the sign of the oscillation. To get information on the sign of the steric asymmetry, the phase shift has to be included. In Fig. 7.11, the phase shift (He-NO) for several final rotational states j' is plotted (at $\beta = 180^o$), as are some corresponding Legendre polynomials. The dashed line with label η_{max} labels the position where the phase shift is maximum (least negative) and stationary. This position dominates within the integral, which is enhanced by the fact that $g_{class}(\gamma_a; \beta)$ has a maximum at this position (the waist of the molecule) as well. Except at the stationary phase point, the molecule-fixed scattering amplitude will show oscillations around 0 where the phase is not stationary, which yields a small contribution in this area. On the other hand, if there is a too large area of stationary phase compared to the oscillations of the Legendre polynomials, the contribution in that area will also be close to 0. This is the reason that the cross section for excitation to high rotational states vanishes for glancing collisions with small phase shifts.

To illustrate how the stationary phase defines the sign of the steric asymmetry, scattering into $j' = 6.5$ is discussed here in some detail. Recall that in the integral for the scattering amplitude a sum of two integrals of Legendre polynomials is found (Eq. 7.26)

$$\frac{d\sigma_{\frac{1}{2},\pm\to j'}}{d\omega} = \frac{j'+\frac{1}{2}}{4k^2} C(\beta)^2 \, \frac{\sin\beta}{\sin\vartheta} \left|\frac{\partial\beta}{\partial\vartheta}\right| \; |g_{j'-\frac{1}{2}}(\beta) \pm g_{j'+\frac{1}{2}}(\beta)|^2.$$

$$\text{with:} \quad g_n = \int_{-1}^{1} g_{class}(\gamma_a; \beta) e^{i\eta(\gamma_a;\beta)} P_n(\cos\gamma_a) d\cos(\gamma_a).$$

The $\pm$ defines orientation, where the $+$ indicates a $(R - NO)$ and the "$-$" an $R - ON$ collision. Recall that the apse serves as quantization axis here. Scattering will be dominated by the value of the Legendre polynomial around the phase-shift maximum γ_{max} (where $\eta(\gamma_a; \beta) = \eta_{max}$). For now a spherical hard shell is assumed so $g_{class}(\gamma_a; \beta)$ is independent of γ_a. Roughly speaking for $j' = 6.5$ one has,

$$\begin{aligned} g_6 &\sim e^{i\eta_{max}} P_6(\cos\gamma_{max}) = \; -0.27 \; e^{i\eta_{max}}, \\ g_7 &\sim e^{i\eta_{max}} P_7(\cos\gamma_{max}) = \; 0.18 \; e^{i\eta_{max}}. \end{aligned} \tag{7.45}$$

For a N-end collision $g_6 + g_7 = -0.09 e^{i\eta_{max}}$ appears in the integral, while for an O-end collision one has $g_6 - g_7 = -0.45 e^{i\eta_{max}}$. It is easily seen that the latter will yield a larger

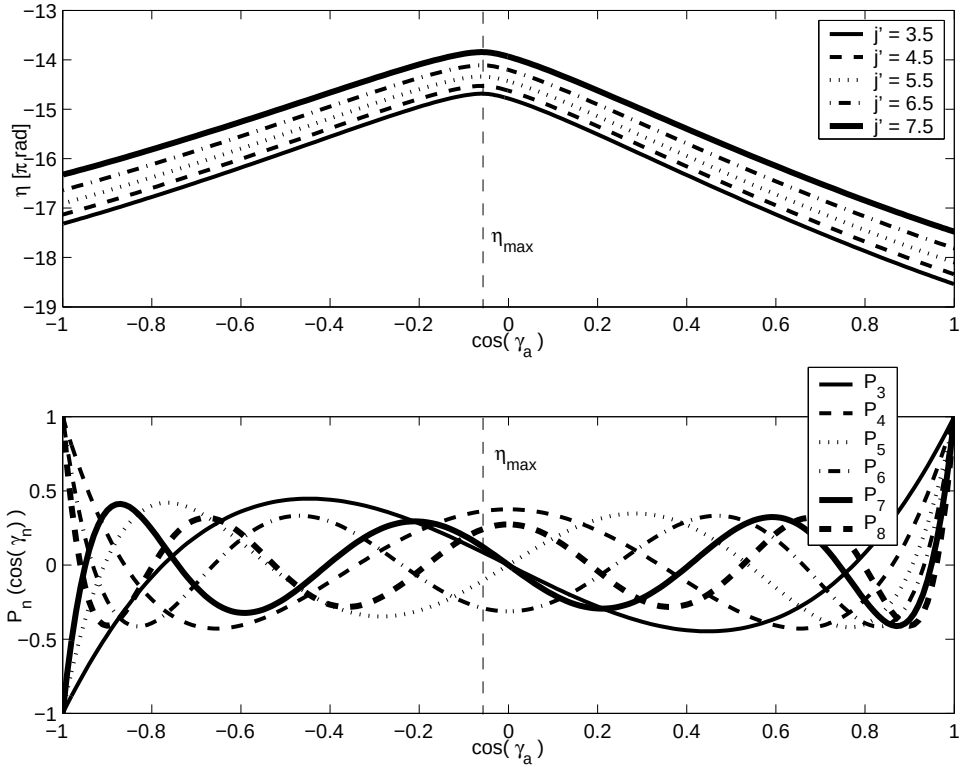

Figure 7.11: The combination of phase shift η (top panel) and the Legendre polynomials (lower panel) fix the sign of the steric asymmetry S. The phase shift drawn here is for collisions with $\beta = 180^o$ (incoming momentum lies along the surface normal). The dashed line with label η_{max} labels the position where the phase shift is maximum (least negative). At this point the phase shift is stationary (the derivative $\frac{d\eta}{d\gamma_a} = 0$), which makes this position dominant within the integral, which is enhanced by the fact that $g_{class}(\gamma_a; \beta)$ has a maximum at this position. Due to the fact that k and k' are larger for Ar-NO than for He-NO, the phase function will be steeper for the Ar-NO system (see Eq. 7.40).

contribution to the differential cross section for a transition to $j' = 6.5$:

$$\frac{d\sigma_{\frac{1}{2}\rightarrow j'=6.5,-}}{d\omega} > \frac{d\sigma_{\frac{1}{2}\rightarrow j'=6.5,+}}{d\omega}. \tag{7.46}$$

According to Eq. 7.1 this will give a negative steric asymmetry, which is also seen in Fig. 7.9. The steric asymmetry will be slightly weakened as explained in Eq. 7.34. The values for S in Fig. 7.9 and 7.10 are not calculated using the stationary phase argument, but the whole integral in Eq. 7.30 is evaluated.

Besides integral cross sections and thus steric asymmetries, the QQT provides differential cross sections. Although until now no differential cross sections have been measured for collisions of oriented NO, they are available for collisions of non-oriented NO with He. Westley et al. [102] performed ion imaging measurements using state selection of the NO with adiabatic cooling for state selection (both components of the Λ doublet present). Recently, Gijsbertsen et al. performed ion imaging experiments with hexapole state selected NO in which only upper component of the Λ doublet ($\epsilon = -1$) is present [11]. Some (raw) ion images [11] are shown in Fig. 7.4. The intensity on an outer ring of these images roughly indicates the differential cross section. In Fig. 7.12 some differential cross sections from the QQT are compared to (extracted) experimental data and data from close coupling calculations. The extraction method is explained in Ref. [11]. The QQT results and experimental data are normalized to the total cross sections as available from HIBRIDON results to enable a good comparison of the angular dependence. There is a difference between the absolute values of the HIBRIDON calculations and QQT calculations. This is easily explained by the use of a hard shell. In order to transfer a lot of kinetic energy into rotation, the potential is more deeply penetrated, causing underestimation of the differential cross section for low rotational states. Scattering into $\overline{\Omega}' = 3/2$ was not taken into account in the QQT, which should result in too large a differential cross section overall for scattering into the $\overline{\Omega}' = 1/2$ states.

7.6 Conclusions

The quasi-quantum-mechanical methodology successfully explains the steric asymmetry and its alternation based on interfering scattering trajectories from a single purely repulsive potential energy surface. It is thereby demonstrated that the steric asymmetry reflects phase differences between scattering from the two ends of the NO molecule. The straightforward quasi quantum mechanical picture provides the first physically simple, yet rigorous, explanation for the behavior of the steric asymmetry, and it can readily be extended to provide predictions of steric effects in other inelastic scattering systems or for reactive collisions. It is shown that the effect of the attractive part of the potential is small and thus that interference between propagation on the A' and A'' surfaces is not responsible for the oscillations.

The differential cross sections calculated for non-oriented NO molecules colliding with He atoms agree reasonably well to experimental results and close coupling calculations. The QQT predicts a parity propensity rule that is also seen in experimental results and results from full quantum mechanical calculations. This rule was not recognized as such

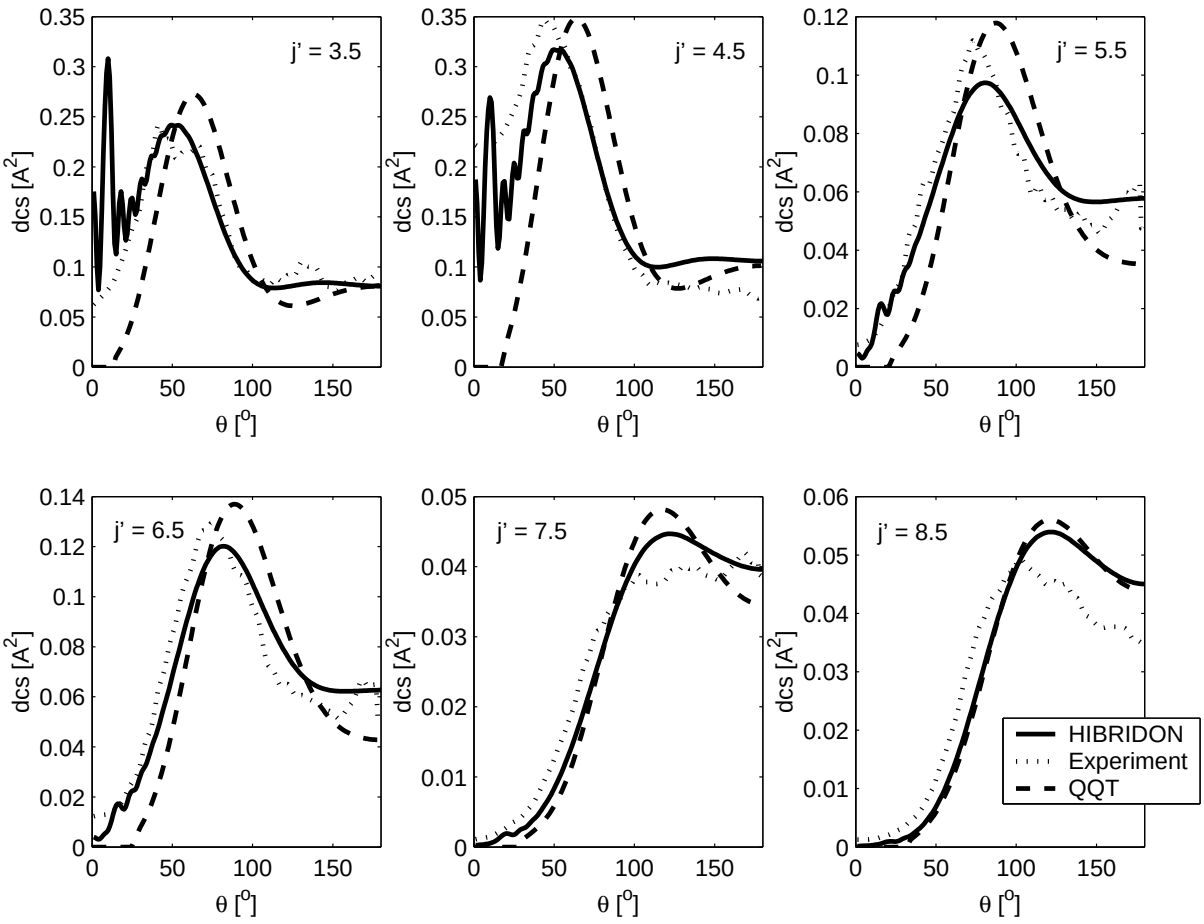

Figure 7.12: Several differential cross sections for parity conserving transitions ($p = p' = -1$). The parity pairs (see also Fig. 7.4) are easily seen in this figure. Both the experimental and QQT results are normalized on the total cross section from close coupling HIBRIDON results. The hard shell approximation causes an underestimation of the differential cross section for low rotational states. For these differential cross sections, the normalization factors are (from low to high rotational states) 1.51, 1.58, 1.15, 1.18, 0.84 and 0.91.

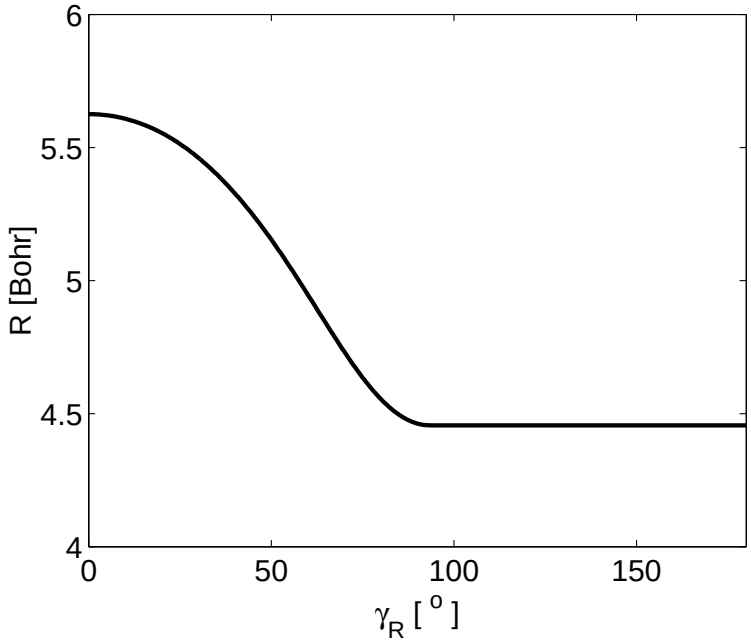

Figure 7.13: A hard shell was prepared such that the N-end (around $\gamma_R = 0^o$) is similar to that used for He-NO collisions, the O-end (around $\gamma_R = 180^o$) is spherical (represented by a horizontal line). Classically no torque can be applied on the spherical end. From the ball and stick model one expects the S to be overall positive, except for elastic collisions ($\Delta j = 0$) where no torque is necessary.

until now. In order to improve qualitative results of the QQT, the potential can be made softer. This will allow the potential to be penetrated more deeply in the case of head-on collisions than in the case of glancing collisions. Low rotational states will then show a larger cross section compared to the current results.

7.7 Appendix: QQT and the sign of the steric asymmetry.

As briefly mentioned before in this work, there still is an important unsolved discrepancy between theory and experiment for collisions of rare gases and NO. There is good agreement as far as the absolute value of the steric asymmetry ratio (S) is concerned, but theory [1] and experiments yield an opposite sign of S. In both [6] and this work, it was decided for now to multiply the experimental values of S with -1 when plotting them in order to enable quantitative comparison. The sign problem for S of collisions with NO is extensively discussed in Refs. [45] and [87]. Although not yet published when Refs. [45] and [87] were published, the QQT provides an important argument in discussions on the

[1] except for Ar-NO calculations in Ref. [2]

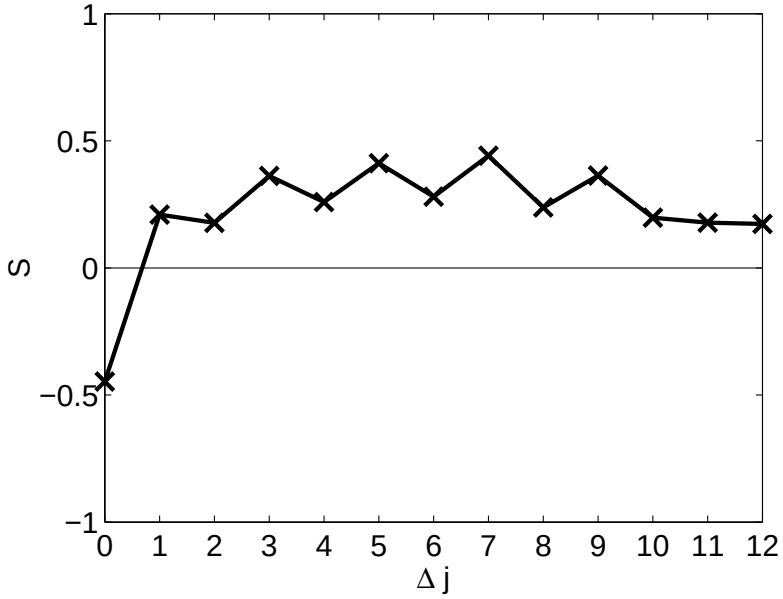

Figure 7.14: Steric asymmetry ratio for the specially designed hard shell in Fig. 7.13. Classically no torque can be applied on the spherical end. From the ball-and-stick model one expects the S to be overall positive, except for elastic collisions ($\Delta j = 0$) where no torque is necessary. The result for S provides a strong indication that the theoretical sign of S is correct.

sign of the steric asymmetry.

All theoretical results - except those of Ref. [2] - for rare gas collisions with oriented NO and OH [46] are, since the revision of Ref. [45], consonant with a so-called classical ball-and-stick model. If a stick is attached to a ball, it is easier to make that system rotate by hitting the stick than by hitting the ball. The torque that can be applied on the stick is larger than on the ball. For Ar colliding with OH the analogy with the ball (O-end) and stick (H-end) is easily seen. Both experiment and theory shows that highest rotational states are preferentially produced by collisions onto the H-end of the molecule. For NO, the ball-and-stick effect is less pronounced, but it is still there. The N-end extends further from the center of mass than the O-end and therefore it allows for a larger torque. It is expected that relatively high rotational states are preferentially due to N-end collisions. Looking at Fig. 7.1 it can easily be seen that this corresponds to theoretical results, while experimental results show that O-end collisions are preferred for high rotational states. Recall that experimental results in Fig. 7.1 are multiplied with a factor -1.

The ball-and-stick model can be exploited to see whether a sign error has been made in the QQT. It is easy to design a hard shell that has extreme a ball-and-stick features. The outcome of calculations with such a shell should immediately make clear what the orientation is. For such a test, the O-end of the He-NO hard shell was made spherical from the minimum of $R_s(\gamma_R)$ on. In Fig. 7.13, the adapted hard shell is shown. The original shell is drawn in Fig. 7.4. The steric asymmetry that follows from the QQT

calculations is shown in Fig. 7.14 and leaves little room for a sign error. Only for elastic collisions ($\Delta j = 0$) is a negative steric asymmetry ratio observed, which means that elastic scattering arises principally from O-end scattering. A positive S is seen for all inelastic channels ($\Delta j > 0$), which implies that the N-end is preferred. This "ball-and-stick effect" becomes more extreme as the stick is extended farther from the center of mass.

Samenvatting

Naar een beter begrip van inelastische atoom-molecuul botsingen

Er is geen scheikunde zonder botsingen. Moleculaire botsingen vormen het uitgangspunt voor alle chemische reacties. Tijdens de botsing wordt impuls en energie overgedragen van de ene aan de andere botsingspartner. Dit kan structurele veranderingen veroorzaken of leidt zelfs tot het uiteenvallen van een molecuul. In het alledaagse "macroscopische"leven zien we het gemiddelde resultaat van een groot aantal "microscopische"botsingen. Individuele botsingen daarentegen zijn veel moeilijker te bestuderen. Een gedetailleerd beeld van zo'n botsing is noodzakelijk om macroscopische verschijnselen goed te kunnen interpreteren. Op de schaal van enkele atomen en moleculen speelt de kwantummechanica daarbij een dominante rol. De uitkomst van een botsing, d.w.z. de eindtoestand waarin een botsend molecuul wordt aangetroffen, wordt bepaald door overgangswaarschijnlijkheden van het ene naar het andere energieniveau.

Het is tegenwoordig mogelijk om voor geschikte systemen individuele botsingen experimenteel onder volledig gecontroleerde omstandigheden (begintoestand, botsingsenergie en eindtoestand van de botsingspartners) te onderzoeken. Hiervoor worden gekruiste bundelmachines gebruikt, eventueel in combinatie met een zespool toestandsselector. Deze toestandsselector maakt het mogelijk om moleculen in een enkele kwantummechanische toestand te selecteren. Vervolgens kun je met gevoelige spectroscopische technieken onderzoeken hoe de bezetting van de energieniveaus verandert door de botsing, bijvoorbeeld als functie van de botsingsenergie of voor verschillende oriëntaties. Deze informatie relateert direct aan de interactiepotentiaal, hoewel het nog steeds niet mogelijk is deze direct te reconstrueren uit metingen.

Dit proefschrift focusseert op botsingen van edelgas atomen met stikstofmonoxide (NO). NO is een radicaal en daarom een chemisch interessant en veel gebruikt modelsysteem. Door een ongepaard elektron heeft NO een halftallig impulsmoment. NO is gevoelig en kwantumtoestand specifiek te detecteren met behulp van spectroscopische technieken zoals "Laser Induced Fluorescence"(LIF) en "Resonance Enhanced Multi Photon Ionization"(REMPI) en is stabiel genoeg voor experimenteel gebruik.

Hoofdstuk 2 en 3 draaien om het teken van de sterische asymmetrie: de oriëntatieafhankelijkheid van botsingen. In de alledaagse chemie spelen oriëntatie-effecten geen rol: alle oriëntaties zijn aanwezig in een ensemble. In een enkele botsing echter verwacht je dat de uitkomst wel afhankelijk is van de oriëntatie van het molecuul. In deze hoofdstukken

wordt gekeken naar de verschillen tussen botsingen van een edelgas op de N-kant en de O-kant van het NO molecuul. Aangezien het NO molecuul een dipoolmoment heeft kan het met elektrische velden worden georiënteerd alvorens te botsen.

Dit soort oriëntatie-effecten wordt gekwantificeerd met behulp van de sterische asymmetrie S:

$$S_{i\to f} = \frac{\sigma^{kop} - \sigma^{staart}}{\sigma^{kop} + \sigma^{staart}}$$

voor een bepaalde overgang van begintoestand i naar eindtoestand f. Hierbij zijn σ^{kop} en σ^{staart} respectievelijk de botsingsdoorsneden voor een botsing op de staart en op de kop van het georiënteerde molecuul. Voor NO wordt over het algemeen de N-kant gezien als "kop", terwijl de O-kant de "staart"vormt. Als S positief is dan zijn het vooral "kop"botsingen die bijdragen aan een bepaalde eindtoestand en als S negatief is, dan zijn dat vooral botsingen op de "staart". Botsingen met $\Delta j = j' - j = \textit{even}$ worden vooral veroorzaakt door botsingen op de N-kant (S is positief), terwijl S negatief is voor botsingen met $\Delta j = \textit{oneven}$. Het rotationeel impulsmoment na en voor botsing wordt aangeduid met respectievelijk j' en j. De meeste[2] theoretische berekeningen geven precies het tegenovergestelde als uitkomst: S is negatief voor botsingen met $\Delta j = \textit{oneven}$ en S is positief voor $\Delta j = \textit{even}$. Voor hoge j' voorspellen HIBRIDON[3] en andere berekeningen een voorkeur voor N-kant botsingen, maar experimenten laten zien dat met name O-kant botsingen tot hoge rotatietoestanden leiden. Ook een simpel klassiek model in combinatie met *ab initio* Ar-NO en He-NO potentiaal oppervlakken geeft aan, dat N-kant botsingen zouden moeten domineren voor hoge Δj. Klassiek gezien, worden immers de hoogste rotatietoestanden vooral veroorzaakt door botsingen op de kant van het molecuul waar het grootste krachtmoment kan worden aangebracht. Voor NO is dit de N-kant.

Verschillende verklaringen voor deze discrepantie worden beschreven in Hoofdstuk 3. Hierbij worden expliciete uitdrukkingen voor de $(j \to j')$ afhankelijke differentiële en integrale botsingsdoorsnede gegeven. Effecten van de keus van het assenstelsel en van de Jacobihoeken op het teken van S worden besproken en bieden geen oplossing. Nieuwe experimentele resultaten - na uitgebreide controle van de experimentele condities - zijn consistent met eerdere uitkomsten. Een mogelijke maar onwaarschijnlijke oplossing is een foute definitie van het teken van het dipoolmoment van NO. Het teken van dit dipoolmoment is nooit gemeten, maar uit berekeningen volgt: N^-O^+. Wanneer dit andersom zou zijn, dan oriënteert het NO molecuul in het experiment tegengesteld aan de verwachte oriëntatie en het experimentele en theoretische teken van S zouden overeen komen.

Hoofdstuk 4 beschrijft een experiment om expliciet het teken van het dipoolmoment van NO te bepalen. Hierbij wordt toestandsgeselecteerd NO georiënteerd in een homogeen electrisch veld en vervolgens met een intense femtosecondelaser beschoten. Het NO molecuul valt uit elkaar (Coulomb explosie) en de fragmenten (bijv. N^{2+} en O^{2+}) worden in het electrisch veld versneld naar de detector. Fragmenten die oorspronkelijk naar de positieve elektrode gericht stonden moeten eerst omkeren, waardoor ze iets langer onderweg zijn (ongeveer 2 ns) dan fragmenten die voor explosie naar de negatieve electrode gericht stonden. Door het aantal vroege fragmenten te vergelijken met het aantal late fragmenten van dezelfde soort kan de oriëntatie van het molecuul op het moment van

[2] uitgezonderd Ar-NO berekeningen in Ref. [2]

[3] na correctie, Ref. [45]

explosie worden bepaald. Door de polarisatie van de laser een kleine hoek te laten maken met het oriëntatieveld is het tijdsverschil van 2 ns "omgezet" in een verschil in plaats van inslag op de detector. Voor NO worden sterke oriëntatie-effecten waargenomen, die wijzen op een dipoolmoment waarbij N negatief is en O positief (N^-O^+). Dit komt overeen met resultaten uit *ab initio* berekeningen en geeft geen verklaring voor het verschil tussen theoretische en experimentele waarden van de sterische asymmetrie S. Om dit resultaat te valideren, is het bovenstaande experiment herhaald met OCS en CH_3F, moleculen waarvan het teken van het dipoolmoment buiten kijf staat. Voor deze moleculen is de waargenomen oriëntatie tegengesteld aan de verwachte oriëntatie. Een mogelijke verklaring is wordt gezocht in de combinatie van het laser- en het oriëntatieveld, maar een definitieve oplossing is nog niet gevonden. Het is op dit moment niet mogelijk op basis van experimentele resultaten een definitieve uitspraak te doen over het teken van het dipoolmoment van NO.

Met een zespool toestandsselector kunnen NO moleculen in een enkele (laag veld zoekende) toestand worden geselecteerd: $j = \frac{1}{2}$, $\overline{\Omega} = \frac{1}{2}$, $\epsilon = -1$. Hierbij is j het rotatie kwantumgetal, $\overline{\Omega}$ het kwantumgetal van de projectie van j op de molecuulas en ϵ de symmetrie index, die -1 is voor de laag veld zoekende (bovenste) component van het Λ-doublet. In hoofdstuk 5 en 6 worden experimenten besproken waarbij differentiële botsingsdoorsneden voor botsingen van He en D_2 met toestandsgeselecteerd NO zijn bepaald. Hiervoor is gebruik gemaakt van de zogenaamde "ion imaging" techniek, waarbij de NO moleculen na botsing worden geïoniseerd (via (1+1') REMPI) en hun 2D snelheidsverdeling wordt afgebeeld op de detector. In hoofdstuk 5 wordt behandeld hoe differentiële botsingsdoorsneden uit deze afbeeldingen worden afgeleid. Hierbij wordt expliciet de detectiewaarschijnlijkheid van verstrooide moleculen in acht genomen. Deze waarschijnlijkheid is afhankelijk van de tijd die de verstrooide moleculen (met verschillende snelheden in het laboratorium) in het detectievolume aanwezig zijn en van alineëring van moleculen door botsingen. Door de vrijwel perfecte toestandsselectie worden botsingen bestudeerd tot op een voorheen onhaalbaar niveau.

Omdat de met de zespool geselecteerde NO moleculen een gedefinieerde pariteit hebben, en ook de detectiestap volledig toestandsselectief is, kan het effect van behoud en verandering van pariteit gedurende de botsing als een geïsoleerd proces worden bestudeerd. De resultaten laten een duidelijk verschil zien tussen botsingen met de bovenste en met de onderste component van het NO Λ-doublet als eindtoestand. Dit kan niet worden veroorzaakt door het energieverschil tussen deze componenten. De differentiële botsingsdoorsneden voor He-NO botsingen komen redelijk overeen met theoretische ("close coupling") berekeningen, wat aangeeft dat de in deze berekeningen gebruikte interactiepotentiaal betrouwbaar is. Botsingen van D_2 met NO laten iets meer voorwaartse verstrooiing zien dan voor He-NO. Hieruit kan worden geconcludeerd dat de D_2-NO interactiepotentiaal iets meer anisotroop is dan die voor He-NO. Rotationele excitatie van de D_2 moleculen is niet waargenomen.

Botsingen naar telkens twee naburige j' niveaus met dezelfde pariteit $p = (-1)^{j-\epsilon/2}$ geven zowel voor He-NO als D_2-NO ongeveer dezelfde botsingsdoorsnede. Deze "pariteitspaartjes"worden aangeduid met nummers n.

$$n = j' - \frac{\epsilon\epsilon'}{2}$$

Deze regel klopt zowel voor spin-baan toestand brekende ($\overline{\Omega}' = 3/2$) als voor spin-baan toestand behoudende ($\overline{\Omega}' = 1/2$) overgangen. De maxima in de differentiële botsingsdoorsneden - die rotationele regenbogen weergeven - zijn bepaald en deze liggen bij grotere strooihoeken in het geval van pariteitsbrekende overgangen dan voor pariteitbehoudende botsingen. Dit is een indicatie dat in het eerste geval de anisotropie van de schil groter is. Dubbele regenbogen - veroorzaakt door botsingen op de N-kant of de O-kant van het NO molecuul - zijn niet waargenomen. Klassiek wordt dit verwacht omdat de NO schil aan de N-kant anders is dan aan de O-kant. Wanneer voor een botsing zowel even als oneven pariteit aanwezig zijn is het mogelijk dat twee maxima in de differentiële botsingsdoorsnede worden waargenomen: één voor pariteitbehoudende en één voor pariteitveranderende botsingen.

Zowel het voorkomen van de hierboven beschreven pariteits-paartjes als de oscillatie van de sterische asymmetrie S als functie van j' worden gevonden in de uitkomsten van volledig kwantummechanische berekeningen. Deze berekeningen geven echter geen inzicht in de fysische achtergrond van deze effecten. Het quasi kwantummechanisch model (QQT) dat wordt beschreven in hoofdstuk 7 beschrijft botsingen in een relatief eenvoudig interferentieplaatje en biedt meer inzicht. De integraal over de impactparameter b is vervangen door een integraal over hoekvariabelen: de oriëntatie van het molecuul en van de "kinematic apse"(KA). Deze KA is gedefinieerd langs de richting van impulsverandering en dient ook als kwantisatie-as. De projectie m_a van j op de KA wordt behouden verondersteld en er is geen interferentie mogelijk tussen verschillende standen van de KA (in tegenstelling tot voor verschillende waarden van b). Hierdoor is het niet meer nodig om grote hoeveelheden gekoppelde vergelijkingen op te lossen. De verstrooiingsamplitude wordt beschreven als (een integraal over) een product van een fasefactor en een Legendre veelterm. De fasefactor wordt momenteel benaderd met behulp van een harde schil interactiepotentiaal. In deze harde-schil-benadering wordt een goede overeenkomst gevonden met kwantummechanische (HIBRIDON) berekeningen wat betreft de sterische asymmetrie en redelijke overeenkomst wat betreft de differentiële botsingsdoorsnede. De oscillatie van S wordt verklaard door interferenties tussen botsingen op verschillende plaatsen op de harde repulsieve NO schil. Het bestaan van pariteits-paartjes wordt in het model (QQT) voorspeld.

Nawoord

Met dit proefschrift is mijn promotietraject aan de Vrije Universiteit bijna afgerond. Al met al heb ik met veel plezier aan mijn onderzoek gewerkt en heb ik zowel op theoretisch als op experimenteel gebied veel geleerd. De kwantummechanica - waarvan ik vrijwel niets wist toen ik bij de VU begon - ben ik een bijzonder intrigerende tak van sport gaan vinden.

Gedurende de afgelopen vier jaar ben ik door veel mensen geholpen. Hen wil ik hier bedanken, allereerst mijn promotor Steven en copromotor Harold voor hun beider betrokkenheid, enthousiasme en voor respectievelijk de vele goede ideeën en het aanbrengen van structuur gedurende mijn tijd als promovendus bij de VU. Behalve mijn begeleiders wil ik ook de rest van de vaste staf binnen Fysische Chemie - Jaap, Nico, Maurice, Arjan, Vincent en Tanja - bedanken voor hun interesse en hulp. Verder wil ik mijn collega AIO's en postdocs Wim, Arno, Harald, Albert, Anouk, Erik, Alrik, Laura en Daniël bedanken voor het feit dat er indien nodig altijd apparatuur geleend kon worden, voor de grote hoeveelheden koek en taart en voor de collegialiteit en gezelligheid. Mijn voorganger Marc wil ik bedanken voor de hulp gedurende het opstarten van mijn onderzoek, ik heb veel aan je proefschrift gehad. Albert, veel succes toegewenst bij het temmen van het blauwe monster. Ik hoop dat je er nog wat mooie resultaten uit kunt halen.

Zonder hulp van de mechanische en de electronica werkplaats zou dit boekje er nog lang niet zijn. Van de mechanische werkplaats wil ik met name Rob bedanken voor de prachtige ionenoptiek die hij heeft gebouwd en zijn hulp bij het opknappen van de oude excimeer laser. Van de electronica werkplaats wil ik in het bijzonder Han, Lex en Peter bedanken voor hun werk bij het ontwerpen van nieuwe apparatuur en vooral omdat ze altijd even tijd vrij wilden maken voor acute problemen.

Het Coulomb explosie experiment om het dipoolmoment van NO te bepalen kon worden uitgevoerd in de XUV-physics groep op het Amolf. Hierbij wil ik Marc bedanken voor het mogelijk maken van dit experiment en de rest van de XUV groep (en Matthias in het bijzonder) voor hun hulp.

Tijdens mijn promotietijd heb ik twee goede studenten mogen begeleiden. Ten eerste Guus, die bijna een jaar heeft meegeholpen aan het opzetten van "ion imaging" experimenten, waarvan we allebei veel hebben geleerd. Als tweede Paul, hij heeft keihard gewerkt aan het NO-dipool experiment op het Amolf. Soms werd daarbij zelfs de laatste trein naar Haarlem gemist...

Om ervaring op te doen met de "Ion Imaging" techniek kon ik enige tijd terecht in de groep van Dave Chandler bij Sandia Livermore (Californië). Ik heb hier veel geleerd en wil Dave hartelijk bedanken voor deze mogelijkheid. Van hetzelfde instituut wil ik Craig Taatjes bedanken voor zijn hulp bij het quasi kwantummechanisch model (QQT).

Zonder mijn Wageningse afstudeerbegeleider Dane Bicanic zou ik nooit op de VU terecht zijn gekomen. Dane, bedankt hiervoor.

Het leven bestaat uit meer dan werk alleen. Allerlei nevenactiviteiten hebben ervoor gezorgd dat ik telkens weer vol goede moed verder kon werken aan mijn onderzoek. Met veel plezier heb ik in het VU-orkest, het VU-kamerorkest, HWSO, Pent'amuse en de WSKOV gespeeld. Collega musici bedankt. Zeker even belangrijk zijn mijn (Wageningse) studievrienden Bas (en Charlotte), Maarten, Dirk, Derk-Jan, Henk (en Petra) en Saskia. Ik hoop dat we nog vaak op wandelvakantie kunnen gaan en regelmatig bij elkaar blijven komen. Bas en Maarten, ik ben blij dat jullie mijn paranimfen willen zijn.

Graag wil ik mijn ouders, Cedrick en (schoon)familie bedanken voor hun interesse en het feit dat ik altijd op ze kan terugvallen. Tot slot wil ik Anneke bedanken voor haar geduld, aandacht en steun.

List of publications

Chapter 2:
What is wrong with the steric asymmetry in atom-molecule collisions?
A. Gijsbertsen, H. Linnartz, J. Klos and S. Stolte, Physica Scripta 72, 2005, p. 1

Chapter 3:
Sign of the state-to-state steric asymmetry of rotationally-inelastic atom-molecule collisions,
A. Gijsbertsen, M. J. L. de Lange, A. E. Wiskerke, H. Linnartz, M. Drabbels, J. Klos and S. Stolte", Chem. Phys. 301, 2004, p. 293

Chapter 5:
Differential cross sections for collisions of hexapole state-selected NO with He,
A. Gijsbertsen, H. Linnartz, G. Rus, A. E. Wiskerke, S. Stolte, D. W. Chandler and J. Klos, J. Chem. Phys. 123, 2005, 224305

Chapter 6:
Parity-dependent rotational rainbows in D_2-NO and He-NO differential collision cross sections,
A. Gijsbertsen, H. Linnartz and S. Stolte, accepted by J. Chem. Phys. 2006

Chapter 7:
Quantum Interference as the Source of Stereo-Dynamic Effects in NO-Rare Gas Inelastic Scattering,
A. Gijsbertsen, H. V. Linnartz, C. A. Taatjes and S. Stolte, J. Am. Chem. Soc. 128, 2006, p. 8777

Bibliography

[1] M. H. Alexander and S. Stolte, J. Chem. Phys. **112**, 8017 (2000).

[2] J. L. van Leuken, J. Bulthuis, S. Stolte, and J. G. Snijders, Chem. Phys. Lett. **260**, 595 (1996).

[3] A. A. Dixit, P. J. Pisano, and P. L. Houston, J. Phys. Chem. A **105**, 11165 (2001).

[4] M. S. Elioff, J. J. Valentini, and D. W. Chandler, Science **302**, 1940 (2003).

[5] M. J. L. de Lange, M. Drabbels, P. T. Griffiths, J. Bulthuis, and J. G. Snijders, Chem. Phys. Lett. **313**, 491 (1999).

[6] M. J. L. de Lange et al., J. Chem. Phys. **121**, 11691 (2004).

[7] H. Kohguchi and T. Suzuki, Annu. Rep. Prog. Chem. Soc. Sec. C. **98**, 421 (2002).

[8] A. E. Wiskerke et al., Faraday Discussions **96**, 297 (1993).

[9] K. H. Kramer and R. B. Bernstein, J. Chem. Phys. **40**, 200 (1964).

[10] M. G. Tenner et al., Surface Science **236**, 151 (1990).

[11] A. Gijsbertsen et al., J. Chem. Phys. **123**, 224305 (2005).

[12] G. Herzberg, *Molecular Spectra and Molecular Structure, Vol. 1, Spectra of Diatomic Molecules*, Van Nostrand and Reinhold Company, New York, 1960.

[13] R. N. Zare, *Angular Momentum: Understanding spatial aspects in chemisty and physics*, John Wiley & Sons, New York, 1988.

[14] J. M. Holas, *Modern Spectroscopy, Third Edition*, Krieger Publishing Co., Malabar, 1996.

[15] P. W. Atkins and R. S. Friedman, *Molecular quantum mechanics*, Oxford Univ. Pr., Oxford, 3. ed., repr. edition, 2001.

[16] M. J. L. de Lange, *Steric and State-to-State Depedence of Rotationally Inelastic Scattering of NO*, PhD thesis, Vrije Universiteit Amsterdam, 2003.

[17] C. Amiot, J. Molec. Spectrosc. **94**, 150 (1982).

[18] J. M. Brown et al., J. Mol. Spectroscopy **55**, 500 (1975).

[19] K. Schreel and J. J. ter Meulen, J. Chem. Phys. **101**, 7639 (1997).

[20] C. A. Burrus and W. Gordy, Phys. Rev. **92**, 1437 (1953).

[21] W. Meerts and A. Dymanus, J. Mol. Spectrosc. **44**, 320 (1972).

[22] M. H. Alexander et al., J. Chem. Phys. **89**, 1749 (1988).

[23] L. Bigio and E. R. Grant, J. Chem. Phys. **87**, 5589 (1987).

[24] P. Andresen and E. W. Rothe, J. Chem. Phys **82**, 3634 (1985).

[25] H. G. Bennewitz, W. Paul, and C. Schlier, Z. Phys. **141**, 6 (1955).

[26] K. H. Kramer and R. B. Bernstein, The Journal of Chemical Physics **42**, 767 (1965).

[27] S. R. Ghandi and R. B. Bernstein, J. Chem. Phys **87**, 6457 (1987).

[28] T. P. Rakitzis, A. J. van den Brom, and M. H. M. Janssen, Science **303**, 1852 (2004).

[29] A. Messiah, *Quantum Mechanics*, Dover Mineola NY, 1999.

[30] C. H. Townes and A. L. Schawlow, *Microwave spectroscopy*, McGraw-Hill, New York, 1955.

[31] A. J. van den Brom et al., J. Chem. Phys. **119**, 4255 (2002).

[32] R. W. Anderson, J. Phys. Chem. **101**, 7664 (1997).

[33] S. Stolte, J. Reuss, and H. L. Schwartz, Physica **57**, 254 (1972).

[34] M. S. Child, *Molecular Collision Theory*, Dover Mineola NY, 1996.

[35] R. D. Levine, *Reaction Dynamics*, Cambridge University Press, Cambridge, 2005.

[36] H. J. Loesch, Adv. Chem. Phys. **42**, 421 (1980).

[37] M. Faubel, Adv. At. Mol. Phys. **19**, 345 (1983).

[38] U. Buck, Comments At. Mol. Phys. **17**, 143 (1986).

[39] B. Whitaker, editor, *Imaging in Molecular Dynamics*, Cambridge University press, Cambridge, 2003.

[40] A. J. R. Heck and D. W. Chandler, Ann. Rev. Phys. Chem. **46**, 335 (1995).

[41] P. L. Houston, J. Phys. Chem. **100**, 12757 (1996).

[42] D. W. Chandler and P. L. Houston, J. Chem. Phys. **87**, 1445 (1987).

[43] A. T. J. B. Eppink and D. H. Parker, Rev. Sci. Instrum. **68**, 3477 (1997).

[44] T. N. Kitsopoulos, C. R. Gebhardt, and T. P. Rakitzis, J. Chem. Phys. **115**, 9727 (2001).

[45] A. Gijsbertsen et al., Chem. Phys. **301**, 293 (2004).

[46] M. C. van Beek, J. J. ter Meulen, and M. H. Alexander, J. Chem. Phys. **113**, 637 (2000).

[47] M. J. L. de Lange et al., Chem. Phys. Lett. **294**, 332 (1998).

[48] S. R. Langhoff, C. W. Bauschlicher, and H. Partridge, Chem. Phys. Lett. **223**, 416 (1994).

[49] S. Green, Chem. Phys. Lett. **23**, 115 (1973).

[50] F. P. Billingsley, J. Chem. Phys. **62**, 864 (1975).

[51] F. P. Billingsley, J. Chem. Phys. **63**, 2267 (1975).

[52] R. de Vivie and S. D. Peyerimhoff, J. Phys. Chem. A **89**, 3028 (1988).

[53] R. Sayós, R. Valero, J. M. Anglada, and M. González, J. Chem. Phys. **112**, 6608 (2000).

[54] M. H. Alexander, Faraday Discuss. Chem. Soc. **113**, 437 (1999).

[55] M. H. Alexander, J. Chem. Phys. **99**, 7725 (1993).

[56] J. Kłos et al., J. Chem. Phys. **112**, 4952 (2000).

[57] A. D. Esposti and H. J. Werner, J. Chem. Phys. **93**, 3351 (1990).

[58] A. Gijsbertsen, H. Linnartz, S. Stolte, and C. A. Taatjes, Quantum interference as the source of stereo-dynamic effects in no-rare gas inelastic scattering, 2006.

[59] HIBRIDON is a package of programs for the time independent quantum treatment of inelastic collisions written by M. H. Alexander, D. E. Manolopoulos, H.J. Werner, and B. Follmeg, with contributions by P. F. Vohralik, D. Lemoine, G. Corey, R. Gordon, B. Johnson, T. Orlikowski, A. Berning, A. Degli-Esposti, C. Rist, P. Dagdigian, B. Pouilly, G. van der Sanden, M. Yang, F. de Weerd, and S. Gregurick. More information and a copy of the code can be obtained from http://www.chem.umd.edu/physical/alexander/hibridon/.

[60] G. Groenenboom, private communications, 2005.

[61] J. M. Hutson and S. Green, MOLSCAT computer code, version 14 (1994), distributed by Collaborative Computational Project No. 6 of the Engineering and Physical Sciences Research Council (UK).

[62] A. R. Hoy, J. W. C. Johns, and A. R. W. McKellar, Can. J. Phys. **53**, 2029 (1975).

[63] M. Drabbels and A. M. Wodtke, Chem. Phys. Lett. **256**, 8 (1996).

[64] D. Matsiev, J. Chen, M. Murphy, and A. M. Wodtke, J. Chem. Phys. **118**, 9477 (2003).

[65] A. M. Arthurs and A. Dalgarno, Proc. Roy. Soc. (London), Ser. A **256**, 540 (1960).

[66] M. H. Alexander, J. Chem. Phys. **76**, 5974 (1982).

[67] M. C. van Beek, G. Berden, H. L. Bethlem, and J. J. ter Meulen, Phys. Rev. Lett. **86**, 4001 (2001).

[68] M. C. van Beek and J. J. ter Meulen, J. Chem. Phys. **115**, 1843 (2001).

[69] M. H. Alexander, J. Chem. Phys. **111**, 7426 (1999).

[70] M. C. van Beek, J. J. ter Meulen, and M. H. Alexander, J. Chem. Phys. **113**, 628 (2000).

[71] S. Stolte and J. Reuss, *Atom-Molecule Collision theory*, chapter 5, page 201, Plenum Press, New York, 1979.

[72] H. J. Loesch, Annu. Rev. Phys. Chem. **46**, 555 (1995).

[73] S. Stolte, *Atomic and Molecular Beams Methods Vol. 14*, chapter 25, page 631, Oxford University Press, New York/Oxford, 1988.

[74] D. Parker, H. Jalink, and S. Stolte, J. Phys. Chem. **91**, 5427 (1987).

[75] C. Maltz, N. O. Weinstein, and D. R. Herschbach, Molec. Phys. **24**, 133 (1972).

[76] K. W. Holtzclaw, W. T. Rawlins, and B. Green, J. Quant. Spectrosc. Radiat. Transf. **55**, 481 (1996).

[77] M. Drabbels and A. M. Wodtke, J. Chem. Phys. **106**, 3024 (1997).

[78] W. T. Rawlins, J. C. Person, M. E. Fraser, S. M. Miller, and W. A. M. Blumberg, J. Chem. Phys. **109**, 3409 (1998).

[79] Y. Kim, J. Fleniken, H. Meyer, M. H. Alexander, and P. Dagdigian, J. Chem. Phys. **113**, 73 (2000).

[80] J. Posthumus, Rep. Prog. Phys. **67**, 623 (2004).

[81] T. Brabec and F. Krausz, Rev. Mod. Phys. **72**, 545 (2000).

[82] H. Niikura et al., Nature **421**, 826 (2003).

[83] T. Kanai, S. Minemoto, and H. Sakai, J. Chem. Phys. **435**, 470 (2005).

[84] J. Itatani et al., Nature **432**, 867 (2004).

[85] J. M. L. J. Reinartz, W. L. Meerts, and A. Dymanus, Chem. Phys. **31**, 19 (1978).

[86] H. Jalink, D. H. Parker, and S. Stolte, Journal of Molecular Spectroscopy **121**, 236 (1987).

[87] A. Gijsbertsen, H. Linnartz, J. Kłos, and S. Stolte, Physica Scripta **72**, 1 (2005).

[88] B. Friedrich and D. Herschbach, J. Chem. Phys. **111**, 6157 (1999).

[89] H. Stapelfeldt and T. Seideman, Reviews of Modern Physics **75**, 543 (2003).

[90] F. Rosca-Pruna and M. J. J. Vrakking, J. Chem. Phys. **116**, 6579 (2002).

[91] K. Tanaka, H. Ito, K. Harada, and T. Tanaka, J. Chem. Phys. **80**, 5893 (1984).

[92] H. Joswig, P. Andresen, and R. Schinke, J. Chem. Phys. **85**, 1904 (1986).

[93] A. G. Suits, L. S. Bontuyan, P. L. Houston, and B. J. Whitaker, J. Chem. Phys. **96**, 8618 (1992).

[94] K. T. Lorenz, M. S. Westley, and D. W. Chandler, Phys. Chem. Chem. Phys **2**, 481 (2000).

[95] N. Yonekura, C. Gebauer, H. Kohguchi, and T. Suzuki, Rev. Sci. Instr. **70**, 2365 (1999).

[96] K. T. Lorenz et al., Science **293**, 2063 (2001).

[97] M. S. Elioff and D. W. Chandler, J. Chem. Phys. **117**, 6455 (2002).

[98] E. A. Wade et al., Chem. Phys. **301**, 1 (2004).

[99] S. D. Jons, J. E. Shirley, M. T. Vonk, C. F. Giese, and W. R. Gentry, J. Chem. Phys. **105**, 5397 (1996).

[100] R. B. Gerber, V. Buch, U. Buck, G. Maneke, and J. Schleusener, Phys. Rev. Lett. **44**, 1397 (1980).

[101] R. Schinke, J. Chem. Phys. **73**, 12 (1980).

[102] M. S. Westley, K. T. Lorenz, D. W. Chandler, and P. L. Houston, J. Chem. Phys. **2**, 473 (2001).

[103] M. Yang and M. H. Alexander, J. Chem. Phys. **103**, 6973 (1995).

[104] H. Kohguchi, T. Suzuki, and M. H. Alexander, Science **294**, 832 (2001).

[105] F. Harren, D. H. Parker, and S. Stolte, Comments At. Mol. Phys. **26**, 109 (1991).

[106] J. I. Cline, K. T. Lorenz, E. A. Wade, J. W. Barr, and D. W. Chandler, J. Chem. Phys. **115**, 6277 (2001).

[107] V. Khare, D. J. Kouri, and D. K. Hoffmann, J. Chem. Phys. **74**, 2275 (1981).

[108] H. Meyer, J. Chem. Phys. **102**, 3151 (1995).

[109] Y. Kim, H. Meyer, and M. H. Alexander, J. Chem. Phys. **121**, 1339 (2004).

[110] M. H. Alexander, Chem. Phys. **92**, 337 (1985).

[111] G. C. Corey and M. H. Alexander, J. Phys. Chem. A **85**, 5652 (1986).

[112] D. J. Kouri and D. K. Hoffman, Theor. Chem. Acc. **103**, 281 (2000).

[113] D. A. Case, D. G. M. McClelland, and D. R. Herschbach, Mol. Phys. **35**, 54 (1978).

[114] J. Kłos, G. Chalasinski, M. T. Berry, R. Bukowski, and S. M. Cybulski, J. Chem. Phys. **112**, 2195 (2000).

[115] D. C. Jacobs and R. N. Zare, J. Chem. Phys. **65**, 5457 (1986).

[116] L. T. Earls, Phys. Rev. **48**, 423 (19735).

[117] D. M. Neumark, A. M. Wodtke, G. N. Robinson, C. C. Hayden, and Y. T. Lee, J. Chem. Phys. **82**, 3045 (1985).

[118] U. Beck, U. Ross, and W. Schlepper, Z. Physik A **293**, 107 (1979).

[119] S. Bosanac, Phys. Rev. A **22**, 2617 (1980).

[120] S. Bosanac and U. Buck, Chem. Phys. Lett. **81**, 315 (1981).

[121] H. J. K. R. Schinke, J. Chem. Phys. **73**, 1222 (1980).

[122] J. M. Bowman and K. T. Lee, J. Chem. Phys. **74**, 2664 (1981).

[123] H. J. K. R. Schinke, J. Chem. Phys. **75**, 3850 (1981).

[124] K. T. Lorenz, D. W. Chandler, and G. C. McBane, J. Phys. Chem. A. **106**, 1144 (2002).

[125] G. C. McBane and S. M. Cybulski, J. Chem. Phys. **110**, 11734 (1999).

[126] R. Schinke and J. M. Bowman, *Molecular Collision Dynamics*, chapter Rotational Rainbows in Atom-Diatom Scattering, page 61, Springer Verlag, Berlin, 1983.

[127] U. Buck and V. Khare, J. Chem. Phys. **97**, 215 (1977).

[128] A. S. Dickenson and D. Richards, Adv. At. Mol. Phys. **18**, 165 (1982).

[129] H. J. Korsch and A. Ernesti, J. Phys. B. **25**, 3565 (1992).

[130] R. W. Fenstermaker and R. B. Bernstein, J. Chem. Phys. **47**, 4417 (1967).

[131] R. J. Cross, J. Chem. Phys. **49**, 1753 (1968).

[132] C. F. Curtiss, J. Chem. Phys. **49**, 1952 (1968).

[133] R. T. Pack, J. Chem. Phys. **60**, 633 (1974).

[134] P. McGuire and D. J. Kouri, J. Chem. Phys. **60**, 2488 (1974).

[135] A. S. Dickenson and D. Richards, J. Phys. B. **6**, 1085 (1978).

[136] V. Khare, D. J. Kouri, and D. K. Hoffmann, J. Chem. Phys. **76**, 4493 (1982).

[137] D. K. Hoffman, J. Chem. Phys **50**, 4823 (1969).

[138] G. T. Evans, R. S. C. She, and R. B. Bernstein, J. Chem. Phys. **682**, 2258 (1985).

[139] R. S. C. She, G. T. Evans, and R. B. Bernstein, J. Chem. Phys. **84**, 2204 (1986).

[140] H. Pauly and J. P. Toennies, *Methods of Experimental Physics*, volume 7, Part A, chapter Neutral-Neutral Interactions, page 227, Academic Press, New York, 1968.

[141] S. C. Althorpe and D. C. Clary, Ann. Rev. Phys. Chem. **54**, 495 (2003).

[142] V. Khare, D. J. Kouri, and D. K. Hoffmann, J. Chem. Phys. **74**, 2656 (1981).

[143] W. A. Lester, *Meth. Comp. Phys.*, volume 10, Academic Press, New York, 1971.

[144] C. W. McCurdy and W. H. Miller, J. Chem. Phys. **67**, 463 (1977).

[145] M. Drabbels, A. M. Wodtke, M. Yang, and M. H. Alexander, J. Phys. Chem. A **101**, 6463 (1997).

[146] F. J. Aoiz, J. E. Verdasco, V. J. Herrero, V. S. Rábanos, and M. H. Alexander, J. Chem. Phys. **119**, 5860 (2003).